Remote monitoring of shallow turbulent flows based on the Doppler spectra of airborne ultrasound

By:

Giulio Dolcetti

A thesis submitted in partial fulfilment of the requirements for the degree of
Doctor of Philosophy

The University of Sheffield
Faculty of Engineering
Department of Mechanical Engineering

November 2016

To my family,

Remote monitoring of shallow turbulent flows based on the Doppler spectra of airborne ultrasound

Abstract

Traditional flow monitoring techniques where the sensors are immersed in the flow are costly, and often need frequent maintenance. Non-contact measurement techniques can be used to determine the hydraulic conditions of free surface flows based on a characterisation of the air-water interface. They are robust, relatively cheap, and can be safely operated, but their applications in shallow turbulent flows such as rivers and open channels are limited by the limited understanding of the free surface roughness behaviour. This research aims at characterising the rough moving surface of shallow turbulent water flows and its interaction with airborne acoustic waves. The purpose of this work is to facilitate the development of accurate and reliable non-contact sensors that can measure the mean surface velocity of shallow turbulent flows from the Doppler spectrum of airborne backscattered ultrasonic waves. The dynamics of the free surface were characterised experimentally in a laboratory flume with a homogeneously rough flat bed, over a range of subcritical flow conditions. The three-dimensional patterns on the free surface can be represented by a model of gravity-capillary waves with random phase. These patterns and their statistics are dominated by the spatial and temporal scales of the stationary waves generated by the interaction with the rough bed in all conditions where the mean surface velocity is larger than the minimum phase velocity of gravity-capillary waves. When the mean surface velocity is smaller than the minimum phase velocity of gravity-capillary waves, the surface shows patterns that travel at the mean surface velocity and can be generated by the non-resonant interaction with turbulence inside the flow. In these conditions, the effects of coherent turbulent structures on the surface dynamics are negligible. A simplified linear model of the free surface dynamics was implemented in two different models of acoustic scattering based on the Kirchhoff approximation. The numerical predictions of the acoustic Doppler spectra in the backscattering and in the forward scattering configuration were compared with the experimental measurements in the same flow conditions. The comparison allows the rigorous interpretation of the measured Doppler spectra, and helps to identify the factors that link them to the behaviour of the free surface. The results can inform the design of more reliable non-contact measurement sensors with applications in shallow turbulent flows. There are important implications for modelling of the interaction between a homogeneously rough bed and the free surface, and for the study of transport and mixing phenomena near the interface.

Acknowledgements

I would like to express my sincere gratitude to Doctor Anton Krynkin, Professor Kirill Horoshenkov, and Professor Simon Tait, for being my supervisors. It was a privilege having such a knowledgeable and supportive team to guide me and motivate me throughout the highs and lows of these intense few years. The knowledge, skills, and attitudes I learnt from them have helped me grow personally and professionally. I am deeply grateful to Doctor Andrew Nichols, of whom I admire the intuition and technical skills. His previous work set the basis of this thesis, and his help with setting up the experimental apparatus and acquisition system was priceless.

This study would not have been possible without the support from ADS LLC. I am grateful to Hal Kimbrough and Matthew Kendall for fostering this collaboration and for the continuous support to the project. I am sincerely grateful to Jim Schutzbach and Jos Dominguez for sharing their expertise and engineering skills, and for understanding the passion for the topics of this study.

Deep gratitude goes to the technical staff of the University of Bradford and University of Sheffield for their technical aid and advice, most notably to Nigel Smith, Kenneth Howell, Paul Osborne, Alex Cargill, and Ben Kitchener.

During these years I had the privilege of meeting some of the most important researchers in the fields of Acoustics and Fluid Mechanics. Some of them had a deep impact on this work, which must be acknowledged. Doctor Miguel Teixeira suggested the interpretation of the free surface patterns based on the interaction of gravity-capillary waves with the static rough bed. Doctor Francisco Ocampo Torres suggested the implementation of the wavelet spectral method, and provided the contact of Doctor Héctor García Nava, who developed the Matlab routine that was used for its calculation. Doctor Chris Keylock suggested the gradual wavelet reconstruction as a way to check the validity of the random linear surface model.

I would like to thank Eslam Gabreil for helping with the calibration of the wave probe arrays, Ethan Gardner and Samuel Hunting for the help with carrying out some of the experiments, Stephen Theofanous for transforming the water waves into music, and my colleagues in Bradford and in Sheffield for their sympathy and encouragement during the various stages of the PhD.

My personal thanks and deep admiration are for my parents and my brother, for Eleonora, and for all friends who showed love and support throughout these last years.

Publications

Journal Publications

G. Dolcetti, K. V. Horoshenkov, A. Krynkin and S. J. Tait. Frequency-wavenumber spectrum of the free surface of shallow turbulent flows over a rough boundary, *Physics of Fluids*, **28**: 105105, 2016.

A. Krynkin, G. Dolcetti, and S. Hunting. Acoustic imaging in application to reconstruction of rough rigid surface with airborne ultrasound waves (under review by Review of Scientific Instruments), 2016.

Conference Publications

A. Krynkin, G. Dolcetti, K. V. Horoshenkov, and T. van Renterghem. Use of scattered airborne acoustics wave-field to recover profile of surface of shallow water flow, In *Proceedings of the Institute of Acoustics*, **37**, 231-234, 2015.

G. Dolcetti, A. Krynkin, and K. V. Horoshenkov. Characterisation of the free surface, turbulent water flows with an array of ultrasonic sensors, In *Proceedings of the 22nd International Congress on Sound and Vibration (ICSV22)*, **4**, 2745-2750, 2015.

G. Dolcetti, A. Krynkin, K. V. Horoshenkov, and S. J. Tait. Analysis of scattered acoustic signals to characterise the behaviour of the free surface of shallow water flows, In *E-proceedings of the 36th IAHR World Congress*, **28**, 2015.

G. Dolcetti, A. Krynkin, K. V. Horoshenkov, and S. J. Tait. The spectrum of the acoustic waves backscattered by the dynamic rough surface of a shallow water flow, In *Proceedings of the Institute of Acoustics*, **36**, 422-429, 2014.

Contents

List of Figures

List of Tables

Nomenclature

Script symbols

Symbol	Description	Units
$\mathcal{G}$	The Green's function.	
$\mathcal{H}(f)$	The Hilbert transform of the function f.	
$\Im(f)$	The imaginary part of the function f.	
$\mathcal{M}$	The Morlet mother wavelet.	
$\Re(f)$	The real part of the function f.	
$\boldsymbol{\mathcal{U}}$	The velocity field in the flow, $\boldsymbol{\mathcal{U}} = (\mathcal{U}, \mathcal{V}, \mathcal{W})$.	$\mathrm{m\,s^{-1}}$

Greek Symbols

Symbol	Description	Units
α	The power-function slope coefficient of the wavenumber power spectrum of the surface elevation.	
α_m	Calibration coefficient of the U-tube manometer.	
β_m	Calibration coefficient of the U-tube manometer.	
χ_q	The cumulant of order q the distribution of the surface elevation.	
δ	The delta function.	
δ_r	The size of the bins used for the calculation of the space-time correlation function.	m
$\delta_{surr.}$	The convergence parameter for the generation of synthetic constrained surrogate time-series with the gradual wavelet reconstruction method.	

ϵ_I	Uncertainty of the surface elevation measurement due to the presence of the meniscus.	m
ϵ_{II}	Uncertainty of the surface elevation measurement due to the flow run-up.	m
ϵ_{III}	Uncertainty of the surface elevation measurement due to the finite distance between the wires.	m
$\Gamma(k, \theta)$	The directional distribution, or factor that describes the dependence of the wavenumber spectrum of the surface elevation on the direction of propagation.	
$\Gamma_\theta(\theta)$	The factor of the directional distribution which shows the dependence on the angle of propagation θ.	
$\Gamma_k(k)$	The factor of the directional distribution which shows the dependence on the wavenumber k.	
Γ_r	The width of the kernel for the interpolation of the correlation function.	
γ_w	Surface tension coefficient. $\gamma_w = 72.75 \times 10^{-3}\,\mathrm{N\,m^{-1}}$ at the temperature of 20 °C.	$\mathrm{N\,m^{-1}}$
κ	The wavenumber of the acoustic waves.	$\mathrm{rad\,m^{-1}}$
λ_3	The skewness coefficient.	
λ_4	The coefficient of kurtosis.	
λ_a	The acoustic wavelength.	m
λ_B	The wavelength of the Bragg waves.	m
μ	The index of the discrete time-series, $t_\mu = \mu\Delta t$, $\mu = 1, 2, ..., M$.	
μ_w	The dynamic viscosity of water, $\mu_w = 1.002 \times 10^{-3}\mathrm{Pa\,s}$ at the temperature of 20 °C.	Pa s
ν	The index representing each waveprobe, e.g., $\nu = 3_{(y)}$ is the third probe of the first lateral array.	
$\hat{\omega}$	The radian frequency normalised by the characteristic frequency of the stationary waves, $\hat{\omega} = \omega/k_0U_0$.	
ω	The radian frequency, $\omega = 2\pi f$.	$\mathrm{rad\,s^{-1}}$
$\Omega(k, \theta)$	The general form of a dispersion relation.	$\mathrm{rad\,s^{-1}}$

ω_a	The radian frequency of the acoustic waves emitted by the source.	$\mathrm{rad\,s^{-1}}$
Ω_B	The frequency of the Bragg scale waves.	$\mathrm{rad\,s^{-1}}$
ω_G	The centre-band radian frequency employed for the analysis of the narrow-band envelope.	$\mathrm{rad\,s^{-1}}$
ω_j	The characteristic frequency of the Morlet wavelet.	$\mathrm{rad\,s^{-1}}$
Ω_s	The dispersion relation of gravity-capillary waves in still water.	$\mathrm{rad\,s^{-1}}$
$\hat{\phi}$	The short-time average of the acoustic phase $\tilde{\phi}$ in time.	rad
Φ	The phase of the complex envelope of the free surface elevation.	rad
Φ^+,Φ^-,Φ^U	Random variables with uniform distribution in the interval between 0 and 2π.	rad
Φ_C	A constant phase.	rad
Φ_W	The phase of the wavelet transform of the surface elevation ζ measured at the probe ν, at the characteristic frequency ω_j, $\Phi_W(x_\nu, y_\nu, t, \omega_j) \equiv \Phi_{W,\nu}(t, \omega_j)$.	rad
$\tilde{\phi}(t)$	The phase of the signal measured with an ultrasonic transducer, as found with the Hilbert transform.	rad
$\check{\Psi}$	The non-dimensional depth-dependent factor of the vertical perturbation velocity w.	
Ψ	The depth-dependent factor of the vertical perturbation velocity w.	$\mathrm{m\,s^{-1}}$
ψ	The angle of incidence of the acoustic waves with respect to the tangent to the average flat surface.	rad
ψ_s	The angle of inclination of the acoustic transducer with respect to the tangent to the average flat surface.	rad
$\boldsymbol{\rho}$	The radial polar co-ordinate in the plane $x - y$.	m
ρ_w	Density of water. $\rho_w = 998.2\,\mathrm{kg\,m^{-3}}$ at the temperature of 20 °C.	$\mathrm{kg\,m^{-3}}$
$\tilde{\boldsymbol{\rho}}$	The co-ordinate along the rough surface Σ.	m
Σ	The rough surface.	

σ	The spatially averaged standard deviation of the free surface elevation, measured in time.	m
σ_ν	The standard deviation of the free surface elevation, measured at the probe ν.	m
Σ_0	The flat surface represented by $z \equiv 0$.	
σ_j^G	The fitted width of the ridge of the normalised streamwise frequency-wavenumber spectrum.	$\mathrm{rad\,m^{-1}}$
σ_W	The width of the Morlet mother wavelet.	
$\sigma_{\omega,G}$	The width of the Gaussian filter.	$\mathrm{rad\,s^{-1}}$
τ	The time-lag.	s
τ_R	The Reynolds stresses.	N
θ	Angle of propagation of a wave with respect to the direction of the mean flow.	rad
θ_m	Angle from the main axis of the acoustic receiver.	rad
θ_s	Angle from the main axis of the acoustic source.	rad
$\theta_{\min}$	Minimum angle of propagation of a stationary wave with respect to the direction of the mean flow.	rad
Υ	The eigenfunctions of a discrete Fourier transform.	
υ	The index of the iterations, for the iterative interpolation of the correlation function.	
$\hat{\varepsilon}$	The correction of the reconstruction of the correlation function.	
ε	The residual of the reconstruction of the correlation function.	
ε_k	The root mean squared average distance between the measured and predicted dispersion relations, evaluated along the wavenumber axis.	$\mathrm{rad\,m^{-1}}$
ϖ	An under-relaxation factor.	
ϱ_w	The similarity ratio, which represents the constrained portion of the surrogate synthetic data.	
ς	The angular polar co-ordinate in the plane $x-y$.	rad
ξ^+,ξ^-,ξ^U	Random variables with normal distribution.	

$\dot{\zeta}$	The time gradient of the free surface elevation.	$\mathrm{m\,s^{-1}}$
$\hat{\zeta}$	The non-dimensionalised free surface elevation.	
ζ	The free surface elevation with respect to the mean surface level, H.	m
$\zeta_{W,\nu}(t, \omega_j)$	The complex wavelet transform of the surface elevation ζ measured at the probe ν, evaluated at the characteristic frequency ω_j.	m

Roman Symbols

Symbol	**Description**	**Units**
$\breve{A}$	The eigenvalue of a discrete Fourier transform.	m
a	A function of the Reynolds number and of the relative submergence.	
$A(\mathbf{k}, \omega)$	The amplitude spectrum of the surface fluctuations.	$\mathrm{m\,s}$
A_j^G	The fitted amplitude of the ridge of the normalised frequency wavenumber spectrum.	
b_θ	The parameter of the directional distribution Γ_θ.	
c	The phase speed of gravity-capillary waves.	$\mathrm{m\,s^{-1}}$
C_1,C_2	Real constants.	
c_a	The speed of sound in air, $c_a = 343\,\mathrm{m\,s^{-1}}$ at the temperature of 20 °C.	$\mathrm{m\,s^{-1}}$
c_g	The group velocity of gravity-capillary waves.	$\mathrm{m\,s^{-1}}$
C_S	The ratio of the frequency-wavenumber spectrum measured along different dispersion relations.	
c_s	The phase speed of gravity-capillary waves in still water.	$\mathrm{m\,s^{-1}}$
$c_{\min}$	The minimum phase speed of gravity-capillary waves in still water, $c_{\min} \approx 0.23\,\mathrm{m\,s^{-1}}$.	$\mathrm{m\,s^{-1}}$
D_m	The angular acoustic response of the receiver.	
D_s	The directivity pattern of the acoustic source.	
d_s	The characteristic size of the bed roughness, or the diameter of the spheres on the flume bed.	m

d_w	The diameter of the conductance wave probe wires.	m
F	The Froude number based on the mean surface velocity and mean water depth, $F = U_0\sqrt{gH}$.	
f	The friction factor, defined as $f = 8(u_*/U_H)$.	
f_s	The sampling frequency.	Hz
f_v	The frequency of vortices shed by a circular cylinder immersed in a water flow.	Hz
G	A type of Green's function.	
g	The gravity constant $g = 9.81\,\mathrm{m\,s^{-2}}$.	$\mathrm{m\,s^{-2}}$
$\bar{h}$	The vector of the multiplicative factor $Q(\mathbf{r})$ of the linear acoustic Doppler model.	$\mathrm{rad\,m^{-2}}$
H	The flow mean depth.	m
$H_0^{(1)}$	The Hankel function of the first kind of order 0.	
H_j	The Hermite polynomial of order j.	
i	The imaginary unit, $i = \sqrt{-1}$.	
I_n	The modified Bessel function of order n.	
J_1	The Bessel function of the first kind.	
$\check{k}$	The non-dimensional wavenumber of the gravity-capillary waves.	
$\hat{k}$	The wavenumber normalised by the wavenumber of the stationary waves, $\hat{k} = k/k_0$.	
$\mathbf{k}$	The wavenumber vector of the free surface patterns, $\mathbf{k} = (k_x, k_y)$.	$\mathrm{rad\,m^{-1}}$
$\mathbf{K}(\omega)$	The inverse of the dispersion relation $\Omega(\mathbf{k})$.	$\mathrm{rad\,m^{-1}}$
k_0	The wavenumber of the stationary waves (chapter 4), or the characteristic wavenumber of the surface elevation (chapter 5).	$\mathrm{rad\,m^{-1}}$
k_1	The wavenumber of the smallest waves resolved by the surface model.	$\mathrm{rad\,m^{-1}}$
k_B	The wavenumber of the Bragg waves.	$\mathrm{rad\,m^{-1}}$

k_s	The Nyquist wavenumber.	$\mathrm{rad\,m^{-1}}$
$k_{x,j}^{G}$	The fitted streamwise wavenumber of the normalised streamwise frequency-wavenumber spectrum.	$\mathrm{rad\,m^{-1}}$
l_0	The characteristic correlation length of the free surface.	m
l_1	The wavelength of the smallest waves resolved by the surface model, $l_1 = 2\pi/k_1$.	m
L_D	The size of the insonificated area.	m
L_F	The size of the Fresnel zone.	m
L_x,L_y	The length of the streamwise and of the lateral arrays of probes, respectively.	m
l_x,l_y	The correlation lengths of the surface elevation in the streamwise and in the lateral direction, respectively.	m
$\mathbf{M}$	The co-ordinates of the acoustic receiver, $\mathbf{M} = (x_m, y_m, z_m)^T$.	m
M	The number of point of a data time series.	
$m_{f,q}$	The statistical moment of order q of the function f, averaged across all probes.	
$m_{f,q}^{(\nu)}$	The statistical moment of order q of the function f, measured at probe ν.	
$\mathbf{n}$	The unit vector normal to the surface.	
n	The exponent of the power-function vertical profile of the average streamwise velocity in the flow.	
N_ζ	The number of bins used to determine the statistical distribution of the free surface elevation, $p_\zeta^\nu(\zeta)$.	
N_p	The number of wave probes in one array.	
N_x,N_y	The number of unique non-negative spatial separations between wave probes of the streamwise and lateral array, respectively.	
$\hat{P}$	The short-time average of the amplitude of the Hilbert transform of the acoustic pressure.	Pa

$\tilde{P}$	The amplitude of the Hilbert transform of the acoustic pressure.	Pa
P	The acoustic potential, or the normalised acoustic pressure in chapter 6.	$\mathrm{m^2\,s^{-1}}$
P_i	The acoustic incident field.	$\mathrm{m^2\,s^{-1}}$
p_a	The acoustic pressure.	Pa
$p_f(f)$	The probability density function of the variable f averaged across all probes.	
$p_f^{(\nu)}(f)$	The probability density function of the variable f measured with the probe ν.	
p	The pressure in water.	Pa
p_m	Pressure difference measured by the U tube manometer.	Pa
$\mathbf{q}$	The linearised vector difference between the scattered and the incident acoustic wavenumber.	$\mathrm{rad\,m^{-1}}$
$\tilde{\mathbf{q}}$	The vector difference between the scattered and the incident acoustic wavenumber.	$\mathrm{rad\,m^{-1}}$
$\tilde{\mathbf{q}}_\perp$	The horizontal component of the vector difference between the scattered and the incident acoustic wavenumber.	$\mathrm{rad\,m^{-1}}$
$Q(\mathbf{r})$	The factor of the linear acoustic Doppler model.	$\mathrm{rad\,m^{-2}}$
Q_S	The acoustic source density.	$\mathrm{s^{-1}}$
Q_v	The volumetric flow discharge, $Q_v = U_m H W_f$.	$\mathrm{m^3\,s^{-1}}$
$\mathbf{q}_\perp$	The horizontal component of the linearised vector difference between the scattered and the incident acoustic wavenumber.	$\mathrm{rad\,m^{-1}}$
q_z	The vertical component of the vector difference between the scattered and the incident acoustic wavenumber.	$\mathrm{rad\,m^{-1}}$
$\bar{r}_e$	The equidistant set of spatial separations.	m
$\bar{r}_n$	The binned non-equidistant set of spatial separations.	m
$\mathbf{R}$	The co-ordinates of a generic location.	

$\mathbf{r}$	The spatial separation, $\mathbf{r} = (r_x, r_y)$.	m
$\tilde{R}_m(\boldsymbol{\rho})$	The distance from the point on the rough surface with co-ordinates (ρ_x, ρ_y, ζ) to the receiver.	m
$\tilde{R}_s(\boldsymbol{\rho})$	The distance from the source transducer to the point on the rough surface with co-ordinates (ρ_x, ρ_y, ζ).	m
R_c	The radius of curvature of the surface elevation, with components R_x and R_y.	m
r_s	The radius of the acoustic source transducer.	m
$R_m(\boldsymbol{\rho})$	The distance from the point on the average flat surface with co-ordinates $(\rho_x, \rho_y, 0)$ to the receiver.	m
$R_s(\boldsymbol{\rho})$	The distance from the source transducer to the point on the average flat surface with co-ordinates $(\rho_x, \rho_y, 0)$.	m
r_n	The non-equidistant set of spatial separations.	m
Re	The Reynolds number based on the mean surface velocity and mean water depth, $Re = \rho_w U_0 H/\mu_w$.	
Re_H	The Reynolds number based on the depth-averaged velocity and mean water depth, $Re_H = 4\rho_w U_H H/\mu_w$.	
Re_w	The Reynolds number based on the mean surface velocity and diameter of the wave probe wires, $Re = \rho_w U_0 d_w/\mu_w$.	
$\bar{\bar{S}}$	The frequency-wavenumber spectrum expressed in matrix form.	$\mathrm{m\,s\,rad^{-2}}$
$\bar{S}_D$	The Doppler spectrum expressed in vector form.	
$\bar{S}_{x,y}(k_x, \omega)$	The normalised frequency-wavenumber spectrum of the free surface elevation non-dimensionalised by its average at the frequency ω, measured along the streamwise and the lateral direction, respectively. $\bar{S}_x(k_x, \omega) = S_x(k_x, \omega)/(S_x(\omega)/k_{s,x})$, $\bar{S}_y(k_y, \omega) = S_y(k_y, \omega)/(S_y(\omega)/k_{s,y})$	
$\mathbf{S}$	The co-ordinates of the acoustic source, $\mathbf{S} = (x_s, y_s, z_s)^T$.	m

$\mathbf{S}^{-}$	The co-ordinates of the image acoustic source, $\mathbf{S} = (x_s, y_s, -z_s)^T$.	m
s	The channel slope.	
$S(\mathbf{k})$	The spatial power spectrum of the free surface elevation, $S(\mathbf{k}) = S(k, \theta)$.	$\mathrm{m}^2\,\mathrm{rad}^{-2}$
$S(\mathbf{k}, \omega)$	The frequency-wavenumber spectrum of the free surface elevation.	$\mathrm{m}^2\,\mathrm{s}\,\mathrm{rad}^{-3}$
$S(\omega)$	The normalised frequency power spectrum of the free surface elevation, averaged across all probes.	$\mathrm{s}\,\mathrm{rad}^{-1}$
S_0	The normalisation factor of the wavenumber spectrum.	
$S_\nu(\omega)$	The normalised frequency power spectrum of the free surface elevation measured by the probe ν.	$\mathrm{s}\,\mathrm{rad}^{-1}$
S_D	The Doppler spectrum of the scattered acoustic potential field.	
$S_{surr.}(\omega)$	The normalised frequency power spectrum of the synthetic surrogate time-series.	$\mathrm{s}\,\mathrm{rad}^{-1}$
$S_{x,y,Z}(k_x, \omega)$	The normalised frequency-wavenumber spectrum of the envelope of the surface elevation, measured along the streamwise and the lateral array, respectively.	$\mathrm{m}\,\mathrm{s}\,\mathrm{rad}^{-2}$
$S_{x,y}(\omega)$	The spatially averaged normalised frequency power spectrum of the free surface elevation calculated from the frequency wavenumber spectrum in the streamwise and lateral direction, respectively.	$\mathrm{s}\,\mathrm{rad}^{-1}$
$S_{x,y}(k_x, \omega)$	The normalised frequency-wavenumber spectrum of the free surface elevation, measured along the streamwise and the lateral array, respectively.	$\mathrm{m}\,\mathrm{s}\,\mathrm{rad}^{-2}$
s_q	The average of the frequency spectral moment of order q across all probes.	$\mathrm{rad}^{\mathrm{q}}\,\mathrm{s}^{-\mathrm{q}}$
$s_q^{(\nu)}$	The frequency spectral moment of order q, measured from $S_\nu(\omega)$	$\mathrm{rad}^{\mathrm{q}}\,\mathrm{s}^{-\mathrm{q}}$
Sr_w	The Strouhal number based on the mean surface velocity and diameter of the wave probe wires, $Re = \rho_w U_0 d_w / \mu_w$.	

T	The length of the measured data in time.	s
t	Time.	s
T_0	The characteristic width of the linearised wave group in time.	s
$\check{U}$	The non-dimensional component of the mean surface velocity in the direction parallel to the wavenumber vector k.	
$\mathbf{u}$	The perturbation velocity field, $\mathbf{u} = (u, v, w)$.	$\mathrm{m\,s^{-1}}$
$\mathbf{u}'$	The perturbation velocity field in the wave reference system, $\mathbf{u}' = (u', v', w')$.	$\mathrm{m\,s^{-1}}$
$\mathbf{u}_a$	The velocity of the acoustic field.	$\mathrm{m\,s^{-1}}$
U'	The component of the time averaged flow velocity parallel to the wavenumber vector of a surface wave.	$\mathrm{m\,s^{-1}}$
$U(z)$	The time averaged flow velocity at the depth z.	$\mathrm{m\,s^{-1}}$
u_*	The shear velocity.	$\mathrm{m\,s^{-1}}$
U_0	The flow mean surface velocity.	$\mathrm{m\,s^{-1}}$
U_H	The depth-averaged velocity.	$\mathrm{m\,s^{-1}}$
V'	The component of the time averaged flow velocity orthogonal to the wavenumber vector of a surface wave.	$\mathrm{m\,s^{-1}}$
$w_\omega(\omega_W, \omega)$	The Fourier transform of the Morlet wavelet with the characteristic frequency ω_W.	
W_f	The flume width.	m
$w_H(\bar{r}_e, \tau_m)$	Window function.	
$w_{i,j}(t)$	The Morlet wavelet with the characteristic frequency ω_j centred at the time t_i.	
$\hat{W}_{x,y}(\bar{r}_e, \tau_m)$	The regularised correlation function of the free surface elevation interpolated at the equidistant set of separations $\bar{r}_e$, measured with the streamwise and lateral array of wave probes, respectively.	

$W(r_x, r_y, \tau)$	The space-time correlation function of the free surface elevation in the two spatial dimensions x and y.	
$W_t^{(n)}(\tau_m)$	The time correlation function of the free surface elevation at the separation r_n.	
$W_{x,y,Z}(\bar{r}_n, \tau_m)$	The space-time correlation function of the envelope of the elevation at the non-equidistant binned separations $\bar{r}_n$, measured with the streamwise and lateral array of wave probes, respectively.	
$W_{x,y}(\bar{r}_n, \tau_m)$	The space-time correlation function of the free surface elevation at the non-equidistant binned separations $\bar{r}_n$, measured with the streamwise and lateral array of wave probes, respectively.	
x,y,z	The flume system of co-ordinates, where x is parallel to the mean surface velocity.	
x',y',z'	The wave system of co-ordinates, where x' is parallel to the wavenumber vector.	
$\bar{Z}_W(t, \omega)$	The weighting function applied to the wavelet spectral method.	m
$\check{z}$	The non-dimensional z-co-ordinate	
$\tilde{Z}$	The complex envelope of the free surface elevation with real and imaginary components Z_R and Z_I, respectively, $\tilde{Z} = Z_R + iZ_I$.	m
$Z_W(x_\nu, y_\nu, t, \omega)$	The amplitude, or absolute value of the wavelet transform of the surface elevation ζ measured at the probe ν, at the characteristic frequency ω, $Z_W(x_\nu, y_\nu, t, \omega) \equiv Z_{W,\nu}(t, \omega)$.	m
$Z_{\nu,\mu}$	The envelope of the free surface elevation, corresponding to the amplitude of the Hilbert transform of $\zeta_{\nu,\mu}$	m
z_c	The location of the critical layer.	
Z	The absolute value of the envelope of the free surface elevation.	m

Acronyms

B&K Brüel & Kjær. xv, xvi, 73–75, 77, 78

DFT Discrete Fourier Transform. 86, 88

GWR Gradual Wavelet Reconstruction. 44–46, 63

IAAFT Iterated Amplitude Adjusted Fourier Transform. 44

LLC. limited liability company. 25

MODWT Maximal Overlap Discrete Wavelet Transform. 44–46

NI National Instrument. 72, 74

pdf probability density function. xvii, xviii, xxi, xxii, 42–44, 46, 47, 63, 87, 98, 104, 106, 108, 109, 112, 114, 115, 142, 144–149

PIV Particle Image Velocimetry. 19, 24, 67

rms root mean square. 73

SPM small perturbation method. 21, 22

SVD singular value decomposition. 27

Chapter 1

Introduction

1.1 Background and motivation

The modelling and measurement of the hydraulic flow conditions in rivers and open channels are of great importance for the forecasting of flood risks, for the study of sediment transport, and for the conservation and enhancement of riverine habitat [e.g. Bates et al., 1997]. As population growth and the effects of climate change become progressively more visible, there is a growing need to better understand these phenomena, and to increase the quality of measurement sensors in order to reduce their uncertainty [e.g. Sayers et al., 2015]. Traditional sensors are installed underwater. This increases the needs and costs of maintenance, limits the flexibility of the measurement system, and involves higher risks for the operators [Costa et al., 2006]. Non-contact measurement devices that can estimate the hydraulic conditions (mainly the flow discharge and/or the flow mean surface velocity) from above the water surface have become increasingly popular [Marcus and Fonstad, 2010], particularly with the advancement of unmanned aerial vehicles which can be used for their deployment. In some cases the physical grounds of this type of measurements have not been rigorously examined, or the direct link between the measured quantities and the physical parameters of the flow require a complex calibration [Marcus and Fonstad, 2008]. As a result, the measurements often rely on empirical laws obtained in limited ranges of conditions. These considerations apply especially to those devices that determine the hydraulic conditions based on the shape and the dynamics of the free surface neglecting the effects of gravity-capillary waves [e.g. Fujita et al., 2007]. The links between the free surface of open-channel and river flows and the hydraulic conditions have not been fully clarified yet, and this causes large uncertainties of the measurements [Welber et al., 2016].

The characterisation of the water surface of turbulent flows is of interest in itself, since it is related to important processes such as the transport of scalars [e.g. Nagaosa and Handler, 2003, 2012] and the mixing of gas [e.g. Lakehal et al., 2003, Turney and Banerjee, 2013]. Various authors have suggested that turbulent coherent structures in a turbulent flow are able to generate characteristic patterns on the free surface [Tsai, 1998, Savelsberg and van de Water, 2009, Fujita et al., 2011, Horoshenkov et al., 2013, Nichols et al., 2016]. If measured properly, these patterns would allow the remote characterisation of the large eddies which are fundamental for the processes of transport and mixing of gas and scalars. Although there is widespread agreement that these patterns form, there is very little experimental evidence of a strong interaction between turbulence and the free surface at least in subcritical flows. In fact, the correlation between the geometry of the free surface and turbulent quantities was found to be very low in the experiments of Fujita et al. [2007] and Savelsberg and van de Water [2009].

The lack of correlation is often attributed to the presence of gravity-capillary waves at the free surface [Savelsberg and van de Water, 2009]. These waves can propagate a long distance from where they formed, and consequently affect the correlation with the local properties of the flow. Gravity-capillary waves have been studied for almost two centuries, in the ocean but also in rivers and open-channels [e.g. Stokes, 1847, Lamb, 1932]. When the studies of Miles [1957] and Phillips [1958] emerged, they provided a new rigorous explanation for the generation of ocean waves by the action of wind. These studies also appeared at a time when radar and sonar technologies were developing rapidly. This synergy was the impulse that drove the advancement of the research on ocean waves and on electromagnetic and acoustic scattering for many years. For reasons that are probably related to economic and strategic interests as well as to the complexity of the mathematical problem, the use of remote monitoring techniques has been largely limited to oceanic applications, somehow neglecting free surface turbulent flows until the last decade [Marcus and Fonstad, 2010].

The standard theory of gravity-capillary waves is based on strong simplifications of the flow dynamics, most relevantly for this thesis as it generally neglects turbulence. Nevertheless, some attempts to apply this theory to turbulent flows have been made. For example, the behaviour of gravity-capillary waves in relation to vortices [Vivanco et al., 1999], turbulent flows [Rashidi et al., 1992, Hodges and Street, 1999], shear flows [Shrira, 1993], and fixed [Kirby, 1986] and mobile rough beds [Kennedy, 1969] has been characterised in the past. All these phenomena have been studied independently, and in most cases the presence of gravity-capillary waves was given as an initial condition. The mechanisms that generate the waves are not yet completely understood, hence the shape and dynamics of the free surface patterns are currently not predictable. On the other hand, experimental techniques to measure these patterns have greatly evolved. Optical [Cobelli et al., 2009] and acoustic [Krynkin et al., 2016] methods for example can now have the required spatial and temporal resolution for these measurements. It is hoped that these technological advancements will generate renewed interest in these topics in the near future, so that the remote monitoring of the hydraulic conditions in turbulent flows can have wider and more reliable application.

This thesis would like to contribute to these developments, by presenting new experimental data on the dynamic patterns at the free surface of turbulent flows, and by testing the application of acoustic Doppler techniques for the measurement of the flow velocity at the surface. The focus is on shallow turbulent flows over homogeneously rough beds, since these can be obtained in a laboratory flume in controlled conditions. Every attempt is made to present the results rigorously and to interpret them based on the existing mathematical and physical theories. In this way it is hoped to obtain a better and more general insight about the underpinning processes than was done empirically in the past. The aim is to show that although patterns of gravity-capillary waves can reduce the correlation between the dynamics of the free surface and the turbulent processes, they still carry useful information about the hydraulic conditions in the flow, and that this information can be retrieved from the measurement of the acoustic field scattered by these waves.

1.2 Research questions

This thesis will address the following research questions:

- Is it possible to interpret the wave patterns at the free surface of a shallow turbulent flows based on the theory of gravity-capillary waves?
- Is there a relation that links the patterns of surface waves and their statistics to the hydraulic properties of the flow, namely the mean surface velocity, the average streamwise velocity profile, and the homogeneous depth?
- Is it possible to relate the characteristics of these patterns with the Doppler spectra of the scattered acoustic field, in order to improve the accuracy of remote measurement techniques applied to shallow turbulent flows?

1.3 Aims and objective

This research aims at improving the understanding of the free surface patterns that form at the free surface of shallow turbulent flows, and at testing the capabilities of acoustic Doppler techniques for the remote characterisation of these patterns and their dynamics. The first objective is to characterise the surface patterns in a range of shallow turbulent flows experimentally in a laboratory flume, by determining their statistics in space and in time, and to provide an interpretation of these measurements based on the theory of gravity-capillary waves in a flow where the time average streamwise velocity varies with the depth. The second objective is to derive a model that describes the shape of the free surface of a shallow turbulent flow and its evolution in time based on the measurements and their interpretation. The third objective is to measure and characterise the Doppler spectra of the acoustic waves scattered by the free surface of these flows. The fourth objective is to compare these measurements with the predictions by a numerical model of acoustic scattering, in order to interpret the experimental results and to validate the model of the free surface. The last objective is to use this interpretation in order to suggest possible future improvements to acoustic remote measurement techniques.

1.4 Thesis structure

This thesis is structured as follows: Chapter 2 summarises the principal results of previous related studies. Section 2.1 discusses the main mechanisms that have been proposed by different authors in order to explain the generation and the dynamic behaviour of the free surface in turbulent flows. Section 2.2 reviews the existing methods to characterise the water surface behaviour, both in the ocean and in shallow turbulent flows. Subsection 2.2.4 presents the existing acoustic measurement techniques for the remote characterisation of the free surface of shallow turbulent flows. Chapter 3 summarises the main mathematical theory and results that are available in the literature and that will be useful for the following analysis. Section 3.1 focuses on the theory of gravity-capillary waves in a flow where the vertical variation of the average streamwise velocity is approximated by a power function. Section 3.2 presents the equations that describe the acoustic field scattered by the rough dynamic water surface, based on the Kirchhoff approximation. Chapter 4 describes the experimental apparatus. This was used in order to collect data about the free surface of shallow turbulent flows over a homogeneously rough bed in a laboratory flume, and about the acoustic field scattered by the dynamic water surface.

Chapter 5 and 6 present the results of the experimental and numerical analyses. Chapter 5 is focused on the experimental characterisation of the free surface patterns with arrays of conductance wave probes. Section 5.1 presents the data analysis procedures. Section 5.2 shows the measurements of the statistics of the free surface measured at a single location. The statistics are analysed both in time and in space in section 5.3, where the frequency-wavenumber spectra of the patterns at the free surface are described. Section 5.3 presents the results of a transient analysis based on the wavelet spectral method, which allows the characterisation of the dispersion relation of the surface patterns from short time-series of the elevation recorded at a limited number of locations. Chapter 6 is focused on the measurements and numerical simulations of the Doppler spectra of the acoustic field scattered by the free surface. Section 6.1 presents the numerical model. The Doppler spectra measured in the backscattering configuration are presented and compared with the predictions by the model in subsection 6.2.1. The results obtained with the forward scattering configuration are shown in section 6.2.2. Chapter 7 summarises the main findings of this thesis, and suggests some future developments.

Chapter 2

Literature review

2.1 Mechanisms for waves formation in turbulent shallow flows

The free surface of a turbulent flow is influenced by a large variety of phenomena. A comprehensive representation of these phenomena is given by the review of Brocchini and Peregrine [2001]. These authors identify the two factors that govern the behaviour of the free surface and its interactions with the turbulent flow assumed at high Reynolds numbers. These factors are represented by a length scale and a velocity scale, which define four regions where the effects of turbulence, gravity, and surface tension have a different relative importance. The typical conditions which are found in turbulent shallow flows vary between weak turbulence and gravity-dominated turbulence. Here Brocchini and Peregrine [2001] identify three classes of surface deformations: passive response to turbulent fluctuations, scars, and waves. The amplitude of these deformations increases with the strength of the turbulence and it is limited by gravity, so that it is well represented by the Froude number.

The passive response of the free surface to turbulence manifests itself clearly at relatively large Froude numbers, when coherent motions inside the flow are able to contrast the effects of gravity. The most common patterns are the so-called dimples that can be observed above the core of a vertical vortex attached at the free surface. Scars are generated by the separation of the flow near the free surface, and appear as sharp indentations often at the margins of a turbulent upwelling or of a horizontal vortex. Waves represent the typical dynamic response of the free surface to a disturbance. They are generated by a matching of scales and velocity with the flow, but can also spread from a localised deformation such as a dimple or a scar. Waves can propagate and focus a long distance away from their origin, making it difficult to identify the cause that generated them. This section reviews the main studies about the mechanisms that produce and affect the patterns at the free surface of shallow turbulent flows, based on the classification proposed by Brocchini and Peregrine [2001]. Larger attention is devoted to the patterns of gravity-capillary waves, since these have been observed more clearly during the experiments described in chapter 5.

2.1.1 Boils, vortices, and scars: the effect of turbulence

Vortex dimples and scars are the manifestation of the interaction between a coherent turbulent structure in the flow and the free surface. Nezu and Nakagawa [1993] used the definition of boils for these phenomena, and distinguished between boils of the first, second, and third kind. Boils of the first and second kind are related to topographic features on the bed, such as dunes, and to secondary currents in the flow, respectively. The focus of this research is on flows over homogeneous non-moving beds, therefore, boils of the first-kind are not considered here. Secondary currents are typical of narrow channels and of flows over movable sediments where the secondary currents are predominant, but they have also been observed over homogeneously rough fixed beds [Rodríguez and García, 2008] and in smooth channels with large aspect ratio [Tamburrino and Gulliver, 2007]. Boils of the second kind are associated with a distribution of high-speed and low-speed longitudinal streaks near the free-surface, and they appear as elongated areas of downwelling and upwelling on the surface [Tamburrino and Gulliver, 2007]. Boils of the third kind are generated by bursting motions, which are found both in smooth and rough-bed channels [Nezu and Nakagawa, 1993]. They correspond to the surface manifestation of the so-called splats and antisplats motions associated with the rising towards the surface of hairpin vortices [Pan and Banerjee, 1995, Kumar et al., 1998] or cane vortices [Khakpour et al., 2012], or to the interaction with surface attached vortices [Tsai, 1998].

The interaction of bursts with the interface creates areas of divergence or convergence of the velocity in the flow, and it does not directly associate with large surface deformations. It is often studied by modelling the free surface as a no-shear flat surface [Nagaosa, 1999, Nagaosa and Handler, 2012]. Attached vortices generate so-called dimples [Brocchini and Peregrine, 2001], which are local depressions above the vortex core. This mechanism of deformation is efficient [Tsai, 1998, Shen et al., 1999], but dimples are difficult to measure because of their point-like structure [Brocchini and Peregrine, 2001]. When vorticity is strong and the turbulent eddies have the scale which is important for surface tension effects, the surface can deform significantly [Brocchini and Peregrine, 2001]. The results are scars which can be observed next to horizontal vortices [Jeong and Moffatt, 1992, Sarpkaya, 1996].

Numerical studies have demonstrated the existence of a local correlation between the elevation and slope of the surface elevation and the flow vorticity and turbulent velocity. Tsai [1998] found larger correlation between streamwise vorticity and free surface elevation, slope, and curvature. This study was based on a Direct Numerical Simulation, with a free-slip boundary condition at the bottom boundary. The larger correlation was associated with the effect of upwelling and downwelling in the initial stages of the interaction between a coherent turbulent structure and the free surface, before the attachment of the oblique vortices to the surface. The correlation of the free-surface curvature with the lateral vorticity was large, and it was related to the generation of turbulence by short waves [Batchelor, 2000, p.365]. Instead, the correlation with the vertical vorticity was small. Zhang et al. [1999] showed that vertical vorticity and free surface elevation are not correlated when the vorticity distribution is not axisymmetric (e.g., for a vortex approaching at an angle). As a vortex approaches the free surface, the horizontal vorticity changes rapidly in the surface layer, and the surface curvature produces secondary vorticity. As a result, the auto-correlation of the horizontal vorticity component drops rapidly below the free surface, and becomes negative [Shen et al., 1999]. This affects the ability to establish the link between the vorticity inside the flow and the characteristics at the surface, especially in the experiments, where the measurement of the flow near the surface is difficult.

This is confirmed by the experimental studies, which show a small correlation between turbulence and the free surface elevation. Fujita et al. [2011] performed a set of experiments in a laboratory flume with a homogeneously rough bed. They found an absolute correlation smaller than 0.15 between the vertical turbulent velocity in the flow and the surface elevation. Savelsberg and van de Water [2009] suggested the use of a modified surface gradient and of the advective term of the Navier-Stokes equation as correlators, to investigate the effect of attached vortices. The correlation was good when turbulence was produced by a partially immersed cylinder, but one order of magnitude smaller in the case of grid turbulence. These observations suggest that the mechanism of interaction between the free surface and turbulence is not limited to the generation of patterns above coherent turbulent structures. Waves can form at the boundaries of an upwelling and then propagate [Longuet-Higgins, 1996], reducing largely the instantaneous and local correlation [Savelsberg and van de Water, 2009].

2.1.2 Gravity-capillary waves generated by turbulent pressure fluctuations

Gravity-capillary waves are commonly observed at the surface of the ocean, where their generation is due to the interaction with the turbulent wind. This interaction occurs according to two mechanisms suggested by Miles [1957] and Phillips [1957], respectively. Of these, the mechanism proposed by Phillips [1957] involves the resonance between turbulent pressure fluctuations in the flow and waves at the surface. Gravity-capillary waves propagate at a characteristic phase velocity which is a function of their wavelength and of the depth (see section 3.1.2). Their growth is promoted, according to Phillips [1957], when the spatial scale and velocity of the pressure fluctuations matches that of the waves on the surface.

Teixeira and Belcher [2006] showed that a similar mechanism can generate gravity-capillary waves when turbulence is in the water. These authors considered the propagation of waves in a linearly sheared laminar flow, and coupled them to the flow turbulence velocity through the value of pressure at the surface. Two types of waves are distinguished. The first type of waves are freely propagating gravity-capillary waves that resonate with turbulence with the same mechanism described by Phillips [1957]. When turbulence is in the water and if the turbulent velocity fluctuations are of order less than $0.1\,\mathrm{m\,s^{-1}}$, gravity-capillary waves can only be excited resonantly if the average flow velocity varies with the depth, and if its maximum is at least equal to the minimum phase velocity for these waves, approximately $0.23\,\mathrm{m\,s^{-1}}$ (equation (3.23)). The resonant growth mechanism is limited by the progressing elongation of the turbulent structures as they interact with the surface, so that the growth is bounded in time. The second type of waves are decaying waves which Teixeira and Belcher [2006] postulate being forced by turbulence. In contrast with the freely propagating gravity-capillary waves, forced waves are believed to propagate at the same velocity of the turbulence pressure disturbance that generated them. The model of Teixeira and Belcher [2006] has been derived for an infinitely deep turbulent flow, where the average velocity varies linearly with the depth and where the effect of the bottom boundary conditions is neglected. Although it does not strictly apply to the conditions of a turbulent shallow flow, their study appears to be the only attempt to explain the mechanism of gravity-capillary waves generation from turbulence in the water.

Because of their characteristic dependence between speed of propagation and wavelength (the dispersion relation), gravity-capillary waves are easily identified by measuring the frequency-wavenumber spectrum of the free surface elevation. There has been a very limited number of numerical [Borue et al., 1995, Guo and Shen, 2010] and experimental [Savelsberg and van de Water, 2009] studies that tried to quantify the frequency-wavenumber spectrum of the waves on a turbulent shallow flow. Borue et al. [1995] modelled the interaction between the surface and the turbulence generated at the bottom of a shallow flow with low Reynolds number. They argued that the surface patterns are generated by large vertical vortices attached at the surface and found a characteristic frequency of the surface patterns related to the amplitude of the vertical flow velocity fluctuations. The results by Borue et al. [1995] show that long waves are forced at this characteristic frequency, while shorter gravity-capillary waves propagate freely due to the rapid dissipation of turbulence at the short scales. They also found that both the spatial spectra of the surface elevation and of the horizontal turbulent velocity followed a power-law of the wavenumber.

Guo and Shen [2010] developed a Direct Numerical Simulation of the free surface over homogeneous isotropic turbulence that solves the fully nonlinear surface equations. In their study there was no mean flow and the depth was infinite. The numerical simulation showed both turbulence related roughness (due to vertical and horizontal vortices) and patterns of freely propagating gravity-capillary waves. Forced waves largely dominated the surface roughness and they followed the same type of dispersion relation defined by Borue et al. (1995). Free waves propagated in all directions starting from the large scale splats and antisplats that were generated by the impingement of turbulent coherent structures. The frequency-wavenumber spectra showed two clear ridges corresponding to forced and free waves respectively. Forced waves were found over a broad range of scales, while freely propagating waves were relatively short. Like Borue et al. [1995], Guo and Shen [2010] suggested that the generation of forced waves is caused by a quasi-resonant interaction with turbulence which is more effective at the lower wavenumbers. The results of Borue et al. [1995] and Guo and Shen [2010] were found for a flow with low Reynolds number and for a flow where the average velocity was zero, respectively. In these conditions, the resonant growth of gravity-capillary waves according to the mechanism proposed by Teixeira and Belcher [2006] cannot occur, and the generation of freely propagating waves is due to nonlinear interactions between forced waves.

Flow conditions which are more representative of shallow turbulent flows have been investigated experimentally by Savelsberg and van de Water [2009]. The measurements reported in their study are the only known experimental results that describe the dispersion of the surface patterns on shallow turbulent flows in three-dimensions. The frequency-wavenumber spectra determined by Savelsberg and van de Water [2009] showed evidence of both forced and freely propagating waves, but they were measured in a flow with grid-generated turbulence which is not representative of the turbulence in open channel shallow flows. The spectral resolution of their spectra was limited. This hindered the observation of the dispersion relation near the dominant scales and did not allow for definitive conclusions on the generation mechanism of the observed free surface patterns.

2.1.3 Gravity-capillary waves in sheared flows

The propagation of gravity-capillary waves is often studied under the assumption that the flow vorticity is everywhere zero [e.g. Lighthill, 2001]. A few authors investigated the dispersion relation of gravity-capillary waves in a flow where the average streamwise flow velocity varies with the depth. In these studies the turbulent velocity fluctuations are neglected, and the flow is modelled as laminar. Biesel [1950] and Abdullah [1949] found the analytical solution for a flow with the exponential and the linear vertical variation of the average streamwise velocity, respectively. These profiles do not approximate well the streamwise velocity profile in a shallow turbulent flow. Shrira [1993] derived a numerical procedure which provides the dispersion relation for an arbitrary velocity profile, but only in the case where the mean depth is infinitely large. The solution proposed by Patil and Singh [2008] applies to the logarithmic profile which is representative of the velocity in shallow turbulent flows, but it is only valid when the waves are much longer than the depth of the flow.

The vertical velocity profile in a turbulent shallow flow with rough boundary can be approximated by a power-law of the vertical co-ordinate [Cheng, 2007]. The dispersion relation in such a flow was first investigated in an appendix by Lighthill to the work of Burns [1953]. Fenton [1973] expanded the analysis, and suggested a numerical procedure that allows the calculation of the dispersion relation in a more general case. Dalrymple [1977] studied the propagation of nonlinear waves in a flow where the average streamwise velocity varies vertically based on a numerical finite difference model, and included the power-function profile with the exponent $n = 1/7$ as a special case. This solution was found as an expansion with respect to the linear velocity profile. Here the measured dispersion relation of gravity-capillary waves in a turbulent flow is compared to the solution for a flow where the average streamwise velocity profile varies like a power-function of the depth, following the procedure described by Fenton [1973]. This is reported in subsection 3.1.2.

When the average flow velocity varies with the depth, an additional mechanism to the one described by Teixeira and Belcher [2006] can promote the resonant growth of waves on the surface. This mechanism is derived assuming the flow to be laminar, and according to the theory derived by Miles [1957] it is the main phenomenon that allows the generation of wind waves in the ocean. When the growth of waves is caused by the vertical variation of the average streamwise velocity in the flow, the mechanism is called critical layer or shear instability. It was first studied by Yih [1972] upon recognition that the surface equations admit solutions where the phase velocity is complex if the average flow is sheared. This causes the exponential growth of the waves. The instability occurs when the average velocity at some depth in the flow (this depth is called the critical layer) coincides with the phase velocity of gravity-capillary waves [Yih, 1972]. This resonance condition is the same required by the theory of Teixeira and Belcher [2006], but the process described by the shear instability does not require the presence of turbulent fluctuations. According to Yih [1972] the instability also requires the critical layer to be an inflexion point of the streamwise velocity profile, a result later dismissed by Morland et al. [1991].

The shear instability can promote the growth of waves that propagate against the mean flow, if the flow mean surface velocity is larger than the minimum phase velocity of gravity-capillary waves measured in still water [Caponi et al., 1991]. The resonant waves can be both two-dimensional (i.e., with the wavefront perpendicular to the direction of the mean flow) and three-dimensional, but two-dimensional waves are more unstable [Morland et al., 1991]. Although the shear instability has been suggested until recently [Young and Wolfe, 2014] as a mechanism capable of generating waves in flows where the average streamwise velocity varies with the depth, so far there is no evidence of this phenomenon to occur in flows that are not strongly stratified.

2.1.4 Waves generated by the interaction with a rough bed

It is well known [e.g. Rayleigh, 1883] that the bed topography can also generate patterns of gravity-capillary waves, which can propagate in all directions in space and in time. The amplitude of the waves generated by the interaction with the rough bed is proportional to the spatial spectrum of the bed roughness at the same wavenumber of the wave. Therefore, this pattern has contributions at all the wavenumbers for which this spectrum is different from zero, although the waves that propagate upstream are expected to have larger amplitude [e.g. Harband, 1976]. When the flow velocity exceeds the minimum phase velocity of gravity-capillary waves, stationary patterns of waves can develop. These waves are the ones which propagate against the flow with the phase velocity equal to the mean surface velocity, so that their resultant frequency is zero.

The generation of waves in a flow with rough boundary has been investigated in the past, for a variety of shapes of the roughness [e.g. Harband, 1976, Lee et al., 1989, Trinh and Chapman, 2013a,b]. In all these studies, the bed roughness was confined in a small region with respect to the horizontal scales of the flow. The waves generated in all directions by the bed roughness sum incoherently, producing a complex three-dimensional pattern in the region near the disturbance. These dynamic patterns have been studied, but mainly with the aim of investigating nonlinear phenomena, such as trains of cnoidal waves, or periodic successions of solitons emitted upstream from a localised disturbance on the boundary [e.g., Lee et al., 1989]. The focus in most studies of the interaction between surface waves in a flow and the rough bottom boundary is on the steady state solution of the problem [e.g., Harband, 1976, Lighthill, 2001]. Here the waves are found interacting constructively to form a pattern similar to the so-called Kelvin wake, which is commonly observed around a ship that travels in still water [Lighthill, 2001, p.269]. This representation applies at very large distance from the disturbance, therefore it does not apply to the case where the bed is uniformly rough. Currently, there are no known models that are able to predict the evolution of free surface waves in three-dimensions when the waves propagate over a nonlinearly sheared flow above a uniformly rough bed [Touboul et al., 2016]. This in spite of the important applications for the dynamics of sediments in hydrological flows [e.g. Kennedy, 1969, Chanson, 2000, Andreotti et al., 2012].

2.1.5 Nonlinear waves

All phenomena discussed in the previous subsections can be explained describing the free surface according to a linear random model. Such a model represents the surface as a linear superposition of independent sinusoidal waves with the amplitude and phase that are randomly distributed. This is the model that is used in this thesis, and it will be discussed with more detail in subsection 3.1.1. Eventual deviations from this linear theory can have large effects for the acoustic scattering by the free surface. The best known example of nonlinear waves are waves of finite amplitude, such as the so-called Stokes waves [Stokes, 1847]. These waves propagate at a phase velocity that increases with their slope [e.g. Lamb, 1932, p.417]. They are characterised by the presence of bound harmonics which are forced to travel at the velocity of the main wave and they are observable from the measurement of the frequency-wavenumber spectrum of the surface elevation [e.g. Herbert et al., 2010].

Other nonlinearities interest equally waves of infinitesimal amplitude and slope, and occur because of the resonant or quasi-resonant interactions among different modes of the surface elevation, leading to a wide range of complex phenomena [Dias and Kharif, 1999, Osborne, 2010]. The phenomena are most often described through a model derived by Zakharov [1968], and called Zakharov equation. The resonance is satisfied by all those combinations of waves for which the sum or difference of the frequencies and of the wavenumbers is equal to zero [Phillips, 1960]. Because of the shape of the dispersion relation, only combinations of at least four waves can interact in the range of gravity waves, while triad-interactions are possible for gravity-capillary waves.

The Zakharov equation is of interest here because it predicts and explains the growth of three-dimensional patterns on the free surface, due to the instability of a two-dimensional wave to small three-dimensional perturbations. These phenomena go under the name of three-dimensional (or modulation) instabilities, they were classified by McLean et al. [1981] and first studied in shallow water by McLean [1982]. The class I instability is the so-called Benjamin-Feir instability, which is the dominant class for small amplitude waves. The class II instability involves the quintet-resonance between three waves and is often associated with the so-called crescent-shaped, or horseshoe waves [Shrira et al., 1996]. A study performed by Zakharov and Shrira [1990] showed that triad-interactions between two surface waves and a critical layer inside the flow when the waves propagate against the flow causes the broadening of the angular spectrum of the waves, along a resonance curve in the wavenumber space that roughly corresponds to a circle with constant radius. The model developed by Zakharov and Shrira [1990] is only valid when the surface spectrum is narrow and when the flow velocity is much smaller than the phase velocity of gravity waves, but it is of notice that this circle resembles the structure of the radial pattern which is observed experimentally in section 5.3.2. Unfortunately, very few studies investigated the modulation instability of the waves in a sheared flow, and only in the case where the average streamwise velocity varies linearly with the depth [e.g. Thomas et al., 2012]. This velocity profile is not representative of shallow turbulent flows.

2.1.6 Power spectra of the surface elevation

The linear random model of the free surface elevation is based on the definition of the power spectrum of the surface elevation. This determines the amplitude of each of the modes of the surface, as a function of both the wavenumber and the frequency. These two parameters are related by a dispersion relation which is assumed known, therefore the spectra are often expressed in terms of either the frequency or the wavenumber alone. A variety of models for the spectrum of the free surface have been proposed by different authors, mainly for the spectrum of ocean waves. Most of these models represent the spectrum as a power-function of the wavenumber or of the frequency, which is eventually multiplied by a directional spread function in order to represent the amplitude of the waves in three-dimensions.

For gravity waves generated by wind in infinitely deep water without mean flow, Phillips [1958] found a dependence of the power spectrum by the power -4 of the wavenumber, or the power -5 of the frequency, based on a dimensional analysis. The -4 exponent was linked to the limiting shape of the waves before breaking, therefore Phillip's spectrum is often referred to as equilibrium spectrum. Kuznetsov [2004] suggested the exponent -4 for the frequency spectrum, based on the argument that breaking is a mainly two-dimensional process. In the limiting case of long waves in shallow water, Kitaigordskii et al. [1975] suggested the exponent -3. This author also showed that the relation between the wavenumber and the frequency spectrum is complicated by the eventual presence of a non-zero mean flow velocity, and by the inclusion of a parameter which in the limit when the frequency is independent by the direction of propagation corresponds to the group velocity. The equilibrium spectrum when expressed in terms of the frequency does not follow a power law in general. Other semi-empirical modifications of the equilibrium spectra have been suggested by different authors. For example, Banner [1990] included the effect of the Doppler shift induced by the longer waves on shorter ripples, and suggested a correction factor to Phillips' fourth-power wavenumber spectrum, leading to the exponent -5 at the high wavenumbers. Belcher and Vassilicos [1997] dismissed this result and proposed the exponent -4 for both the wavenumber and the frequency equilibrium spectra.

The frequency spectrum is generally easier to measure experimentally, because it only requires the measurement of the elevation at one location. Experimental measurements in the ocean gave support to the power-function behaviour of the frequency spectrum. For instance, Pierson and Moskowitz [1964] and Hasselmann et al. [1973] found an agreement with the exponent -5, while Donelan et al. [1985] based their formula on the exponent -4. These three works together represent some of the most cited semi-empirical models of the ocean spectrum, namely the Pierson-Moskowitz model, the JONSWAP model, and the Donelan spectrum. Relatively more recent formulations [Elfouhaily et al., 1997] still retain the power-function dependence while attempting a unified description.

The power-function decay of the wavenumber power spectrum was demonstrated independently in the context of wave turbulence statistics. Wave turbulence studies the statistics of homogeneous random weakly nonlinear waves as they mutually interact [Nazarenko and Lukaschuk, 2016] and is based largely on the Zakharov nonlinear model. In weak wave turbulence, the nonlinearities take the form of a slowly varying envelope function. Then, mutual interactions among waves lead to cascades of energy across a separation of scales, yielding power spectra with a similar form to the Kolmogorov spectrum in hydrodynamic turbulence. The slope of wave turbulence spectra depends on the direction of the energy flux and on the order of the interactions, therefore on the types of waves involved. The theory of wave turbulence predicts the exponents $-5/2$ and -4 for the wavenumber and the frequency spectra, respectively, for gravity waves subject to a direct cascade [e.g. Nazarenko and Lukaschuk, 2016]. These are modified to $-7/3$ and $-11/3$, respectively, in the case of an inverse cascade of energy. Gravity waves in shallow water have the exponents of the frequency spectrum equal to $-4/3$ for a direct cascade, and -1 for an inverse cascade [Zakharov, 1999]. Capillary waves admit triad interactions, therefore the exponent for the direct cascade modifies as $-19/4$ for the wavenumber spectrum and $-17/6$ for the frequency spectrum [Zakharov and Filonenko, 1967, Falcon et al., 2007].

Wave turbulence theory is based on a homogenous and isotropic representation of the free surface, which is not applicable to ocean waves where the direction of the wind introduces strong anisotropy. This did not prevent the comparison between the wave turbulence spectra and the equilibrium spectra [Nazarenko and Lukaschuk, 2016]. Similarly, power functions models have been employed as a reference for the spectra of the surface elevation generated by the interaction with turbulence. For instance, Borue et al. [1995] showed that the wavenumber power spectrum of turbulence-generated waves integrated over all directions of propagation decays with a small slope between -1 and -2. In contrast, Savelsberg and van de Water [2009] measured a much steeper decay with the exponent of approximately -8 for the waves generated in a flow with grid-stirred turbulence. Smolentsev and Miraghaie [2005] did not quantify the slope of the spectra measured in an inclined flume, but observed its increase with the Froude number at the higher frequencies. The spectra of the surface elevation determined by Teixeira and Belcher [2006] also show evidence of a power-function dependence on the wavenumber, which is apparently related to the spectrum of turbulence used for their analysis. For the waves in a shallow turbulent flow, where the flow velocity is comparable with the phase velocity of gravity-capillary waves and the wave field is largely anisotropic, there is no theory that predicts the shape of the spectra, and the comparison with existing theories derived in different context is somewhat arbitrary. The power-function spectra have the advantage of being easily parametrised with a limited number of parameters, and they allow the calculation of the characteristic slope and curvature analytically (see subsection 6.1.2). Therefore, they are used in chapter 6 as a simplified model to represent the interaction of the rough dynamic surface with the acoustic pressure field. In that chapter, different values of the spectrum slope are used, in order to show the dependence of the scattered acoustic field by this parameter. The direct measurements of the frequency spectra in chapter 5 show that the power function shape is a reasonable approximation in a limited range of frequencies and flow conditions.

2.2 Measurement of the free surface dynamics

A variety of techniques to measure the elevation of the free surface in time and/or in space have been used by different authors in the past. While some of these techniques apply only to the measurements in controlled laboratory conditions, others have applications for the measurements in geophysical flows. For the experiments reported in chapter 5, the surface elevation was characterised both in time and in space using two-dimensional arrays of conductance wave probes. Similar arrays were used for example by Donelan et al. [1985] to measure the frequency-wavenumber spectrum of ocean waves, and by Horoshenkov et al. [2013] to characterise the space-time correlation function of the surface in shallow turbulent flows over a homogeneously rough bed. The conductance wave probes are described in section 4.3 with more detail. The focus in this section is on remote measurements of the surface elevation, where the sensors are not in direct contact with the free surface (although they can be both above or below it). The existing techniques fall in three main categories according to the physics of the phenomenon which is being used: optical (including laser) methods, technologies based on radio waves (including microwaves), and acoustic methods.

There is a set of requirements for the measurement techniques that can be adopted in a shallow turbulent flow. The full characterisation of the dynamic behaviour of the free surface of these flows requires the simultaneous measurement of the free-surface elevation in time and in space. The patterns on the free surface are expected to be three-dimensional. The horizontal scales of these patterns vary from the shortest scales with the order of a few millimetres to the largest scales of the same order of the depth (see [Horoshenkov et al., 2013], and the results in section 6.2 for the quantification of the shortest scales). The standard deviation of the surface elevation is found in the range between 0.05 mm to 2 mm across the flow conditions investigated here and also by Horoshenkov et al. [2013] and Krynkin et al. [2014]. Assuming the homogeneous mean depth of the flow of the order of 0.1 m, and the Froude number near 0.5, the mean surface velocity is expected in the order of $0.5\,\mathrm{m\,s^{-1}}$. Based on these estimates, the characteristic frequency expected for the patterns on the surface is between 5 Hz for the large scales comparable with the depth and 100 Hz for the shorter scales of a few millimetres. Therefore measurement techniques must have a high spatial resolution especially in the vertical direction, they must be able to record the surface elevation over a relatively large area, and they must allow measurements at high frequency (or be robust to aliasing).

2.2.1 Optical methods

A few authors have attempted to develop an experimental technique that allows the simultaneous measurement of the free surface elevation and of the surface flow velocity field. The technique derived by Law et al. [1999] measures the flow velocity field on a vertical plane with a standard Digital Particle Image Velocimetry (PIV) method [Willert and Gharib, 1991]. The measurement plane is defined by a thin laser sheet generated below the surface. A fluorescent dye is added to the water, and the surface elevation is measured as a sharp gradient of light intensity at the intersection between the laser sheet and the free surface. A similar procedure but without the use of dye was implemented by Fujita et al. [2011] in order to study the correlation between free surface patterns and the flow turbulent velocity field in a set of shallow turbulent flows over a homogeneously rough bed. The high horizontal spatial resolution makes these methods ideal for observing the shorter scales on the free surface. On the other hand, the spectral resolution with these methods is generally low because of the limited field of view of the camera, and because of the generally low frequency of sampling.

The surface gradient detector developed by Zhang and Cox [1994] measures the slope of the free surface in a two-dimensional region from the refraction or reflection of collimated light emitted by a coloured screen. The method was applied successfully in the reflective mode version by Dabiri and Gharib [2001] and Dabiri [2003] to the study of the free surface of a horizontally sheared flow. The size of the measurement area in these studies was limited. Dabiri and Gharib [2001] discuss the uncertainties of the method, which are mainly related to aberrations of light in the reflective mode. Zappa et al. [2008] developed a technique that reconstructs the free surface slope based on the polarisation of scattered non-polarised light. The range of surface slopes that can be measured with reflection-based techniques is generally limited [Jähne et al., 1992].

The refraction of a light source placed below the channel bottom was used for example by Jähne et al. [2005]. The free surface synthetic Schlieren method described by Moisy et al. [2009] is based on the refraction of non-collimated light at the free surface, and uses a random pattern of dots. Bock and Hara [1995] introduced a technique that measures the slope of the free surface in two orthogonal directions from the refraction of a scanning laser beam. A similar technique applied to the measurement of the surface slope at one single location was implemented by Hughes et al. [1977] with the laser source installed below the water surface and by Lange et al. [1982] with the laser source above the water surface. The technique described by Bock and Hara [1995] was implemented by Savelsberg and van de Water [2009] for the study of the patterns at the surface of a turbulent flow with grid-generated turbulence, in a laboratory flume. Refraction-based methods require either the light source to be immersed in water, or the flow bottom to be transparent, therefore they are not practical for the measurements of flows over a rough non-transparent boundary.

The reconstruction of the free surface elevation based on the reflection of a random pattern of light recorded with two cameras was described by Tsubaki and Fujita [2005]. The first measurements of short surface waves in the ocean were based on stereo photography [e.g. Schumacher, 1950]. The specular reflection of light from the water surface occurs at a location that depends on the geometry of the acquisition system. The reconstruction requires either the projection of a pattern of light and the use of dye [e.g. Tsubaki and Fujita, 2005], or the solution of a minimisation problem based on physical constraints [e.g. Gallego et al., 2011].

An accurate technique based on the airborne projection of a two-dimensional fringe pattern on the free surface is the Fourier transform profilometry [Takeda et al., 1982], which was extended to the measurement of the water free surface by Cobelli et al. [2009] and Maurel et al. [2009]. The method was applied to the measurement of the frequency-wavenumber spectrum of gravity-capillary wave turbulence in a wave tank [i.e., Herbert et al., 2010, Cobelli et al., 2011, Aubourg and Mordant, 2015]. In its implementation, the technique requires adding a white dye to the water in order to improve its light diffusivity. This requirement makes the profilometry technique (and the other techniques that require the use of dye) less practical for the measurement of the free surface of turbulent flows due to the large amount of water that often needs to be recirculated by the system, and the large test area size.

2.2.2 Scattering of radio waves from the surface of the ocean

The dynamics and topography of the ocean surface have been studied for many years based on the measurement of radar scattering [e.g. Hauser et al., 2005, chap.5]. The measurements have been performed with a wide range of frequencies from platforms, ships, aircrafts, and satellites. The most common configuration is the so-called backscattering or monostatic configuration, where the scattered waves are recorded by an antenna at the same location of the emitter. In this case the statistics of the surface are obtained based on the intensity and on the Doppler spectrum of the return signal, or sea echo. The alternative configuration, called forward-scattering or bistatic configuration, has the receiver antenna on the opposite side of the emitter with respect to the scattering surface, and it is seldom used for oceanic measurements with a few exceptions [e.g. Awada et al., 2006].

The scattering of electromagnetic waves by the water surface is a complex problem, which is usually simplified by means of a set of approximations. The most common types of approximations are the Kirchhoff approximation and the small perturbation method (SPM). The Kirchhoff approximation represents the scattering from any point on the rough surface as if it occurred from a plane tangent to the surface at the same point [e.g. Bass and Fuks, 1979, p.220]. This is the type of approximation which is used mainly in this thesis. It is presented with more detail in section 3.2.1, where the conditions for its validity are discussed. The SPM assumes that the amplitude of the surface corrugation with respect to a flat plane is small compared to the projection of the incident electromagnetic waves in the direction normal to such plane (typically in the vertical direction) [e.g. Bass and Fuks, 1979, p.72]. In the ocean the typical scales of the waves range from a few metres to some millimetres, and the shorter waves are typically much smaller in amplitude. Radar backscattering is mostly influenced by a limited range of scales which depend on the frequency of the signal and the geometric configuration. This allows treating the scattering from short waves with the SPM, while including the effects of the longer waves in terms of the Kirchhoff approximation. This composite approach is usually referred to as two-scale model, or composite-roughness model [Wright, 1968, Valenzuela, 1968]. Other approximations based on a higher-order expansion of the Kirchhoff model consider the scattering from parabolic surfaces instead of planes [e.g. Ivanova and Broschat, 1993, Guerin et al., 2010].

The radar emitters and antennas used for ocean scattering measurements are usually characterised by large apertures and consequently narrow directivity. This allows the measurements to be performed in the so-called Fraunhofer zone, where the size of the scattering surface is effectively small compared to the distance between the emitter and the antenna to the surface. If this condition is satisfied, the problem of scattering can be greatly simplified (see for example the derivation in subsection 3.2.2, where a similar simplification is obtained assuming the correlation length of the surface to be much smaller than the distance from the acoustic transducer and receiver).

The majority of the experimental studies of scattering from the ocean are performed in the Fraunhofer zone, where the size of the scattering region is much smaller than its distance from the source and the receiver of the scattered waves. In this case the backscattering in a specific direction is governed by the interaction between the electromagnetic waves and the surface waves which satisfy a so-called Bragg resonance condition [Crombie, 1955, Barrick, 1972]. The wavelength of the Bragg resonant surface waves is equal to half the wavelength of the incident electromagnetic wave divided by the cosine of the angle of incidence (see equation (3.127)). The intensity of the backscattered electromagnetic field is related directly to the amplitude of the Bragg waves on the surface [e.g. Barrick, 1972]. In the ocean, these waves propagate at a velocity which neglecting nonlinear effects is governed by a simple dispersion relation. Therefore, the Doppler spectra of the backscattered field at first order shows two sharp peaks at the frequency of the Bragg waves. This allows for example the direct measurement of the currents in the ocean from the shift of the Bragg Doppler peaks [Stewart and Joy, 1974, McGregor et al., 1997].

The nonlinearities of the ocean surface complicate the scattering of electromagnetic waves. These effects are particularly important for Bragg scattering because of its high response to specific wavelengths on the surface. The most direct manifestation of the nonlinear behaviour of the free surface is the modulation of the Doppler spectrum of the scattered electromagnetic field. This is explained by terms of the second-order of an SPM expansion, which increase the width of the Doppler peaks near the Bragg frequencies (see subsection 3.2.2). The amplitude of the second-order spectrum depends on two coupling coefficients, representing the hydrodynamic and the scattering (electromagnetic) coupling, respectively. The hydrodynamic coupling coefficient has been calculated by Weber and Barrick [1977] based on a second-order small slope expansion of the irrotational free surface equations in an infinitely deep ocean. It relates to the nonlinear interaction between one freely propagating wave and a forced (evanescent, [Weber and Barrick, 1977]) wave. The scattering coupling coefficient relates to the multiple scattering of the acoustic or electromagnetic waves between the two surface waves [Lipa and Barrick, 1986]. This can have a relatively large amplitude even when the slope of the free surface is small, if the vector difference between the wavenumbers of the surface waves statisfies the Bragg resonance conditions. If the coupling coefficients are known, the measurement of the Doppler spectra in specific conditions allow the inversion of the spectrum of the free surface, thus providing more information than what is obtained from the first-order Bragg peaks [Lipa and Barrick, 1986, Holden and Wyatt, 1992].

Another nonlinear phenomenon that similarly affects the Doppler spectra of the scattered acoustic waves is the modulation of short waves by longer and larger waves. When short waves propagate on longer waves, they experience different types of modulations: (i) the velocity of the short waves is modulated by the perturbation velocity of the long wave, (ii) the wavenumber is modulated due to straining by the long wave, (iii) the width and amplitude of the short waves are also modulated,

(iv) the short waves are tilted as they travel along the sides of the long wave, and (v) the short waves are displaced vertically by the long wave. Each of these modulations have been expressed by various authors [e.g. Keller and Wright, 1975, Hara and Plant, 1994] in terms of transfer functions that multiply the backscattered spectrum, when scattering occurs in the Fraunhofer zone. Four transfer functions are commonly defined, one for the generic hydrodynamic modulation [Keller and Wright, 1975, Hara and Plant, 1994] (including the wavenumber and amplitude modulations), one for the tilt modulation [Keller and Wright, 1975, Hara and Plant, 1994], one for the vertical displacement [Hara and Plant, 1994] (range modulation), and one for the velocity modulation [Keller et al., 1994]. These are discussed with more detail in subsection 3.2.2, where an estimate of these transfer functions is derived based on a simplified expansion analysis.

The models described above are based on a perturbation with respect to the linear representation of the free surface, which strongly simplifies the actual surface dynamics and the physics of scattering. Zakharov's model is believed to represent more realistically the nonlinearities of the free surface, but it is of hard and lengthy implementation [Nouguier et al., 2009]. More accurate studies of backscattering by ocean waves have been performed numerically with slightly simplified nonlinear models of the free surface, and were usually based on Monte Carlo simulations [e.g. Rino et al., 1991, Toporkov and Brown, 2000, Johnson et al., 2001]. These studies compared the predictions of linear and nonlinear hydrodynamic models applied to the Doppler spectrum of electromagnetic waves scattered from two-dimensional ocean wind waves. The calculations were performed with a Kirchhoff model and with a two-scale model [Johnson et al., 2001], and with an iterative extension of the Kirchhoff model [Rino et al., 1991, Toporkov and Brown, 2000]. Random realisations of the free surface were generated based on the Pierson-Moskowitz spectrum [Pierson and Moskowitz, 1964], and then evolved in time according to the three models. The linear model corresponded to the one employed in this thesis and described in subsection 6.1.1. The three studies implemented a nonlinear model derived by Creamer et al. [1989], which is accurate to the second-order of the surface slope. The same model was applied in three-dimensions by Soriano et al. [2006], together with a boundary elements method for the electromagnetic scattering. Creamer's model does not include surface tension effects, therefore it cannot be used for modelling capillary waves. Its application is also computationally demanding, as it requires $\mathcal{O}(N_\rho^2)$ operations, where N_ρ is the number of points on the modelled surface. Johnson et al. [2001] used an additional nonlinear model proposed by West et al. [1987], which is based on a small slope expansion of the hydraulic velocity potential at the surface, and it is accurate to any order. This latter model requires the integration in time of the differential equations governing the evolution of the physical variables, and it was found subject to instabilities by Johnson et al. [2001]. Both nonlinear models predict broader Doppler spectra than the linear model (the model by West et al. [1987] has the broadest spectra), showing the importance of the surface nonlinearities for the Doppler spectra. These results were confirmed by Nouguier et al. [2011a,b] based on a set of scattering models including the parabolic Kirchhoff expansion by Guerin et al. [2010], using both Monte Carlo and statistical simulations with a small-slope Lagrangian weakly nonlinear surface model [Nouguier et al., 2009]. It should be noted that none of the hydrodynamic models cited here are readily applicable to modelling of the free surface of shallow turbulent flows, for which the surface dynamics are still largely unknown.

2.2.3 Applications of optical and radio-based techniques for monitoring of channel and river flows

Some of the measurement techniques reported in the previous subsections have been proposed for the characterisation of the free surface of turbulent flows and rivers. These include both optical and radio-based methods. In most cases the aim was to obtain a measure of the mean surface velocity of the flow. Stereographic methods have been used for field measurements, also in rivers [e.g. Gallego et al., 2011]. They can record the elevation on large areas, but with limited spatial resolution, and typically with low frequency. Methods based on the recording of natural or artificial light reflected by the surface with a camera [Chou et al., 2004] also have potential applications in the field. The intensity of the reflected light depends on the slope of the patterns on the surface, and the relationship between the measured quantities and the physical elevation of the surface is found only empirically [e.g. Chou et al., 2004]. The accuracy of these methods depends largely on the quality of the illumination. Alternative techniques such as the Space-Time Image Velocimetry [Fujita et al., 2007] are intermediate between Large Scale PIV methods that track the position of single scatterers and the methods based on the reflection of natural light. The relation between the measurements with these techniques and the shape of the free surface is not clear.

A range of sensors that estimate the flow velocity in partially filled pipes and open channel flows based on the measurement of the Doppler spectrum of electromagnetic waves are available in the market. LaserFlow by Teledyne ISCO uses the scattering of an airborne laser beam focused below the free surface, therefore assuming the surface to be homogeneously flat. Q-Eye Radar MT by HydroVision, RG-30 by Sommer, and Flo-Dar by Hach all record the Doppler spectrum of microwaves at the frequency of approximately 24 GHz (K-band) backscattered by the free surface. These systems also implement a pulsed ultrasonic sensor in order to measure the mean flow depth, without accounting for the surface fluctuations. These electromagnetic Doppler sensors are characterised by a narrow directivity, and they estimate the velocity of the free surface based on the Bragg scattering mechanism assuming that the surface moves at the mean surface velocity, without accounting for the presence of gravity-capillary waves.

In spite of the relatively large number of applications of Doppler techniques for the remote monitoring of turbulent flows, the scientific studies on the subject have been limited. Plant et al. [2005] developed a microwave coherent radar system to estimate the surface velocity of natural rivers from the Doppler spectrum of the backscattered waves. They interpreted the Doppler spectra in the same way as it is traditionally done in the studies of the ocean surface. They detected two broad Bragg peaks that correspond to advancing and receding waves and defined the characteristic flow velocity as the average between the two peaks. They were able to obtain accurate estimations of the velocity from sensors mounted under a bridge, on a cableway, on the river bank, and even on an airplane and a helicopter. The Bragg peaks were easily detected in presence of rain, but they were difficult to identify under clear weather conditions, when only one wide and asymmetric peak in the spectrum became visible. In this case the velocity estimations became less accurate and often ambiguous. The unpredictability of the performance of radar Doppler sensors in rivers was confirmed by Costa et al. [2006], who used both microwave and UHF radar systems. An apparently better fit with the measured surface and depth-averaged velocities was reported by other authors [Wang et al., 2007, Shen and Wen, 2010, Welber et al., 2016]. So far these methods have found only limited applications. All the above studies are purely experimental and they lack a rigorous investigation of the dynamics of the free surface and of the scattering process. This has impeded the correct interpretation of the experimental results.

2.2.4 Applications of acoustic techniques for monitoring of channel and river flows

ADS limited liability company (LLC.) produces two types of airborne ultrasonic sensors that measure the free surface of turbulent flows in partially filled pipes and in manholes. ADS Echo measures the homogeneous mean surface depth in manholes based on the recording of focused pulses. ADS CS5 measures the mean surface flow velocity in partially filled pipes based on the Doppler spectrum of the ultrasonic waves backscattered by the free surface, and the homogeneous mean surface depth based on scattering of ultrasonic pulses. The only known scientific study of airborne acoustic ultrasound Doppler methods applied to turbulent flows was reported by Fukami et al. [2008]. In this study the analysis procedure was not described, and examples of the measured Doppler spectra were not provided. The sensitivity of the system was found varying unpredictably with the flow conditions, suggesting the need for a more detailed investigation of the underlying phenomena. More recent studies in acoustics have tried to directly measure the surface elevation from the measurement of the airborne ultrasonic acoustic field scattered by the free surface. These followed two approaches, the stationary phase method and an inversion method based on the principles of acoustic holography, respectively.

The applications of the stationary phase method to the scattering from a rough surface have been known for long time [Barrick, 1968]. The method allows the reconstruction of a rough scattering surface at one single location based on the measurement of the phase of the scattered acoustic signal. The application of the stationary phase method to the reconstruction of the surface elevation with airborne ultrasounds was demonstrated by Wang et al. [1991] for a flat layer of water, and extended by Nichols et al. [2013] to the measurement of the local elevation of a rough water surface. These authors implemented the method in a laboratory flume to measure two-dimensional patterns of forced gravity waves as well as the patterns on the surface of a set of shallow turbulent flows. The stationary phase method was also applied successfully by Krynkin et al. [2014] to the measurement of the standard deviation of the free surface elevation in a range of shallow turbulent flow conditions in a laboratory flume.

The requirements for the applicability of the stationary phase method were identified by Nichols et al. [2013], and they pose some limitations to the range of hydraulic conditions where the method can be applied accurately. More sophisticated methods which implement arrays of transducers and/or receivers have been developed. Ultrasound-based imaging is common in medical science [e.g. Fenster et al., 2001] and in non-destructive testing [e.g. Zhang et al., 2010]. Here the emitted signal is generally broadband (a pulse), and the shape of the scatterer is obtained by combining both the spatial and temporal information in the scattered signal. Broadband signals have applications for the reconstruction of the water free surface elevation as well, but these are generally limited to underwater acoustics. For example, Walstead and Deane [2013] reconstructed the shape of nearly-sinusoidal two-dimensional water waves from the scattering of broadband ultrasonic signals recorded underwater by a single receiver. The same technique was applied by Walstead and Deane [2016] but with arrays of receivers in order to reconstruct the shape of waves in a shallow sea environment.

In air the use of broadband signals is made difficult by the poor coupling with the material of the transducer [Chimenti, 2014], and the number of receivers that can be used simultaneously is limited. Accurate measurements of the rough surface are possible, but only with impractical and expensive experimental setups [e.g. Robertson et al., 2002]. Krynkin et al. [2016] developed an alternative technique that recovers the shape of the surface from the inversion of the Kirchhoff scattering integral. In this case the measurements are performed with a number of receivers smaller than the number of locations where the surface elevation needs to be reconstructed. As a result, the problem is underdetermined. The inversion is calculated using techniques which are common in generalised acoustic holography [Maynard et al., 1985, Veronesi and Maynard, 1989], such as the singular value decomposition (SVD) with Tikhonov regularisation [Williams, 2001, Leclère, 2009].

Chapter 3

Theoretical background

This chapter describes the derivation of the mathematical equations and relations which are used throughout the following chapters. Section 3.1 is focused on the fluid dynamic equations which describe the evolution of the free surface of a shallow turbulent flow. Here the free surface is represented as a linear superposition of sinusoidal waves. In section 3.1.2 the dispersion relation of gravity-capillary waves, i.e., the relation between their wavenumber and frequency, is presented for the waves that propagate in a flow where the average streamwise velocity varies vertically according to a power-function of the depth. This relation is compared to the measurements of the frequency-wavenumber spectra of the surface elevation in chapter 5. The empirical model of the power-function time averaged streamwise velocity profile is described in subsection 3.1.4. Models of the statistics of the free surface elevation based on a linear and weakly nonlinear model are presented in subsection 3.1.6. These models are also compared with the experimental measurements in chapter 5, based on the gradual wavelet reconstruction technique reported in subsection 3.1.7. Alternative models of the surface elevation consider random distribution of wave packets. The derivation of the equations that describe the evolution of wave packets, or wave groups, are reported in subsection 3.1.3. The statistics of the amplitude of these packets, the so-called envelope, are described in subsection 3.1.8 as obtained for linear and weakly nonlinear waves. The model of wave groups is the basis for an analysis procedures that allow the characterisation of the spatial and temporal statistics of the free surface. This procedure is described in subsection 3.1.9, and it is applied to the experimental measurements in subsections 5.4.2.

Subsection 3.2.1 presents the standard derivation of the integral equations that describe the acoustic field scattered by a rough smooth surface based on the Kirchhoff approximation. Subsection 3.2.2 discusses the scattering by a dynamic surface, and the resulting Doppler spectrum of the scattered acoustic field. The results in these subsections were used for the modelling of the acoustic scattering and for the measurement of the statistics of the rough surface based on the measured scattered field in chapter 6.

3.1 Derivation of the free surface model

3.1.1 Linear free surface model with random phase

The dynamic model of the free surface implemented in chapter 6 in order to study the Doppler spectrum of the scattered acoustic field is based on a linear model of gravity-capillary waves with random phase and amplitude. The main assumption in this section is that the free surface elevation is statistically stationary, which means that its statistics are independent of the spatial location and of time. The surface elevation function, ζ, is defined as the instantaneous local deviation of the flow depth from its local average in time, which is called H. The depth is the distance between the bottom and top boundaries of the flow, evaluated along the direction normal to the slope of the bottom boundary. The roughness of the bottom boundary is not considered explicitly in the equations presented here. In the experiments reported in the thesis, the system of reference has the origin on the undisturbed average flat surface, with the z-axis normal to the slope of the bottom boundary and pointing upwards, so that $z = -H$ at the bottom and $z = \zeta$ at the free surface. The depth H is constant and uniform in space and in time. The flume reference system has the direction x parallel to the mean surface velocity, and the direction y such that x, y, and z form an orthogonal triad. The surface elevation is a function of the two spatial dimensions x and y and of the time t, therefore it is written as $\zeta(x, y, t)$.

Based on the assumption of stationarity, it is possible to write a realisation of the free surface elevation in space and in time in the form of a Fourier integral,

$$\zeta(x, y, t) = \Re\left\{\int_0^\infty \iint_{-\infty}^\infty A(\mathbf{k}, \omega) e^{i[\mathbf{k}\cdot\boldsymbol{\rho} - \omega t + \Phi]} d\mathbf{k} d\omega\right\}, \tag{3.1}$$

where $\boldsymbol{\rho} = (x, y)$, $\mathbf{k} = (k_x, k_y)$ is the wavenumber vector, ω is the radian frequency, and Φ is the initial phase which is usually taken as a random variable uniformly distributed between 0 and 2π. The symbol $\Re$ indicates that only the real part of the integral should be considered. This applies to the rest of the discussion in this section, therefore the symbol will be omitted in the rest of this section. $A(\mathbf{k}, \omega)$ is called the amplitude spectrum of the water surface elevation. The frequency-wavenumber spectrum of the surface elevation is indicated by $S(\mathbf{k}, \omega)$, and it is defined as

$$S(\mathbf{k},\omega)=\iiint_{-\infty}^{\infty}<\zeta(x,y,t)\zeta(x+\rho_x x,y+\rho_y y,t+\tau)>e^{-i[\mathbf{k}\cdot\boldsymbol{\rho}-\omega\tau]}d\boldsymbol{\rho}d\tau, \qquad (3.2)$$

where $<>$ denotes the average across x, y, and t, and $\mathbf{r}=(r_x,r_y)$ and τ are the spatial and temporal separations. The integrals in equations (3.1) and (3.2) are generalisations of the complex Fourier transform in the limit as the area of integration tends to infinity, i.e.,

$$\int_{-\infty}^{\infty}f(x)dx=\lim_{x_0\to\infty}\frac{1}{x_0}\int_{-x_0}^{x_0}f(x)dx, \qquad (3.3)$$

where $x\in(-x_0,x_0)$. The quantity

$$W(\mathbf{r},\tau)=<\zeta(x,y,t)\zeta(x+r_x,y+r_y,t+\tau)> \qquad (3.4)$$

is called the space-time correlation function of the surface elevation. Equation 3.2 can be calculated directly from the measurement of the correlation function in order to determine the frequency-wavenumber spectrum, which is done in chapter 5. The amplitude spectrum and the frequency-wavenumber spectrum are related by

$$|A(\mathbf{k},\omega)d\mathbf{k}d\omega|^2=S(\mathbf{k},\omega)d\mathbf{k}d\omega. \qquad (3.5)$$

One can represent the wavenumber vector in polar co-ordinates k and θ, where $k=|\mathbf{k}|$ and θ is the angle between $\mathbf{k}$ and the direction x. The angular spatial spectrum is then defined as

$$S(\mathbf{k})=S(k,\theta)=\int_0^{\infty}S(k,\theta,\omega)d\omega, \qquad (3.6)$$

while the frequency spectrum is

$$S(\omega)=\int_0^{2\pi}\int_0^{\infty}S(k,\theta,\omega)kdkd\theta. \qquad (3.7)$$

In section 3.1.2 it is shown that the definition of ζ based on equation (3.1) satisfies the Navier-Stokes equations and the equation of continuity at the first order of the wave amplitude and slope, for an incompressible and inviscid fluid where the depth and the time averaged streamwise flow velocity are uniform in the directions x and y. The linearisation of these equations is valid under some circumstances which will be made clear. It allows separating the contribution of each wave with the wavenumber $\mathbf{k}$ and the frequency ω. This procedure enables to determine a relation between the frequency and the wavenumber,

$$\omega = \Omega(\mathbf{k}) = \Omega(k, \theta), \tag{3.8}$$

which is called the dispersion relation.

The fact that the waves follow an explicit and deterministic dispersion relation simplifies the calculation of the spectra, and allows the prediction of the temporal evolution of the free surface based on the knowledge of the spatial spectrum and of the initial conditions. In fact, the spatial spectrum can be calculated as

$$S(\mathbf{k}) = \int_0^\infty S(\mathbf{k}, \omega)\delta(\omega - \Omega(\mathbf{k}))d\omega = \frac{1}{2}S(\mathbf{k}, \Omega(\mathbf{k})), \tag{3.9}$$

where δ is a delta function. Consequently, equation (3.1) is simplified as

$$\zeta(x, y, t) = \iint_{-\infty}^{\infty} A(\mathbf{k}, \Omega(\mathbf{k}))e^{i[\mathbf{k}\cdot\boldsymbol{\rho} - \Omega(\mathbf{k})t + \Phi]}d\mathbf{k}. \tag{3.10}$$

In equation (3.9) the symmetry of the spectrum, i.e.,

$$S(\mathbf{k}, -\omega) = S(-\mathbf{k}, \omega), \tag{3.11}$$

was used.

Often the frequency spectrum is more easily measured than the spatial spectrum. The relation between the two spectra is not straightforward. The frequency spectrum is written in polar co-ordinates as

$$S(\omega) = \int_0^{2\pi}\int_0^\infty S(k, \theta, \omega)\delta(\omega - \Omega(k, \theta))kdkd\theta. \tag{3.12}$$

If the dispersion relation can be inverted, i.e., if a function $K(\omega, \theta)$ which satisfies

$$\Omega(K(\omega, \theta), \theta) = \omega \tag{3.13}$$

exists, then equation (3.12) becomes, after a change of variable [e.g., Kitaigordskii et al., 1975],

$$S(\omega) = \int_0^{2\pi} \frac{S(K(\omega), \theta)}{|\partial\Omega/\partial k|_{k=K(\Omega,\theta)}} K(\omega, \theta)d\theta, \tag{3.14}$$

where

$$c_g = \partial\Omega/\partial k \tag{3.15}$$

is called the group velocity. Equation (3.14) is used in section 5.3 in order to justify the measured peaks of the frequency spectrum at the frequency where the group velocity is equal to zero.

3.1.2 Dispersion relations

In this subsection, the dispersion relation of gravity-capillary waves propagating in a flow with constant uniform depth H and with the average streamwise velocity $U(z)$ that varies in general with the depth z is considered. Two cases are considered. In the first case the flow is irrotational, and the flow velocity is constant with the depth, i.e.,

$$U(z) \equiv U_0. \tag{3.16}$$

In the second case the vertical velocity profile in a turbulent shallow flow with rough boundary is approximated by a power-law of the vertical co-ordinate [Cheng, 2007], such as

$$U(z) = U_0 \left(1 + \frac{z}{H}\right)^n . \tag{3.17}$$

The relation between the exponent n and the Reynolds number and relative submergence of the flow is discussed in subsection 3.1.4.

The solution when the flow is irrotational is well known. The solution when the average streamwise velocity profile follows equation (3.17) can be found numerically based on a procedure suggested by Fenton [1973]. The derivation of both solutions is given in the Appendix A. The flow is assumed to be inviscid and incompressible, and the fluid domain extends to infinity along both the x- and the y-direction. The density of air is neglected, and the boundary equations are linearised assuming that (i) the wave perturbation velocity is much smaller than the average streamwise velocity at the surface, (ii) the amplitude of the surface fluctuations is much smaller than the homogeneous mean depth, and (iii) the spatial gradient of the surface elevation is very small. The bed roughness is neglected, and the boundary conditions at the bed and at the free surface are expanded near $\zeta = -H$ and $\zeta = 0$, respectively. The solution considers a single plane sinusoidal wave with the wavenumber vector $\mathbf{k}$, the frequency ω, and the phase velocity

$$c = \frac{\omega}{k} . \tag{3.18}$$

In the irrotational case the phase velocity of the gravity-capillary waves is found as

$$c(k,\theta) = |U_0 \cos(\theta)| \pm \sqrt{\left(g + \frac{\gamma_w}{\rho_w} k^2\right) \tanh(kH)}\,, \tag{3.19}$$

where g is the gravity constant, and γ_w and ρ_w are the surface tension coefficient and the density of water, respectively. The corresponding dispersion relation is

$$\Omega(k,\theta) = |kU_0 \cos(\theta)| \pm \sqrt{\left(g + \frac{\gamma_w}{\rho_w} k^2\right) k \tanh(kH)}\,. \tag{3.20}$$

The two signs in equations (3.19) and (3.20) represent the waves that propagate upstream (−) and downstream (+), respectively. Equation (3.20) shows that the constant flow velocity induces a shift of the frequency proportional to the scalar product of the wavenumber and the mean velocity vectors. The shift is represented by the non-dispersive part of the equation, and it corresponds to

$$\Omega(k,\theta) = kU_0 \cos(\theta)\,. \tag{3.21}$$

Equation (3.20) is used in section 5.3 and compared to the measured dispersion relation in a shallow turbulent flow.

In still water, where $U_0 = 0$, the phase velocity in still water takes the form

$$c_s = \sqrt{\left(g + \frac{\gamma_w}{\rho_w} k^2\right) \tanh(kH)}. \tag{3.22}$$

This has a minimum in water at ambient temperature,

$$c_{\min} \approx 0.23\,\mathrm{m\,s^{-1}}. \tag{3.23}$$

When the average streamwise velocity profile follows equation (3.17), the phase velocity of gravity-capillary waves is given by [Fenton, 1973]

$$c^2 = \frac{\left(g + \frac{\gamma_w}{\rho_w} k^2\right) \check{\Psi}(0)}{(\check{U} - 1)[(\check{U} - 1) - n\check{U}\check{\Psi}(0)]}, \tag{3.24}$$

where

$$\check{U} = U_0 \cos(\theta)/c, \tag{3.25}$$

θ is the angle formed by the wavenumber $\mathbf{k}$ with respect to the streamwise direction, and $\check{\Psi}(0)$ is found by integrating numerically an initial value problem. Here the integration was performed with a fourth-order Runge-Kutta method on a grid of

100 points between $\check{z} = -1$ and $\check{z} = 0$, where $\check{z}$ is the non-dimensionalised vertical co-ordinate. The equation that needs to be integrated is singular when $0 < c < U_0$, which occurs for the waves with $|c_s| < U_0$ and with $\cos(\theta) < 0$. Therefore, a solution with the power function velocity profile was not attempted for these waves. The factor $\check{U}$ depends on the phase velocity c, therefore the solution was found with a least square non-linear fitting procedure based on the trust-region-reflective method and implemented in the 'lsqnonlin' standard function in Matlab R2015b [Coleman and Li, 1996].

The dispersion relation based on the power function velocity profile is given by

$$\Omega(k, \theta) = kc, \tag{3.26}$$

where c is determined from equation (3.24). In section 5.3 it is shown that equations (3.24) and (3.26) approximate well the measured dispersion relation in a shallow turbulent flow over a homogeneous rough bed.

3.1.3 Group velocity

The dispersion relations described in the previous section have a nonlinear dependence from the wavenumber k. This has consequences for the dynamics of groups of waves, which are analysed in subsection 5.3.3. Consider once again the spectral representation of the free surface based on equation 3.10, and investigate the case where the spectrum $S(\mathbf{k})$ is narrow, i.e., it decays rapidly from a maximum at the wavenumber k_p. For simplicity only the two dimensional case is considered, i.e.,

$$A(\mathbf{k}) = A(k, \theta)\delta(\theta). \tag{3.27}$$

The discrete form of the integral of equation 3.10 is written as

$$\zeta(x,t) = \Re\left\{ e^{i[k_p x - \Omega(k_p)t]} \sum_l A(k_l) e^{i[(k_l - k_p)x - (\Omega(k_l) - \Omega(k_p))t + \Phi_l]} \Delta k \right\}, \tag{3.28}$$

where $l = 1, 2, \ldots$ is the wavenumber index, such that $k_l = l\Delta k$. The argument of the exponent on the right hand side of equation (3.28) can be expanded in a Taylor series near k_p, i.e.,

$$k_l = k_p + \Delta k, \tag{3.29a}$$

$$\Omega(k_l) = \Omega(k_p) + \frac{\partial \Omega(k_p)}{\partial k}\Delta k + \mathcal{O}(\Delta k^2), \tag{3.29b}$$

from which ζ is expressed as

$$\zeta(x,t) = \Re\left[\tilde{Z}(x,t)e^{i[k_p x - \Omega(k_p)t]}\right], \tag{3.30}$$

where $\tilde{Z}$ is the complex envelope of the surface elevation, with amplitude Z and phase Φ, i.e.,

$$\tilde{Z}(x,t) = Z(x,t)e^{i\Phi(x,t)}. \tag{3.31}$$

At the first order of Δk, $\tilde{Z}$ is defined by

$$\tilde{Z}(x,t) = e^{i\Delta k\left[x - \frac{\partial\Omega(k_p)}{\partial k}t\right]} \sum_{l,\ |k_l - k_p| \lesssim \Delta k} A(k_l)e^{i\Phi_l}. \tag{3.32}$$

Equation (3.32) shows that the envelope of a narrow-band system of waves moves with the velocity equal to the group velocity. This observation is used in section 5.3.3 in order to demonstrate that the amplitude of the surface elevation (including the patterns with the largest amplitude) move in a way that is in agreement with the theory of gravity-capillary waves.

3.1.4 Power-function streamwise velocity profiles in shallow turbulent flows

The power-function profile of equation (3.17) can approximate the average streamwise velocity profile in a shallow turbulent flow over an hydraulically rough bed [Cheng, 2007]. The nonlinear terms of the averaged Navier-Stokes equations are commonly represented in the form of the Reynolds stresses, τ_R [e.g. Schlichting and Gersten, 1979, p.562]. The friction velocity at the wall is defined as

$$u_* = \sqrt{\tau_R/\rho_w}. \tag{3.33}$$

The ratio H/d_s is called the relative submergence, where d_s is the characteristic size of the bed roughness. The friction velocity is related to the section-averaged streamwise velocity U_H by the relation

$$f = 8\left(\frac{u_*}{U_H}\right)^2, \tag{3.34}$$

where f is called the Darcy Weisbach friction factor [Schlichting and Gersten, 1979, p.610].

Cheng [2007] proposed an empirical formula for f that interpolates the measurements of the friction factor obtained by Nikuradse [1950] between the smooth bed condition and the completely rough bed condition. This formula is written as

$$f = \left(0.316 Re_H^{-0.25}\right)^a \left\{ \left[2\log\left(\frac{2H}{d_s}\right) + 1.74 \right]^{-2} \right\}^{1-a}, \tag{3.35}$$

where a is defined as

$$a = \left[1 + \left(\frac{Re_H d_s}{640H} \right)^2 \right]^{-1}, \tag{3.36}$$

and

$$Re_H = 4\rho_w U_H H/\mu_w \tag{3.37}$$

is the Reynolds number based on the mean depth and on the section-average velocity U_H. μ_w is the dynamic viscosity of water. Cheng [2007] also observed that empirical measurements of the ratio $\sqrt{f}/n$ suggest this ratio is almost constant and equal to

$$1.0 \leq \sqrt{f}/n \leq 1.2, \tag{3.38}$$

with the best fit-curve represented by

$$1/n = 1.37 f^{-0.43}. \tag{3.39}$$

The exponent n increases when the Reynolds number increases, and when the relative submergence decreases. Equations (3.35) and (3.39) allow the calculation of the exponent n based on the Reynolds number and the relative submergence. This is shown in section 4.2, where the measurements of the exponent of the streamwise velocity profile in a shallow flow with homogeneously rough bed are compared with the predictions by these two equations.

3.1.5 Stationary waves

As discussed in subsection 2.1.4, the presence of a rough bed can cause the appearance of three-dimensional and dynamic patterns at the free surface of a shallow flow. The steady state solution of these patterns [e.g. Harband, 1976] is singular at the wavenumber $k_0(\theta)$ that satisfies

$$\Omega(k_0(\theta), \theta) = 0. \tag{3.40}$$

This means that whenever equation (3.40) has a solution, the waves with the wavenumber k_0 propagating in the direction θ tend to dominate the pattern of the free surface. These waves are called stationary waves.

The wavenumber k_0 can be found in the irrotational case from the solution of

$$k_0 U_0 \cos\theta = -\sqrt{\left(g + \frac{\gamma_w}{\rho_w} k_0^2\right) k_0 \tanh\left(k_0 H\right)}, \tag{3.41}$$

based on equation (3.46). These waves are essentially the waves which propagate upstream (with the minus sign in equation (3.41)) with the phase velocity in still water (equation (3.22)) equal to the projection of the mean surface velocity along the wavenumber vector. Introducing the surface tension makes so that the phase velocity has a minimum (equation (3.23)). As a result, the stationary waves can only form if

$$U_0 \geq c_{\min}. \tag{3.42}$$

There is also a minimum of the angle θ for these waves, which is equal to

$$\theta_{\min} = \pi - \cos^{-1}\left(c_{\min}/U_0\right), \tag{3.43}$$

so that $\theta_{\min} \leq \theta(k_0) \leq 2\pi - \theta_{\min}$. Within this range of direction, (3.41) has two solutions, one for the gravity waves with the smaller wavenumber and the other one for the capillary waves with the larger wavenumber. Of these, the gravity waves tend to dominate, although capillary waves can become predominant if the spectrum of the boundary is dominated by short wavelengths.

Lighthill [Burns, 1953] found an analytical expression for the wavenumber of the stationary waves in a flow where the average streamwise velocity varies like a power-function of the depth (equation (3.17)). Introducing the effect of the surface tension, this expression is

$$k_0 \frac{I_{-1/2-n}(k_0 H)}{I_{1/2-n}(k_0 H)} = \frac{g + \frac{\gamma_w}{\rho_w} k_0^2}{U_0^2 \cos^2\left(\pi - \theta\right)}, \tag{3.44}$$

where I_n is the modified Bessel function of order n. In chapter 5 it is shown that the prediction of the wavenumber of stationary waves based on equation (3.44) approximates well the measurement of the stationary patterns in most of the measured flow conditions.

FIG. 3.1 shows the two components $k_{0,x}$ and $k_{0,y}$ of the wavenumber of the stationary waves calculated for an irrotational flow, and for a flow with the vertical profile of the average streamwise velocity described by equation (3.17), with $n = 1/3$. Here the mean surface velocity and the mean depth of the flow were $U_0 = 0.5\,\mathrm{m\,s^{-1}}$ and $H = 0.1\,\mathrm{m}$, respectively. It is seen that the minimum wavenumber modulus is found in the direction $\theta = \pi$ for the waves that propagate in the negative x-

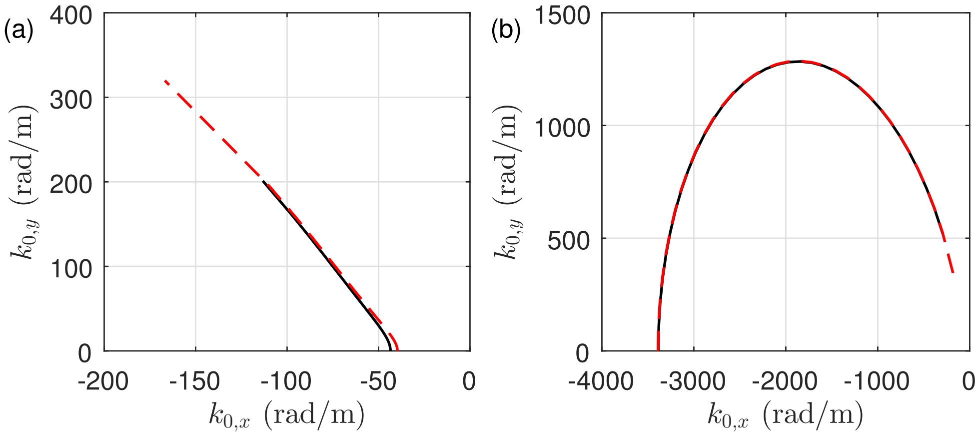

Figure 3.1: The components $k_{0,x}$ and$k_{0,y}$ of the wavenumber of the stationary waves calculated (red) for an irrotational flow (equation (3.41)) and (black) for a flow with the 1/3 power-function vertical profile of the average streamwise velocity (equation (3.44)). $U_0 = 0.5\,\mathrm{m\,s^{-1}}$, $H = 0.1\,\mathrm{m}$. (a) Solution in the gravity-dominated range, and (b) solution in the capillary-dominated range.

direction with $k_y = 0$. The difference between the two equations (3.41) and (3.44) is very small in this flow condition, and becomes non-noticeable in the capillary range. The gravity-waves solution at $\theta = \pi$ in FIG. 3.1a shows that k_0 is larger when it is calculated for the power-function velocity profile.

In the measurements described in chapter 5 only the waves propagating along the x-direction corresponding to the solution in the gravity-dominated range of wavenumbers are observed. The stationary pattern appears to be essentially two-dimensional in these measurements, and there is no clear evidence of the angular distribution represented in FIG. 3.1. Therefore, in the rest of this thesis k_0 always indicates the gravity-dominated value of k_0 which can be determined from equation (3.44) assuming $\theta = \pi$.

The experimental results described in chapter 5 also show the existence of an additional three-dimensional pattern of waves, which includes both propagating and stationary waves. This pattern corresponds to waves propagating in all directions, with the wavenumber modulus k equal to k_0. The amplitude of these waves varies with the direction of propagation, and it is maximum for the stationary waves propagating in the direction $\theta = \pi$. This pattern is not explained by any of the known theories about the interaction of the free surface with a static bed, although it appears to be governed by the wavenumber of the stationary waves predicted by equation (3.44). The dispersion relation of the pattern, as derived for the flow with the power-function velocity profile, can be found from

$$\Omega(k_0, \theta) = k_0 c(k_0, \theta), \tag{3.45}$$

where $c(k_0,\theta)$ is determined based on equation (3.24) for a power-function streamwise velocity profile, and θ varies between 0 and 2π radians.

The same pattern when described by the irrotational theory is represented by the dispersion relation

$$\Omega(k_0,\theta) = k_0 U_0 \cos(\theta) \pm \sqrt{\left(g + \frac{\gamma_w}{\rho_w} k_0^2\right) k_0 \tanh(k_0 H)}. \tag{3.46}$$

Based on the definitions

$$k_x = k\cos(\theta), \tag{3.47a}$$

$$k_y = k\sin(\theta), \tag{3.47b}$$

$$k = \sqrt{k_x^2 + k_y^2}, \tag{3.47c}$$

$$\theta = \tan^{-1}(k_y/k_x). \tag{3.47d}$$

equation 3.46 can be written in terms of the streamwise and of the lateral wavenumbers

$$\Omega(k_x) = U_0 k_x \pm \sqrt{\left(g + \frac{\gamma_w}{\rho_w} k_0^2\right) k_0 \tanh(k_0 H)}, \tag{3.48a}$$

$$\Omega(k_y) = U_0 \sqrt{k_0^2 - k_y^2} \pm \sqrt{\left(g + \frac{\gamma_w}{\rho_w} k_0^2\right) k_0 \tanh(k_0 H)}, \tag{3.48b}$$

respectively. Equation (3.48a) is a straight line in the plane $k_x - \omega$ which intercepts the ω-axis at the characteristic frequency of the stationary waves in still-water,

$$\Omega_s(k_0) = \sqrt{\left(g + \frac{\gamma_w}{\rho_w} k_0^2\right) k_0 \tanh(k_0 H)}, \tag{3.49}$$

while equation (3.48b) corresponds to an ellipse with semi-axes k_0 and $\Omega_s(k_0)$ in the plane $k_y - \omega$. It is shown in chapter 5 that the equations (3.48) approximate well the measurements of the dispersion relation of the waves in the laboratory flume.

It should be noted that whenever the velocity of the flow is smaller than the minimum of the phase velocity, $c_{\min}$, the stationary waves cannot form. When the flow velocity approaches the value of $c_{\min}$, the theory predicts the infinite amplitude of the surface elevation [Dias and Kharif, 1999]. In this case, the steady state expansion shows that no waves are found in the far field from the disturbance. The measurements in chapter 5 confirm that the stationary waves cannot form when the mean surface velocity is smaller than $c_{\min}$. No measurement was performed close enough to the condition $U_0 = c_{\min}$ in order to observe the eventual increase of the wave amplitude in that condition.

3.1.6 Probability distributions of free surface waves

This subsection presents the expected statistics of the surface elevation based on a linear and a weakly nonlinear model of the surface. These models are compared to the measurements of the surface elevation in subsection 5.2 in order to evaluate the eventual importance of nonlinearities in the tested flow conditions. The most straightforward way to identify the eventual presence of nonlinearities is to investigate the statistics of the surface elevation measured at a single location in time. With reference to the spectral representation of the free surface elevation based on equation (3.10), the following quantities are defined [Longuet-Higgins, 1963],

$$\Upsilon = e^{i[\mathbf{k}\cdot\boldsymbol{\rho} - \Omega(k,\theta)t]}, \tag{3.50a}$$

$$\breve{A} = \xi e^{i\Phi}, \tag{3.50b}$$

where

$$\int_{\mathbf{k}-d\mathbf{k}/2}^{\mathbf{k}+d\mathbf{k}/2} \xi d\mathbf{k} = A(\mathbf{k})d\mathbf{k}. \tag{3.51}$$

Υ represents a deterministic trigonometric function, i.e., the eigenfunction of a Fourier series expansion. ξ is the amplitude of the discrete Fourier transform of the surface elevation ζ with the spectral resolution $d\mathbf{k}$, and it is a Gaussian random variable with zero average. Φ is the phase of the same transform, and it is uniformly distributed in the interval between $-\pi$ and π. $\breve{A}$ is the complex eigenvalue obtained by the transform.

In order to make the relation with a discrete Fourier transform explicit, all terms of equations (3.50) are associated with an index j, which represents the term of the transform at the discrete set of wavenumbers $\mathbf{k}_j$. Assuming the statistics to be stationary and homogeneous, Υ is evaluated at $\boldsymbol{\rho} = 0$ and $t = 0$ for simplicity, so that its argument is zero for all indices j. Equations (3.50) become

$$\Upsilon_j = 1, \tag{3.52a}$$

$$\breve{A}_j = \xi_j e^{i\Phi_j}, \tag{3.52b}$$

and equation (3.10) is written as

$$\zeta = \sum_j \Upsilon_j \breve{A}_j. \tag{3.53}$$

All terms of equation (3.53) are assumed to be linearly independent. Therefore, due to the so-called law of large numbers, the probability density function of ζ is Gaussian with variance [Longuet-Higgins, 1963]

$$\sigma^2 = \sum_j \sigma_j^2, \tag{3.54}$$

where σ_j^2 is the variance of the random variable ξ_j. The pdf is described by

$$p_\zeta(\zeta) = \frac{1}{\sigma\sqrt{2\pi}} e^{-\frac{\zeta^2}{2\sigma^2}}. \tag{3.55}$$

When the nonlinear terms of the boundary conditions are considered, the surface equations have a solution of the form (here presented up to the third order of σ which is assumed small, following Weber and Barrick [1977])

$$\zeta = \sum_j \Upsilon_j \breve{A}_j + \sum_{j,l} \Upsilon_{j,l} \breve{A}_j \breve{A}_l + \sum_{j,l,m} \Upsilon_{j,l,m} \breve{A}_j \breve{A}_l \breve{A}_m, \tag{3.56}$$

where the coefficients $\Upsilon_{j,l}$ and $\Upsilon_{j,l,m}$ are functions of $\mathbf{k}_j$, $\mathbf{k}_l$, and $\mathbf{k}_m$ and they are of order k and k^2, respectively. If all waves are linearly independent, then the products $\breve{A}_j \breve{A}_l$ and $\breve{A}_j \breve{A}_l \breve{A}_m$ are identically zero, and one obtains the same result of equation (3.53). The weak nonlinearity of the surface causes small deviations of the Gaussian statistics which can be quantified.

The statistical moment of order q of the free surface elevation is defined as

$$m_{\zeta,q} = <\zeta^q> . \tag{3.57}$$

Longuet-Higgins [1963] introduce the cumulants of the distribution, which are defined (up to the third order) by

$$\chi_1 = m_{\zeta,1}, \tag{3.58a}$$
$$\chi_2 = m_{\zeta,2} - m_{\zeta,1}^2, \tag{3.58b}$$
$$\chi_3 = m_{\zeta,3} - 3m_{\zeta,1}m_{\zeta,2} + 2m_{\zeta,1}^3, \tag{3.58c}$$
$$\chi_4 = m_{\zeta,4} - 4m_{\zeta,3}m_{\zeta,1} - 3m_{\zeta,2}^2 + 12m_{\zeta,2}m_{\zeta,1}^2 - 6m_{\zeta,1}^4. \tag{3.58d}$$

The advantage of a formulation based on the cumulants rather than on the moments of the distribution is that the cumulant of a sum of independent variables is equal to the sum of the cumulants of each variable. The standard deviation σ and the coefficients of skewness, λ_3, and of kurtosis, λ_4, are defined as [Longuet-Higgins, 1963]

$$\sigma = m_{\zeta,2}^{1/2} = (\chi_2 + m_{\zeta,1}^2)^{1/2}, \tag{3.59a}$$

$$\lambda_3 = m_{\zeta,3} m_{\zeta,2}^{-3/2} = \chi_3/\chi_2^{3/2}, \tag{3.59b}$$

$$\lambda_4 = m_{\zeta,4} m_{\zeta,2}^{-2} = 3 + \chi_4/\chi_2^2, \tag{3.59c}$$

respectively. If the coefficients $\breve{A}_j$ are only weakly linearly dependent, the cumulants of order q higher than 1 are of order $\sigma^{2(q-1)}$. Hence, it is possible to expand the probability distribution function in powers of σ, neglecting the higher orders. The expansion leads to a representation in terms of Hermite polynomials. At the second order of σ^2, this has the form

$$p_\zeta(\zeta) = \frac{1}{\sqrt{2\pi\chi_2}} e^{-\bar{\zeta}^2/2} \left[1 + \frac{1}{6}\lambda_3 H_3 + \frac{1}{24}(\lambda_4 - 3) H_4 + \frac{1}{72}\lambda_3^2 H_6 \right], \tag{3.60a}$$

$$H_3 = \bar{\zeta}^3 - 3\bar{\zeta}, \tag{3.60b}$$

$$H_4 = \bar{\zeta}^4 - 6\bar{\zeta}^2 + 3, \tag{3.60c}$$

$$H_6 = \bar{\zeta}^6 - 15\bar{\zeta}^4 + 45\bar{\zeta}^2 - 15, \tag{3.60d}$$

where $\bar{\zeta}$ is the normalised elevation,

$$\bar{\zeta} = (\zeta - \chi_1)/\sqrt{\chi_2}. \tag{3.61}$$

Equations (3.55) and (3.60) are compared with the measured pdf of the surface elevation in subsection 5.2. It is shown that in some flow conditions equation (3.60) approximates better the measured pdf. The derivation proposed by Longuet-Higgins [1963] is based on a weakly nonlinear representation of the free surface and it does not consider the mutual interactions among waves described in subsection 2.1.5, since these imply the existence of a relation between the phases, and therefore the invalidation of the random phase Gaussian model. Based on the analysis performed by Longuet-Higgins [1963] it is expected that the coefficient of kurtosis (the scaled coefficient $\lambda_4 - 3$ in the notation used here) would be of the same order of λ_3^2. In all the measured conditions in chapter 5, $\lambda_4 - 3$ is found much larger than λ_3^2. According to Creamer et al. [1989], large values of the kurtosis compared to λ_3^2 suggest the existence of quartet interaction among waves for the deep water case. The same result was obtained by Janssen [2009] in the shallow water case with an analysis based on the Zakharov equation.

3.1.7 Generation of constrained surrogate time series with the gradual wavelet reconstruction

In chapter 6 the linear spectral model of the surface elevation based on equation (3.10) is used extensively in order to model the scattering of the acoustic pressure field by the dynamic surface. As discussed in the previous subsection, this linear model leads to the Gaussian statistics of the surface elevation and of its slope. These statistics were measured in a laboratory flume over a wide range of flow conditions, and the results of the measurements discussed in subsection 5.2.2 show a small variation from the Gaussian statistics in some flow conditions. It is useful to quantify the statistical significance of these variations. The purpose is to determine if the linear model is able to reproduce accurately the behaviour of the free surface. This corresponds to a statistical null hypothesis that needs to be tested.

A simple way to test this hypothesis is to generate a set of synthetic constrained surrogate data sets with the same properties of the measured data, such as the probability density function and the Fourier power spectrum, that satisfy the null hypothesis. Since there is no limit to the number of surrogates that can be generated, the variability of the statistical moments can be evaluated directly by a Monte Carlo simulation. This allows the empirical calculation of the statistical significance of the experimental observations. The most straightforward way to do so is to measure the Fourier spectrum of the experimental data, randomise its phase, and generate the surrogates by the inverse Fourier transform. This approach was followed by Osborne et al. [1986] and it is directly relevant to the spectral representation given by equation (3.10). The practical implementation of the method is not straightforward, though, due to the finite length of the data set [Theiler et al., 1992]. Such an approach also allows only the eventual rejection of the null hypothesis, but it does not quantify the degree of nonlinearity required by the surrogates in order to justify the eventual significant deviations from the linear statistics.

An alternative procedure that overcomes the above limitations is the Gradual Wavelet Reconstruction (GWR) method proposed by Keylock [2006] and later improved by Keylock [2007] and Keylock [2010]. The procedure is based on the Iterated Amplitude Adjusted Fourier Transform (IAAFT) method developed by Theiler et al. [1992]. This method introduces an additional rank-order matching step to the Fourier transform method described by Osborne et al. [1986], which ensures that the pdf of the surrogate data coincides with that of the original data series. With respect to the IAAFT method, the GWR method implements the Maximal Overlap Discrete Wavelet Transform (MODWT) in spite of the Fourier transform. The surrogate data sets generated with the GWR method are characterised by a parameter

ϱ representing the similarity to the original data. ϱ is calculated as the ratio of the energy of the original data (the square of the wavelet transform of the surface elevation) which is not randomised. When $\varrho = 0$ the surrogates are fully random. As ϱ is increased, a progressively larger fraction of the original data is left unchanged, while only the remaining fraction is randomised. When $\varrho = 1$ the surrogate coincides with the original data set. Varying the parameter ϱ makes it possible to quantify how similar the surrogates must be to the original data sets in order to show the same statistics.

The algorithm of the GWR method is as follows [Keylock, 2010], for a set value of the parameter $0 \leq \varrho \leq 1$:

1. calculate the wavelet transform of the original data with the MODWT;
2. order the squared coefficients of the MODWT in descending order and calculate their cumulative sum;
3. identify the smallest set of rank-ordered coefficients for which the cumulative sum is larger or equal than the total sum multiplied by the parameter ϱ. These coefficients are called fixed;
4. for each scale:
    (a) remove all the non-fixed coefficients, and interpolate through the fixed ones with a piecewise cubic Hermitian polynomial method [Fritsch and Carlson, 1980] in time,
    (b) randomise the order of the non-fixed coefficients, and then add them to the interpolated sequence of coefficients at the non-fixed locations,
    (c) calculate the amplitude of the Fourier transform of these coefficients in time,
    (d) randomise all coefficients,
    (e) calculate the phase of the Fourier transform of the randomised coefficients calculated at step 4d,
    (f) calculate the inverse Fourier transform based on the amplitude of the coefficients found at step 4c and with the phase of the randomised coefficients found at step 4d,
    (g) order all squared coefficients in increasing order, and replace the values of the coefficients calculated at step 4f with the ones determined at step 4b one by one, from the smallest to the largest,
    (h) replace the values of the fixed coefficients in their original location,

   (i) calculate the Fourier power spectrum of the set of coefficients found at step 4f with the ones at step 4b, and determine the average squared difference between the two spectra,

   (j) repeat steps from 4d to 4i until the average squared difference is smaller than a chosen threshold,

5. calculate the inverse MODWT of the shuffled and rescaled coefficients calculated at the end of step 4j;

6. apply the rank-order matching step 4g to the whole data set in order to match the pdf of the original signal.

The resulting synthetic constrained data set has the same pdf and frequency power spectrum of the original data. When $\varrho = 0$, none of the wavelet coefficients are fixed. In this case, the surrogate data corresponds effectively to a linear superposition of independent random functions with a uniform random distribution of the phase. When ϱ is increased, the coefficients with the largest amplitude are fixed at their original location in time. This constrains both the scale and the location in time of the largest events, while the less energetic scales and the remaining portion of the time series are still represented by a linear model. The surrogate data can have an increasing degree of nonlinearity, as it becomes progressively more similar to the original data. With the GWR method it is possible to simulate nonlinear data, and to observe the evolution of the statistics of the surrogates while the nonlinearity increases progressively.

3.1.8 Statistics of the wave envelope

When the spectrum of the surface elevation is narrow, the surface is represented by equation (3.30) [Longuet-Higgins, 1984]. Bitner [1980] considered the pdf of the absolute value of the envelope function,

$$Z(t) = |\tilde{Z}(0,t)|, \tag{3.62}$$

measured at a single point $x = 0$. The time-derivative of the complex envelope $\tilde{Z}(t)$ is of order $\Delta k \partial\Omega/\partial k$, which is small if the spectrum is narrow. Neglecting both time derivatives of the amplitude and phase of the envelope, $\dot{Z}$ and $\dot{\Phi}$ (see equation (3.31)), respectively, Bitner [1980] determined the pdf of the absolute envelope $Z(t)$ for a weakly nonlinear system of waves following Longuet-Higgins [1963], although Bitner [1980] did not consider the last term of order λ_3^2 for the expansion in equation

(3.60a). This pdf is given by

$$p_Z(Z) = \frac{Z}{2\sigma^2} e^{-\frac{Z^2}{2\sigma^2}} \left[1 + \frac{1}{8}(\lambda_{40} + \lambda_{04} + \lambda_{22}) - \frac{Z^2}{8\sigma^2}(\lambda_{40} + \lambda_{04} + \lambda_{22}) \right. \\ \left. + \frac{Z^4}{64\sigma^4}(\lambda_{40} + \lambda_{04} + \lambda_{22}) \right], \tag{3.63}$$

where

$$\lambda_{40} = \left\langle \left(\frac{Z_R - <Z_R>}{\sigma} \right)^4 \right\rangle - 3, \tag{3.64a}$$

$$\lambda_{04} = \left\langle \left(\frac{Z_I - <Z_I>}{\sigma} \right)^4 \right\rangle - 3, \tag{3.64b}$$

$$\lambda_{22} = \left\langle \left(\frac{Z_R - <Z_R>}{\sigma} \right)^2 \left(\frac{Z_I - <Z_I>}{\sigma} \right)^2 \right\rangle - 1. \tag{3.64c}$$

In equation (3.64) Z_R and Z_I are the real and the imaginary components of the complex envelope $\tilde{Z}$, respectively, and <> denote ensemble averaging. If ζ and its time-derivative $\dot{\zeta}$ are Gaussianly distributed (i.e., for linear waves), then

$$\lambda_{40} = \lambda_{04} = \lambda_{22} = 0, \tag{3.65}$$

and the pdf of Z is the Rayleigh distribution

$$p_Z(Z) = \frac{Z}{2\sigma^2} e^{-\frac{Z^2}{2\sigma^2}}. \tag{3.66}$$

Equations (3.63) and (3.66) are used in subsection 5.2.3 in order to determine if the statistics of the amplitude of the surface fluctuations can be explained by a linear or weakly nonlinear model of random waves.

3.1.9 The Wavelet spectral method

The wavelet spectral method [Donelan et al., 1996] allows the direct calculation of the surface dispersion relation from the measurement of the elevation at a limited number of locations, and it is applied to the experimental measurements in section 5.4. The main assumptions of the method are the validity of the representation of equation (3.30), and the slow evolution of the envelope in time relative to the time scale of the surface fluctuations. This is formally valid when the group of waves has a narrow spectrum, although the method still applies when the spectrum is relatively wide because of the filtering by the wavelet transform [Longuet-Higgins, 1963].

Mollo-Christensen and Ramamonjiarisoa [1978] suggested that the statistics of the free surface of the oceans could be described by a random combination of wave groups of finite spatial length, propagating with permanent shape of their envelope. Although envelopes of permanent shape only exist within a nonlinear framework [e.g. Hui and Hamilton, 1979], Mollo-Christensen and Ramamonjiarisoa [1978] suggested a simplified representation with the form

$$\zeta(\boldsymbol{\rho}, t) = -e^{-\left(\frac{\partial \Omega}{\partial k} T_0\right)^{-2}\left(\frac{\mathbf{k}\cdot\boldsymbol{\rho}}{k} - \frac{\partial \Omega}{\partial k} t\right)^2} \sin\left(\mathbf{k}\cdot\boldsymbol{\rho} - \Omega t\right), \tag{3.67}$$

where T_0 defines the width of the group which moves at the group velocity $\partial\Omega/\partial k$. In equation (3.67) $\boldsymbol{\rho}$ represents the radial co-ordinate, i.e., $\boldsymbol{\rho} = (x, y)$. Donelan et al. [1996] recognised a similarity between the Gaussian shape of the wave envelope in equation (3.67) and the definition of the Morlet mother wavelet given by

$$\mathcal{M}(t) = \frac{1}{\sigma_W \sqrt{\pi}} e^{it - \frac{t^2}{2\sigma_W^2}}, \tag{3.68}$$

where σ_W is the width of the mother wavelet. The wavelet with scale ω_j centred at time t_i is found as

$$w_{i,j}(t) = \omega_j^{-1/2} \mathcal{M}(\omega_j (t - t_i)), \tag{3.69}$$

and the wavelet transform is defined as

$$\zeta_W(t_i, \omega_j) = \int \zeta(t) w_{i,j}^*(t) dt, \tag{3.70}$$

where $*$ represents the complex conjugate. It is assumed that

$$\left| \frac{t}{T_0} \left(\frac{t}{T_0} - \frac{2r}{\frac{\partial \Omega}{\partial k} T_0} \right) \right| \ll 1, \tag{3.71}$$

where $\mathbf{k}$ in polar co-ordinates is represented by the modulus k and by the angle with respect to the streamwise direction θ according to equations (3.47).Substituting equation (3.67) into equation (3.70), the phase of the wavelet transform measured at the location $\boldsymbol{\rho}_l$ is

$$\Phi_W(t_i, \omega_j, \boldsymbol{\rho}_l) = \mathbf{k}(t) \cdot \boldsymbol{\rho}_l - \omega_j t_i + \Phi_C, \tag{3.72}$$

where Φ_C is a constant.

The measurement of the phase of the wavelet transform at a set of locations $\boldsymbol{\rho}_l$ allows the calculation of the wavenumber $\mathbf{k}(\omega_j)$ at each frequency ω_j and therefore of the dispersion relation $\Omega(\mathbf{k})$ as the solution of a least square minimisation problem [p.73 Hauser et al., 2005]. This solution is valid as an approximation even when the assumption of equation (3.71) does not hold. With a simpler approach [Donelan et al., 1996], $\Phi_W(t_i, \omega_j, \boldsymbol{\rho}_l)$ can be measured at two pairs of locations a and b with co-ordinates $(\boldsymbol{\rho}_1, \boldsymbol{\rho}_2)$ and $(\boldsymbol{\rho}_3, \boldsymbol{\rho}_4)$, respectively, such that

$$\Delta\Phi_a(t_i, \omega_j) = \Phi_W(t_i, \omega_j, \boldsymbol{\rho}_1) - \Phi_W(t_i, \omega_j, \boldsymbol{\rho}_2) = \mathbf{k}(t_i, \omega_j) \cdot (\boldsymbol{\rho}_1 - \boldsymbol{\rho}_2), \tag{3.73a}$$

$$\Delta\Phi_b(t_i, \omega_j) = \Phi_W(t_i, \omega_j, \boldsymbol{\rho}_3) - \Phi_W(t_i, \omega_j, \boldsymbol{\rho}_4) = \mathbf{k}(t_i, \omega_j) \cdot (\boldsymbol{\rho}_3 - \boldsymbol{\rho}_4). \tag{3.73b}$$

The following geometrical parameters are defined

$$\Delta\rho_a = |\boldsymbol{\rho}_1 - \boldsymbol{\rho}_2|, \tag{3.74a}$$

$$\Delta\rho_b = |\boldsymbol{\rho}_3 - \boldsymbol{\rho}_4|, \tag{3.74b}$$

$$\Delta\varsigma_a = \tan^{-1}\left[\frac{(\boldsymbol{\rho}_1 - \boldsymbol{\rho}_2) \cdot \mathbf{i}_y}{(\boldsymbol{\rho}_1 - \boldsymbol{\rho}_2) \cdot \mathbf{i}_x}\right], \tag{3.74c}$$

$$\Delta\varsigma_b = \tan^{-1}\left[\frac{(\boldsymbol{\rho}_3 - \boldsymbol{\rho}_4) \cdot \mathbf{i}_y}{(\boldsymbol{\rho}_3 - \boldsymbol{\rho}_4) \cdot \mathbf{i}_x}\right], \tag{3.74d}$$

where $\mathbf{i}_x$ and $\mathbf{i}_y$ are the unitary vectors in the directions x and y, respectively. If $\boldsymbol{\rho}_l$, $l = 1, 2, ..., 4$ are not co-linear, and if

$$|k(t_i, \omega_j)\Delta\rho_{a,b}| \ll \sigma_W, \tag{3.75}$$

then [Donelan et al., 1996]

$$\begin{aligned} k(t_i, \omega_j) = &\left[\frac{\Delta\Phi_a(t_i, \omega_j)}{\Delta\rho_a} \sin(\Delta\varsigma_b) - \frac{\Delta\Phi_b(t_i, \omega_j)}{\Delta\rho_b} \sin(\Delta\varsigma_a)\right] / \\ &\left[\sin(\Delta\varsigma_b - \Delta\varsigma_a) \cos(\theta(t_i, \omega_j))\right], \end{aligned} \tag{3.76}$$

and the angle θ with respect to the streamwise direction is

$$\theta(t_i, \omega_j) = \tan^{-1}\left[\frac{\Delta\Phi_a(t_i, \omega_j)\Delta\rho_b \cos(\Delta\varsigma_b) - \Delta\Phi_b(t_i, \omega_j)\Delta\rho_a \cos(\Delta\varsigma_a)}{\Delta\Phi_b(t_i, \omega_j)\Delta\rho_a \sin(\Delta\varsigma_a) - \Delta\Phi_a(t_i, \omega_j)\Delta\rho_b \sin(\Delta\varsigma_b)}\right], \tag{3.77}$$

In chapter 5 equation (3.76) is used in order to calculate the dispersion relation from two orthogonal pairs of waveprobes, i.e., with

$$\Delta\varsigma_a = 0, \tag{3.78a}$$

$$\Delta\varsigma_b = \pi/2. \tag{3.78b}$$

In this case the dispersion relation is characterised in the two orthogonal directions x and y by

$$k_x(t_i, \omega_j) = \frac{\Delta\Phi_a(t_i, \omega_j)}{\Delta\rho_a}, \tag{3.79a}$$

$$k_y(t_i, \omega_j) = \frac{\Delta\Phi_b(t_i, \omega_j)}{\Delta\rho_b}. \tag{3.79b}$$

The application of the wavelet spectral method relies on a set of assumptions about the behaviour of the envelope, and on a set of conditions about the geometrical arrangement of the measurements locations. The condition represented by equation 3.75 corresponds to the requirement that the wavelength is small compared to the width of the wavelet at the frequency ω_j. This ensures that the wavelet transforms at all locations overlap substantially in time, so that the instantaneous calculation of the wavenumber is meaningful. Similar requirements are that the phase difference should be measurable without ambivalence, i.e.,

$$|k(t_i, \omega_j)\Delta\rho_{a,b}| < 2\pi, \tag{3.80}$$

and that the distance of each measurement location from the maximum of the envelope is small relative to the size of the envelope (equation (3.71)).

From these three conditions it is suggested to choose $\Delta\rho_{a,b}$ small, which contrasts with the requirement of minimising the uncertainty since the latter is proportional to $\Delta\rho_{a,b}^{-1}$. The condition of equation (3.71) is not satisfied when the wave group is approaching the measurement area, which means that the method can only work in a statistical sense. In this case, the condition of equation (3.71) is replaced by

$$l_0/\max(\Delta\rho) \gg 1, \tag{3.81}$$

where l_0 is the characteristic correlation length, i.e., the distance at which the spatial correlation vanishes. The wavelet spectral method is also not expected to work if there are more than one group simultaneously at the same frequency and with similar amplitude, or if the inversion of the dispersion relation $\Omega(\mathbf{k})$ is multi-valued, since then the phase of the wavelet transform would be equal to

$$\Phi_W(t_i, \omega_j, \boldsymbol{\rho}_l) = \sum_m \mathbf{k}_m(t_i, \omega_j) \cdot \boldsymbol{\rho}_l - \omega_j t_i + \Phi_C, \tag{3.82}$$

where $\mathbf{k}_m(\omega_j)$ is the wavenumber prescribed by each dispersion relation at the frequency ω_j. In both cases the system of equations (3.73) is underdetermined and the solution cannot be found. In section 5.4 the probability density functions $p_k(k_x)$, $p_k(k_y)$, and $p_\theta(\theta)$ is calculated from the measurements of the surface elevation in a shallow turbulent flow. The results show that the method can still be applied if the spectrum has a dominant peak at each frequency, i.e., if the waves that follow one single dispersion relation are much larger than any other wave.

3.2 Acoustic model

This section presents the mathematical theory that describes the scattering of an acoustic pressure field by a rough dynamic surface. The focus is on the Kirchhoff approximation, which applies to the scattering of ultrasonic waves by the rough surface of shallow turbulent flows. The Kirchhoff approximation is described in subsection 3.2.1. This equation is able to explain the measurements of the Doppler spectra of the scattered field presented in section 6.2, according to a model derived in subsection 3.2.2. The application of this model requires performing a Monte Carlo simulation, which is computationally expensive. A simplified linear model is derived in subsection 3.2.2, and it is also compared to the measurements in section 6.2. The deviations of the measurements from both models are believed to be caused by weak nonlinearities of the free surface. The expected effects of such nonlinearities on the Doppler spectra of the scattered acoustic field are therefore described in subsection 3.2.2, based on the results available in the literature. The equations reported in this section are used in chapter 6 in order to inform the discussion of the experimental measurements of the scattered acoustic pressure. These equations are also the basis of the data analysis procedure described in the same chapter.

3.2.1 Acoustic scattering from a rough surface

The acoustic field can be represented in terms of the velocity potential P [e.g. Morse and Ingard, 1968, p.248][Bass and Fuks, 1979, p.7]. All acoustic quantities are multiplied by a factor $\exp(i\omega_a t)$. When the acoustic field is represented as a linear composition of waves with frequency ω_a, the relation between the acoustic potential and the acoustic pressure corresponds to a multiplication by a constant. Therefore in chapter 6 the same symbol P represents the measured acoustic pressure field, for simplicity of the notation. The scattering of the acoustic potential field generated by a transducer with vector co-ordinates $\mathbf{S} = (x_s, y_s, z_s)$ from a rough surface Σ represented by the equation $z = \zeta(\boldsymbol{\rho})$, $\rho = \sqrt{(x^2 + y^2)}$, is considered.

The derivation of the Kirchhoff scattering equations is reported in Appendix B, following Morse and Ingard [1968] and Bass and Fuks [1979]. It is assumed that the surface is acoustically rigid, i.e.,

$$\frac{\partial P(\tilde{\boldsymbol{\rho}})}{\partial \mathbf{n}} = 0, \text{ where } \tilde{\boldsymbol{\rho}} \in \Sigma, \tag{3.83}$$

where $\tilde{\boldsymbol{\rho}} = (x, y, \zeta(x, y))$ and $\mathbf{n}$ is the unit vector normal to the surface defined as

$$\mathbf{n} = \frac{\mathbf{i}_z - \nabla\zeta}{\sqrt{1 + |\nabla\zeta|^2}}, \tag{3.84}$$

and $\mathbf{i}_z$ is the unit vector in the vertical direction z such that the average of ζ over z is 0.

The Kirchhoff approximation assumes that at all locations on the rough surface the acoustic field is equal to the reflection of the incident field P_i from the plane tangent to the surface locally [Bass and Fuks, 1979, p.220]. κ is the acoustic wavenumber. The incident field at the location $\mathbf{R}$ due to a source transducer in $\mathbf{S}$ is defined in the far-field $\kappa R = \kappa|\mathbf{R} - \mathbf{S}| \gg 1$ as

$$P_i(R, \theta_s) = D_s(\theta_s)\frac{e^{i\kappa|\mathbf{R}-\mathbf{S}|}}{|\mathbf{R} - \mathbf{S}|} \tag{3.85}$$

in the three-dimensional case, and

$$P_i(R, \theta_s) = D_s(\theta_s)\frac{e^{i\kappa|\mathbf{R}-\mathbf{S}|}}{\sqrt{|\mathbf{R} - \mathbf{S}|}} \tag{3.86}$$

in the two-dimensional case, respectively. The two-dimensional case corresponds to the scattering from the surface $\zeta = \zeta(x)$. In equations (3.85) and (3.86) $D_s(\theta_s)$ is the directivity pattern of the transducer. The transducer is modelled as a circular piston with radius r_s set in a plane rigid baffle of infinite size. θ_s is the angle with respect to the axis of the piston. The directivity is found in the far-field from the piston where

$$\frac{R}{r_s} \gg 1, \tag{3.87}$$

as [Morse and Ingard, 1968, p.381] (see also the derivation in Appendix B)

$$D_s(\theta_s) = 2\frac{J_1(\kappa r_s \sin\theta_s)}{\kappa r_s \sin\theta_s}, \tag{3.88}$$

where J_1 is the Bessel function of the first kind.

The local replacement of the rough surface by a flat plane requires that the shape of the rough surface varies smoothly and slowly in a region with the size much larger than the acoustic wavelength. This is expressed by the so-called Kirchhoff condition [Bass and Fuks, 1979, p.222]

$$\kappa R_c \sin^3 \psi \gg 1, \tag{3.89}$$

where ψ is the complementary of the angle between the wavenumber vector of the incident field and the normal to the surface, called the angle of incidence, and R_c is the radius of curvature of the surface. Thorsos [1988] showed that the Kirchhoff approximation still provides a good approximation when the less strict condition

$$2\kappa R_c \sin^3 \psi > 1, \tag{3.90}$$

is satisfied. The Kirchhoff approximation neglects the contribution to the field at one location on the surface coming from the reflections by the rest of the surface. This corresponds to the zero-th order of the so-called Born approximation [Morse and Ingard, 1968, p.413]. The field measured at the location $\mathbf{M} = (x_m, y_m, z_m)$ can be seen as the sum of an infinite number of spherical (or cylindrical) waves with infinitesimal amplitude, each coming from a point on the surface with the vector co-ordinates $\tilde{\boldsymbol{\rho}}$.

The response of a real receiver to the waves coming from different angles is represented by a function $D_m(\theta_m)$ analogous to equation (3.88), where θ_m is the angle with respect to the axis of the receiver. The vector distances from the source to the location $\tilde{\boldsymbol{\rho}}$ on the surface, and from $\tilde{\boldsymbol{\rho}}$ to the receiver, are defined as

$$\tilde{\mathbf{R}}_s = \tilde{\boldsymbol{\rho}} - \mathbf{S}, \tag{3.91a}$$

$$\tilde{\mathbf{R}}_m = \mathbf{M} - \tilde{\boldsymbol{\rho}}. \tag{3.91b}$$

The notation is simplified by introducing the quantity

$$\tilde{\mathbf{q}} = -\kappa \nabla (\tilde{R}_m + \tilde{R}_s), \tag{3.92}$$

with components

$$\tilde{q}_x = -\kappa \left[\frac{x - x_s}{\tilde{R}_s} - \frac{x_m - x}{\tilde{R}_m} \right] \tag{3.93a}$$

$$\tilde{q}_y = -\kappa \left[\frac{y - y_s}{\tilde{R}_s} - \frac{y_m - y}{\tilde{R}_m} \right] \tag{3.93b}$$

$$\tilde{q}_z = -\kappa \left[\frac{\zeta - z_s}{\tilde{R}_s} - \frac{z_m - \zeta}{\tilde{R}_m} \right], \tag{3.93c}$$

and

$$\tilde{\mathbf{q}}_\perp = (\tilde{q}_x, \tilde{q}_y). \tag{3.94}$$

$\tilde{\mathbf{q}}$ represents the vector difference between the scattered and the incident acoustic wavenumbers.

Expanding the spatial gradient of the incident field in the direction $\mathbf{n}$ and neglecting the terms of order $\mathcal{O}[(\kappa\tilde{R}_{s,m})^{-1}]$, the acoustic potential field at the receiver $\mathbf{M}$ in the three-dimensional case is found as

$$P(\mathbf{M}) = D_m(\mathbf{S})D_s(\mathbf{M})\frac{e^{i\kappa|\mathbf{M}-\mathbf{S}|}}{|\mathbf{M}-\mathbf{S}|} + \frac{1}{i4\pi}\int_{\Sigma_0} D_m(\tilde{\boldsymbol{\rho}})D_s(\tilde{\boldsymbol{\rho}})\frac{e^{i\kappa\left(\tilde{R}_s+\tilde{R}_m\right)}}{\tilde{R}_s\tilde{R}_m}(\tilde{q}_z - \tilde{\mathbf{q}}_\perp\cdot\nabla\zeta)d\boldsymbol{\rho}, \tag{3.95}$$

where the integration is carried out with respect to the co-ordinate $\boldsymbol{\rho} = (x, y, 0)$ defined on the flat surface Σ_0 which lies on the plane x-y. The following quantities are defined, by projecting the surface Σ with equation $z = \zeta$ on the flat surface Σ_0 with equation $z \equiv 0$,

$$\mathbf{R}_s = \boldsymbol{\rho} - \mathbf{S}, \tag{3.96a}$$

$$\mathbf{R}_m = \mathbf{M} - \boldsymbol{\rho}. \tag{3.96b}$$

$\tilde{\mathbf{R}}_s$ and $\tilde{\mathbf{R}}_m$ correspond to the vector distances from the source with co-ordinates $\mathbf{S}$ to the point with co-ordinates $\boldsymbol{\rho}$ on the flat surface, and from the point $\boldsymbol{\rho}$ to the receiver $\mathbf{M}$, respectively. These distances can be expanded with respect to $\mathbf{R}_m$ and $\mathbf{R}_s$, respectively, i.e.,

$$\tilde{\mathbf{R}}_{m,s} \approx \mathbf{R}_{m,s} + \frac{\partial\tilde{R}_{m,s}}{\partial z}\zeta\mathbf{i_z} + \frac{\partial^2\tilde{R}_{m,s}}{\partial z^2}\zeta^2\mathbf{i_z} + ..., \tag{3.97}$$

which yields

$$\tilde{R}_{m,s} = R_{m,s}\left\{1 + \frac{(\zeta - z_{m,s})}{R_{m,s}}\frac{\zeta}{R_{m,s}} + \left[1 - \frac{(\zeta - z_{m,s})^2}{R^2_{m,s}}\right]\frac{\zeta^2}{R^2_{m,s}} + \mathcal{O}\left(\frac{\zeta^3}{R^3_{m,s}}\right)\right\}. \tag{3.98}$$

If the following inequality is satisfied,

$$\frac{\sin^2(\psi)\kappa\sigma^2}{R_{m,s}} \ll 1, \tag{3.99}$$

where ψ is the angle of $\mathbf{R}_{m,s}$ measured from the horizontal, and σ is the standard deviation of the rough surface [Bass and Fuks, 1979, p.227], then the terms of order $\mathcal{O}(\zeta^2/R^2_{m,s})$ can be neglected in the exponential term of equation (3.95). It is also possible to neglect the small terms of order $\mathcal{O}(\zeta/R_{m,s})$ at the denominator of the same equation. $\tilde{\mathbf{q}}$ is expanded as

$$\tilde{\mathbf{q}} = \mathbf{q} + \mathcal{O}\left(\frac{\zeta^2}{R_{m,s}^2}\right), \tag{3.100}$$

where

$$\mathbf{q} = -\kappa\nabla(R_s + R_m), \tag{3.101}$$

with components

$$q_x = -\kappa\left[\frac{x - x_s}{R_s} - \frac{x_m - x}{R_m}\right], \tag{3.102a}$$

$$q_y = -\kappa\left[\frac{y - y_s}{R_s} - \frac{y_m - y}{R_m}\right], \tag{3.102b}$$

$$q_z = \kappa\left[\frac{z_s}{R_s} + \frac{z_m}{R_m}\right], \tag{3.102c}$$

and with

$$\mathbf{q}_\perp = (q_x, q_y). \tag{3.103}$$

$\mathbf{q}_\perp$ differs from $\tilde{\mathbf{q}}_\perp$ because it is calculated based on the distances from the source and from the receiver to the flat surface, R_s and R_m, respectively.

If the source and the receiver have a relatively narrow directivity and do not face each other directly, it is possible to neglect the direct field by assuming

$$D_m(\mathbf{S})D_s(\mathbf{M}) \approx 0. \tag{3.104}$$

Substituting equations (3.101) and (3.103) in equation (3.95), and expanding $D_m(\tilde{\boldsymbol{\rho}})$ and $D_s(\tilde{\boldsymbol{\rho}})$ at $\boldsymbol{\rho}$, one finds

$$P(\mathbf{M}) = \frac{1}{i4\pi}\int_{\Sigma_0} D_m(\boldsymbol{\rho})D_s(\boldsymbol{\rho})\frac{e^{i[\kappa(R_s+R_m)-q_z\zeta]}}{R_sR_m}\left(q_z - \mathbf{q}_\perp\cdot\nabla\zeta\right)d\boldsymbol{\rho}. \tag{3.105}$$

By assuming further that $\mathbf{q}_\perp\cdot\nabla\zeta \ll 1$, which is valid for relatively large angles of incidence $\kappa\nabla\zeta\cos(\psi) \ll 1$ and when the surface slope is small, one finally obtains

$$P(\mathbf{M}) = \frac{1}{i4\pi}\int_{\Sigma_0} D_m(\boldsymbol{\rho})D_s(\boldsymbol{\rho})\frac{e^{i[\kappa(R_s+R_m)-q_z\zeta]}}{R_sR_m}q_z d\boldsymbol{\rho}. \tag{3.106}$$

In the two-dimensional case the scattering from a surface $\zeta(x)$ is considered. The equivalent of equation (3.95) is given by

$$\begin{aligned} P(\mathbf{M}) = D_m(\mathbf{S})D_s(\mathbf{M})\frac{e^{i\kappa|\mathbf{M}-\mathbf{S}|}}{\sqrt{|\mathbf{M}-\mathbf{S}|}}+ \\ -\frac{1}{8\pi\sqrt{2\kappa\pi}}\int_{\Sigma_0} D_m(\tilde{\boldsymbol{\rho}})D_s(\tilde{\boldsymbol{\rho}})\frac{e^{i\kappa\left(\tilde{R}_s+\tilde{R}_m\right)}}{\sqrt{\tilde{R}_s\tilde{R}_m}}(\tilde{q}_z-\tilde{q}_x\zeta_x)dx. \end{aligned} \tag{3.107}$$

By expanding R_s, R_m, and $\mathbf{q}$ near $z=0$, and neglecting the direct field based on equation (3.104), the two-dimensional version of equation (3.105) is found as

$$P(\mathbf{M}) = \frac{1}{8\pi\sqrt{2\kappa\pi}}\int_{\Sigma_0} D_m(x)D_s(x)\frac{e^{i[\kappa(R_s+R_m)-q_z\zeta]}}{\sqrt{R_sR_m}}\left(q_z-\tilde{q}_x\zeta_x\right)dx. \tag{3.108}$$

In the case when $\mathbf{q}\cdot\nabla\zeta \ll 1$, equation (3.108) is simplified as

$$P(\mathbf{M}) = \frac{1}{8\pi\sqrt{2\kappa\pi}}\int_{\Sigma_0} D_m(x)D_s(x)\frac{e^{i[\kappa(R_s+R_m)-q_z\zeta]}}{\sqrt{R_sR_m}}q_z dx. \tag{3.109}$$

Equations (3.105) to (3.109) describe the acoustic field scattered by a rough surface which is constant in time. In chapter 5 it is shown that the standard deviation of the time-gradient of the surface elevation in the tested flow conditions was of the order of $0.01\,\mathrm{m\,s^{-1}}$, while the phase velocity of the gravity-capillary waves on the surface was of the order of $1\,\mathrm{m\,s^{-1}}$. Both quantities are much smaller than the speed of sound in air, which is equal to $343\,\mathrm{m\,s^{-1}}$ at the temperature of 20°. Under these conditions, the scattered acoustic field $P(\mathbf{M},t)$ at the instant t is represented by equations (3.105) to (3.109) where ζ is replaced by the instantaneous surface elevation $\zeta(x,y,t)$. These equations were used in chapter 6 in order to calculate numerically the Doppler spectrum of the scattered acoustic field based on a Monte Carlo simulation. The scattered acoustic field was computed numerically based on equations (3.105) and (3.108) for a random realisation of the surface elevation ζ. This was evolved in time according to the dispersion relation of gravity-capillary waves. The scattered field $P(\mathbf{M},t)$ was then computed at a set of discrete instants in time. The resulting time series was analysed in order to determine the acoustic Doppler spectrum for that surface realisation. Equations (3.106) and (3.109) were implemented in a linear model of the acoustic Doppler spectrum, which is described in subsection 3.2.2.

3.2.2 Doppler spectrum of the scattered acoustic field

In this subsection the dynamics of the surface are introduced explicitly by expressing the surface elevation ζ as a function of the two spatial co-ordinates x and y and of the time t. It is assumed like in the previous section that the time-derivative of the surface elevation is slow compared to the speed of sound. The calculation of the acoustic field $P(\mathbf{M}, t)$ at each instant t, with $\zeta(x, y, t)$ that changes with time, allows determining the power spectrum of the scattered field as the Fourier transform of the correlation function in time. The Doppler spectrum is defined as the power spectrum of the scattered field when it is expressed as a function of the shifted frequency $\omega - \omega_a$, where ω_a is the frequency of the incident acoustic field. Adopting the same convention of section 3.2.1, where the factor $\exp(i\omega_a t)$ is omitted in the definitions, the Doppler power spectrum of the scattered field is defined simply as

$$S_D(\mathbf{M}, \omega) = \frac{1}{2\pi} \int_{-\infty}^{\infty} < P(\mathbf{M}, t) P^*(\mathbf{M}, t + \tau) > e^{i\omega\tau} d\tau, \qquad (3.110)$$

where <> represents ensemble averaging.

Doppler spectrum with small Rayleigh parameter

The interpretation of the Doppler spectra obtained experimentally or with the Monte Carlo simulation is not straightforward. In some conditions, the equations of acoustic scattering can be simplified, in order to show more clearly the relation between the dynamics and the topology of the surface and the Doppler acoustic spectra. The result is a linear model of the Doppler spectrum, which is used in section 6.2 in order to calculate the spectrum of the surface elevation from the measured Doppler spectra. The derivation follows Bass and Fuks [1979] and is based on equation (3.106), which describes the potential of the acoustic field scattered by a three-dimensional surface when the gradient of the surface elevation is small. It is reported in Appendix C.

It is assumed that ζ is Gaussian distributed, and that its spatial correlation decays rapidly in both directions x and y, so that the size of the area which is important for the integration of equation (3.106) is represented by the scales l_x and l_y in the x- and in the y-direction, respectively. It is further assumed that the standard deviation of ζ, called σ, is small relative to the vertical component of the acoustic wavenumber vector, i.e.,

$$q_z \sigma \ll 1. \qquad (3.111)$$

Then l_x and l_y are the correlation lengths of the surface elevation ζ in the two directions [Bass and Fuks, 1979, p.376]. If the transducer and the receiver are at the same height above the surface, and if one considers either the backscattering configuration ($\mathbf{M} \equiv \mathbf{S}$) or the reflection at the specular point ($R_s \equiv R_m$), then the condition of equation (3.111) satisfies

$$[2\kappa \sin{(\psi_s)}\sigma]^2 \ll 1, \tag{3.112}$$

where ψ_s is the angle of incidence of the source transducer. The term on the left-hand side of equation (3.112) is called the Rayleigh parameter. It is then assumed that the correlation length l_x and l_y in the x- and y-direction, respectively, is much smaller than the distance to the transducer and to the receiver from the surface, i.e.,

$$\frac{l_{x,y}}{R_{s,m}} \ll 1, \tag{3.113}$$

and that the horizontal dimension of the scattering surface is large compared to $l_{x,y}$.

It is also assumed that [Bass and Fuks, 1979, p.322]

$$\frac{\kappa l_x^2 \sin^2 \psi_s}{R_{s,m}} \ll 1, \tag{3.114a}$$

$$\frac{\kappa l_y^2}{R_{s,m}} \ll 1, \tag{3.114b}$$

which require that the correlation radius is much smaller than the size of the Fresnel zone, defined as

$$L_F = \sqrt{\frac{R_{s,m}}{\kappa \sin^2{(\psi_s)}}}. \tag{3.115}$$

Further assumptions require that

$$\frac{l_x \cos{(\psi_s)}}{R_{s,m}} \ll 1, \tag{3.116a}$$

$$\frac{l_x^2 \sin^2{(\psi_s)}}{R_{s,m}^2} \ll 1, \tag{3.116b}$$

$$\frac{l_y^2}{R_{s,m}^2} \ll 1, \tag{3.116c}$$

and also

$$\frac{\kappa\sigma l_x \sin(2\psi_s)}{R_{s,m}} \ll 1, \tag{3.117a}$$

$$\frac{\kappa\sigma l_x^2 \sin^3(\psi_s)}{R_{s,m}^2} \ll 1, \tag{3.117b}$$

$$\frac{\kappa\sigma l_y^2 \sin(\psi_s)}{R_{s,m}^2} \ll 1. \tag{3.117c}$$

Finally, it is assumed that the directivity of the transducer and of the receiver vary slowly in space in a region with size $l_{x,y}$.

The Fourier transform in space and time of the correlation function is called the frequency-wavenumber spectrum of the surface elevation, $S(\mathbf{k}, \omega)$, and it is defined by equation (3.2). This spectrum is assumed to be stationary, i.e., independent of space and time. If the Rayleigh parameter is small, neglecting terms of order higher than $q_z^2\sigma^2$, and assuming that $D_m^2(\boldsymbol{\rho})D_s^2(\boldsymbol{\rho})$ is large only in a finite region of the surface with size L_D, such that

$$\frac{L_D^2}{R_{s,m}^2} \ll 1, \tag{3.118}$$

one obtains (see Appendix C)

$$\begin{aligned} S_D(\mathbf{M}, \omega) = &\int_{-\infty}^{\infty} Q(\boldsymbol{\rho}(\mathbf{q}_\perp)) \left[1 - q_z^2(\boldsymbol{\rho}(\mathbf{q}_\perp))\sigma^2\right] \delta(\omega)\delta(\mathbf{q}_\perp) d\mathbf{q}_\perp + \\ &+ \sum_j \int_{-\infty}^{\infty} Q(\boldsymbol{\rho}(\mathbf{q}_\perp)) q_z^2(\boldsymbol{\rho}(\mathbf{q}_\perp))\sigma^2 S(\mathbf{k}_j, \omega_j)\delta(\omega - \omega_j)\delta(\mathbf{q}_\perp - \mathbf{k}_j) d\mathbf{q}_\perp, \end{aligned} \tag{3.119}$$

where

$$Q(\boldsymbol{\rho}) = \frac{q_z^2(\boldsymbol{\rho})}{32\pi^3\kappa} \frac{D_m^2(\boldsymbol{\rho})D_s^2(\boldsymbol{\rho})}{R_m(\boldsymbol{\rho})R_s(\boldsymbol{\rho})} [R_m(\boldsymbol{\rho}) + R_s(\boldsymbol{\rho})]^{-1}. \tag{3.120}$$

The neglected terms of order higher than $q_z^2\sigma^2$ were considered for example by Lipa and Barrick [1986]. They correspond to the second-order spectrum, which is related to the nonlinear interactions among waves (see subsection 2.2.2).

If the surface elevation moves in time according to a dispersion relation

$$\omega_j = \Omega(\mathbf{k}_j), \tag{3.121}$$

which has the inverse $\mathbf{K}(\omega)$ such that

$$\Omega(\mathbf{K}(\omega_j)) = \omega_j, \tag{3.122}$$

then

$$S_D(\mathbf{M},\omega) = \begin{cases} Q(\boldsymbol{\rho}_0)\left[1 - q_z^2(\boldsymbol{\rho}_0)\sigma^2\right], & \omega = 0, \\ Q(\boldsymbol{\rho}(\mathbf{K}(\omega)))S(\mathbf{K}(\omega),\omega)q_z^2(\mathbf{K}(\omega))\sigma^2, & \omega \neq 0, \end{cases} \tag{3.123}$$

where

$$\mathbf{q}_\perp(\boldsymbol{\rho}_0) = 0 \tag{3.124}$$

defines $\boldsymbol{\rho}_0$ as the location of the specular point. A similar result was reported by Barrick [1972] based on a small perturbation expansion. It is easy to verify that the same derivation holds for the two-dimensional case, with the factor $Q(\boldsymbol{\rho})$ defined by

$$Q(\boldsymbol{\rho}) = \frac{q_z^2(\boldsymbol{\rho})}{256\pi^4\kappa^2}\frac{D_m^2(\boldsymbol{\rho})D_s^2(\boldsymbol{\rho})}{[R_m(\boldsymbol{\rho}) + R_s(\boldsymbol{\rho})]}. \tag{3.125}$$

Equation (3.123) shows that the Doppler spectrum at the frequency ω is proportional to the power spectrum of the surface elevation at the wavenumber $\mathbf{K}(\omega) = \mathbf{q}_\perp$, which in turn is related to the frequency spectrum of the elevation $S(\omega)$ through equation (3.14). $\mathbf{q}_\perp$ is associated with a specific direction of scattering. Considering the backscattering configuration where $\mathbf{M} = \mathbf{S}$, and $R_m = R_s$, then

$$\mathbf{q}_\perp(\boldsymbol{\rho}) = \frac{2\kappa}{R_s}(\boldsymbol{\rho}_s - \boldsymbol{\rho}), \tag{3.126}$$

where $\boldsymbol{\rho}_s = (x_s, y_s)$. In this case, the acoustic field backscattered in the direction where the directivity of the source transducer is maximum has

$$|\mathbf{q}_\perp| = 2\kappa\cos(\psi_s) = k_B, \tag{3.127}$$

which is called the wavenumber of the Bragg waves. If the directivity is narrow, the backscattering is mainly related to the interaction with the waves with wavenumber k_B, and with the frequency $\Omega(k_B)$. As a result, the Doppler spectrum shows a peak at the frequency

$$\Omega_B = \Omega(k_B) = 2\kappa c(k_B)\cos(\psi_s), \tag{3.128}$$

where $c(k_B)$ is the phase velocity of the Bragg waves.

Doppler modulations by nonlinearities of the surface elevation

The derivation so far assumed that the free surface elevation has a correct representation in terms of a linear Fourier series with random amplitude and phase. The modulation of the Doppler spectrum due to nonlinearities of the free surface was mentioned in subsection 2.2.2. In chapter 6 it is shown that the measured acoustic

Doppler spectra show wider peaks than is expected based on a numerical linear model of the water surface elevation. It is suggested that the widening of the peaks of the measured spectra is caused by the nonlinear behaviour of the water surface. This subsection presents a few formulae to estimate the widening of the Bragg peaks due to the nonlinearity of the water surface. The derivation of the modulations due to multiple waves interactions requires a nonlinear model of the free surface. Such a model has not been derived for the free surface of shallow turbulent flows over a homogeneously rough bed. Therefore, only the modulation of short waves by longer waves is considered here. The order of magnitude of the widening of the Bragg peaks due to the short wave-long wave interaction can be found based on a simplified first-order expansion of equations (3.123), (3.127), and (3.128).

The transfer function for the range modulation was estimated for example by Hara and Plant [1994] and it was found negligible when $z_s \gg \sigma$. Keller and Wright [1975] and Hara and Plant [1994] calculated the correction due to tilt and straining to the backscattered power based on a small perturbation theory of backscattering, in the Fraunhofer zone. The correction due to straining from a long wave with perturbation velocity u was found to be proportional (here assuming that the Doppler spectrum is proportional to the backscattered power, as it is in the Fraunhofer zone) to

$$\Delta S_D(\mathbf{M}, \omega) \approx S_D(\mathbf{M}, \omega) \frac{k_0 u}{\Omega(k_0)} \frac{1}{\sqrt{S(k_B, \Omega(k_B))}}. \tag{3.129}$$

Equation (3.129) is based on the assumption that $k_0 u/\Omega(k_0) = u/c(k_0)$ is small, which is not valid if the long wave is almost stationary.

The correction due to tilting of the short Bragg waves can be calculated simply for a two-dimensional surface with the wavenumber of the longer wave equal to k_0, assuming the tilt-angle to be of order

$$\Delta\psi \approx \tan^{-1}(k_0\sigma). \tag{3.130}$$

With a simple first-order expansion of equation (3.127), the Bragg wavenumber varies by the amount

$$\Delta k_B \approx -2\kappa \sin(\psi_s) \tan^{-1}(k_0\sigma), \tag{3.131}$$

due to the tilt. With the same approach applied to equation (3.128), one can find

$$\Delta\omega \approx \frac{d(k_B c(k_B))}{dk} \Delta k_B = c_g(k_B) \Delta k_B. \tag{3.132}$$

According to equation (3.132) the widening of the Doppler spectra due to the tilt modulation is proportional to the group velocity of the Bragg waves. The variation of the amplitude of the spectrum can be determined in a similar way from equation (3.123) in the conditions where this equation holds. The same correction suggested by Keller and Wright [1975] can be found by expanding equation (3.123) near $k - k_B = \Delta k_B = 0$. With a simpler approach, assuming the slow variation of $Q(\boldsymbol{\rho}(\mathbf{K}(\omega)))$ and $q_z^2(\mathbf{K}(\omega))$, and assuming a surface spectrum with the dependence $\propto k^{-\alpha}$, one finds

$$\Delta S_D(\mathbf{M}, \omega) \approx \alpha S_D(\mathbf{M}, \omega) \tan(\psi_s) \tan^{-1}(k_0 \sigma). \tag{3.133}$$

The effect of the velocity modulation on the Doppler spectrum width was investigated for example by Keller et al. [1994]. These authors found that the largest effect is caused by the modulation of the waves smaller than the Bragg scales by intermediate scales, which are themselves modulate by the longer waves. Here it should be sufficient to estimate the variation of the Doppler frequency $\Delta\omega$ directly from a characteristic perturbation velocity of the long wave $u \approx k_0 \sigma c(k_0) \cosh(k_0 H)$, i.e.,

$$\Delta\omega \approx \; 2\kappa k_0 \sigma c(k_0) \coth(k_0 H) \cos(\psi_s). \tag{3.134}$$

Equations (3.132) and (3.134) represent the expected increase of the width of the peaks of the acoustic Doppler spectra due to the modulation of the short Bragg waves by the longer dominant waves. The dominant waves have been assumed to have the wavenumber of the stationary waves, k_0, in agreement with the experimental results presented in chapter 5. These equations are used in chapter 6 in order to explain the wider peaks of the experimentally measured acoustic Doppler spectra relative to those of the spectra predicted with the numerical model.

3.3 Summary

This chapter presented the derivation of the equations and relations which are used for the interpretation of the experimental results described in chapter 5, and for the derivation of the numerical model of the acoustic Doppler spectra described in chapter 6. The dispersion relation of gravity-capillary waves in a shallow turbulent flow has been obtained for an irrotational flow (equation (3.20)), and for a flow where the time averaged streamwise velocity varies as a power-function of the depth (equations (3.24) and (3.26)). The power-function streamwise velocity profile (equation (3.17)) is governed by the value of the exponent n. This was estimated based on equations (3.35) and (3.39) for the tested flow conditions, as reported in section 4.2. The dispersion relations have been derived for an incompressible and inviscid flow where the effects of the bed roughness is neglected. In subsection 5.3.2 it is shown that the dispersion relations derived under these assumptions represent well the measured dispersion relations in the measured flow conditions. The patterns on the free surface are found to be dominated by the stationary waves generated by the interaction with the rough bed in all the tested conditions where the mean surface velocity was larger than the minimum phase velocity of gravity-capillary waves (equation (3.23)). The wavenumber of the stationary waves was determined based on equations (3.41) and (3.44) for the irrotational flow and for the flow with the power-function velocity profile, respectively. The three dimensional patterns observed experimentally are described by equations (3.48). Patterns of non-dispersive waves for which the dispersion relation is given by equation (3.21) are also observed in subsection 5.3.2.

The pdf's of the surface elevation (equations (3.55) and (3.60)) and of the amplitude of the wave envelope (equations (3.63) and (3.66)) described in subsections 3.1.6 and 3.1.8 are compared to the measurements with conductance waveprobes in subsections 5.2.2 and 5.2.3, respectively. These pdf's are based on a linear (equations (3.55) and (3.66)) or weakly nonlinear (equations (3.60) and (3.63)) model of the water surface. The comparison was aimed at assessing the validity of the linear model implemented in chapter 6. The statistical significance of the observed nonlinearities was evaluated based on the GWR method following the procedure described in subsection 3.1.7. The group velocity of the patterns on the free surface was determined experimentally in terms of the velocity of the wave envelope, according to the analysis reported in subsection 3.1.3. The experimental results are presented in subsection 5.3.3, where the measured velocity is compared with the prediction given by equation (3.15). The observations in subsection 5.3.3 suggest the possibility to use the wavelet spectral method described in subsection 3.1.9 in order to characterise the dispersion relation of the surface patterns from the measurement of the surface elevation at a few locations. The applicability of the wavelet spectral method is subject to a set of conditions reported in subsection 3.1.9. The measurement of the spatial correlation function of the wave envelope described in subsection 5.3.3 was used in order to identify the set of flow conditions where the method can be applied. The dispersion relation and the angle of propagation of the waves was calculated with equations (3.76) and (3.77), respectively. The results are reported in section 5.4.

The measurements of the Doppler spectra of the scattered acoustic field in a range of subcritical flow conditions are reported in chapter 6. In order to provide a rigorous interpretation of the measurements, these were compared with the results of two numerical models of the acoustic Doppler spectra. Both models were based on the Kirchhoff approximation, which is defined by equation (3.90). The validity of this approximation in the range of conditions described in this thesis is discussed in subsection 6.1.2. The first model calculated the scattered acoustic field in time based on equations (3.105) and (3.108) for a set of dynamic random realisations of the scattering water surface. These were generated based on equation (3.10) assuming the power spectrum of the surface elevation to be described by a power function of the wavenumber, similarly to the studies reported in subsection 2.1.6. The second model corresponds to the linear model illustrated in subsection 3.2.2. With this model the acoustic Doppler spectra were calculated based on equation (3.123) and with equation (3.120) or (3.125) in three or in two dimensions, respectively. The model was valid when a set of conditions which have been reported in subsection 3.2.2 were satisfied. The validity of these conditions in the range of tested flow conditions is discussed in subsection 6.1.4. The same linear model can be used in order to reconstruct the frequency spectrum of the surface elevation based on the measurement of the Doppler spectrum of the scattered acoustic field. The procedure that allows such a reconstruction is described in subsection 6.1.5, and the results of the reconstruction are presented in subsection 6.2.2. The comparison between the measured acoustic Doppler spectra and the Doppler spectra predicted by both numerical models show that the former had broader peaks at the frequency of the Bragg scale waves. It is suggested that the broader peaks were caused by nonlinear effects which were not considered in the models. The effects of the modulation of the short Bragg waves by the longer waves on the free surface have been quantified with equations (3.132) and (3.134). The predictions obtained with these equations are compared with the measurements in subsection 6.2.3 as a mean to quantify the importance of these effects.

Chapter 4

Experimental apparatus

4.1 Flume setup

All the experiments described in this thesis were performed in a recirculating rectangular laboratory flume. The flume was 12.6 m long, and 0.459 m wide. An adjustable gate at the downstream end of the flume allowed uniform depth to be maintained along the channel. The flow discharge and the bed slope could be regulated in order to obtain the desired flow depth and mean surface velocity. The flume bed was covered with three layers of hexagonally packed plastic spheres with the diameter of 25.4 mm and density of $1400\,\mathrm{kg\,m^{-3}}$. A schematic of the flume is shown in FIG. 4.1. A picture of the rough bed is shown in FIG. 4.2.

The depth of the flow was measured at five streamwise positions between 7.43 m and 10.1 m from the inlet. At each streamwise position, the depth was measured at the flume centreline and at two additional locations at half the distance between the centreline and each side wall. In this way it was demonstrated that the slope

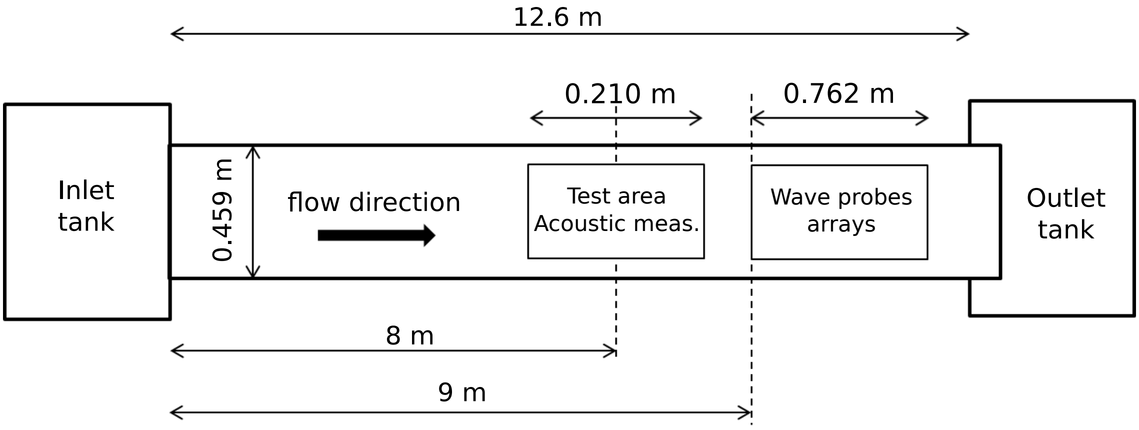

Figure 4.1: Schematic of the experimental flume. Dimensions are not to scale.

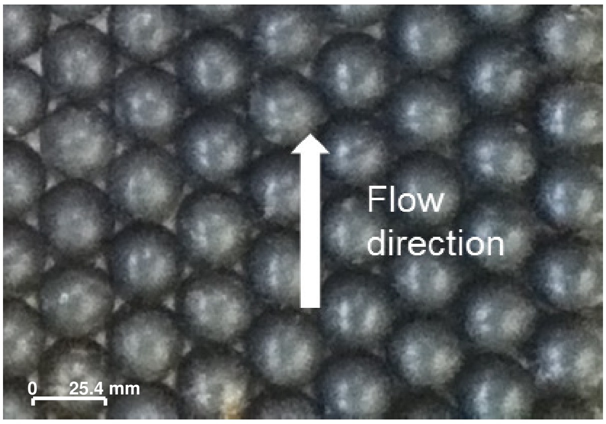

Figure 4.2: A photograph of the flume bed.

of the free surface coincided with the slope of the bed, with the uncertainty of $\pm 2.3 \times 10^{-4}$. At each measurement location, a manual point gauge was progressively lowered towards the surface from above, until its tip was observed to be submerged for approximately 50 % of the time. The procedure was repeated three times at each location, and a mean value was taken. The gate at the flume outlet was adjusted until the averages of the depth at each location were within ±0.7 mm. The mean depth, H, was then defined as the average across all measurements at all locations. Due to the adopted procedure, the uncertainty of the mean depth was ±0.7 mm. The depth datum was set at the distance $d_s/4$ below the crests of the spheres. This datum corresponds to the geometric centre of the hemispheric surface with radius $d_s/2$. The same datum was suggested by Nakagawa et al. [1975], as it provides the appropriate fitting of the streamwise velocity distribution by Nikuradse logarithmic law. Nezu and Nakagawa [1993] found that the level where the time-averaged velocity is zero is between $0.15d_s$ and $0.3d_s$.

Two different velocities of the flow were measured. (i) The mean surface velocity, U_0, was measured by timing the passage of neutrally buoyant particles across a fixed streamwise distance of 1.53 m. Plascoat Talisman 30 powder was used as seeding particles. U_0 was the average of 10 measurements in each flow condition. The standard deviation across these measurements was below 3.5 % of U_0. (ii) The cross section-averaged velocity, U_H, was calculated from the volumetric flow discharge, Q_v, and from the flow cross-section calculated from the uniform flow depth and the channel width. The flow discharge was measured from the pressure drop across a calibrated orifice plate in the flume inlet pipe, using a U tube manometer. It varied as a power of the pressure difference measured by the manometer, as [5167-1, 1997]

$$Q_v = U_H H W_f = \alpha_m p_m^{\beta_m} / \rho_w, \tag{4.1}$$

where p_m is the pressure difference measured by the manometer, W_f is the flume width, ρ_w is the water density, $\beta_m = 0.5$ [5167-1, 1997], and α_m is a calibration coefficients which was equal to 11.39 for the setup used here. Equation (4.1) does not consider the flow within the pores of the layers of spheres, therefore it overestimates the velocity U_H. Nichols [2015] compared the result of equation (4.1) with the depth integrated velocities obtained via a PIV method in a wide range of subcritical flow conditions in the same flume and with the same bed roughness. Nichols [2015] found that when the pressure difference was smaller than 30 mm, the measured discharge was approximated better by equation (4.1) with $\alpha_m = 9.56$ and $\beta_m = 0.658$. These values take into account the real cross-section including the porous layers, and were used in all conditions where $p_m < 30\,\mathrm{mm}$. The original correlation was used in the conditions where $p_m \geq 30\,\mathrm{mm}$, where it was found to be more accurate. Assuming the uncertainty of the measurement of the flume width to be negligible, the relative uncertainty of U_H was estimated as

$$\frac{dU_H}{U_H} = \beta_m \frac{dp_m}{p_m} - \frac{dH}{H}. \tag{4.2}$$

The second term of equation (4.2) is of the order of 1 %, assuming $dH = 0.7\,\mathrm{mm}$. The manometer was filled with water, and the pressure difference could be determined with accuracy $dp_m = \pm 2\,\mathrm{mm}_{\mathrm{H_2O}}$. The first term of equation (4.2) was estimated as $\beta_m dp_m/p_m = \pm 66\,\%$ ($dU_H = \pm 0.11\,\mathrm{m\,s^{-1}}$) when $H = 42.2\,\mathrm{mm}$, $U_H = 0.17\,\mathrm{m\,s^{-1}}$, and $\beta_m dp_m/p_m = \pm 2\,\%$ ($dU_H = \pm 0.01\,\mathrm{m\,s^{-1}}$) when $H = 99.0\,\mathrm{mm}$, $U_H = 0.54\,\mathrm{m\,s^{-1}}$.

4.2 Estimation of the streamwise velocity profile

The characterisation of the dispersion relation of gravity-capillary waves in a turbulent flow which was described in section 3.1.2 requires the knowledge of the exponent n which fits the average streamwise velocity profile with the power-function represented by equation (3.17) with the exponent n. The measurements of the depth-averaged velocity U_H were used in order to determine the value of n in all flow condition, based on the formulae suggested by Cheng [2007] (equations (3.35) and (3.39), in sub-section 3.1.4). These formulae show the dependence of n on the submergence H/d_s and on the modified Reynolds number based on the depth-averaged flow velocity, Re_H. The equations were calibrated against the measurements of the streamwise velocity profile performed by Nichols [2015] in the same flume and with the same bed roughness with a PIV system. Each of the measurements of $U(z)$ reported by Nichols [2015] was fitted with a straight line in double logarithmic co-ordinates in order to identify the representative values of the exponent n.

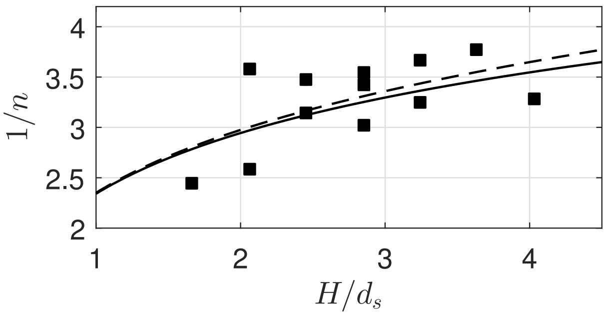

Figure 4.3: The exponent n of the power-function average streamwise velocity profile in the flume. (squares) best interpolation to the velocity profile data measured by Nichols [2015], (lines) equations (3.35) and (4.3) for (dashed) $Re_H = 10^4$, and (solid) $Re_H = 5 \times 10^5$.

The deviations between the measurements of $U(z)$ and the fitted power-function profiles at each depth were found smaller than 8 % of $U(z)$ at each depth z in the range $0.2 \leq z/H \leq 0.8$. Based on the measured modified Reynolds number R_H and submergence H/d_s, the values of n which had been identified for each condition were then compared with the equations (3.35) and (3.39) proposed by Cheng [2007]. These equations provided a good estimate of the measured n when equation (3.39) was modified in the form

$$n^{-1}\sqrt{f} = 1.0, \tag{4.3}$$

where the friction factor f was calculated based on equation (3.35).

FIG. 4.3 shows the values of $1/n$ determined from the measurements of Nichols [2015] compared with the predictions based on equations (3.35) and (4.3). The measurements reported by Nichols [2015] had $4.7 \times 10^4 \leq Re_H \leq 2.9 \times 10^5$, and $1.7 \leq H/d_s \leq 4$. The fitted exponent n varied between $1/2.4$ and $1/3.3$, and had the minimum $n = 1/3.8$ at the submergence $H/d_s = 3.6$. Across all the conditions tested here, Re_H varied between 2.8×10^4 and 2.1×10^5, and $1.6 \leq H/d_s \leq 4.0$. These parameters were used for the estimation of n in all conditions, based on equations (3.35) and (4.3). These estimates are reported in table 4.2. The estimated exponent n varied between $1/2.8$ and $1/3.5$. In the range of flow conditions described here, the change of the dispersion relation due to the change of n between these two values is comparable with the resolution of the measurements. The maximum difference between the dispersion relations (equations (3.26)) when n varies from $1/2.8$ to $1/3.5$ is $2.3\,\mathrm{rad\,m^{-1}}$, measured along the wavenumber axis. The change of n from $n = 1/2.4$ to $n = 1/3.8$ produced a change of the dispersion relation which was estimated as $4.5\,\mathrm{rad\,m^{-1}}$. In comparison, the maximum resolution of the measurements was estimated as $4.05\,\mathrm{rad\,m^{-1}}$. In light of the marginal effect of the exponent of the streamwise velocity profile across the measured conditions, all the analysis described in chapter 5 was derived with the representative value $n = 1/3$.

4.3 Measurement of the free surface elevation with arrays of conductance waveprobes

A conductance wave probe measures the surface elevation at a single location in time. By arranging a set of probes in space, the spatial and temporal characteristics of the free surface can be measured with a known resolution. Each conductance wave probe comprises of two thin conductive metal wires that are anchored separately but close to each other to the flume bed. 0.24 mm thick tinned copper wires were used for the experiments described in this thesis. The two wires were parallel and tensioned and they pierced the water surface vertically. The spacing between the wires was 13 mm for the longitudinal array, and 10 mm for the transverse arrays. An alternating current was passed through the wires, so that the voltage at their free ends was a function of the water conductivity and varied linearly with the instantaneous submergence.

The uncertainty of the surface elevation measurements with wave probes depends on a set of parameters. Krynkin et al. [2014] identified the three most important parameters as (i) the meniscus effect induced by surface tension, (ii) the deformation of the free surface due to the pressure distribution near the wires, and (iii) the finite separation between the wires. Krynkin et al. [2014] estimated the uncertainty due to the meniscus, ϵ_I, as half the wire diameter, i.e., $\epsilon_I \sim 0.12\,\text{mm}$. The meniscus is expected to oscillate vertically together with the surface [Krynkin et al., 2014], therefore the error associated with it consists in a constant bias of the measurements. This bias was eliminated by removing the linear trend of the measurements in time at each probe. As a result, the effect of the meniscus is not believed to affect the measurements reported here. The pressure distribution in the region close to the wires deforms the free surface by an extent which Krynkin et al. [2014] estimated to be comparable to the wire diameter, $\epsilon_{II} \sim 0.24\,\text{mm}$. This estimate was based on the assumption that gravity balances the excess static pressure at the stagnation point. Assuming instead that the surface tension is the dominant restoring force, as is expected due to the small diameter of the wires, the magnitude of the surface deformation is estimated as

$$\epsilon_{II} \sim \frac{\rho_w U_0^2 d_w^2}{8\pi^2 \gamma_w}, \tag{4.4}$$

where d_w is the diameter of the wires, U_0 is the mean surface velocity, γ_w is the surface tensions coefficient, and ρ_w is the density of water. In the range of flow conditions described here, the uncertainty due to the pressure distribution near the wires was estimated as $\epsilon_{II} \sim 10^{-2}\,\text{mm}$.

Krynkin et al. [2014] also estimated the uncertainty due to the finite separation between the wires, ϵ_{III}, as a function of the characteristic wavelength of the surface deformation and of the correlation function in the direction transverse to that of the flow. Based on the discussion by Krynkin et al. [2014] for a similar range of flow conditions as those reported here, ϵ_{III} is expected to vary between 33 % and 2 % of the characteristic amplitude of fluctuations when the separation is equal to 13 mm.[1] The smaller uncertainty is expected for the deeper and faster flows. The uncertainty decreases to 22 % and 1 % of the characteristic amplitude of the fluctuations, respectively, when the separation is decreased to 10 mm (along the transverse array of probes). In terms of absolute values, the uncertainty varies between 0.03 mm and 0.11 mm with the separation of 13 mm, and between 0.02 mm and 0.07 mm with the separation of 10 mm. These uncertainties were calculated assuming that the surface waves have the wavefront perpendicular to the plane of the two wires. Instead, the measurement of the waves that propagate parallel to the mean flow, with the wavefront parallel to the plane of the two wires, is not affected by this type of uncertainty. Hence, the effect of the finite separation is that of a low-pass filtering of the transverse component of the surface spatial spectrum, which limits the horizontal resolution of the measurements without causing aliasing. The resolution can be approximated by the value of the separation between the wires. The spectra reported in this thesis are shown up to the wavenumbers of 100 rad m^{-1} and 150 rad m^{-1} in the streamwise and in the transverse direction, respectively. These correspond to the wavelengths of 62.8 mm and 41.9 mm, or 4.83 and 4.19 times the wires separation, respectively. These wavelengths are within the maximum resolution of each wave probe.

An additional source of error for the measurements of the surface elevation with conductance wave probes is caused by the vibrations of the wires. These are induced by vortices that are shed periodically from the immersed portion of the probes, and can generate a fictitious fluctuation of the signal at the characteristic frequency of the vortices. Such a frequency can be estimated from the value of the Strouhal number, determined for a two-dimensional flow over a circular cylinder. The Strouhal number is defined as

$$Sr_w = \frac{f_v d_w}{U_0}, \tag{4.5}$$

where f_v is the frequency of the vortices, d_w is the diameter of the wires, and U_0 is the mean surface velocity. Sr_w is a function of a Reynolds number based on the

---

[1] These values were found assuming that the characteristic spatial period of the free surface is $2\pi/k_0$, and the correlation length is π/k_0, in accordance with the results presented in chapter 5. The characteristic amplitude of fluctuations is represented by the standard deviation σ.

diameter d_w,

$$Re_w = \frac{\rho_w U_0 d_w}{\mu_w}, \tag{4.6}$$

where ρ_w and μ_w are the density and the dynamic viscosity of water, respectively. In the range of flow conditions investigated here Re_w varied between 45 and 143. Sr_v is estimated to be in the range between 0.12 and 0.18, respectively [Posdziech and Grundmann, 2007]. As a result, the shedding frequency of the vortices was estimated to be between 142 Hz and 450 Hz, respectively. The wave probes data series were filtered with a second order band-pass Butterworth filter with the cutoff frequencies of 0.1 Hz and 20 Hz. Therefore, the effects of the vibrations of the conductance wave probes at the frequency of vortex shedding is believed to be negligible for the analysis presented here.

In summary, the accuracy of the measurements with conductance wave probes was estimated to be approximately 0.01 mm for the waves propagating in the streamwise direction, and between 0.02 mm and 0.07 mm for the waves propagating in the transverse direction. The horizontal resolution of the measurements was 62.8 mm and 41.9 mm in the two directions, respectively. The measurements were performed continuously for an overall duration of 5 minutes at the sampling frequency of 500 Hz, and analysed in segments of 10 seconds each. Twenty-four conductance wave probes were distributed in order to form three separate non-equidistant arrays. The arrangement of the three arrays is shown in FIG. 4.4 and 4.5. One streamwise array of 8 probes was aligned along the flume centreline, with the first probe called $1_{(x)}$ at the distance of 9 m from the inlet. The length of the streamwise array was 762.5 mm. The minimum distance between the probes was equal to 12.5 mm (between probes $7_{(x)}$ and $8_{(x)}$), and is associated with the maximum resolution of the streamwise array. The two remaining arrays were orthogonal to the centreline and comprised of 8 probes each, which were distributed in between the centreline and the flume side wall on the left hand side (looking towards the outlet). The first transverse array had the length of 167.2 mm and it was positioned at the same streamwise distance from the inlet as the probe $1_{(x)}$. The maximum resolution in the transverse direction was represented by the The second transverse array had the length of 168.8 mm and it was positioned at the same streamwise distance from the inlet as the probe $4_{(x)}$. Data was acquired simultaneously at the longitudinal array and at one of the transverse arrays, for each measurement. For the purpose of the analysis, the probe $1_{(x)}$ was shared by the longitudinal array and by the first transverse array ($1_{(x)} \equiv 1_{(y)}$), and the probe $4_{(x)}$ was shared by the longitudinal array and by the first transverse array ($4_{(x)} \equiv 1_{(y')}$). This increased the effective number of probes in the arrays y and y' to 9. The second array y' was not used for the analysis presented here, but it is shown for completeness. The co-ordinates of each probe relative to probe $1_{(x)}$

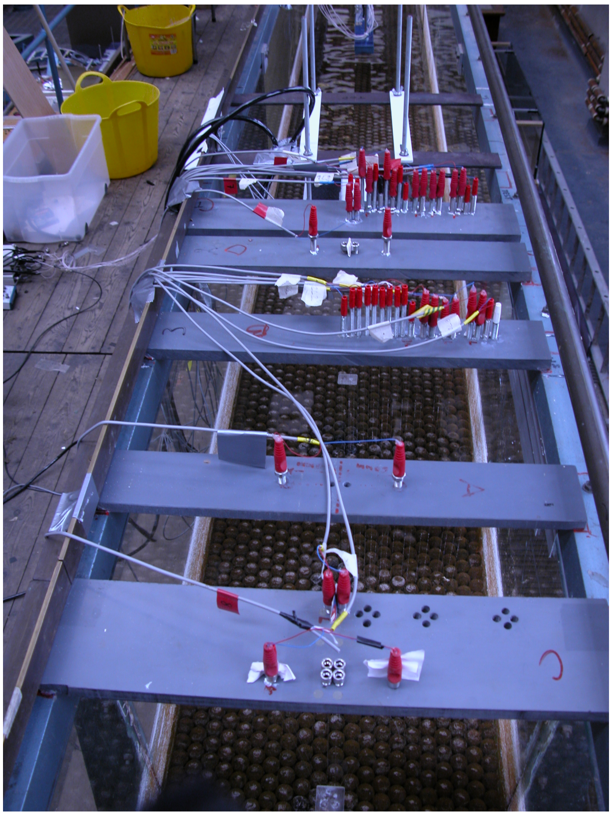

Figure 4.4: Picture of the arrays of conductance wave probes. Flow direction is top to bottom.

are shown in FIG. 4.5 and reported in Table 4.1. The x-axis runs along the channel centreline and the origin of the axes is 9 m from the inlet.

The conductance wave probes were connected to a set of Churchill Controls WM1A wave monitors. The analogue output of the wave monitors was digitised by two 8 channels National Instrument (NI) data acquisition cards, and recorded with an NI PXIe-8108 embedded control system with LabView. The synchronisation between the two acquisition cards was checked in a separate measurement, with the same sampling period used for the measurements, $1/f_s = 0.002\,\text{s}$. The delay was less than the sampling period, and it could not be quantified. Every probe was

Table 4.1: The spatial distribution of the conductance wave probes

Array	Probe location[a] (mm)								
	1	2	3	4	5	6	7	8	9
x $(y \equiv 0)$	0	26.0	116.5	297.5	541.5	694.5	750.0	762.5	
y $(x \equiv 0)$	0	17.5	35.0	51.5	69.0	95.0	119.0	151.0	167.2
y' $(x \equiv 297.5)$	0	18.4	35.5	51.3	69.1	95.7	121.2	150.3	168.8

---

[a] The origin of the x-y co-ordinates is 9 m downstream from the inlet, along the centreline. The co-ordinates in the table are along the x-axis for the array x, and along the y axis for the arrays y and y'.

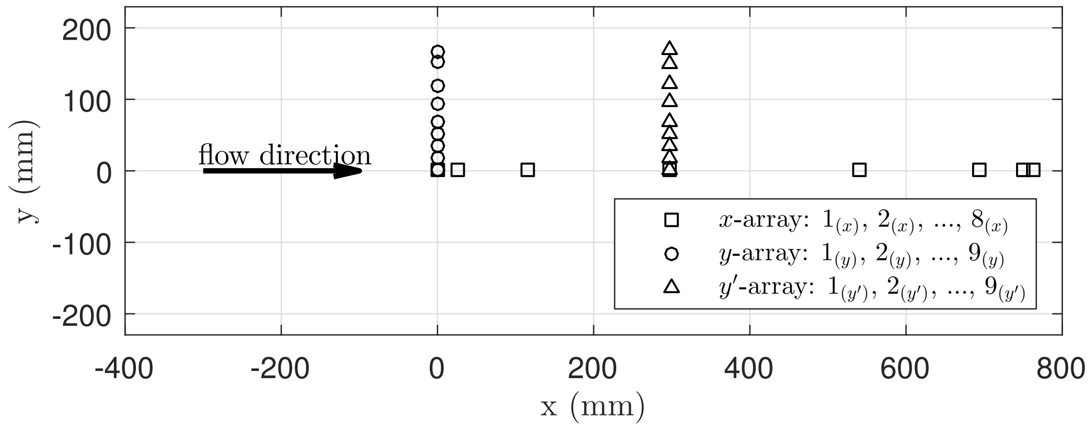

Figure 4.5: The arrangement of the arrays of conductance wave probes.

calibrated at 6 constant depths from 30 mm to 130 mm in still water and with the channel slope of $s = 0$. The mean temperature of the water during the calibration was 15.6 °C. The mean temperature was 24.4 °C during the tests with the flow. The average voltage output was measured at each depth and the line of best fit was applied to the data to determine the calibration function separately for each probe. The calibration sensitivity of the probes varied between 0.146 V mm^{-1} and 0.032 V mm^{-1}, with the average of 0.113 V mm^{-1}. The lower sensitivity was found for probes $1_{(y)}$ and $3_{(y)}$ and was caused by the different length of the cables which connected the probes to the wave monitor, and consequently the different voltage offset. The probes along the transverse arrays were connected alternately to the same wave monitors. In some cases this required reducing the gain of the monitor to ensure that the measurements were within the dynamic range of the acquisition system. The data acquisition system had an accuracy of 0.3 mV, that corresponds to a 0.003 mm average vertical resolution. The wave probes recordings in still water were characterised by a very slow unsteady drift in time (less than 10^{-2} mm over ten seconds). As a result, the root mean square (rms) noise level estimated from a 10 min measurements was approximately 0.05 mm, which was reduced below 0.01 mm by filtering with the second order Butterworth filter prior to the analysis.

4.4 Acoustic measurements

4.4.1 Acoustic apparatus

The acoustic apparatus was used in order to measure the Doppler spectrum of the scattered airborne acoustic waves. The analysis procedure and results of these measurements are reported in section 5.1. The setup comprised of a 70 mm directional ultrasonic transducer (Pro-Wave ceramic type 043SR750) and two 1/4” B&K 4939-

A-011 microphones with Type 2670 pre-amplifiers. The ultrasonic transducer was connected directly to a Tektronix AFG 3022C function generator which emitted a 43 kHz sinusoid with peak-to-peak amplitude of 10 V. The two microphones had the sensitivity of $4.043\,\mathrm{mV\,Pa^{-1}}$ and $3.955\,\mathrm{mV\,Pa^{-1}}$, respectively. The signal recorded by the microphones was amplified by a B&K NEXUS Conditioning Amplifier Type 2692-A, with the gain set to $1\,\mathrm{V\,Pa^{-1}}$. The charge amplifier had an embedded band-pass filter with pass band between 20 Hz and 100 kHz. The output of the power module was digitised and recorded by the same NI PXIe-8108 embedded control system which was used with the conductance wave probes. The direct output from the function generator was also digitised and recorded on a separate channel. The acquisition was performed at the sampling frequency of 500 kHz, for short intervals of 1 s duration.

The Doppler spectrum was defined as the frequency power spectrum of the scattered acoustic pressure signal determined with the standard discrete Fourier transform in time. Prior to the calculation of the spectrum, the signal was filtered with a second-order band-pass Butterworth filter between the frequencies $0.9\omega_a$ and $1.1\omega_a$, where ω_a was the frequency of the output of the source transducer. The recorded signal was then detrended, and multiplied by a Hanning window function of the same duration. The spectrum was the average of 50 independent measurements, each with the length of one second.

4.4.2 Characterisation of the acoustic response and directivity of the Doppler setup

In order to model the acoustic scattering by the water surface, it was necessary to characterise the acoustic response of the receivers in space and the directivity pattern of the acoustic source, namely D_m and D_s, respectively.

Based on factory specifications, the free-field response of the B&K microphones at normal incidence is flat within ±1 dB between 2 Hz and 100 kHz when the protection grid has been removed. The directivity pattern of the B&K 4939-A-011 microphones was obtained from the official documentation [BK]. It is shown in FIG. 4.6, where the directivity was normalised by the maximum amplitude at 0°.

The directivity pattern of the 70 mm ultrasonic transducer was measured in an anechoic chamber, at the same frequency at which the transducer was driven in the flume. In the anechoic chamber, the transducer was mounted on a frame installed right above the centre of a 60 mm high automatic rotating table, at the distance of 645 mm from the ground and with the axis perpendicular to the axis of revolution.

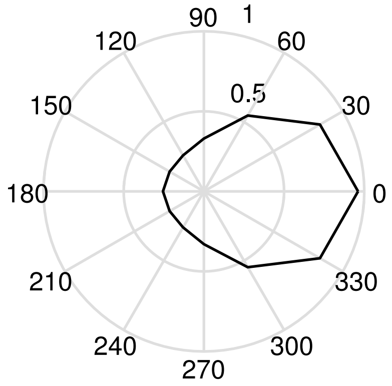

Figure 4.6: The normalised directivity pattern of the B&K 4939-A-011 microphones. Data from accompanying documentation [BK].

The table completed one full revolution in approximately 1 min. The transducer was driven with a sinusoidal signal with the frequency of 43 kHz and amplitude of 10 V peak-to-peak. For the characterisation of the directivity of the 70 mm directional ultrasonic transducer, a setup with a different type of microphones was used. This setup consisted of two 1/4” G.R.A.S. 46BF microphone sets, connected to two G.R.A.S. power modules Type 12AK with neutral (”Lin”) filter setting and 40 dB gain. One of the microphones was installed on the same rotating frame as the transducer, and it provided the reference output which enables to correct for the eventual drift of the ultrasonic source. The second microphone was installed on a fixed frame, at the same height of the source, so that the rotation of the transducer allowed the full characterisation of the directivity in one single measurement. The measurement set up is shown in FIG. 4.7.

The directivity was measured at 4 distances from the centre of the source, 200 mm, 400 mm, 500 mm, and 1000 mm. The signal was recorded in very short intervals of 1 ms, at the frequency of 1 MHz. A separate acquisition was triggered every 0.01 s. Each segment of the measured signal, P, was filtered with a band-pass second-order Butterworth filter between the frequencies of 30 kHz and 50 kHz. The initial and final tails of the segment were removed, and the signal was Hilbert transformed in order to obtain its analytic form. The amplitude, $\tilde{P}$, was then averaged across the single segment in order to obtain the short-time average of the acoustic pressure, $\hat{P}(\theta_s)$, where θ_s is the angle of orientation of the source axis with respect to the measurement microphone. For the adopted rotation speed, θ_s was approximately constant during 1 ms, and it varied by approximately 10^{-3} rad during 0.01 s. The recording lasted for 5 revolutions of the rotating table, and the final directivity $D_s(\theta_s)$ was the average at each θ_s across all revolutions.

The directivity pattern of a baffled round transducer in the far-field can be approximated by the acoustic pressure produced by an oscillating piston with rigid

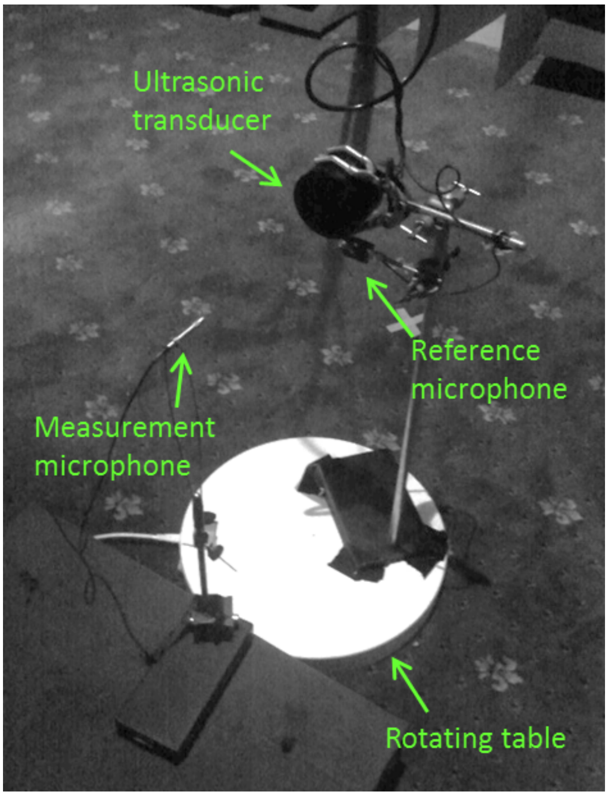

Figure 4.7: A photograph of the set up to measure the ultrasonic source directivity pattern. The distance from the ultrasonic transducer to the measurement microphone is 400 mm.

baffle [Morse and Ingard, 1968, p. 381], as reported in section 3.2.1. The measured directivity pattern is shown in FIG. 4.8. The best fit with equation (3.88) is found with $r_s = 20\,\text{mm}$, which shows that the effective diameter of the transducer was equal to 40 mm. The directivity pattern in FIG. 4.8 has a narrow main lobe with the width of approximately 30°. The side lobes predicted by equation (3.88) are absent at the smaller distance of 200 mm from the source, and are smaller than the theoretical prediction at the larger distance.

The acoustic setup was installed in the experimental flume at the distance of 8 m from the inlet. FIG. 4.9 shows a picture of the directional transducer and of the first microphone, in the actual installation condition. The transducer was attached to a fixed frame from above, with the centre of the active surface suspended at the height of 200 mm from the mean water surface level. The latter was defined as the time-averaged position of the free surface, right below the transducer. The position of the transducer was equidistant from both side walls of the flume. The transducer axis was inclined downwards at $\psi_s = 30°$ with respect to a plane parallel to the mean water surface level, facing towards the inlet. As a result, the projection of the main directivity lobe was at the distance of 7.65 m from the inlet. This was within the region of uniform depth, as verified by the measurements with the manual

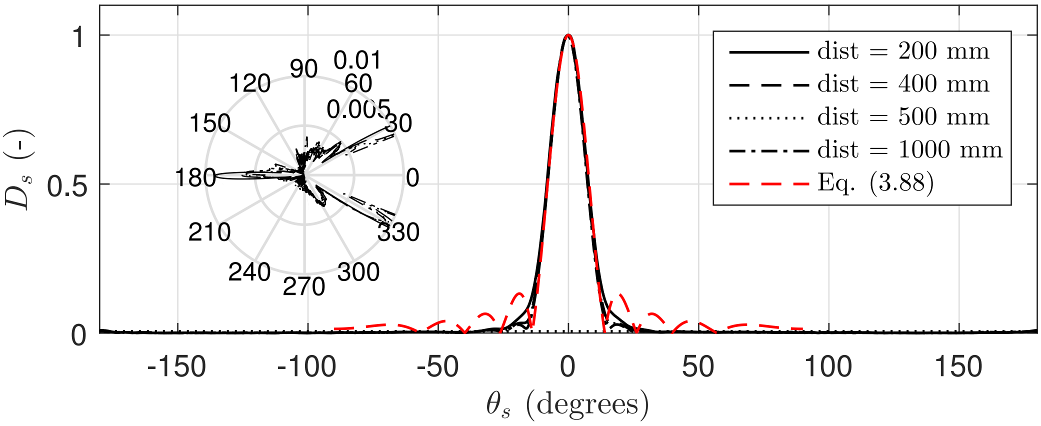

Figure 4.8: Normalised measured directivity pattern of the directional ultrasonic transducer (Pro-Wave ceramic type 043SR750) at the frequency of 24 kHz. (red) Directivity of the oscillating piston with rigid baffle, equation (3.88), with $r_s = 20$ mm. The inset shows the directivity outside of the main lobe.

depth gauges. The effective insonificated area can be defined as the region where $D_s(\theta_s) \geq 0.5$. The size of this area was $L_D = 239$ mm along the x-direction, and $L_D = 56$ mm along the y-direction.

The first of the two B&K microphones was installed at the distance of 59.5 mm from the centre of the transducer. The axis of the microphone was parallel to that of the transducer, also facing towards the inlet. The second microphone was installed closer to the flume inlet, at the same height from the mean water surface level as the ultrasonic transducer. This microphone was inclined by the same angle ψ_s with respect to the mean water surface plane, but facing towards the outlet (and towards the transducer). The position of the microphones and of the transducer were vertically adjusted before each measurement in order to maintain the same distance from the water surface. The vector co-ordinates of the transducer, $\mathbf{S} = (x_s, y_s, z_s)^T$, and of the two microphones, $\mathbf{M_1} = (x_{m,1}, y_{m,1}, z_{m,1})^T$ and $\mathbf{M_2} = (x_{m,2}, y_{m,2}, z_{m,2})^T$, respectively, were

$$\mathbf{S} = \begin{pmatrix} \cot\psi_s \\ 0 \\ 1 \end{pmatrix} 200\,\text{mm}, \tag{4.7a}$$

$$\mathbf{M_1} = \begin{pmatrix} \cot\psi_s + 0.2975\sin\psi_s + 0.01\cos\psi_s \\ 0 \\ 1 - 0.2975\cos\psi_s + 0.01\sin\psi_s \end{pmatrix} 200\,\text{mm}, \tag{4.7b}$$

$$\mathbf{M_2} = \begin{pmatrix} -\cot\psi_s \\ 0 \\ 1 \end{pmatrix} 200\,\text{mm}. \tag{4.7c}$$

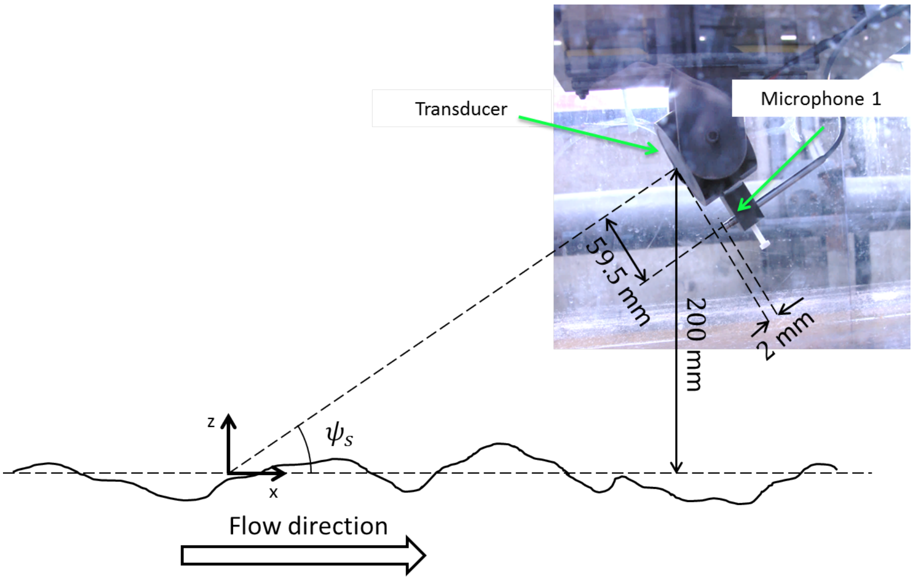

Figure 4.9: The arrangements for the 70 mm directional ultrasonic transducer (Pro-Wave ceramic type 043SR750) and the first 1/4" B&K 4939-A-011 microphone, in the actual installation. Dimensions are not to scale.

Here the origin of the system of reference is located on the plane of the mean surface, at the point of intersection with the direction of maximum directivity of the transducer. The z-axis is oriented outwards from the water flow, and the $x-$ axis is oriented along the centreline towards the flume outlet. It is noted that the second microphone was positioned along the line of specular reflection of the main directivity lobe of the transducer. The first microphone was close to the transducer, therefore it recorded the signal backscattered from the free surface. Both microphones lie outside of the main directivity lobe which is shown in FIG. 4.8, so that the direct acoustic field was negligible. It was noted during the measurements that the reflection of sound from the second microphone affected the signal recorded by the microphone number one. Therefore the second microphone was removed from the flume during the measurements with microphone one.

4.5 Experimental conditions

Thirteen different flow conditions were studied. Each flow condition was unique in terms of the uniform flow mean depth, H, and the slope, s, of the flume. These parameters are reported in Table 4.2 together with the measured mean surface velocity U_0, and the characteristic Froude and Reynolds numbers based on U_0 and H,

$$F = U_0/\sqrt{gH}, \tag{4.8}$$

and

$$Re = \rho_w U_0 H / \mu_w, \tag{4.9}$$

respectively. Here g is the gravity constant.Table 4.2 also reports the measured standard deviation of the free surface fluctuations, σ. σ was determined as the average standard deviation across all the probes of the streamwise array, in accordance with the procedure described in section 5.1.1.

The wavenumber of the stationary waves, k_0, estimated from equation (3.44) for each flow condition is also given in Table 4.2. The non-dimensional parameter $k_0 H/\pi$ corresponds to twice the ratio between the depth and the wavelength of the stationary waves. In a deep irrotational flow, $k_0 H = 1/F^2$. When k_0 is determined for the 1/3 power function profile which approximates the streamwise average velocity profile of a shallow turbulent flow (equation (3.17)), the parameter $k_0 H$ has the same meaning of a squared Froude number [Burns, 1953]. In an attempt to investigate the behaviour of the free surface when the Froude number changes, the different flow conditions reported in Table 4.2 were grouped based on the value of $k_0 H/\pi$. Each flow condition is designated by a number between 1 and 13, in descending order of $k_0 H/\pi$. The flow conditions 2 to 5 have $k_0 H/\pi > 1.4$ and $F < 0.5$, therefore they are representative of relatively deep flows with a low Froude number. The flow conditions 10 to 13 have $k_0 H/\pi < 1$ (the stationary waves are longer than $2H$) and $0.61 \leq F \leq 1$, and they represent the largest Froude number flows across all measurements. The conditions 6 to 9 have $1 \leq k_0 H/\pi \leq 1.36$ and they constitute the intermediate range of Froude number across all measurements ($0.52 \leq F \leq 0.61$). The threshold values of 1 and 1.4 have been chosen arbitrarily in order to give the same number of flow conditions in each group. Condition 1 has the mean surface velocity lower than the minimum phase velocity of gravity capillary waves, therefore the stationary waves cannot exist under this flow condition and it is impossible to define k_0 based on equation (3.44).

Table 4.2: Test flow conditions

Flow condition	H (mm)	s (-)	U_0 ($\mathrm{m\,s^{-1}}$)	F (-)	Re (-)	σ (mm)	k_0 ($\mathrm{rad\,m^{-1}}$)	k_0H/π (-)	$1/n$ (-)
1	42.2	0.001	0.19	0.30	8.0×10^3	0.05	-	-	2.8
2	72.9	0.001	0.35	0.41	2.5×10^4	0.40	89.7	2.08	3.3
3	101.0	0.001	0.41	0.41	4.1×10^4	0.50	63.6	2.05	3.5
4	42.2	0.002	0.30	0.47	1.3×10^4	0.25	131.5	1.77	2.8
5	101.3	0.002	0.49	0.49	4.9×10^4	1.79	45.1	1.45	3.5
6	43.0	0.003	0.34	0.52	1.5×10^4	0.49	99.7	1.36	2.8
7	73.1	0.002	0.46	0.54	3.4×10^4	1.21	52.4	1.22	3.3
8	40.5	0.004	0.36	0.57	1.5×10^4	0.34	89.5	1.15	2.8
9	43.4	0.005	0.40	0.61	1.7×10^4	0.46	72.6	1.00	2.8
10	99.0	0.003	0.60	0.61	5.9×10^4	2.03	31.4	0.99	3.5
11	72.4	0.003	0.54	0.64	3.9×10^4	1.17	39.4	0.91	3.3
12	43.1	0.006	0.43	0.66	1.8×10^4	0.57	63.8	0.88	2.8
13	73.2	0.004	0.58	0.68	4.2×10^4	1.10	34.8	0.81	3.3

4.6 Summary

This chapter has described the experimental setup used for all the measurements reported in this thesis. The characteristics of each tested flow condition have been reported in section 4.5. The arrays of wave probes described in section 4.3 were used for the characterisation of the dynamic behaviour of the free surface in these conditions. The results of this analysis are reported in chapter 5. The acoustic setup described in section 4.4 was used in order to measure the Doppler spectrum of the acoustic pressure field scattered by the dynamic rough surface. These measurements are described in chapter 6.

Chapter 5

Wave probes analysis of the free surface

The purpose of the experimental analysis described in this chapter was to identify a suitable model that could describe the dynamic behaviour of the free surface of shallow turbulent flows over a rough boundary, in a variety of flow conditions. The first objective was to investigate the mechanisms which produce the patterns on the free surface of shallow turbulent flows. A number of different phenomena which can cause the deformation of the free surface have been discussed in section 2.1. These can be summarised in three main categories: the interaction with turbulence in the flow, the interaction with the rough static boundary, and the shear instabilities due to the vertical variation of the average streamwise velocity. Additional instabilities and mutual interactions among waves can promote the growth of waves and modify the spectrum of the free surface, but they are not considered here as a generation mechanism. The interaction with turbulence can manifest itself in terms of the localised deformation generated by coherent turbulent structures, or of the resonant and non-resonant interaction with the turbulent pressure fluctuations. The interactions with the rough boundaries and the shear instabilities can cause the growth of patterns of gravity-capillary waves. In this chapter the results of experiments in a laboratory flume with rough boundary are used to discuss how relevant is each of these mechanisms for the free surface dynamics in shallow turbulent flows.

The second objective of this chapter was to test the hypothesis that the dynamics of the free surface of shallow turbulent flows can be described with a linear model of gravity-capillary waves. The model was introduced in subsection 3.1.1, it is used for the acoustic analysis in chapter 6, and it is described with more detail in subsection 6.1.1. It represents the free surface elevation in terms of a Fourier series in time and in space, where each Fourier coefficient is characterised by an amplitude, a phase velocity, and a phase. The phase of the Fourier coefficients is a random variable with uniform distribution. The amplitude is derived from the spectrum of the surface elevation. The phase velocity is determined based on a dispersion relationship. The latter two quantities are characterised empirically in this chapter, from the measurements of the frequency-wavenumber spectra of the surface elevation. An objective of this chapter was to demonstrate that such a model of the surface elevation is able to represent the measured statistics of the free surface correctly. This is done in section 5.2, based on the comparison with the linear and weakly nonlinear models presented in subsections 3.1.6 and 3.1.8.

The third objective of this chapter was to identify the characteristic spatial and temporal scales of the patterns on the free surface, and to establish a relationship between them and the main hydraulic quantities. These relationships would allow the characterisation of the hydraulic quantities remotely, based on the measurement of the free surface. The analysis and the data presented in this chapter have a progressively increasing degree of complexity, beginning with the characterisation of the statistics of the free surface at one location and ending with the non-stationary analysis based on the wavelet spectral method. This incremental approach provides a set of tools that would allow the remote characterisation of the flow parameters with (acoustic) instrumentations of increasing complexity. The experimental apparatus that provided the raw data for the analysis has been described in Chapter 4. The fundamentals of the analysis techniques have been described in Chapter 3 together with their relationship with the theory of gravity-capillary waves.

This chapter is organised as follows: Section 5.1 reports the definitions of the mathematical operators and descriptors which have been used in order to characterise the statistical behaviour of the free surface, as well as the details of the data analysis procedure. Section 5.2 investigates the statistics of the free surface elevation and of its envelope measured at one single location in space. Section 5.3 extends the analysis to one additional spatial dimension, and presents the spatial correlation functions and the one dimensional frequency-wavenumber spectra of both the surface elevation and of its envelope. The assumption in these first sections (to an extent motivated by the results of section 5.2) is that of the statistical stationarity of the free surface. Section 5.4 describes the results of the wavelet spectral method applied to the measurements of the free surface elevation. This method does not require the stationarity of the statistics, therefore the results in that section are more general. Section 5.5 summarises the main results of this chapter, and describes the final conclusions.

5.1 Data analysis and procedures

5.1.1 Definitions

This section reports a list of the definitions of all functions and parameters which are used in the rest of this chapter. The free surface elevation measured at probe ν and at time μ is defined as

$$\zeta_{\nu,\mu} = \zeta(x_\nu, y_\nu, t_\mu), \tag{5.1}$$

where $t_\mu = \mu\Delta t$, $\mu = 0, 1, ..., M-1$ is the sampled time vector and x_ν and y_ν are the co-ordinates of the wave probe with index ν reported in Table 4.1. $\nu = 1_{(x)}, 2_{(x)}, ..., 8_{(x)}$ for the streamwise array, and $\nu = 1_{(y)}, 2_{(y)}, ..., 8_{(y)}$ for the lateral array, respectively. $\Delta t = 1/f_s$ is the sampling period, and each measurement has the duration $T = (M-1)\Delta t$ in time.

The statistical moment of order q of the free surface elevation ζ measured at probe ν is defined according to equation (3.57) as

$$m^{(\nu)}_{\zeta,q} = \frac{1}{M}\sum_{\mu=0}^{M-1}\left(\zeta_{\nu,\mu} - <\zeta_{\nu,\mu}>_\mu\right)^q, \tag{5.2}$$

where $<\zeta_{\nu,\mu}>_\mu$ is the time-average of $\zeta_{\nu,\mu}$, which equals 0 by definition. The spatially averaged moment is defined as

$$m_{\zeta,q} = \frac{1}{N_p}\sum_{\nu=1}^{N_p} m^{(\nu)}_{\zeta}, \tag{5.3}$$

where N_p is the number of probes along the array. The standard deviation of the surface elevation corresponds to the square root of the second moment,

$$\sigma_\nu = \sqrt{m^{(\nu)}_{\zeta,2}}, \tag{5.4}$$

and the spatially averaged standard deviation is defined as

$$\sigma = \sqrt{m_{\zeta,2}}. \tag{5.5}$$

Unless otherwise stated, σ always corresponds to the values calculated from the measurements with the streamwise array, with $N_p = 8$. These values are reported in Table 4.2 for each flow condition. The quantities

$$\lambda_3 = m_{\zeta,3}/m^{3/2}_{\zeta,2}, \tag{5.6}$$

and

$$\lambda_4 = m_{\zeta,4}/m_{\zeta,2}^2, \tag{5.7}$$

are the skewness and the kurtosis of ζ, respectively.

The time-gradient of ζ, $\dot{\zeta}_{\nu,\mu}$, was determined as

$$\dot{\zeta}_{\nu,\mu} = \frac{\zeta_{\nu,\mu+1} - \zeta_{\nu,\mu}}{\Delta t}. \tag{5.8}$$

The envelope of the free surface elevation, $Z_{\nu,\mu}$, was determined from the Hilbert transform of the surface elevation $\zeta_{\nu,\mu}$. The definition of the Hilbert transform is

$$\mathcal{H}\left(\zeta_{\nu,\mu}\right) = \frac{1}{\pi}\int_{-\infty}^{\infty} \frac{\zeta(x_\nu, y_\nu, t'_\mu)}{t - t'} dt'. \tag{5.9}$$

The envelope is defined as

$$Z_{\nu,\mu} = |\zeta_{\nu,\mu} + i\mathcal{H}\left(\zeta_{\nu,\mu}\right)|, \tag{5.10}$$

while the phase of the signal is

$$\Phi_{\nu,\mu} = \Im\left\{\log\left[\zeta_{\nu,\mu} + i\mathcal{H}\left(\zeta_{\nu,\mu}\right)\right]\right\} = \tan\left[\frac{\mathcal{H}\left(\zeta_{\nu,\mu}\right)}{\zeta_{\nu,\mu}}\right], \tag{5.11}$$

where $\Im\{x\}$ represents the imaginary part of the generic variable x. In practice, $\mathcal{H}\left(\zeta_{\nu,\mu}\right)$ was computed with the 'hilbert' function available in Matlab R2015b. This function calculates the Discrete Fourier Transform (DFT) of $\zeta_{\nu,\mu}$ and produces the imaginary part in the reciprocal domain as a replica of the original signal with a lag-quadrature shift, then it sums $\zeta_{\nu,\mu}$ and the imaginary shifted replica to generate the analytic signal. The procedure is the same as described for example by Longuet-Higgins [1984], but with the opposite sign of the imaginary part (i.e., with a lead-quadrature shift). It was then necessary to modify the sign of $\mathcal{H}\left(\zeta_{\nu,\mu}\right)$ in order to obtain a consistent representation. The moments of the gradient $\dot{\zeta}_{\nu,\mu}$ and of the envelope $Z_{\nu,\mu}$, $m_{\dot{\zeta},q}^{(\nu)}$ and $m_{Z,q}^{(\nu)}$, respectively, follow from equation (5.2) with the obvious substitution of ζ by the relevant quantity. The standard deviation and the coefficients of skewness and kurtosis of $\dot{\zeta}_{\nu,\mu}$ and of $Z_{\nu,\mu}$ are defined as $\sigma_{\dot{\zeta}}$, $\lambda_{\dot{\zeta},3}$, $\lambda_{\dot{\zeta},4}$, and σ_Z, $\lambda_{Z,3}$, $\lambda_{Z,4}$, respectively.

The discrete statistical distribution of the free surface elevation measured by the probe ν, $p_\zeta^{(\nu)}(\zeta)$, was determined by binning the measured values of ζ into $N_\zeta = 63$ equidistant bins between $-3\sigma_\nu$ and $3\sigma_\nu$. The statistical distribution of $\dot{\zeta}$ was determined in the same way as $p_{\dot{\zeta}}^{(\nu)}(\dot{\zeta})$, with $N_{\dot{\zeta}} = 63$ equidistant bins between $-3\sigma_{\dot{\zeta}}$ and $3\sigma_{\dot{\zeta}}$. The number of bins was chosen empirically in order to ensure the convergence of the measured distribution. The pdf of the envelope $Z_{\nu,\mu}$, indicated by $p_Z^{(\nu)}(Z)$, was determined in the same way as $p_\zeta^{(\nu)}(\zeta)$, with only the positive $N_\zeta/2$ bins.

The normalised frequency power spectrum of the free surface elevation measured by the probe ν at the frequency ω, $S_\nu(\omega)$, was determined as

$$S_\nu(\omega) = \frac{1}{2\Delta\omega}\left|\frac{1}{\sigma_\nu M}\sum_{\mu=0}^{M-1}\zeta_{\nu,\mu}e^{-i\omega t_\mu}\right|^2, \tag{5.12}$$

where $\Delta\omega = 2\pi f_s/M$. $S_\nu(\omega)$ was calculated with the 'fft' function in Matlab R2015b at the discrete frequencies $\omega_j = j2\pi f_s/M$, $j = 0, 1, ..., M/2-1$, and later normalised such that

$$\sum_{j=0}^{M/2-1} S_\nu(\omega_j)\Delta\omega = 1. \tag{5.13}$$

The average frequency spectrum $S(\omega)$ was defined as the average of $S_\nu(\omega)$ across all probes. The q-th spectral moment was defined as

$$s_q^{(\nu)} = \sum_{j=0}^{M/2-1} \omega_j^q S_\nu(\omega_j)\Delta\omega. \tag{5.14}$$

The standard definition of the normalised space-time correlation function is

$$W(r_{x,n}, r_{y,n}, \tau_m) = \sum_{\eta=1}^{N_p}\sum_{\nu=1}^{N_p}\sum_{\mu=0}^{M-1}\frac{\zeta(x_\nu, y_\nu, t_\mu)\zeta(x_\eta, y_\eta, t_\mu - \tau_m)}{\sigma_\nu\sigma_\eta}, \tag{5.15}$$

where $r_{x,n} = x_\nu - x_\eta$ and $r_{y,n} = y_\nu - y_\eta$. The wave probes were distributed along the non-equidistant arrays reported in table 4.1. Therefore the above definition would lead to large gaps of the correlation function in the two spatial dimensions. The alternative definition of the correlation function which was adopted here was based on one single array of probes in one direction only, i.e.,

$$W_x(r_{x,n}, \tau_m) = W(r_{x,n}, 0, \tau_m), \tag{5.16a}$$

$$W_y(r_{y,n}, \tau_m) = W(0, r_{y,n}, \tau_m), \tag{5.16b}$$

were considered instead of the full correlation function W in the two spatial dimensions. From now on the analysis procedure and definitions are presented for the measurements with the streamwise array only. Therefore only the correlation in the x direction is considered, and $r_{x,n}$ is represented as r_n to simplify the notation. The extension of all definitions to the measurements with the lateral array is straightforward. Each combination of two probes (ν, η) of the same array was used in order to determine the temporal correlation function $W_t^{(n)}(\tau_m)$ at the spatial separation $r_n = x_\nu - x_\eta$,

$$W_t^{(n)}(\tau_m) = \sum_{\mu=0}^{M-1} \frac{\zeta(x_\nu, t_\mu)\zeta(x_\eta, t_\mu - \tau_m)}{\sigma_\nu \sigma_\eta}. \tag{5.17}$$

All combinations of two probes (ν, η) which spatial separation r_n was similar within a distance $\pm\delta_r$ were identified. For these combinations, the average separation $\bar{r}_n$ was determined, so that $N_{\bar{r}_n}$ was the number of pairs with $\bar{r}_n - \delta_r \leq x_\nu - x_\eta \leq \bar{r}_n + \delta_r$, and the number of unique separations $\bar{r}_n$ was $2N_x - 1$. N_x was the number of non-negative separations. The space-time correlation function was then estimated by binning the temporal correlation functions $W_t^{(n)}(\tau_m)$ and calculating the average inside each bin, i.e.,

$$W_x(\bar{r}_n, \tau_m) = \frac{1}{N_{\bar{r}}} \sum_{n, r_n \approx \bar{r}_n} W_t^{(n)}(\tau_m). \tag{5.18}$$

The binning of the correlation function was performed in order to improve the convergence of the interpolation algorithm described in sub-section 5.1.3 in light of the uncertainty of the location of the probes. δ_r was set to 5 mm. This value appeared to give a stable average of the measured correlation function. The zero time-lag correlation function was defined as

$$W_x(\bar{r}_n, 0). \tag{5.19}$$

The two-dimensional space-time correlation function calculated with equation (5.18) was still defined on a non-equidistant set of spatial separations $\bar{r}_n$, in general. The frequency-wavenumber spectra determined from the DFT of such a function would be affected by strong leakage. An iterative algorithm combined with a sinc function reconstruction procedure was applied to the measured correlations in order to obtain the accurate interpolation of the correlation function onto a new equidistant set of separations. The technique is explained with more detail in sub-section 5.1.3. The result of the interpolation was the regularised correlation function $\hat{W}_x(\bar{r}_e, \tau_m)$, which was defined at the equidistant separations $\bar{r}_e$.

The frequency-wavenumber spectrum was calculated with the two-dimensional DFT of $\hat{W}_x(\bar{r}_e, \tau_m)$ at the discrete frequencies ω_j and wavenumbers $k_{x,l} = l2\pi/(2N_x -$

1)$\Delta\bar{r}_e$, $l = -N_x+1, -N_x+2, ..., N_x-1$,

$$S_x(k_{x,l},\omega_j) = \sum_{m=0}^{2M-1} \sum_{e=-N_x+1}^{N_x-1} w_H(\bar{r}_e,\tau_m)\hat{W}_x(\bar{r}_e,\tau_m)\exp\left[i\left(k_{x,l}\bar{r}_e - \omega_j\tau_m\right)\right]\Delta\bar{r}_e\Delta\tau, \tag{5.20}$$

where $\Delta\bar{r}_e = 2L_x/2(N_x-1)$, $\Delta\tau = 2T/2(M-1)$, L_x was the spatial length of the array of probes, and $w_H(\bar{r}_e,\tau_m)$ was a two-dimensional window function. A standard two-dimensional Hanning window,

$$w_H(\bar{r}_e,\tau_m) = 0.25\left[1-\cos\left(\frac{\pi\left(\bar{r}_e+L_x\right)}{L_x}\right)\right]\left[1-\cos\left(\frac{\pi\left(\tau_m+T\right)}{T}\right)\right], \tag{5.21}$$

was used for the analysis. The frequency wavenumber spectrum $S_x(k_{x,l},\omega_j)$ was normalised such that

$$\sum_{j=1}^{M/2}\sum_{l=-N_x+1}^{N_x-1} S_x(k_{x,l},\omega_j)\Delta k_x\Delta\omega = 1,. \tag{5.22}$$

It is shown in sub-section 5.3.2 that the amplitude of the frequency-wavenumber spectra of the free surface elevation decays rapidly with the frequency. In order to improve the visualisation of such spectra, a wavenumber-wise normalisation of the spectrum,

$$\bar{S}_x(k_x,\omega) = S_x(k_x,\omega)/[S_x(\omega)/k_{s,x}], \tag{5.23}$$

was introduced, where $k_{s,x}$ was the Nyquist wavenumber calculated for the stream-wise array. $S_x(\omega_j)$ was the equivalent of a spatially averaged frequency spectrum, obtained by integrating equation (5.20) over the wavenumber axis only, i.e.,

$$S_x(\omega_j) = \sum_{l=-N_x+1}^{N_x-1} S_x(k_{x,l},\omega_j)\Delta k_x. \tag{5.24}$$

In practice, the frequency spectra $S(\omega)$, the correlation functions $W_x(\bar{r}_n,\tau_m)$ and $\hat{W}_x(\bar{r}_e,\tau_m)$, and the frequency-wavenumber spectra $S_x(k_x,\omega)$ were all calculated from a set of independent measurements of ζ, each being 10 seconds long. All the quantities reported in the rest of this chapter were the average across all such 10 seconds long segments, which were assumed to represent a set of independent realisations. These averaged quantities are indicated by the same symbols as the one defined here for a single realisation, in order to simplify the notation.

5.1.2 Generation of constrained surrogate time series with the gradual wavelet reconstruction

The basic principle of the method of generating constrained surrogate synthetic time series with the gradual wavelet reconstruction [Keylock, 2006, 2007, 2010] was outlined in sub-section 3.1.7, as well as the fundamental algorithm. Here the implementation of the version of the algorithm described by Keylock [2010] to the measured wave probes data is briefly presented. The surrogates were generated based on a single reference signal for each condition. This was the calibrated signal $\zeta_{\nu,\mu}$ recorded at one single probe ν, and it was priorly detrended in time and band-pass filtered with the cut-off frequencies of 0.1 Hz and 20 Hz. The signal was not downsampled in order to improve the convergence of the statistical distributions, especially of the gradient $\dot{\zeta}_{\nu,\mu}$. 2^{18} samples of the signal $\zeta_{\nu,\mu}$ were used for the analysis, which corresponded to 524.288 s with the sampling frequency of 500 Hz. The analysis followed the algorithm [Keylock, 2010] described in sub-section 3.1.7. Similarly to Keylock [2010], a Daubechies least-asymmetric wavelet with 16 vanishing moments was employed. The wavelet transforms were computed with the 'wmtsa' [WMTSA, 2006] package developed for Matlab by Charlie Cornish based on the book by Percival and Walden [2000]. The convergence was tested in terms of the squared difference between the average power spectra of the original signal and of the surrogates. The spectra were calculated separately at each scale after splitting the signal into segments of the length of 2^{12} samples, corresponding to 8.192 s. Both signals were pre-multiplied by a standard Hanning window of the same length prior to the calculation of the spectra. This prevented issues of convergence due to the boundary discontinuities. The convergence parameter was defined as

$$\delta_{surr.} = \frac{\sqrt{\sum_{j=1}^{2^{18}} \left[S(\omega_j) - S_{surr.}(\omega_j)\right]^2}}{\sum_{j=1}^{2^{18}} S(\omega_j)}, \tag{5.25}$$

where $S(\omega_j)$ was the power spectrum of the measured elevation at the frequency ω_j, and $S_{surr.}(\omega_j)$ was the power spectrum of the surrogate. The iterations were halted when $\delta_{surr.}$ was smaller than 10^{-3}, or when it changed by less than 10^{-6} between two consecutive iterations, which occurred before 100 iterations.

5.1.3 Reconstruction of the space-time correlation function from measurements with non-equidistant arrays of probes

The interpolation of the correlation function $W_x(\bar{r}_n, \tau_m)$ on an equidistant set of spatial separations $\bar{r}_e$ was performed with an iterative algorithm combined with a sinc function reconstruction procedure, where the sinc function was defined as

$$\mathrm{sinc}(r) = \frac{\sin(\pi r)}{\pi r}. \tag{5.26}$$

Alternative kernels have been considered in the literature, such as the Gaussian, Laplacian, and rectangular kernels [Babu and Stoica, 2010]. The sinc kernel was chosen because it is directly related to the Sampling Theorem [Shannon, 1949]. This kernel gives more accurate results than the Lomb-Scargle periodogram for non-uniformly sampled signals with harmonic components [Rehfeld et al., 2011] and it defines a valid estimator of the correlation function [Stoica and Sandgren, 2006]. Compared to other kernels, it ensures the positive semidefiniteness of the interpolated correlation function [Babu and Stoica, 2010]. An iterative algorithm introduced by Gröchenig [1993] was added to the sinc interpolation method described by Stoica and Sandgren [2006] and Maymon and Oppenheim [2011] to further minimise the leakage due to non-orthonormality of the sinc coefficients when they are projected on the non-equidistant set of sampling locations.

The equidistant set of separations, $\bar{r}_e$, was defined as $\bar{r}_e = e\Delta\bar{r}_e$, where $\Delta\bar{r}_e = L_x/(N_x - 1)$, in accordance with Rehfeld et al. [2011]. At the first iteration, the interpolation $\hat{W}_x(\bar{r}_e, \tau_m)^{(1)}$ of $W_x(\bar{r}_n, \tau_m)$ was calculated as

$$\hat{W}_x(\bar{r}_e, \tau_m)^{(1)} = \sum_{n=-N_x+1}^{N_x-1} W_x(\bar{r}_n, \tau_m)\,\mathrm{sinc}\left[\frac{2\,(\bar{r}_e - \bar{r}_n)}{\Gamma_r \Delta\bar{r}_e}\right]. \tag{5.27}$$

Γ_r was an arbitrary numeric coefficient that defined the width of the reconstruction kernel. The Fourier spatial transform of $\hat{W}_x(\bar{r}_e, \tau_m)^{(1)}$ is equal to the convolution of the spectrum of $W_x(\bar{r}_n, \tau_m)$ with the spectrum of the kernel function. As noted by Rehfeld et al. [2011], the sinc kernel interpolation corresponds to applying a low-pass filter to the original correlation function, where the cut-off wavenumber decreases when Γ_r increases. On the other hand, the iterative procedure becomes unstable if the kernel width $\Gamma_r\Delta\bar{r}_e$ is much smaller than the maximum gap in the non-equidistant set $\bar{r}_n$. With the relatively sparse arrays of probes that were described in chapter 4, the best compromise between the conservation of the spatial spectrum and the stability of the reconstruction was found when $\Gamma_r = 2$. The same value was used in the benchmark test described by Rehfeld et al. [2011].

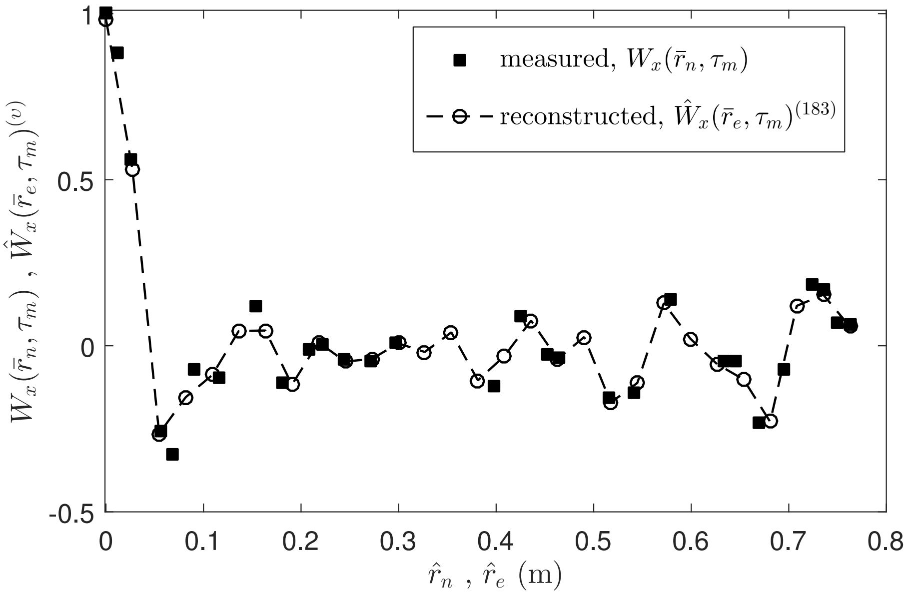

Figure 5.1: An example of the correlation functions at 0 time lag, for condition 11: (squares) estimated directly, $W_x(\bar{r}_n, 0)$, (circles) reconstructed through the proposed iterative procedure at the 183-th iteration, $\hat{W}_x(\bar{r}_e, 0)^{(183)}$.

Equation (5.27) corresponds to the discrete sinc transform of $W_x(\bar{r}_n, \tau_m)$ performed at each time separation τ_m from the set of separations $\bar{r}_n$ to the set $\bar{r}_e$. It is easy to find that the coefficients of this transform are not linearly independent if $\bar{r}_n$ are non-equidistant. This produced spurious contributions to the regularized correlation $\hat{W}_x(\bar{r}_e, \tau_m)^{(1)}$. In order to improve the quality of the interpolation, the following procedures suggested by Gröchenig [1993] were applied: (i) The discrete sinc transform was applied to the original irregularly sampled correlation in space, $W_x(\bar{r}_n, \tau_m)$, at each time separation τ_m. (ii) The inverse sinc transform was applied to the initial guess of the reconstructed correlation, $\hat{W}_x(\bar{r}_e, \tau_m)^{(1)}$. The result was $W_x(\bar{r}_n, \tau_m)^{(1)}$, which was defined on the original set of samples, $\bar{r}_n$. If the reconstructed signal is bandlimited to $\pi/\Delta\bar{r}_e$ the inverse transform does not produce additional errors, because it is applied to the regularly spaced set $\bar{r}_e$, where the coefficients are linearly independent [Maymon and Oppenheim, 2011]. (iii) The residual at the first iteration, $\varepsilon(\bar{r}_n, \tau_m)^{(1)}$ was found from the difference between $W_x(\bar{r}_n, \tau_m)^{(1)}$ and $W_x(\bar{r}_n, \tau_m)$. (iv) The residual was then transformed to the regular set $\bar{r}_e$, to produce $\hat{\varepsilon}(\bar{r}_e, \tau_m)^{(1)}$. (v) This was subtracted from the initial guess of $\hat{W}_x(\bar{r}_e, \tau_m)^{(1)}$ in order to reduce the effect of nonlinearities. The result was the improved estimate $\hat{W}_x(\bar{r}_e, \tau_m)^{(2)}$. The steps (ii) to (v) were repeated until the residual became smaller than a chosen threshold. Here the threshold was defined as 1 % of the maximum of the correlation function, which corresponds to $W_x(0, 0) \equiv 1$. The convergence was reached usually within the first 200 iterations.

The inverse transform (step (ii)) of $\hat{W}_x(\bar{r}_e, \tau_m)^{(\upsilon)}$ at the υ-th iteration was written as

$$W_x(\bar{r}_n, \tau_m)^{(\upsilon)} = \sum_{e=-N_x+1}^{N_x-1} \hat{W}_x(\bar{r}_e, \tau_m)^{(\upsilon)} \operatorname{sinc}\left[\frac{2(\bar{r}_n - \bar{r}_e)}{\Gamma_r \Delta\bar{r}_e}\right]. \tag{5.28}$$

The residual $\varepsilon(\bar{r}_n, \tau_m)^{(\upsilon)}$ (step (iii)) was given by

$$\varepsilon(\bar{r}_n, \tau_m)^{(\upsilon)} = W_x(\bar{r}_n, \tau_m)^{(\upsilon)} - W_x(\bar{r}_n, \tau_m). \tag{5.29}$$

The discrete transform applied to $\varepsilon(\bar{r}_n, \tau_m)^{(\upsilon)}$ (step (iv)) produced the correction at the υ-th iteration,

$$\hat{\varepsilon}(\bar{r}_e, \tau_m)^{(\upsilon)} = \sum_{n=-N_x+1}^{N_x-1} \varepsilon(\bar{r}_n, \tau_m)^{(\upsilon)} \operatorname{sinc}\left[\frac{2(\bar{r}_e - \bar{r}_n)}{\Gamma_r \Delta\bar{r}_e}\right]. \tag{5.30}$$

The improved estimate at the iteration $\upsilon + 1$ (step (v)) was

$$\hat{W}_x(\bar{r}_e, \tau_m)^{(\upsilon+1)} = \hat{W}_x(\bar{r}_e, \tau_m)^{(\upsilon)} - \varpi\hat{\varepsilon}(\bar{r}_e, \tau_m)^{(\upsilon)}. \tag{5.31}$$

where ϖ is an under-relaxation factor that controls the convergence, which was set to $\varpi = 0.1$. $\hat{\varepsilon}(\bar{r}_e, \tau_m)^{(\upsilon)}$ was used as the convergence parameter. FIG. 5.1 shows an example of the measured correlation function at 0 time-lag, $W_x(\bar{r}_n, 0)$, and of the corresponding interpolation, $\hat{W}_x(\bar{r}_e, 0)$, both found for a single realisation in flow condition 11.

5.1.4 Gaussian fitting of the wavenumber-frequency spectra

In order to quantify the difference between the proposed dispersion relations and the measured spectra, the same strategy described by Herbert et al. [2010] was applied here. FIG. 5.2a shows an example of the average streamwise frequency-wavenumber spectrum measured in condition 13. The spectrum has two large peaks with the frequency $\omega = 0$. At the higher frequency, the energy of the spectrum is mainly concentrated along two lines, where the spectrum forms two characteristic ridges. The ridges of the streamwise spectra $S_x(k_x, \omega)$ have been identified by fitting the spatial spectrum at each frequency ω_j, $S_x(k_x, \omega_j)$, with the function

$$S(k_x, \omega_j) = A_j^G \exp\left[-\left(\frac{k_x - k_{x,j}^G}{\sqrt{2}\sigma_j^G}\right)^2\right]. \tag{5.32}$$

A least square non-linear fitting procedure based on the trust-region-reflective method and implemented in the 'lsqnonlin' standard function in Matlab r2015b [Coleman

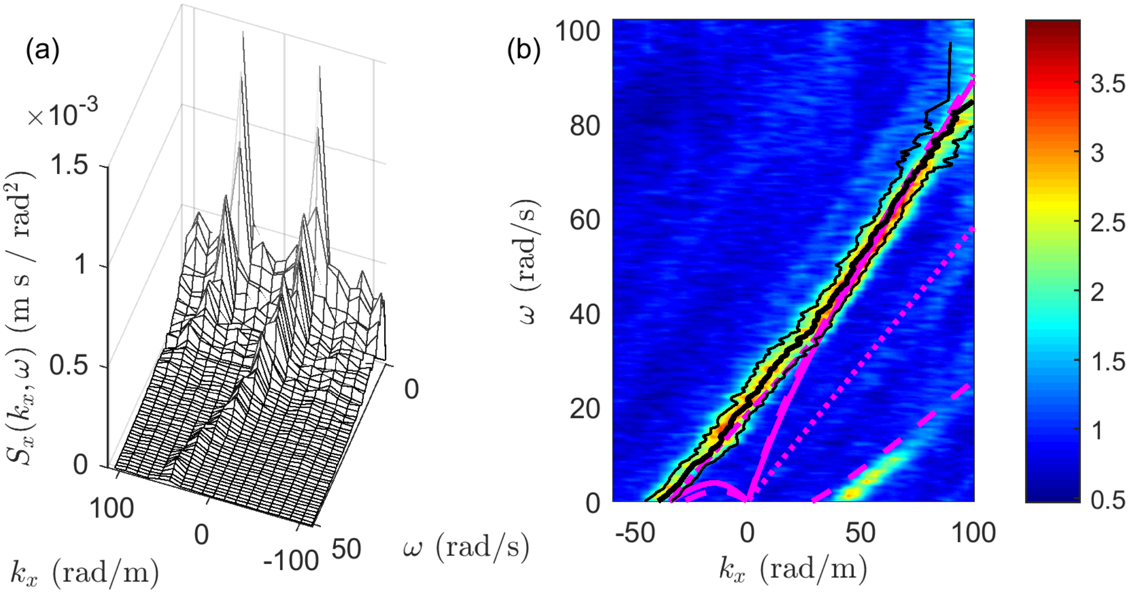

Figure 5.2: (a) An example of the streamwise frequency-wavenumber spectrum $S_x(k_x,\omega)$, measured in condition 13. (b) The Gaussian fitting of one ridge of the normalised streamwise spectrum, $\bar{S}_x(\hat{k}_x,\hat{\omega})$, for condition 13. (dashed, magenta) Irrotational dispersion relation, equation (3.20). (solid, magenta) Dispersion relation with the 1/3 velocity profile, $\theta = 0$, equation (3.26). (dotted, magenta) Non-dispersive relation, equation (3.21). (dashed-dotted, magenta) Dispersion relation with the 1/3 velocity profile, with constant $k = k_0$, equation (3.45). (solid, black, thick line) Centres of the spectrum at each frequency, $k^G_{x,j}$ (equation (5.32)). (solid, black, thin lines) $k^G_{x,j} \pm \sigma^G_j$.

and Li, 1996] was used in order to find the parameters A^G_j, $k^G_{x,j}$, and σ^G_j, which provide the best fit with the measurements $S_x(k_x,\omega)$ at each frequency ω_j. The maximum fit indicated the centres of the measured ridges, $k^G_{x,j}$, as well as their width along the wavenumber axis, σ^G_j. An example of the fitted frequency-wavenumber spectrum is shown in FIG. 5.2 for condition 13. The finite width σ^G_j of the spectral ridges was close to the spectral resolution and it was caused by the numerical analysis procedure. In fact, the application of the same analysis to synthetic data series obtained with the linear surface model described in chapter 6 and with a prescribed dispersion relation yielded similar values of σ^G_j across the whole spectrum.

The accuracy of the theoretical dispersion relations reported in subsection 3.1.2 was quantified as follows. Each of the dispersion relations $\Omega(k_x)$ represented by equations 3.20, 3.26, and 3.21, were inverted (analytically or numerically) in order to determine the relation $K_x(\omega_j)$ that satisfies $\Omega(K_x(\omega_j)) = \omega_j$. The distance between $k^G_{x,j}$ and $K_x(\omega_j)$ provided a measure of the uncertainty of the proposed model at such frequency. This corresponds to the distance between the thick black line and the magenta coloured lines in FIG. 5.2, measured horizontally. The global fitting of the different models was then quantified in terms of the root mean square average of this distance across the whole frequency range where each model applied,

$$\varepsilon_k = \sqrt{\left\langle \left(K_x(\omega_j) - k_{x,j}^G\right)^2 \right\rangle_{\omega_j \in \Omega(K_x)}}. \tag{5.33}$$

5.1.5 Wave groups analysis

In subsection 3.1.3 it was shown that the envelope of groups of waves with a narrow-banded spectrum moves with the so-called group velocity, which is different in general from the mean surface velocity. The envelope of the free surface elevation, $Z_{\nu,\mu}$ was determined based on equation (5.10) from the measurements at all probes, and in all flow conditions. This was then subject to the same analysis procedure applied to the surface elevation in order to determine the zero time-lag correlation function and the frequency-wavenumber spectra of $Z_{\nu,\mu}$. In order to represent correctly the dynamics of the wave groups in terms of their amplitude, the surface elevation had to be filtered so that the narrow-band representation carried a physical interpretation. This was done as suggested by Longuet-Higgins [1984] by convolving the frequency spectrum with a square function centred about the characteristic frequency of the group, and then inverting the Fourier transform in order to obtain the filtered time-series. Dankert et al. [2003] used a 3D-Gabor filter in order to obtain the same result from a two dimensional frequency-wavenumber spectrum. The filters were applied in both cases in the reciprocal domain (in the case of Dankert et al. [2003] represented by the three-dimensional frequency-wavenumber space). The approach followed by Dankert et al. [2003] could not be applied here, because the frequency-wavenumber spectra were obtained from an estimate of the space-time correlation function, which is a real function. Therefore the phase information of the original signal was not available.

A combination of both methods was therefore applied here. The signal at each probe was filtered in the one-dimensional frequency domain following Longuet-Higgins [1984], but with a Gaussian filter (which corresponds to the one-dimensional version of the 3D-Gabor filter employed by Dankert et al. [2003]) with the centre frequency ω_G and the characteristic width $\sigma_{\omega,G}$. The filtered spectrum was computed by multiplying the Fourier spectrum of the original time-series $\zeta_{\nu,\mu}$ by the function $\exp\left[-(\omega-\omega_G)^2/2\sigma_{\omega,G}^2\right]$ at each frequency ω. Only the real part of the frequency spectrum was convoluted with the filter, while the complex conjugate was turned to zero. The inverse Fourier transform of the convoluted spectrum then yielded a complex signal, for which the absolute value corresponded to the envelope of the group with centre frequency ω_G, evaluated locally at the single wave probe. Therefore, this process allowed the direct calculation of the envelope without requiring the application of the Hilbert transform.

5.1.6 Application of the wavelet spectral method

The wavelet spectral method presented by Donelan et al. [1996] and described in subsection 3.1.9 was implemented here in a simplified version which only employs three probes aligned in pairs along orthogonal directions. Based on the discussion in subsection 3.1.9, the distance between the probes must be small compared to the characteristic scales of the free surface, but not to small in order not to affect the uncertainty of the measurements. Probes $1_{(x)} \equiv 1_{(y)}$, $2_{(x)}$, and $3_{(y)}$ were employed here, since they allowed the measurement in two directions with the maximum separation between probes of 26 mm. The co-ordinates of these probes have been reported in Table 4.1. The algorithm to compute the wavelet transforms was kindly provided by Dr. Héctor García Nava (Autonomous University of Baja California). This was based on a Morlet wavelet defined by equation (3.68). This has the Fourier spectrum

$$w_\omega(\omega_j, \omega) = \exp\left[-\frac{1}{\sqrt{2}}\left(\frac{\omega - \omega_j}{0.220636\omega_j}\right)^2\right], \tag{5.34}$$

where $\omega_j = 2\pi/\lambda_j$ is the characteristic frequency based on the wavelet scale λ_j. The Morlet wavelet was chosen in accordance with the study by Donelan et al. [1996]. These authors compared the results of the wavelet spectral method obtained with the Morlet and Meyer wavelets, and argued that the Meyer wavelets have poorer frequency resolution. The Morlet wavelets represent a non-orthonormal set, but their spectrum decays rapidly away from the centre frequency. Therefore the typical spectral resolution can be improved by introducing intermediary scales which are quasi-independent of the standard set of logarithmically scaled scales [Donelan et al., 1996]. The Morlet wavelet is also more representative of the physics of the free surface waves, since the Gaussian envelope prescribed by these wavelets can be seen as an approximation of the sech^2 envelope [Hui and Hamilton, 1979] typical of soliton-like wave groups of permanent form. An example of the Morlet wavelet $w(\omega_j, t)$ (equation (3.69)) with the characteristic frequency $\omega_j = 1$ is shown in FIG. 5.3. The scale of the Morlet wavelets has a direct correspondence with the frequency of a sinusoidal wave. Therefore in the rest of this chapter the characteristic frequency of the Morlet wavelet is indicated simply as ω, in order to simplify the notation.

The wavelet transform was performed in the reciprocal frequency domain, and it was applied to the measurement of the surface elevation recorded individually by each probe. The signal was detrended, filtered, and downsampled prior to the trans-

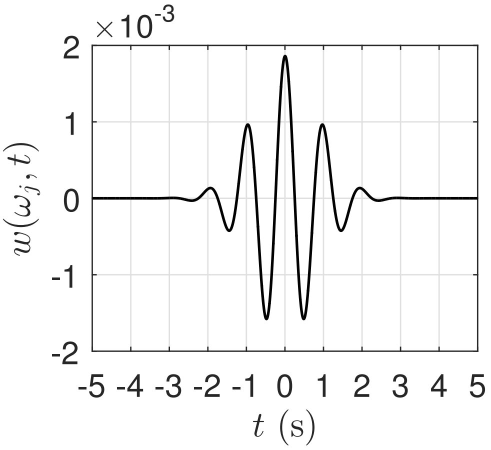

Figure 5.3: An example of the Morlet wavelet with $\omega_j = 1$.

form. The result of the wavelet transform applied to each probe was the complex quantity

$$\zeta_{W,\nu}(t,\omega) = Z_W(x_\nu, y_\nu, t, \omega) e^{i\Phi_W(x_\nu,y_\nu,t,\omega)} = Z_{W,\nu}(t,\omega) e^{i\Phi_{W,\nu}(t,\omega)}. \tag{5.35}$$

The two phase differences,

$$\Delta\Phi_x(t,\omega) = \Im\left\{\log\left[\frac{\zeta_{W,2_{(x)}}(t,\omega)}{\zeta_{W,1_{(x)}}(t,\omega)}\right]\right\}, \tag{5.36a}$$

$$\Delta\Phi_y(t,\omega) = \Im\left\{\log\left[\frac{\zeta_{W,3_{(y)}}(t,\omega)}{\zeta_{W,1_{(y)}}(t,\omega)}\right]\right\}, \tag{5.36b}$$

were computed from each pair of probes. The wavenumbers in the streamwise and transverse direction were calculated as

$$k_x(t,\omega) = \Delta\Phi_x(t,\omega) / \left[x_{2_{(x)}} - x_{1_{(x)}}\right], \tag{5.37a}$$

$$k_y(t,\omega) = \Delta\Phi_y(t,\omega) / \left[y_{3_{(y)}} - y_{1_{(y)}}\right]. \tag{5.37b}$$

The wavelet spectral method is expected to provide an accurate measurement of the wavenumbers only if all probes are instantaneously being crossed by the same wave group. It will be shown that the angle of propagation of the waves calculated with the wavelet spectral method is subject to rapid changes when the amplitude of the wavelet transform is minimum. This indicates the boundary between two separate wave groups. When such a boundary is located between the probes, the phases measured by each probe are not related, and the calculation of the wavenumber based on equations (5.37a) and (5.37b) is incorrect. The measurements of the wavenumber based on the wavelet spectral method are analysed here in terms of the pdf's of k_x and k_y at each frequency. In order to improve the quality of the results, the distributions of k_x and k_y were weighted by the geometric average of the instantaneous amplitude of the wavelet transform at all probes, i.e., the pdf's were computed based on the following definition,

$$p_k(k_x,\omega) = Pr\left[k_x(t,\omega)\frac{\sqrt{Z_{W,2_{(x)}}(t,\omega)Z^2_{W,1_{(x)}}(t,\omega)Z_{W,3_{(y)}}(t,\omega)}}{\sum_\mu\sqrt{Z_{W,2_{(x)}}(t,\omega)Z^2_{W,1_{(x)}}(t,\omega)Z_{W,3_{(y)}}(t,\omega)}}\right], \tag{5.38a}$$

$$p_k(k_y,\omega) = Pr\left[k_y(t,\omega)\frac{\sqrt{Z_{W,2_{(x)}}(t,\omega)Z^2_{W,1_{(x)}}(t,\omega)Z_{W,3_{(y)}}(t,\omega)}}{\sum_\mu\sqrt{Z_{W,2_{(x)}}(t,\omega)Z^2_{W,1_{(x)}}(t,\omega)Z_{W,3_{(y)}}(t,\omega)}}\right]. \tag{5.38b}$$

The angle of propagation was calculated as

$$\theta(t,\omega) = \tan^{-1}\left[k_y(t,\omega)/k_x(t,\omega)\right]. \tag{5.39}$$

The pdf of the angle θ, $p_\theta(\theta,\omega)$ was defined similarly to equations (5.38).

The analysis was performed at 32 logarithmically spaced frequencies ω between $0.785\,\mathrm{rad\,s^{-1}}$ and $169.1\,\mathrm{rad\,s^{-1}}$, which yield a number of four scales per octave. The typical set of wavelet scales has one scale per octave. If the set is orthogonal, as is the case of the Meyer wavelets, this ensures that the coefficients of the wavelet transform are linearly independent. This is never the case for the Morlet wavelets. The set of frequencies (scales) adopted here was chosen because it allowed the resolution required by the analysis.

5.2 Single-point statistics

The aim of this section was to characterise the statistics of the surface elevation ζ, of its time gradient $\dot{\zeta}$, and of the envelope Z at one location fixed in space. These quantities were defined in section 5.1. The first objective was to verify if these statistics are in agreement with a linear model of the surface elevation, such that ζ could be expanded in a trigonometric series where all coefficients of the series are mutually independent and the phase of each trigonometric function is a homogeneously distributed random variable. This model is used in chapter 6 in order to predict and analyse the statistics of the acoustic pressure field scattered by the dynamic rough surface. In this section the measurements of the pdf of the surface elevation and of its envelope are compared with the linear and weakly nonlinear models described by equations (3.55) and (3.66), and by equations (3.60) and (3.63), respectively. The significance of the eventual deviations from the linear statistics are quantified based on the comparison with synthetic surrogate data, generated with the gradual wavelet reconstruction method following the procedure described in subsection 5.1.2. The surrogate data generated in this way has the same statistics of the surface elevation. Therefore, the statistics of the time gradient of the elevation are used as a reference and need to be introduced.

The second objective of the analysis presented in this section was to identify the eventual link between the statistics of the free surface and the hydraulic quantities of the flow. The results of the measurements of the frequency spectra in all conditions are presented at the beginning of this section. The relation between the parameters of the spectra (namely, the first two spectral moments, defined by equation (5.14)) and the hydraulic quantities is investigated. This link would allow the indirect measurement of such quantities based on the characterisation of the free surface behaviour at one single location. The measurements of the frequency spectra also inform the development of the free surface dynamic model used in chapter 6.

The results in this section have further implications regarding the identification of the mechanisms that generate the patterns on the free surface. The hypothesis which is being tested in this case is whether the statistics of the envelope of the elevation (which is representative of the amplitude of the surface fluctuations) are in agreement with a linear or weakly nonlinear model. This model suggests that the variations of the amplitude in time can be explained by the contribution from a large number of infinitesimal waves distributed randomly. This seems to be in contrast with the theories which predict that localised deformations of the surface can relate to isolated coherent turbulent structures in the flow [Tsai, 1998, Savelsberg and van de Water, 2009, Fujita et al., 2011, Nichols et al., 2016]. Therefore, the measurement of the statistics of the envelope described in subsection 5.2.3 may help clarifying the mechanisms that are of more importance for the generation of the waves. The consequences for the characterisation of the interaction between turbulence and the free surface is discussed with more detail in section 5.5.

5.2.1 Frequency spectra of the free surface elevation

An example of the free surface elevation measured with two wave probes on the x-axis (probes $1_{(x)}$ and $2_{(x)}$) is shown in FIG. 5.4. The average of the frequency power spectra $S_\nu(\omega)$ across separate realisations was calculated directly from the surface elevation measured at each probe, based on equation (5.12). The signal at each probe was previously split into 59 segments, each with the length of 10 s. The average frequency power spectra were determined as the average across all the segments, which were assumed to represent a set of independent realisations. Due to

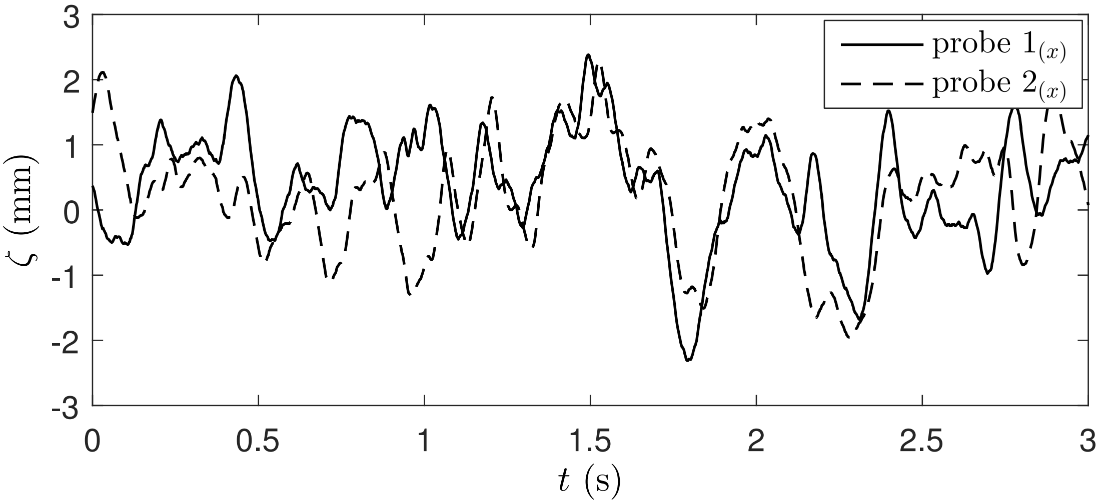

Figure 5.4: An example of the time series of the free surface elevation for condition 13, before filtering and downsampling. (solid) Probe $1_{(x)}$. (dashed) Probe $2_{(x)}$. The mean surface velocity was $U_0 = 0.58$ m/s, and the distance between the probes 26 mm.

the normalisation represented by equation (5.13), $\sigma^2 S_\nu(\omega)$ corresponds to the power spectral density of the elevation, which has the dimensions of $\mathrm{m^2\,s\,rad^{-1}}$.

FIG. 5.5 shows the power spectral density for conditions 1, 4, 7, and 10, measured from all probes of the streamwise array $(1_{(x)}, ..., 8_{(x)})$. These conditions are representative of the range of the typical spatial and temporal scales across all flow conditions. All spectra here and in the following sections are plotted up to the cut-off frequency of the Butterworth filter, which was equal to 20 Hz, or 126 $\mathrm{rad\,s^{-1}}$. The high frequency portion of the spectra can still be influenced by the numerical filter. In most conditions (see FIG. 5.5a, c, and d) the spectra are relatively insensitive of the location of the probe. This demonstrated that the properties of the free surface were homogeneous across the test section. In conditions 2, 3, 8, and 12, the spectra showed the same trend observed in FIG. 5.5, but the variation of the amplitude in the intermediate range of frequencies (between 10 $\mathrm{rad\,s^{-1}}$ and 80 $\mathrm{rad\,s^{-1}}$) among the different probes was larger. The measurements with manual gauges did not evidence a stronger inhomogeneity of the mean depth in these conditions. In all conditions, the power spectral densities decrease towards the higher frequency, and have the largest amplitude at the frequency $\omega = 0$. The amplitude of the spectra is two orders of magnitude larger in conditions 4, 7, and 10, than in condition 1.

FIG. 5.6a shows the first moment of the frequency power spectra, $s_1^{(\nu)}$ (equation (5.14), with $q = 1$) for all the measured conditions, plotted against $k_0 U_0$. $k_0 U_0$ is the frequency of the gravity waves with wavenumber k_0 (equation (3.44)), when they propagate in still water. $s_1^{(\nu)}$ grows almost proportionally to $k_0 U_0$. This can be expected, since the frequency is proportional to U_0 at the first approximation, based

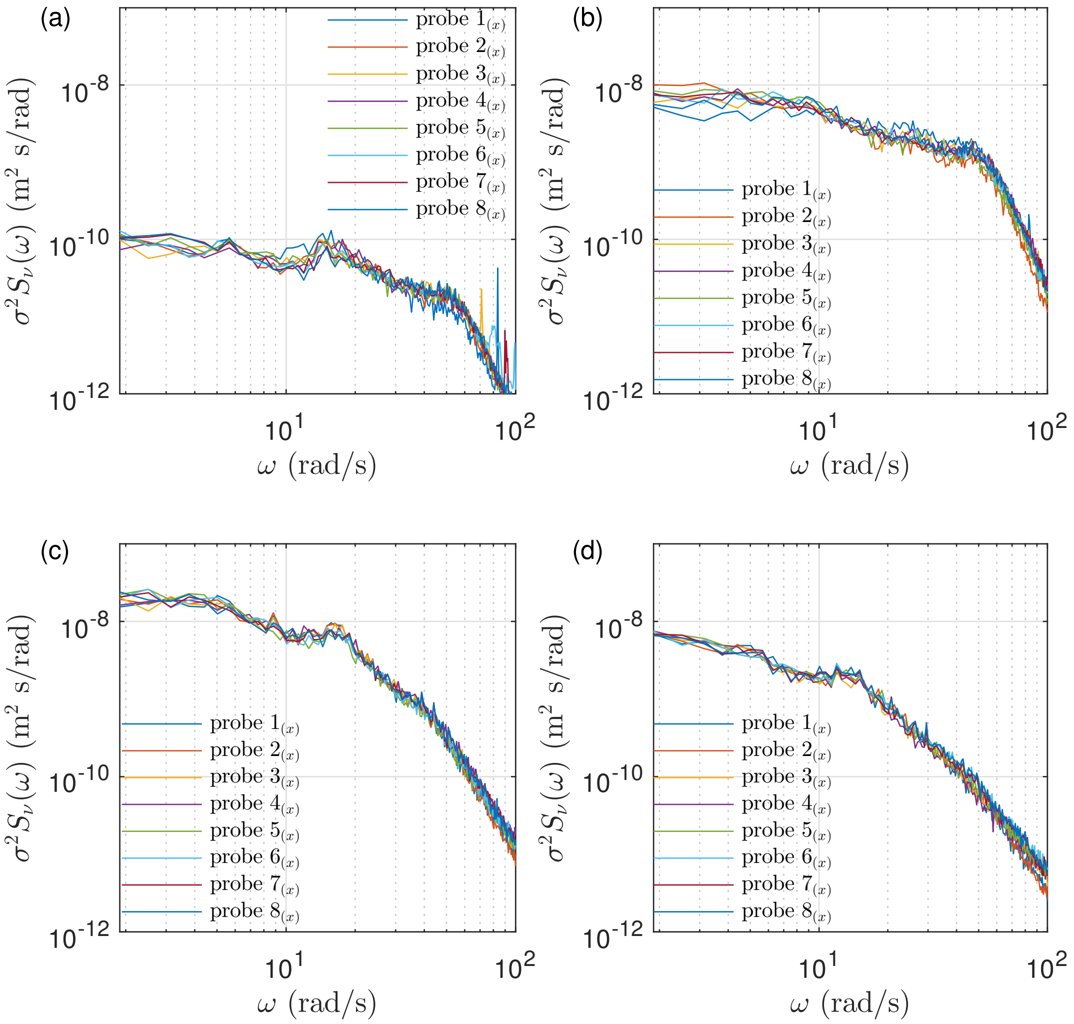

Figure 5.5: The power spectral density $\sigma^2 S_\nu(\omega)$ measured with probes $1_{(x)}$ to $8_{(x)}$. (a) Condition 1. (b) Condition 4. (c) Condition 7. (d) Condition 10. The high-frequency part of the spectra is influenced by the numerical filter applied to the data.

on the dispersion relation represented by equation (3.20). A linear fit through the average values of $s_1^{(\nu)}$ across probes $1_{(x)}$ to $8_{(x)}$ provided the empirical relation

$$s_1 = 0.501\, k_0 U_0. \tag{5.40}$$

When the spectrum decays smoothly from the frequency $\omega = 0$ like the ones in FIG. 5.5, s_1 is a measure of the width of such spectrum. The variance of the free surface elevation, σ^2, is a measure of the squared amplitude of the patterns on the free surface, and it represents the area under the power spectral densities, $\sigma^2 S_\nu(\omega)$. Therefore, σ^2 can be related to the spectrum width s_1. FIG. 5.6b shows the variation of $2\log(\sigma)$ as a function of the logarithm of $k_0 U_0$. This is approximated well by the empirical relation

$$\sigma^2 = e^{(6.66)}\,(k_0 U_0)^{-6.50}\ \ (\mathrm{m}^2), \tag{5.41}$$

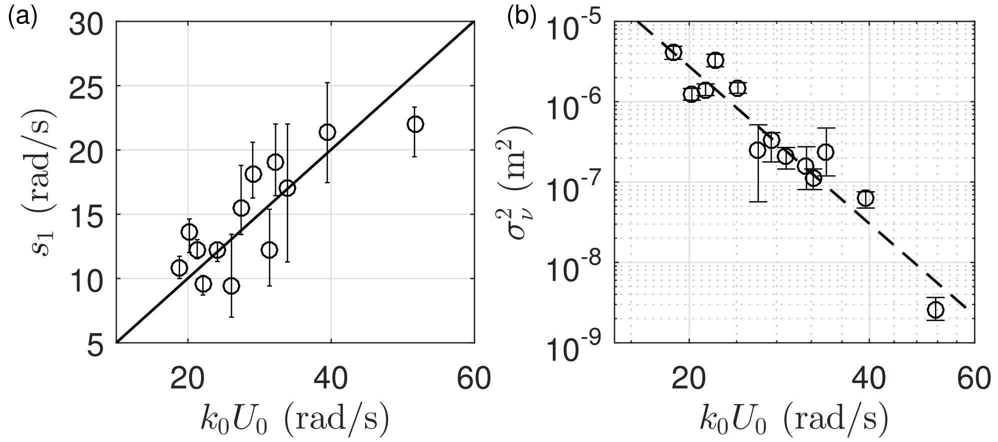

Figure 5.6: (a) The first spectral moment $s_1^{(\nu)}$ (equation (5.14)). (solid line) Fitted linear relation, equation (5.40). (b) The variance of the free surface elevation, σ^2. (dashed line) Fitted relation, equation (5.41). The circles are the average across all probes of the streamwise array, $1_{(x)}$ to $8_{(x)}$. The bars represent the maxima and minima measured across all probes of the same array.

which was obtained by a linear fit of the average values represented in FIG. 5.6b expressed in logarithmic co-ordinates. Equation (3.41) can be approximated by $k_0 \approx g/U_0^2$ when $k_0H/\pi \geq 1$ and $k_0 \gg \sqrt{\rho_w g/\gamma_w}$. Although dimensionally non consistent, equation 5.41 shows that σ grows approximately with $U_0^{3.25}$ in these conditions.

The apparent linear relationship between the first spectral moment and the frequency k_0U_0 suggests k_0U_0 as a candidate non-dimensionalising parameter. FIG. 5.7 shows the non-dimensionalised averaged power spectra $S(\hat{\omega})$ measured in all flow conditions, where the non-dimensional frequency was defined as

$$\hat{\omega} = \frac{\omega}{k_0U_0}. \tag{5.42}$$

$S(\hat{\omega})$ was the average across all probes of the streamwise and of the lateral array of $S_\nu(\hat{\omega})$, and $S_\nu(\hat{\omega})$ was the average across all 10 seconds long data time-series recorded at the probe ν. In condition 1 k_0 cannot be determined, therefore the spectrum in FIG. 5.7a is plotted against the non-dimensional frequency $\omega U_0/g$. The different flow conditions have been grouped according to the parameter k_0H_0 in order to evidence the eventual dependence on the Froude number, as explained in section 4.5. The frequency spectra show the similar behaviour when plotted against the non-dimensional frequency $\hat{\omega}$, for each range of k_0H_0. The spectrum of the flow condition 1 in FIG. 5.7a has a peak at the frequency $\omega U_0/g = 0.3$. The other spectra in FIG. 5.7b-d decay smoothly from a maximum that tends asymptotically to $\hat{\omega} = 0$. The rate of decay of the frequency spectra increases towards the higher frequencies. The increase occurs near the frequency $\hat{\omega} = 2$ in FIG. 5.7b-d, and near the frequency

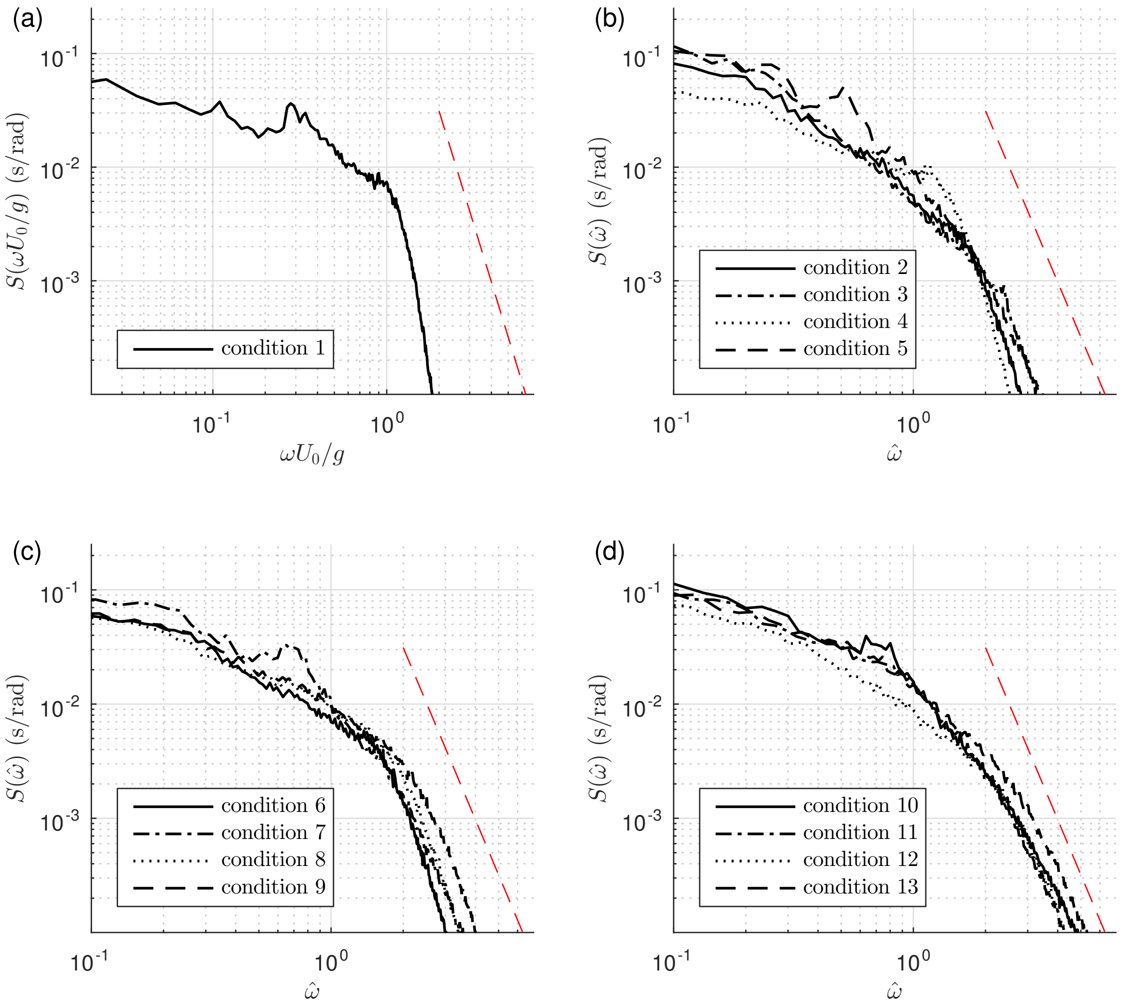

Figure 5.7: The normalised averaged frequency power spectra of the free surface elevation, $S(\hat{\omega})$, plotted against the non-dimensional frequency $\hat{\omega}$. (dashed, red) Power law decay $\propto \hat{\omega}^{-5}$, shown for reference. The high-frequency part of the spectra is influenced by the numerical filter applied to the data. Note the different scaling in (a).

$\omega U_0/g = 1$ in the condition 1. The power function law $S(\hat{\omega}) \propto \hat{\omega}^{-5}$ is shown in FIG. 5.7 for reference. The comparison with the measurements in FIG. 5.7b-d shows that the decay of the frequency spectra in the region $\hat{\omega} > 2$ is slower for the higher Froude number conditions (FIG. 5.7d) than for the lower and intermediate Froude number conditions (FIG. 5.7b, c).

5.2.2 Probability distribution of the free surface elevation

This subsection shows the measurements of the statistics of the surface elevation ζ and of the time-gradient $\dot{\zeta}$ in the flow conditions reported in Table 4.2. The statistics of the surface elevation are compared with the predictions by a linear and a weakly nonlinear model of the surface elevation. The statistics of the time-gradient

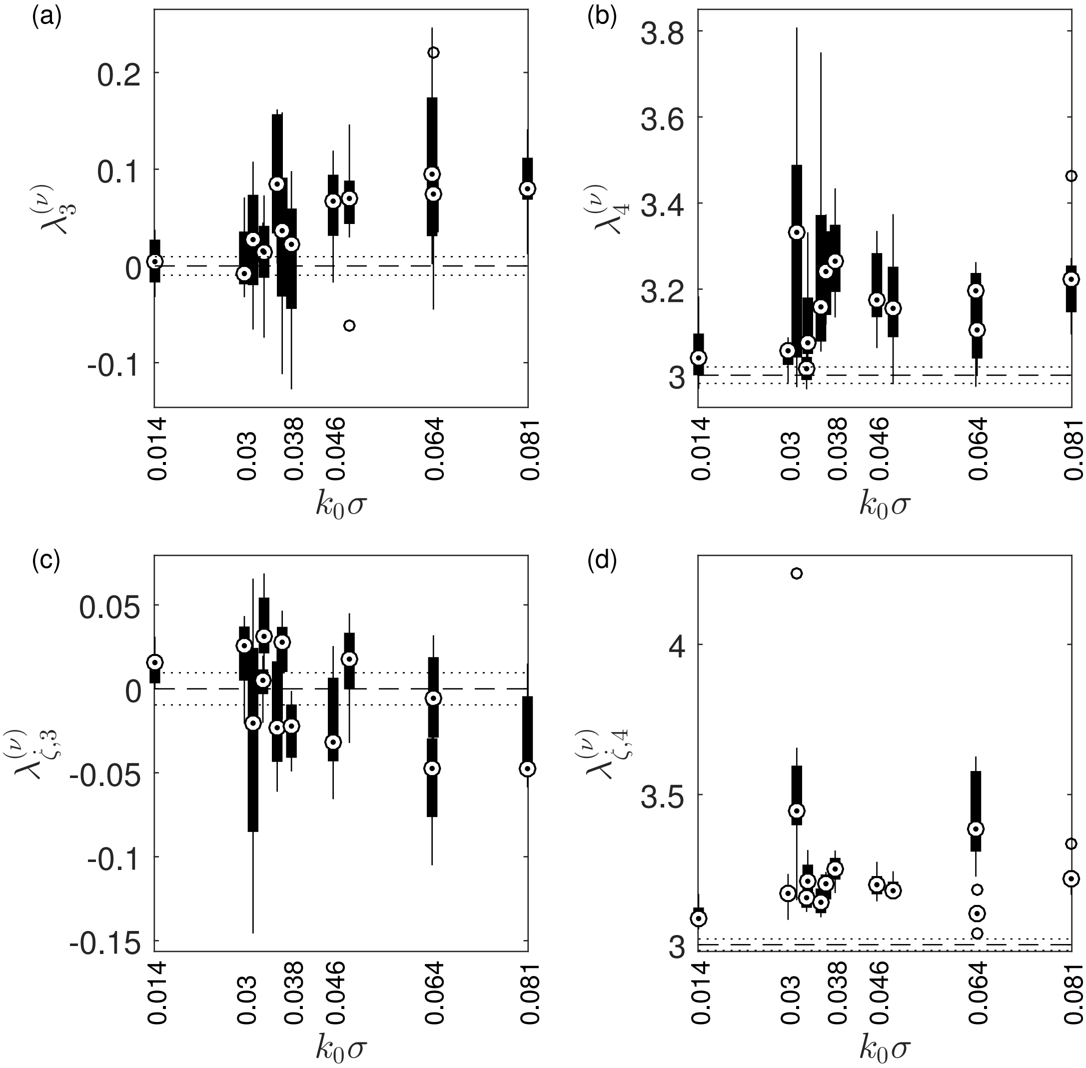

Figure 5.8: (a) Third moment (skewness) of ζ. (b) Fourth moment (kurtosis) of ζ. (c) Third moment (skewness) of $\dot{\zeta}$. (d) Fourth moment (kurtosis) of $\dot{\zeta}$. The circles with central dot are the median of the normalised moments measured at all 15 probes ν. The lower and upper edges of each box represent the first and third quartile, respectively. The bars show the maxima and minima across all probes, or the distance equal to 1.5 times the interquartile range from the first and the third quartile, whichever was smaller. The points which distance from the median was larger than 1.5 times the interquartile range were treated as outliers and plotted individually as empty circles. The dashed lines show the theoretical values for the Gaussian distribution. The dotted lines show the theoretical values ± twice the standard error (95% confidence).

were calculated in order to allow the comparison with the synthetic surrogate time series constructed with the gradual wavelet reconstruction method. This comparison provides a quantitative test of the hypothesis that the surface statistics can be described by a linear model. This hypothesis is at the basis of the numerical model of acoustic scattering by the dynamic rough surface developed in chapter 6.

The statistical moments of the surface elevation ζ and of the time-gradient $\dot{\zeta}$ were calculated up to the third order (equations (5.2)-(5.3)) at each probe. FIG. 5.8 shows the normalised third and fourth moments (the skewness and the kurtosis, respectively) of both quantities. Table 5.1 summarises the results for all flow conditions, and includes the first moment (the average) of the time-gradient $\dot{\zeta}$.

The values reported in table 5.1 are the average across the probes $1_{(x)}$ to $8_{(x)}$ for the parameters s_1 and σ, and the median across all probes for the standard deviation of the gradient $\dot{\zeta}$ and for the skewness and kurtosis of ζ and of $\dot{\zeta}$. The statistical moments were analysed in relation with the characteristic slope of the free surface elevation, $k_0\sigma$, and with the normalised standard deviation, σ/H. Both quantities must be small in order to be able to apply the linearised theory reported in section 3.1. FIG. 5.8 and table 5.1 show that the third and fourth moments of ζ are close to the values expected for a Gaussian random variable. The standard error for the skewness, calculated for a sample size of 2^{18}, is equal to 0.005, while that for the kurtosis is equal to 0.010 [Wright and Herrington, 2011]. Although λ_3 and $\lambda_4 - 3$ are small in all flow conditions, their deviation from zero is larger than the standard error in most conditions, suggesting a small but significant deviation of the distribution from normality. Both moments increase when the characteristic slope $k_0\sigma$ is larger than approximately 0.035 and $\sigma/H > 0.01$. The third moment of $\dot{\zeta}$ is very close to 0 in all conditions. This shows that the slope of the waves was nearly symmetrically distributed, in contrast with observations in the ocean [Longuet-Higgins, 1963]. In contrast, the fourth moment deviates substantially from the one expected from a Gaussian distributed variable. The standard deviation of $\dot{\zeta}$, $\sigma_{\dot{\zeta}}$, grows proportionally with σ (see table 5.1).

Table 5.1: Statistics of the surface elevation

Flow condition	k_0U_0 (rad m^{-1})	s_1 (rad m^{-1})	σ (mm)	$k_0\sigma$ (-)	σ/H (-)	λ_3 (-)	λ_4 (-)	p-value Gauss	p-value Eq.(3.60)	$\sigma_{\dot\zeta}$ mm s^{-1}	$\lambda_{\dot\zeta,3}$ (-)	$\lambda_{\dot\zeta,4}$ (-)	p-value Gauss	p-value Eq.(3.60)
1	51.6	21.5	0.05	.014	.001	-.006	3.046	-	0.01	1.8	.006	3.078	-	0.13
2	31.4	13.9	0.40	.036	.006	.014	3.087	-	0.01	6.7	-.011	3.137	0.30	0.19
3	26.1	12.1	0.50	.032	.005	.007	3.181	-	0.40	5.9	.015	3.287	-	0.30
4	39.5	24.4	0.25	.033	.006	.014	3.024	-	0.12	7.2	.009	3.133	0.05	0.32
5	22.1	9.4	1.79	.081	.018	.081	3.219	-	0.07	23.3	-.038	3.230	-	0.01
6	33.9	20.2	0.49	.049	.011	.030	3.128	-	-	11.0	.010	3.193	-	0.63
7	24.1	12.3	1.21	.064	.017	.066	3.120	-	0.02	20.1	-.012	3.106	-	0.12
8	32.2	21.0	0.34	.030	.008	.000	3.047	-	-	8.9	.025	3.157	-	0.30
9	29.0	19.5	0.46	.033	.011	.003	3.074	-	-	12.1	.031	3.223	-	0.35
10	18.8	11.1	2.03	.064	.021	.092	3.213	-	-	30.8	-.052	3.394	-	-
11	21.3	13.1	1.17	.046	.016	.071	3.195	-	0.01	20.4	-.035	3.214	-	0.03
12	27.4	17.4	0.57	.036	.013	.020	3.145	-	0.34	13.3	.025	3.231	-	-
13	20.2	14.6	1.10	.038	.015	.025	3.232	-	-	21.8	-.033	3.314	-	0.18

FIG. 5.9 shows the pdf of the surface elevation measured at all probes, $p_\zeta(\zeta)$, for the conditions 1 and 10. These were the conditions where the pdf of $\dot{\zeta}$ had the smallest and largest skewness, respectively. The skewness of $\dot{\zeta}$ is used here in order to quantify the significance of the deviation of the statistics from the linear Fourier model. Therefore, these two conditions represented the smallest and the largest nonlinearity, respectively. By demonstrating that the weakly nonlinear model applies to these conditions, the applicability to all the intermediate conditions is also demonstrated. In FIG. 5.9, the measured pdf's were compared with the Gaussian distribution which is representative of a linear model of the free surface (equation (3.55)), and with the third-order correction proposed by Longuet-Higgins [1963] (equation (3.60)). The latter was calculated based on the cumulants determined by equations (3.58) from the measured statistical moments $m_{\zeta,q}$, and not based on the wavenumber spectra of the surface elevation as suggested by Longuet-Higgins [1963] since these could not be measured. The pdf proposed by Longuet-Higgins [1963] approximates the measurements in both conditions very well. The correction is negligible for condition 1 (FIG. 5.9a, c), which probability is essentially Gaussian. The distribution for condition 10 (FIG. 5.9b, d) shows a slight positive skewness of the distribution, with larger tails in the positive range of elevations. These are seen more clearly in FIG. 5.9d, in logarithmic co-ordinates.

A Kolmogorov-Smirnov test was performed on the measured pdf of ζ and of $\dot{\zeta}$ in order to test the null hypothesis that the distributions of the surface elevation and of its slope are represented by the Gaussian pdf (equation (3.55)) or by the weakly nonlinear pdf proposed by Longuet-Higgins [1963] (equation (3.60)). The p-values calculated in both cases are reported in table 5.1, as determined for the wave probe with the median skewness of $\dot{\zeta}$. The p-value is omitted when smaller than 0.01. The null hypothesis of a Gaussian pdf of ζ is rejected at 1% confidence level in all conditions. The hypothesis of a Gaussian pdf of $\dot{\zeta}$ cannot be rejected in conditions 2 and 4. In contrast, the null hypothesis represented by the weakly nonlinear distribution of equation (3.60) cannot be rejected in most flow conditions, although the confidence level is smaller than 5% in all conditions but 3, 4, 5, and 12 for p_ζ, and in conditions 5, 10, 11, and 12 for $p_{\dot{\zeta}}$. This suggests that the weakly nonlinear pdf approximates better the statistical distribution of the surface elevation in the tested range of flow conditions.

It should be noted that equation (3.60) was determined by Longuet-Higgins [1963] based on an expansion over the cumulants of the distribution. This expansion assumes that the higher statistical moments are of higher order with respect to the characteristic wave amplitude σ. According to Longuet-Higgins [1963], if the weak nonlinearity that produces the slight deviation from the Gaussian pdf in

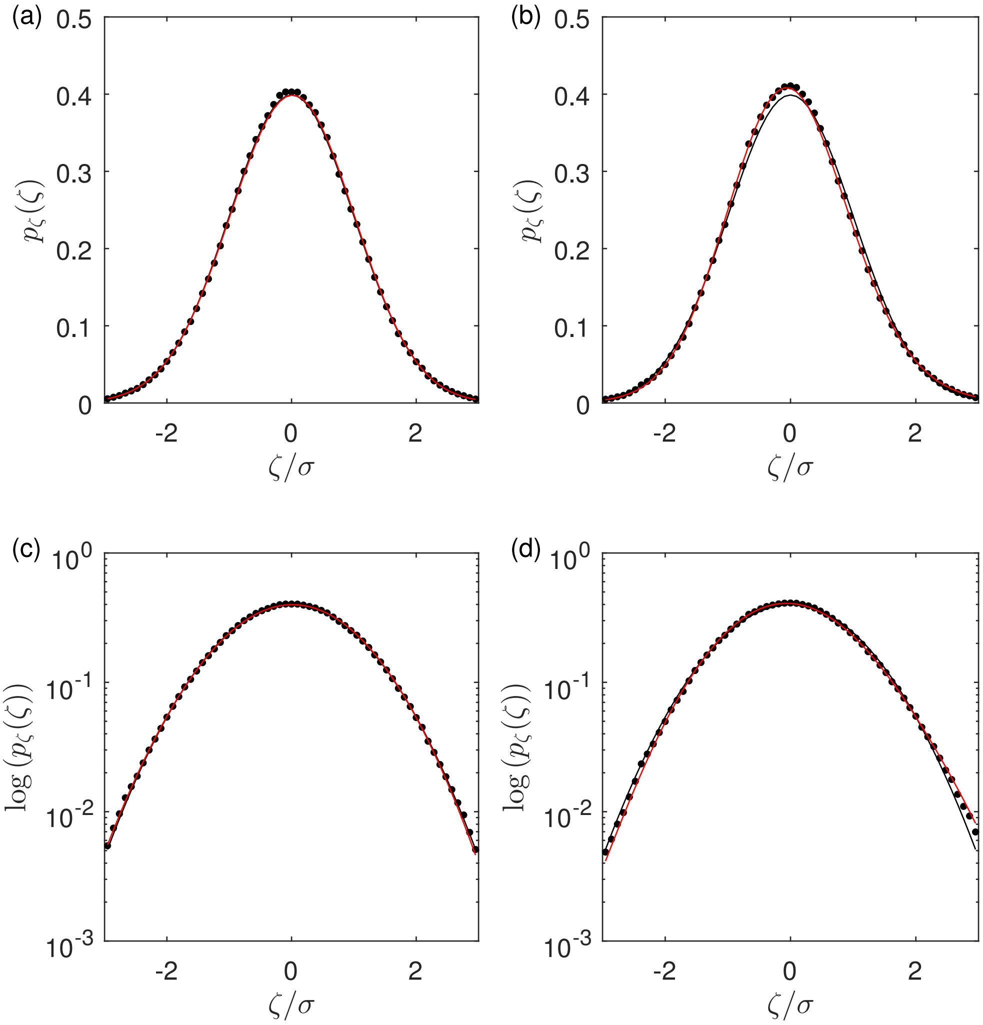

Figure 5.9: The pdf of ζ, $p_\zeta(\zeta)$, measured at all probes for (a, c) condition 1 and (b, d) condition 10. (black line) Gaussian distribution, equation (3.55), (red line) third-order correction proposed by Longuet-Higgins [1963], equation (3.60).

FIG. 5.9b, d, is not due to resonant interactions among waves, then the corrected coefficient of skewness $\lambda_4 - 3$ should be of order λ_3^2. Table 5.1 shows that $\lambda_4 - 3$ is at least of the same order of λ_3 in all conditions. This shows that the theory of Longuet-Higgins [1963] does not apply to the measured conditions, although equation (3.60) approximates very well the data. The larger value of the kurtosis can suggest the existence of interaction among the waves, according to Creamer et al. [1989], Janssen [2003, 2009]. Alternative explanations may relate to patterns on the surface generated by the interaction with turbulence. The skewness and the kurtosis of the elevation appear to be both very small in all conditions, and the statistics can be considered quasi-Gaussian in general.

The statistical significance of these observation was tested by comparing with the statistics of constrained surrogate time-series data, generated with the gradual wavelet reconstruction method suggested by Keylock [2006] and later improved by

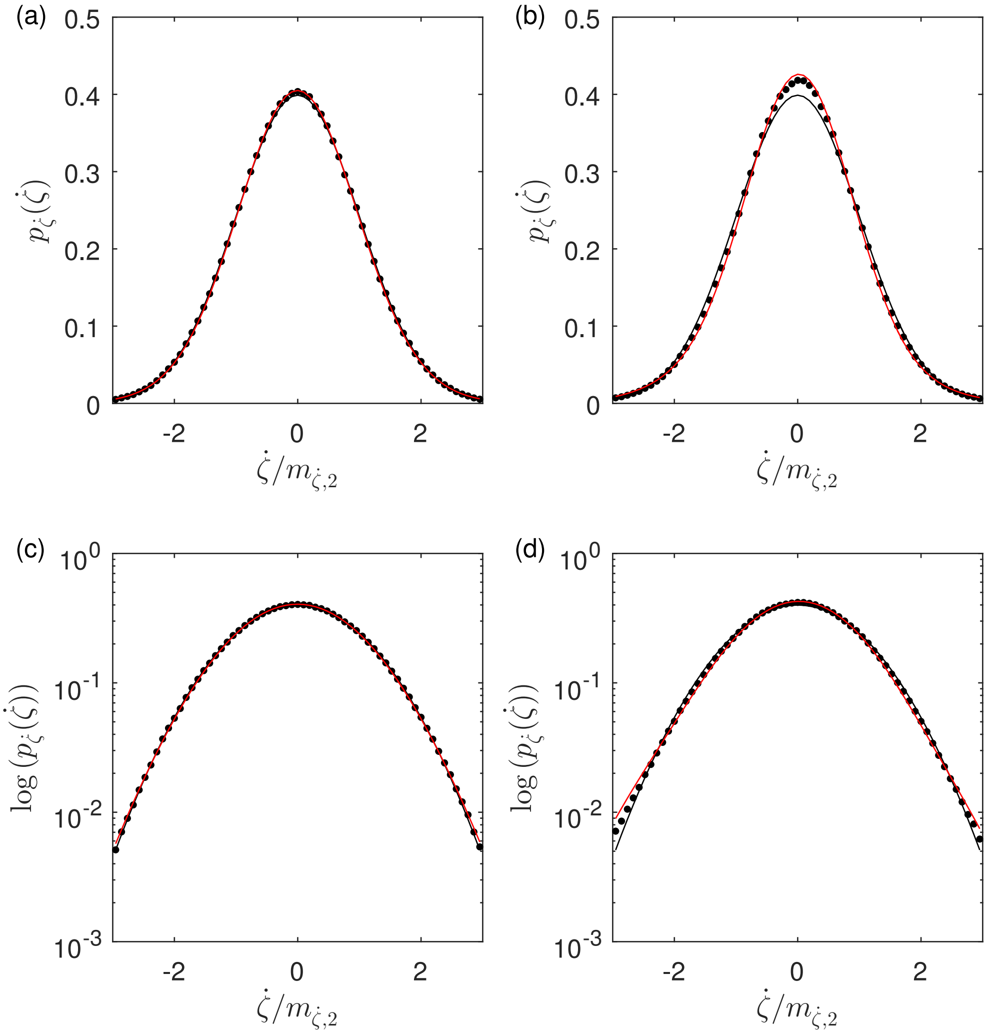

Figure 5.10: The pdf of $\dot{\zeta}$, $p_{\dot{\zeta}}(\dot{\zeta})$, measured at all probes for (a, c) condition 1 and (b, d) condition 10. (black line) Gaussian distribution, equation (3.55), with $\dot{\zeta}$ in place of ζ, (red line) third-order correction proposed by Longuet-Higgins [1963], equation (3.60).

Keylock [2007] and Keylock [2010]. The algorithm of the procedure was summarised in sub-section 3.1.7. The Gradual wavelet reconstruction method conserves the pdf of the surface elevation, therefore the comparison with the measured statistics cannot be performed in terms of the statistics of ζ. Following Keylock [2010], the statistics of the time-gradient of the elevation, $\dot{\zeta}$, were analysed instead. The probability density functions of $\dot{\zeta}$, $p_{\dot{\zeta}}(\dot{\zeta})$, are shown in FIG. 5.10 for the same flow conditions. The measured distributions were compared with the Gaussian distribution which was obtained from equation (3.55) by substituting ζ with $\dot{\zeta}$. $p_{\dot{\zeta}}(\dot{\zeta})$ is approximately Gaussian in condition 1, while in condition 10 both the central peak and the tails are larger than predicted by equation (3.55). This is the same behaviour which had been observed from the pdf of ζ, which demonstrates that the statistics of $\dot{\zeta}$ are a valid metric of the non-linearity. The average of the gradient $\dot{\zeta}$ was negligible in all conditions, and the largest absolute value of the skewness of $\dot{\zeta}$ was 0.052.

A set of 19 surrogates per each flow condition were generated, using the signal recorded by the probe which recorded the median skewness of $\dot{\zeta}$ as the reference time-series. FIG. 5.11 shows the skewness and the kurtosis of $\dot{\zeta}$ calculated from all realisations of the surrogates for conditions 1 and 10, represented against the similarity ratio, ϱ. This represents the constrained portion of the surrogate synthetic data. The statistics of the surrogates are compared in the same figure with the measurements across all wave probes in the same two conditions. As ϱ increased, the signal was more similar to the original data, and the moments converged to the measured value. The difference between the statistics of the surrogates and those of the wave probes data was considered to be significant when the measured moments deviated from the value of the first or third quartile by an amount larger than 1.5 times the inter-quartile range (corresponding to a 99.3 % confidence threshold for a Gaussian distribution).

Based on the results shown in FIG. 5.11a, c, the deviation of the third and fourth moment of $\dot{\zeta}$ with respect to the values expected from a Gaussian distributed random variable is not significant in condition 1 when $\varrho = 0$. This proves that the nonlinearities were negligible in condition 1. In condition 10 at least 60 % of the energy of the signal had to be constrained in order for the surrogates to show similar statistics, which signifies that the original time-series was less linear. Such a relatively large value of ϱ does not mean that the statistics of the surface were largely nonlinear in condition 10, but rather it suggests that the nonlinearity of the surface gradient was related to scales which are not the dominant ones. In fact, the statistical distributions in condition 10 were approximated well by the weakly nonlinear models derived by Longuet-Higgins [1963] and by Bitner [1980] for the statistics of ζ and of Z, respectively. The statistics of the surface elevation were weakly nonlinear in condition 10.

The same analysis applied to all flow conditions showed that in all conditions except condition 10, the value of the skewness of $\dot{\zeta}$ was not significantly different from that expected for a linear process with Gaussian distribution. This confirms that the deviation from the linear model was larger in condition 10 than in the remaining conditions. Across all flow conditions, condition 3, 6, 8, and 12 showed a statistically significant deviation in terms of the kurtosis of $\dot{\zeta}$ (the deviation became not significant in conditions 3, 6, and 12 when $\varrho = 0.2$, in conditions 8 when $\varrho = 0.4$) but not of its skewness. No significant deviation in terms of either the skewness of the kurtosis of $\dot{\zeta}$ was observed in the remaining conditions 1, 2, 4, 5, 7, 9, 11, and

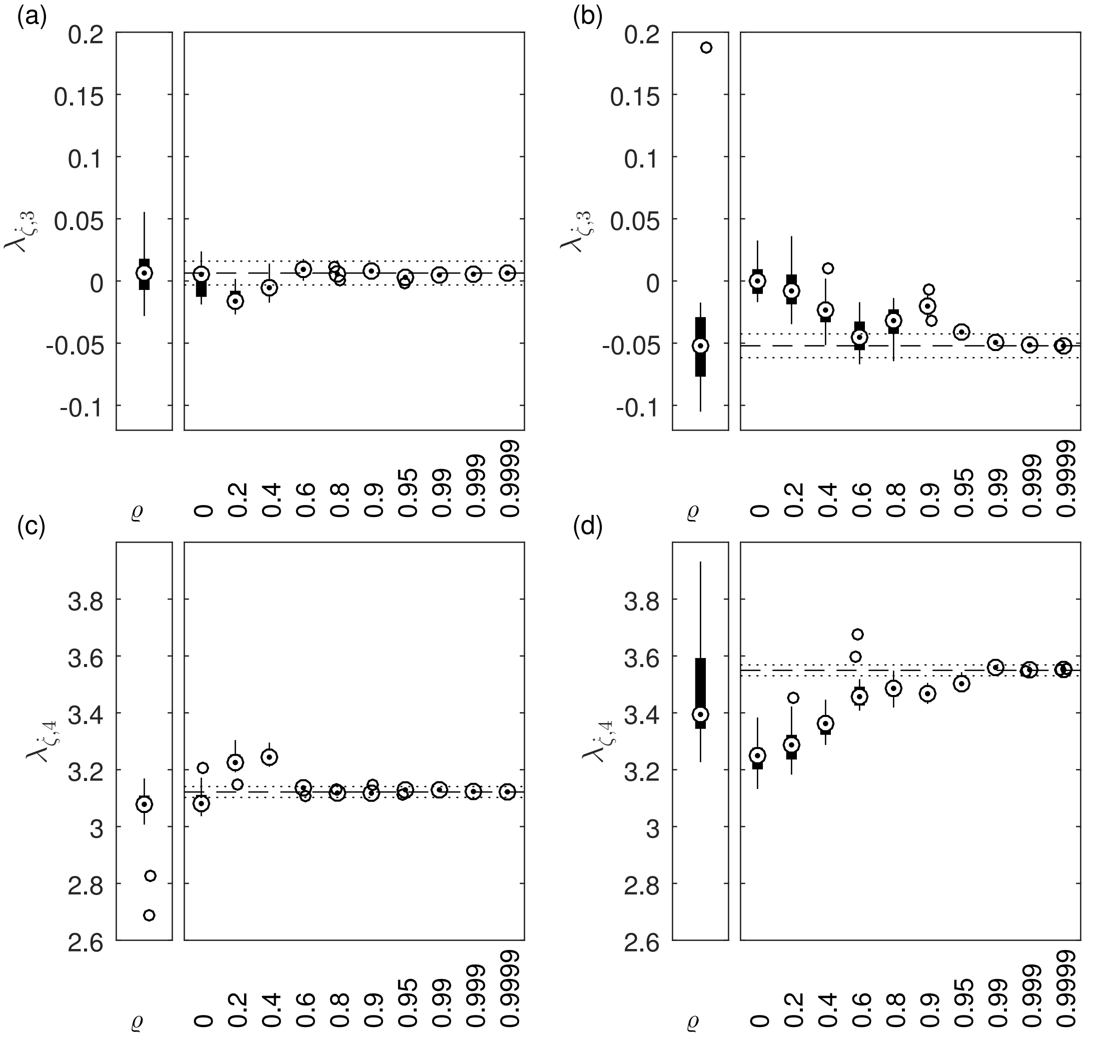

Figure 5.11: The (a, b) skewness and (c, d) kurtosis of the surface gradient $\dot{\zeta}$, calculated for the 19 surrogates of the measurements for condition 1 (a, c), and condition 10 (b, d), plotted against the parameter ϱ. The separate plot on the left shows the same quantities calculated with all the wave probes. (dashed) The skewness and kurtosis of $\dot{\zeta}$ measured with probe 5. (dotted) The skewness and kurtosis ± twice the respective standard error. Probe 5 had the median value of the skewness of $\dot{\zeta}$ across all probes, and the measurement with this probe was the reference for all surrogates in both conditions.

13. In these conditions, the linear model of the surface elevation is expected to be more representative.

5.2.3 Envelope statistics

Previous studies of the interaction between turbulence and the free surface [Tsai, 1998, Dabiri and Gharib, 2001, Dabiri, 2003, Savelsberg and van de Water, 2009] attempted to find a direct correlation between the turbulence quantities (most often the vorticity, or a function of it) and the shape of the free surface. These attempts were based on the assumption that the largest deformation of the free surface occurs above a coherent turbulent structure, which represents a local forcing. Savelsberg and van de Water [2009] suggested that freely propagating gravity-capillary waves can reduce the local correlation by travelling a long distance away from the region where they have been generated. These authors still postulate that the maxima of the amplitude of the surface fluctuations are localised above the turbulent structure that generated them, while gravity-capillary waves radiate away from it. In this subsection, the statistics of the amplitude of the surface fluctuations (the envelope) are investigated.

Figure 5.12 shows example of the envelope $Z_{\nu,\mu}$ computed for conditions 1, 4, 7, and 10, with equation (5.10) applied to the measurements with probe $1_{(x)}$. The surface elevation ζ is also shown for reference. The behaviour of the envelope is highly irregular, and shows peaks with the amplitude larger than four times the surface standard deviation (see FIG. 5.12c, at $tk_0U_0/2\pi \approx 10\,\mathrm{s}$). The envelope had a high-frequency modulation which made it less smooth in conditions 7, and 10 (FIG. 5.12c, d), and a low-frequency large modulation which sometimes reduced its amplitude almost to 0 apparently without a clear periodicity. Both these effects are due to the broadness of the frequency spectrum [Longuet-Higgins, 1984].

FIG. 5.13 shows the pdf of the envelope Z_μ and of the phase Φ_μ calculated for all wave probes for conditions 1 and 10 from equations (5.10) and (5.11). These conditions had the smallest and the largest nonlinearity, as discussed in the previous subsection. The pdf of Z_μ, $p_Z(Z)$ were compared with the Rayleigh statistical distribution which is expected for a Gaussian linear process [Longuet-Higgins, 1957] (equation (3.66)), and with the weakly nonlinear distribution obtained by Bitner [1980] (equation (3.63)). The pdf of Z_μ follows very closely equation (3.66) in condition 1. In condition 10, $p_Z(Z)$ shows a slight deviation from the Rayleigh distribution, whereas it is represented well by the weakly nonlinear distribution (equation(3.63)). The good fit with the linear and weakly nonlinear models suggests that the amplitude of the surface fluctuations is represented well by a linear superposition of random waves, and that coherent patterns are negligible. The distributions of the phase, $p_\Phi(\Phi)$ are essentially uniform in both conditions, although a slight deviation can be observed in FIG. 5.13d for condition 10 where the probability of $\Phi = \pi/2$ is slightly larger than that of $\Phi = 0$.

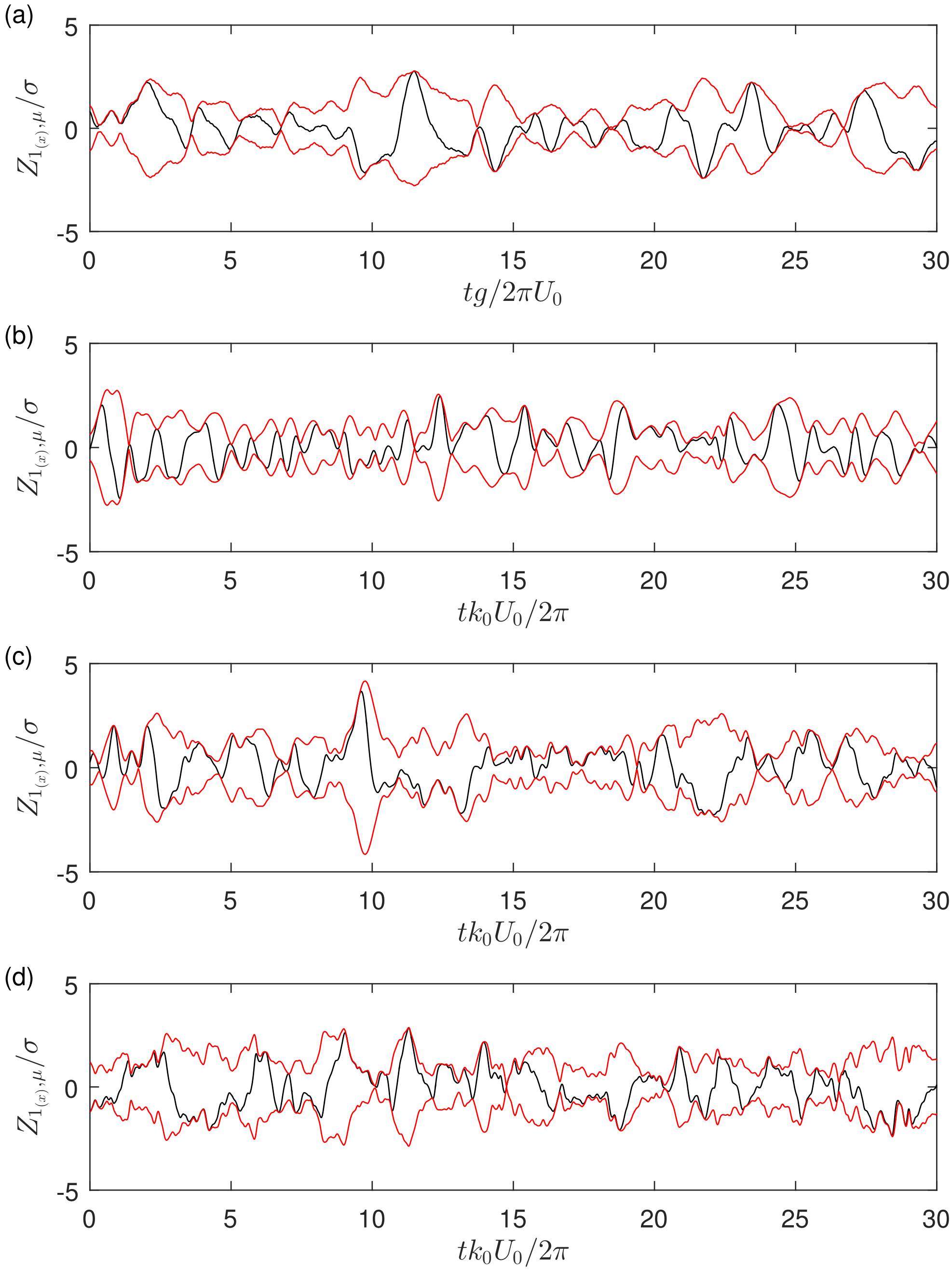

Figure 5.12: Examples of the wave envelope $Z_{\nu,\mu}$ calculated with equation (5.10) from the measurements with wave probe $\nu = 1_{(x)}$ for (a) condition 1, (b) condition 4, (c) condition 7, and (d) condition 10. (black) The original signal, $\zeta_{1_{(x)},\mu}$, (red) $Z_{1_{(x)},\mu}$. Both $Z_{1_{(x)},\mu}$ and $-Z_{1_{(x)},\mu}$ are shown.

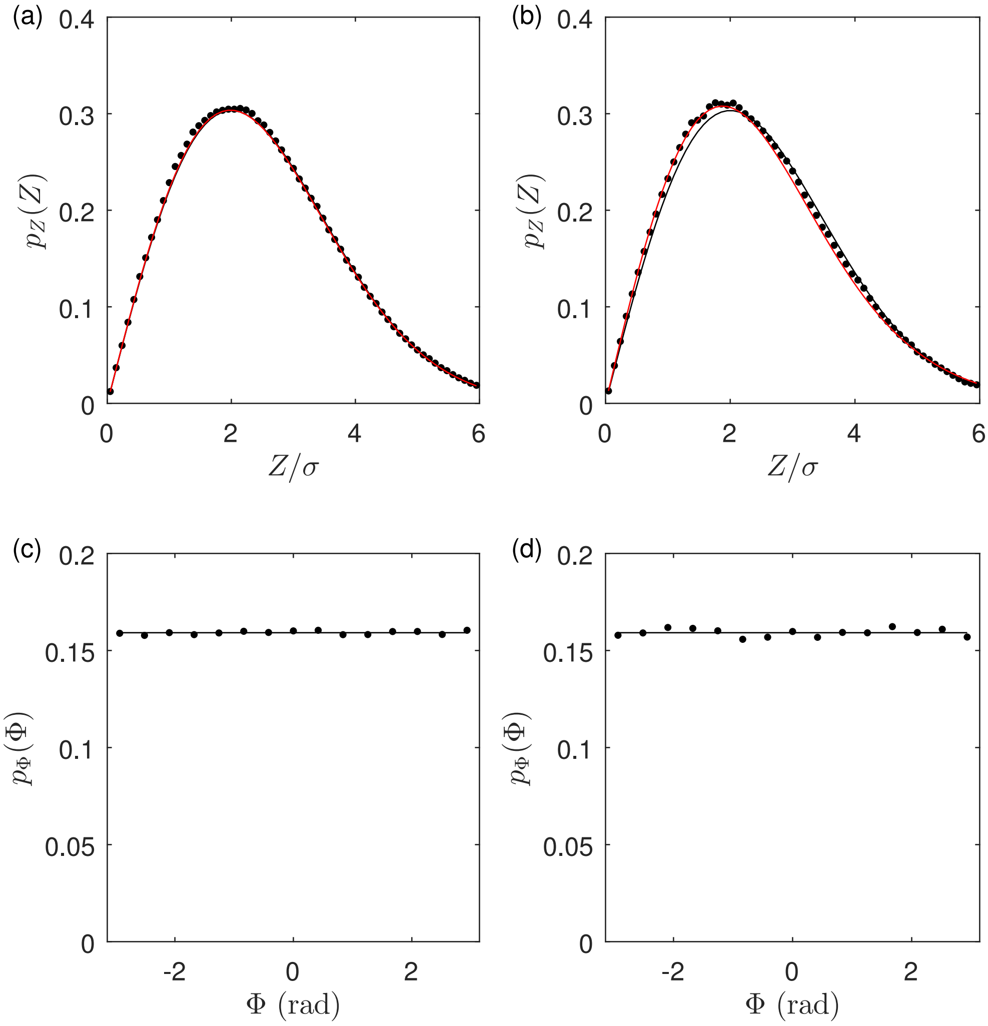

Figure 5.13: The pdf's (a, b) $p_Z(Z)$ and (c, d) $p_\Phi(\Phi)$ of the surface envelope and phase, respectively, measured across all wave probes. (a, c) Condition 1, and (c, d) condition 10. (black line) Rayleigh distribution [Longuet-Higgins, 1957], equation (3.66). (red line) The weakly nonlinear distribution suggested by Bitner [1980], equation (3.63).

5.2.4 Discussion

The results in this section have shown the frequency spectra and the pdf's of the surface elevation ζ, of its time-gradient $\dot{\zeta}$, and of the envelope and phase, Z and Φ, respectively. The average frequency spectra $S(\omega)$ presented in FIG. 5.7 scaled consistently with the parameter k_0U_0, which represents the characteristic frequency of the stationary waves with the wavenumber k_0 when they propagate in still water. This scaling was confirmed by the empirical relation between the spectral moment s_1 and the parameter k_0U_0, equation 5.40. The variance of the free surface elevation (which corresponds to the zero-th order moment s_0 of the power spectral density $\sigma^2S(\omega)$) was also found scaling with k_0U_0. The frequency spectra decayed less rapidly at the larger frequencies when $k_0 H/\pi < 1$ and the Froude number was larger. This indicated that more energy was found in the relatively shorter and faster waves when the Froude number increased, in agreement with the progressive shift of the spatial correlation function. Smolentsev and Miraghaie [2005] also observed the increase of the frequency spectrum at the higher frequencies when the Froude number was increased, and related this effect to the interaction with turbulence. The decrease of the slope of the spectrum means the increase of the first and second order spatial gradients of the free surface elevation, hence it is associated with a rougher surface. This shows that the increase of the Froude number causes the surface to be more rough. These results suggest the existence of a direct link between the statistics of the free surface measured at one location, and the hydraulic quantities of the flow (namely the mean surface velocity U_0 and the wavenumber of the stationary waves k_0, which is controlled by the mean depth H, the mean surface velocity, and the exponent of the velocity profile n, according to equation (3.44)). This was one of the objectives of the discussion in this section.

The results of the statistical analysis which were summarised in Table 5.1 have shown that a linear model with the random distribution of the phase would be representative of the statistics of the free surface in most of the flow conditions which have been investigated here. The significance of the deviations from the statistical distributions which would be expected based on such model has been quantified based on the analysis of a set of constrained surrogates, obtained with the gradual wavelet reconstruction method [Keylock, 2006, 2007, 2010]. The unconstrained surrogates obtained with $\varrho = 0$ in condition 1 (FIG. 5.11a, c) and in conditions 2, 4, 5, 7, 9, 11, and 13 have similar statistics to the original data, so that a random phase linear model of the free surface elevation is expected to represent well the statistics of the real surface. In all conditions, the average of $\dot{\zeta}$ was found very small, and the deviation of the skewness of $\dot{\zeta}$ was not significant (see Table 5.1).

Other flow conditions, e.g., condition 10, showed a significant degree of nonlinearity of the free surface statistics. The degree of nonlinearity apparently related to the parameters $k_0\sigma$ and σ/H, as shown in FIG. 5.8 and in Table 5.1. This is predicted by the derivation of the linearised surface equations reported in subsection 3.1.2. The statistical distribution of ζ in condition 10 (FIG. 5.9b, d) was slightly positively skewed, and had larger tails towards the positive elevation. This suggests the presence of sharper crests and more shallow troughs. It was noted that although the weakly nonlinear pdf proposed by Longuet-Higgins [1963] approximates the measurement very well, the fact that the kurtosis of the surface elevation was of the same order of magnitude of the skewness is in contrast with the model proposed by this author. This could be explained by the existence of some interaction among waves at the third order [Creamer et al., 1989, Janssen, 2003, 2009]. Both moments of $\dot{\zeta}$ in FIG. 5.11b, d, have suggested a statistically significant (although weak) nonlinearity of the free surface in condition 10 and less strongly in conditions 3, 6, 8, 10, and 12. These weak nonlinearities may have visible effects on the statistics of the scattered acoustic field, as it is shown in chapter 6.

Some additional conclusion can be drawn from the presented results, about the dynamics of the free surface in shallow flows, and their generation mechanism. The results presented here have shown that the statistics of the free surface are essentially those typical of a composite process, where the fluctuations are generated by a large number of independent events. The large localised peaks of the wave amplitude which could be observed in some of the measurements (for example in FIG. 5.12c for condition 7, near $tk_0U_0/2\pi = 10$, where $Z_\mu > 4\sigma$) can be explained by an essentially linear combination of independent random processes. This was demonstrated by the good fit between the measured statistics of the envelope and the two linear and weakly nonlinear models. These observations suggest that the forcing mechanism which produces the free surface fluctuations is predominantly random, and that coherent events such as turbulent bursts are likely to play a relatively marginal role. As a result, the local correlation between the surface elevation and the turbulent coherent structures is expected to be small, which is confirmed by the numerical and experimental studies by other authors [Tsai, 1998, Savelsberg and van de Water, 2009, Fujita et al., 2011]. The validity of these observations may be limited to shallow flows, where the small depth and the short time-scales of the flow limit the growth of coherent structures of sufficient energy to deform the free surface. It is suggested that the interaction with these structures may become stronger in deeper and/or slower flows.

5.3 Space-time statistics

The results described so far show the complexity of the temporal evolution of the free surface when measured at a single point. Because gravity waves are dispersive, it is impossible to determine the corresponding spatial statistics of the free surface of a turbulent flow from the analysis of time-series data alone [Savelsberg and van de Water, 2009]. The aim of this section was to investigate the spatial characteristics of the free-surface. This was done in terms of the spatial correlation function and the frequency-wavenumber spectra of the surface elevation ζ in two orthogonal spatial dimensions. The same type of analysis was also applied to the envelope Z of the band-passed free surface elevation, and the results are reported in sub-section 5.3.3. The first objective was to verify the presence of dispersive and non-dispersive waves on the free surface, and to compare their dispersion relation with the relations proposed in section 3.1.2. These two types of waves have been related to different processes which are able to generate the free surface fluctuations, namely the interaction with turbulence and the interaction with the rough static bed or with the sheared flow based on an inviscid model. The second objective was to identify the characteristic spatial as well as temporal scales of the free surface, and possibly to establish a direct link between these and the hydraulic quantities of the flow. These two objectives would improve the understanding of the processes which are responsible for the generation of waves on the free surface of shallow turbulent flow. A third objective was to observe the change of the dispersion relation due to the streamwise velocity profile according to the analysis in subsection 3.1.2, which would allow the characterisation of such profile remotely from the measurement of the dynamic surface. The results in this subsection will inform the application of the wavelet spectral method, which results are shown in the next section 5.4. The analysis also provides additional insight into the morphology of the free surface in the two spatial dimensions and in time.

5.3.1 Spatial correlation function

Firstly, the spatial characterisation of the free surface was obtained in terms of the space-time correlation function of the free surface elevation, and specifically in terms of the spatial correlations at zero time-lag, $W_x(r_{n,x}, 0)$ and $W_y(r_{n,x}, 0)$. These functions represent the instantaneous correlation measured along the streamwise and the transverse direction, respectively. The average across all realisations of the correlation at zero time-lag are shown in FIG. 5.14 for each flow condition. The spatial separations $r_{n,x}$ and $r_{n,y}$ were the non-equidistant, non-binned separations between the probes along the streamwise array and the first transverse array, respectively. In conditions 2 to 13, the spatial separations were non-dimensionalised based on the quantity $2\pi/k_0$, which corresponds to the wavelength of the stationary waves based on equation (3.44). In condition 1 equation (3.44) has no solutions, therefore the separations were non-dimensionalised based on $2\pi U_0^2/g$, which is the wavelength of the stationary waves determined for an infinitely deep flow if the surface tension is negligibly small. The various flow conditions have been grouped based on the parameter k_0H/π. FIG. 5.14a shows the results for condition 1, FIG. 5.14b shows the results for the conditions with the smaller Froude number (conditions 2 to 5), FIG. 5.14c for the conditions with the intermediate Froude number (conditions 6 to 9), and FIG. 5.14d for the conditions with the larger Froude number (conditions 10 to 13).

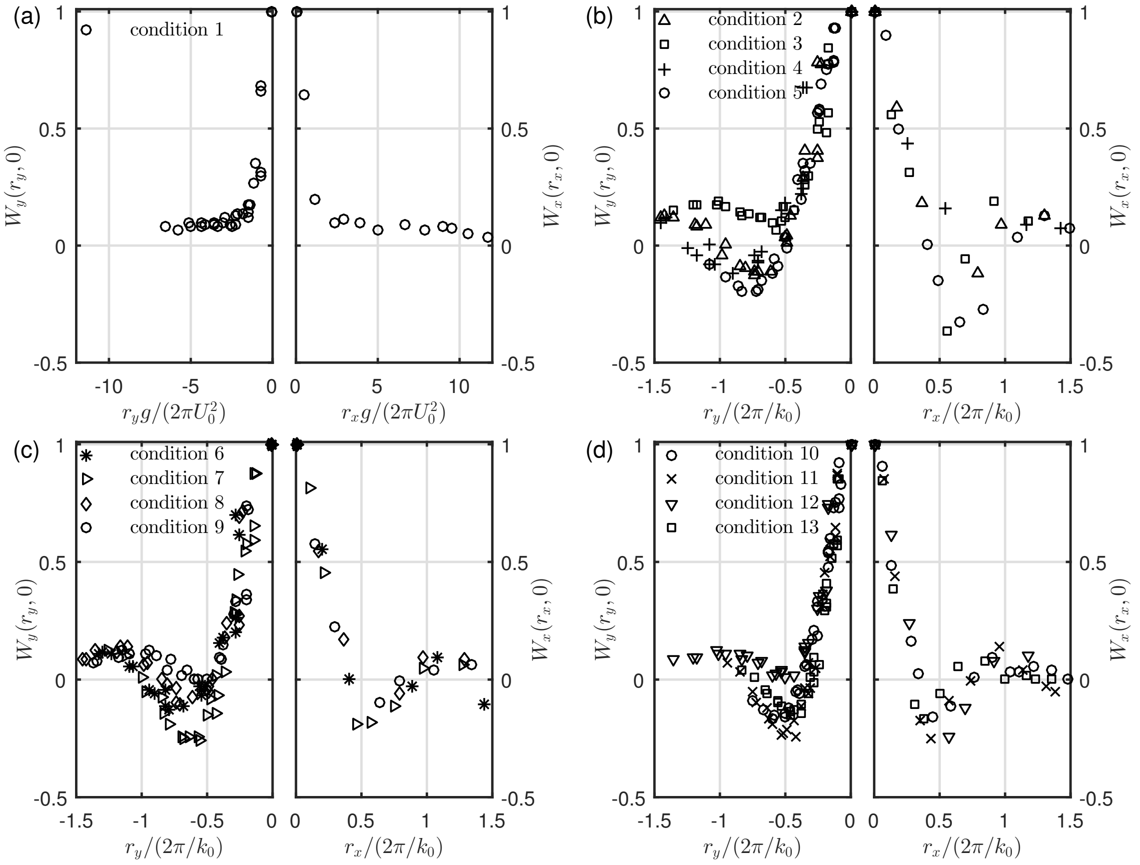

Figure 5.14: The normalised spatial correlation at zero time lag, with normalised spatial separation, $rk_0/2\pi$. The negative x-axis shows the lateral correlation, $W_y(r_{n,y},0)$, while the positive x-axis shows the streamwise correlation, $W_x(r_{n,x},0)$. (a) Condition 1, (b) conditions 2 to 5 ($F < 0.5$), (c) conditions 6 to 9 ($0.52 \leq F \leq 0.61$), (d) conditions 10 to 13 ($0.61 \leq F \leq 0.68$). Note the different scaling in (a), where k_0 cannot be defined.

The correlation function for the condition 1 in FIG. 5.14a decays monotonously and symmetrically from $r_n = 0$ in both directions. $W_x(r_{n,x},0)$ and $W_y(r_{n,x},0)$ decays rapidly below 0.15 at $r_n g/(2\pi U_0^2) = 1.5$, which corresponds to $r_n = 35\,\text{mm}$. This shows that the patterns on the free surface were isotropic and had the horizontal scales comparable with the depth of the flow, $H = 42.2\,\text{mm}$. The correlation function remains approximately equal to 0.1 between $r_n g/(2\pi U_0^2) = 2$ and $r_n g/(2\pi U_0^2) = 10$ ($r_n = 231\,\text{mm}$, only observable in the streamwise direction), then it decays rapidly to zero.

The remaining flow conditions shown in FIG. 5.14b, c, d display the fluctuation of $W_x(r_{n,x},0)$ and $W_y(r_{n,y},0)$ with a minimum between $r_n/(2\pi/k_0) = 0.5$ and $r_n/(2\pi/k_0) = 0.8$ and a relative maximum between $r_n/(2\pi/k_0) = 1$ and $r_n/(2\pi/k_0) = 1.6$. The smaller values are found for the higher Froude number conditions of FIG. 5.14d, and the larger for the lower Froude number conditions of FIG. 5.14b. The fluctuations are not observed for the streamwise correlation $W_x(r_{n,x},0)$ in the condition 4 (FIG. 5.14b), and the minimum of the transverse correlation $W_{n,y}(r_y, 0)$ is positive in the conditions 3 (FIG. 5.14b), 9 (FIG. 5.14c) and 12 (FIG. 5.14d). The spatial correlations are slightly asymmetric, and the larger negative minimum is found for the streamwise correlation $W_x(r_{n,x}, 0)$. The decay rate of the correlation in the region $r_n/(2\pi/k_0) \leq 0.5$ is similar in both directions, and more rapid at the higher Froude numbers. In the lower and intermediate Froude number conditions where $k_0H/\pi > 1$ (FIG. 5.14b, c) the correlation function is equal to 0.5 at $r_n/(2\pi/k_0) \approx 0.2$. In the higher Froude number conditions where $k_0H/\pi < 1$ (FIG. 5.14d) the value of 0.5 is attained at $r_n/(2\pi/k_0) \approx 0.15$.

5.3.2 Frequency-wavenumber spectra

FIG. 5.15a-b show the contours for the logarithm of the dimensional frequency-wavenumber spectra $\log_{10} \sigma^2 S_x(k_x, \omega)$ and $\log_{10} \sigma^2 S_y(k_y, \omega)$ measured along the x- and y-directions, respectively, for the flow condition 13. Four contours are plotted in 5.15a-b for each order of magnitude. In order to improve the visualization at the higher frequencies, FIG. 5.15c-d also show the colormaps for the corresponding normalized frequency-wavenumber spectra $\bar{S}_x(\hat{k}_x, \hat{\omega})$ and $\bar{S}_y(\hat{k}_y, \hat{\omega})$, found from equation (5.23). The colours in FIG. 5.15c-d are a linear scale. The wavenumber and frequency axes in FIG. 5.15c-d have been non-dimensionalised based on the quantities k_0 and k_0U_0, respectively, where $\hat{\omega} = \omega/k_0U_0$ and $\hat{k} = k/k_0$. The negative $\hat{k}_x$ represents the solution where $c < 0$, i.e., the waves that travel upstream in the laboratory frame of reference. The dimensional spectra show some clear ridges the width of which is constant and comparable to the spectral resolution Δk_x and Δk_y in FIG. 5.15a and 5.15b, respectively. Away from the ridges the spectra show a noise floor which is almost constant at the same frequency, and it was a consequence of measuring with a non-equidistant array of sensors. The amplitude of the ridges is between 2 and 7 times the noise amplitude at each frequency. After normalisation, the noise floor appears constant across the whole spectrum, with the level ≈ 1 in FIG. 5.15c-d. The maximum of the dimensional frequency-wavenumber spectra in FIG. 5.15a is found near $\omega = 0$ and $k_x = \pm 40\,\mathrm{rad\,m^{-1}}$, which compares well with the wavenumber of the stationary waves, $k_0 = 34.8\,\mathrm{rad\,m^{-1}}$.

In the region where $\hat{\omega} \geq 2$, the streamwise spectrum $S_x(\hat{k}_x, \hat{\omega})$ in FIG. 5.15c shows a ridge which extends from $\hat{k}_x \approx 1$ to $\hat{k}_x \approx 3$. This ridge is approximated well by the two dispersion relations of equation 3.26 and equation (3.20), assuming $\theta = 0$ and therefore $k_y = 0$. Where $\hat{\omega} \geq 2$, the transverse spectrum $S_y(\hat{k}_y, \hat{\omega})$ in FIG. 5.15d has a ridge with $\hat{k}_y \approx 0$. Both relations indicate the presence of gravity-capillary waves which propagated in the positive x-direction, but only parallel to the flow

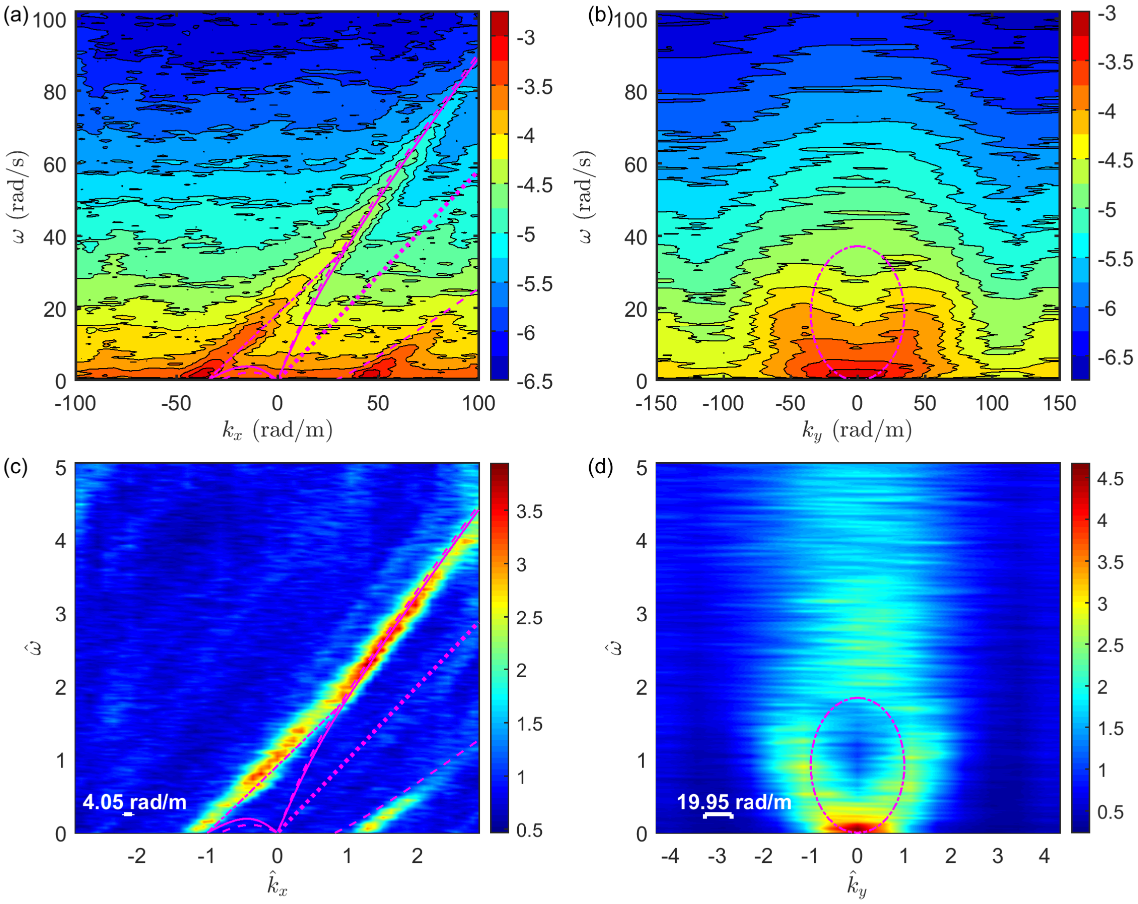

Figure 5.15: (a) Contour plot of the dimensional frequency-wavenumber spectrum for condition 13, $\log_{10}(\sigma^2 S_x(k_x,\omega))$, (b) Transverse spectrum $\log_{10}(\sigma^2 S_y(k_y,\omega))$. (c) The normalised frequency-wavenumber spectrum, $\bar{S}_x(\hat{k}_x,\hat{\omega})$, (d) normalised transverse frequency wavenumber-spectrum $\bar{S}_y(\hat{k}_y,\hat{\omega})$. (dashed) Irrotational dispersion relation, equation (3.20). (solid) Dispersion relation with the 1/3 velocity profile, $\theta = 0$, equation (3.26). (dotted) Non-dispersive relation, equation (3.21). (dashed-dotted) Dispersion relation with the 1/3 velocity profile, with constant $k = k_0$, equation (3.45).

velocity (i.e., $\theta = 0$ and $k = |k_x|$). The maxima along the ridge in FIG. 5.15c were identified with the Gaussian fitting procedure described in sub-section 5.1.4 [Herbert et al., 2010]. The results of the fitting procedure for condition 13 are shown in FIG. 5.2b, compared to the dispersion relations of equations (3.20) and (3.26). The root mean squared average difference between the maxima and the proposed relations is $\varepsilon_k = 2.8$ rad/m based on the irrotational relation (equation (3.20)), and $\varepsilon_k = 3.7$ rad/m based on the 1/3 velocity profile (equation (3.26)).

The region of the spectrum in FIG. 5.15c for which $-1 < \hat{k}_x < 1$ is characterized by a ridge that closely follows a straight line connecting the point $\hat{k}_x = -1$, $\hat{\omega} = 0$ with the point $\hat{k}_x = 1$, $\hat{\omega} = 2$, and crossing the ordinate axis at $\hat{\omega} = 1$. This ridge is approximated well by equation (3.45), which represents a radial pattern of waves with the constant modulus of the wavenumber, $|k| = k_0$, where k_0 was found from equation (3.44). The intersection of the spectral ridge with the axis $\hat{\omega} = 0$ in FIG. 5.15c occurs at $k_x \approx -40\,\mathrm{rad\,m^{-1}}$ ($\hat{k}_x \approx -1.15$), which is close to $k_0 = 34.8\,\mathrm{rad\,m^{-1}}$. The root mean squared average difference between the spectral ridge in FIG. 5.15c and equation (3.45) is $\varepsilon_k = 5.7\,\mathrm{rad\,m^{-1}}$ in the frequency interval $0 \leq \hat{\omega} \leq 2$. Equation (3.45) corresponds approximately to an ellipse in FIG. 5.15d. This approximates well the curved ridges of the transverse spectrum $S_y(\hat{k}_y, \hat{\omega})$ in the region $-1 \leq \hat{k}_x \leq 1$ and $0 \leq \hat{\omega} \leq 2$ in this figure.

The proposed dispersion relations slightly underestimate the frequency of the measured spectrum in the region $-1 < \hat{k}_x < 1$ of FIG. 5.15c, and overestimate it in the region $\hat{k}_x > 2$. These shifts are comparable to the resolution of the spectrum, and they were caused by the uncertainty of the velocity measurements. ε_k changes from $\varepsilon_k = 5.7\,\mathrm{rad\,m^{-1}}$ to $\varepsilon_k = 4.5\,\mathrm{rad\,m^{-1}}$ where $\hat{\omega} < 2$ and from $\varepsilon_k = 3.7\,\mathrm{rad\,m^{-1}}$ to $\varepsilon_k = 3.2\,\mathrm{rad\,m^{-1}}$ where $\hat{\omega} > 2$, respectively, if the mean surface velocity is reduced from $0.58\,\mathrm{m\,s^{-1}}$ to $0.56\,\mathrm{m\,s^{-1}}$, which was within the measurement uncertainty. The estimated spectral resolution was $4.05\,\mathrm{rad\,m^{-1}}$.

The part of the frequency-wavenumber spectrum in FIG. 5.15c for which $\hat{k}_x > 1$ shows an additional ridge at the frequencies $\hat{\omega} < 2$. This ridge extends from $\hat{k}_x \approx 1$ and $\hat{\omega} = 0$ to $\hat{k}_x \approx 2.5$, where $\hat{\omega} \approx 1$. The first point corresponds to the condition of stationary waves. The ridge represents the irrotational relation of equation (3.20), this time assuming that the waves propagate in the direction opposite to that of the flow, i.e., $\theta = \pi$. This relation overestimates slightly the frequencies of the ridge, which is expected since the streamwise velocity profile is not taken into account in equation (3.20). The slow waves in the region $\hat{k}_x \geq 1$ and $0 \leq \hat{\omega} \leq 1$ of FIG. 5.15c were gravity-capillary waves which propagated against the flow with the phase velocity in still water (equation 3.22) slower than U_0, so that they were advected downstream with $0 < c < U_0$. In this way they differed from the radial waves described earlier which phase velocity could be negative, even though both types of waves occupied the same range of frequencies. In FIG. 5.15d, only one type of waves (with the two curved ridges that follow the dashed-dotted lines) is clearly recognisable in the same frequency range. From the observation of the two separate spectra $S_x(\hat{k}_x, \hat{\omega})$ and $S_y(\hat{k}_y, \hat{\omega})$ in FIG. 5.15c, and d, it was not possible to say whether or not these ridges should also be attributed to the waves with $0 < c < U_0$. The slowly propagating two-dimensional waves have been observed in flow condition 3 and in the higher Froude number conditions 10 to 13, but they were not clearly recognisable in the remaining intermediate conditions. It is likely that this was caused by the limited spatial resolution of the adopted array of wave probes. Because of these limitations, and because the dispersion relation with the 1/3 velocity profile

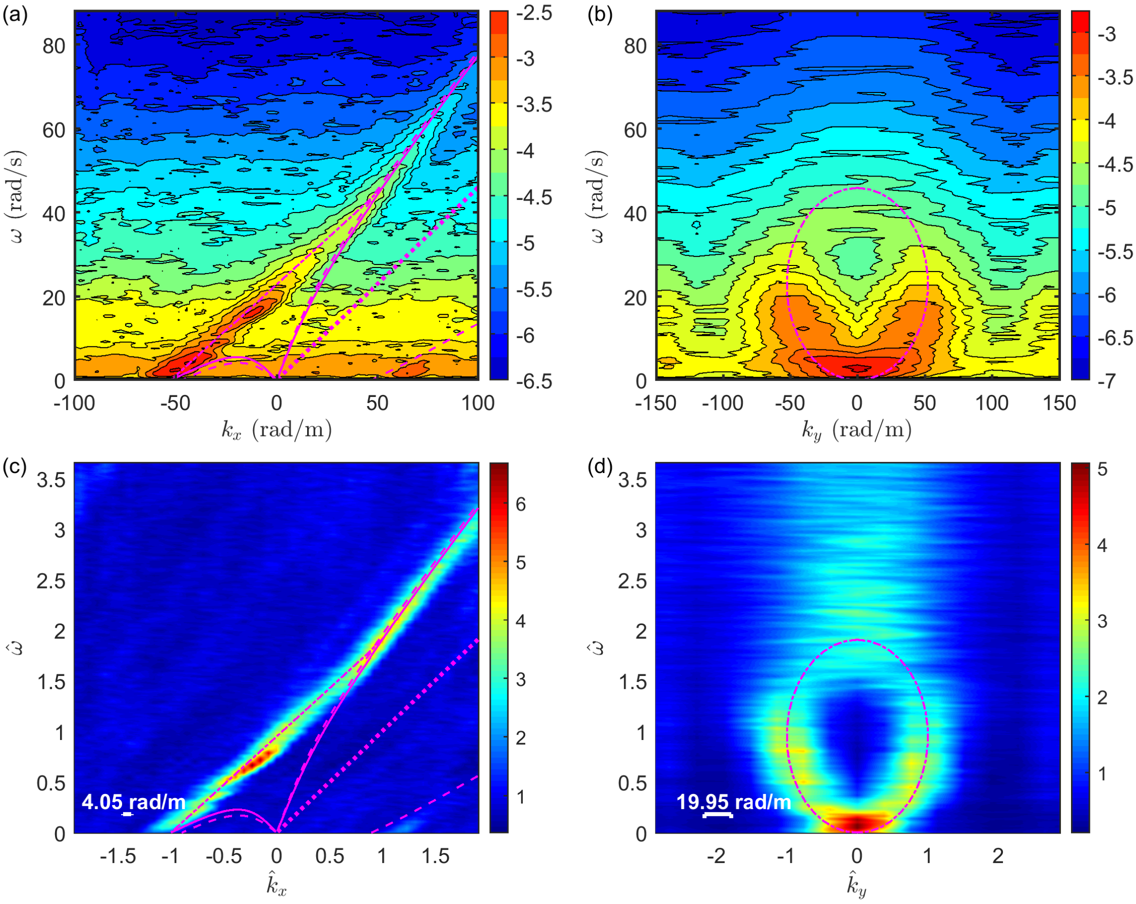

Figure 5.16: (a) Contour plot of the dimensional frequency-wavenumber spectrum for condition 7, $\log_{10}(\sigma^2 S_x(k_x,\omega))$, (b) Transverse spectrum $\log_{10}(\sigma^2 S_y(k_y,\omega))$. (c) The normalised frequency-wavenumber spectrum, $\bar{S}_x(\hat{k}_x,\hat{\omega})$, (d) normalised transverse frequency wavenumber-spectrum $\bar{S}_y(\hat{k}_y,\hat{\omega})$. (dashed) Irrotational dispersion relation, equation (3.20). (solid) Dispersion relation with the 1/3 velocity profile, $\theta = 0$, equation (3.26). (dotted) Non-dispersive relation, equation (3.21). (dashed-dotted) Dispersion relation with the 1/3 velocity profile, with constant $k = k_0$, equation (3.45).

was not determined for these waves, the Gaussian fitting was not applied in this region of the spectrum.

The data for the intermediate Froude number flow conditions show a similar behaviour to the case which was described in the previous paragraphs. FIG. 5.16a-b show the dimensional frequency wavenumber spectra for the flow condition 7. FIG. 5.16c-d show the corresponding normalised spectra. The spectra in FIG. 5.16 show the same ridges as in FIG. 5.15. The slow upstream waves advected downstream with the positive wavenumber and low frequency are less clear from the streamwise spectrum in FIG. 5.16c than those visible in FIG. 5.15c, which was attributed to the limited spatial resolution of the measurements. The maximum of the spectrum of FIG. 5.16a is at the frequency $\omega \approx 0$ and the wavenumber $k_x = \pm 60\,\mathrm{rad\,m^{-1}}$, which compares well with the wavenumber of the stationary waves, $k_0 = 52.4\,\mathrm{rad\,m^{-1}}$. The

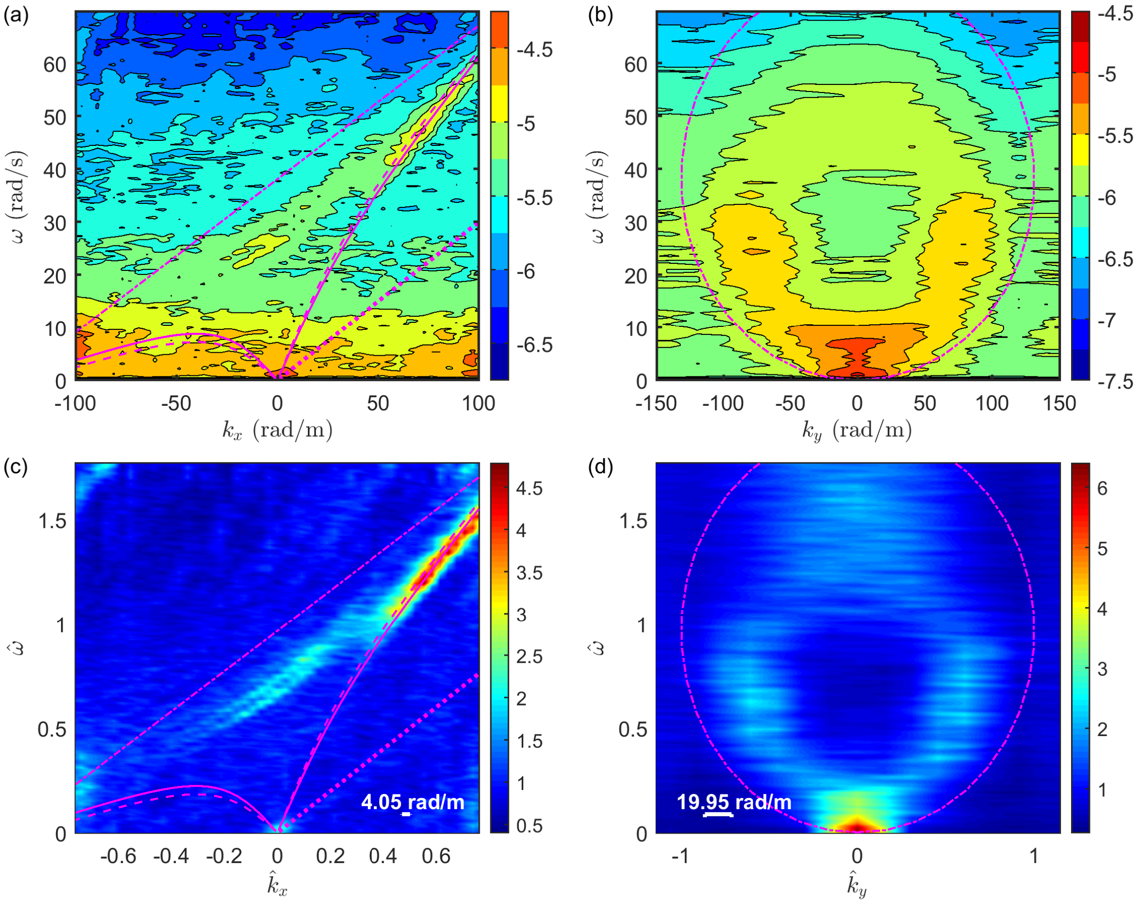

Figure 5.17: (a) Contour plot of the dimensional frequency-wavenumber spectrum for condition 4, $\log_{10}(\sigma^2 S_x(k_x, \omega))$, (b) Transverse spectrum $\log_{10}(\sigma^2 S_y(k_y, \omega))$. (c) The normalised frequency-wavenumber spectrum, $\bar{S}_x(\hat{k}_x, \hat{\omega})$, (d) normalised transverse frequency wavenumber-spectrum $\bar{S}_y(\hat{k}_y, \hat{\omega})$. (dashed) Irrotational dispersion relation, equation (3.20). (solid) Dispersion relation with the 1/3 velocity profile, $\theta = 0$, equation (3.26). (dotted) Non-dispersive relation, equation (3.21). (dashed-dotted) Dispersion relation with the 1/3 velocity profile, with constant $k = k_0$, equation (3.45).

agreement with the dispersion relation of the radial pattern in the frequency range $0 \leq \hat{\omega} \leq 2$ in FIG. 5.16c-d is better than in FIG. 5.15c-d, with $\varepsilon_k = 2.1\,\mathrm{rad\,m^{-1}}$ in the region $\hat{\omega} < 2$ and $\varepsilon_k = 2.7\,\mathrm{rad\,m^{-1}}$ in the region $\hat{\omega} > 2$.

The pattern of the measured frequency-wavenumber spectra repeats very consistently for all the tested flow conditions, with the exception of conditions 1 and 4. The former requires a separate discussion because the mean surface velocity $U_0 < c_{min}$ did not allow the formation of stationary waves. The frequency-wavenumber spectra for flow condition 4 are shown in FIG. 5.17. In this condition the dispersion relation with the 1/3 velocity profile predicts the wavelength of the stationary waves equal to $2\pi/k_0 = 47.8\,\mathrm{mm}$, which is comparable to the shortest waves that could be accurately measured by the streamwise array, where $k_0 \Delta r_e/(2\pi) = 0.55$. The streamwise frequency-wavenumber spectrum in FIG. 5.17c shows a cloud of points enclosed within the region of $\hat{k}_x \approx -0.8$ and $0 \leq \hat{\omega} \leq 0.5$. This was caused by the limited spatial resolution of the array. There is a ridge that corresponds to the gravity waves propagating downstream (equation (3.26)), which extends from $\hat{k}_x \approx 0.4$ to $\hat{k}_x = 0.9$ and from $\hat{\omega} \approx 1$ to $\hat{\omega} \approx 1.8$, hence with $k_x < k_0$. There is a second ridge that goes from $\hat{k}_x \approx -0.2$ to $\hat{k}_x \approx 0.3$ and from $\hat{\omega} \approx 0.5$ to $\hat{\omega} \approx 1.2$, but this is strongly curved and it does not follow the prediction based on the radial pattern with the constant modulus of the wavenumber $k = k_0$ (equation (3.45)). The root mean squared difference from this prediction calculated with equation (5.33) is equal to $\varepsilon_k = 34.1\,\mathrm{rad\,m^{-1}}$, estimated between $\hat{\omega} = 0$ and $\hat{\omega} = 2$. The transverse spectrum shown in FIG. 5.17d has the similar behavior to that of the flow conditions discussed so far, but the region where $\hat{k}_y \neq 0$ is within $0.2 \leq \hat{\omega} \leq 1.3$, and the maximum transverse wavenumber is $\hat{k}_y \approx 0.6$. These observations suggest that the radial pattern of waves had the modulus of the wavenumber smaller than k_0 in condition 4. The curved ridge in FIG. 5.17a also suggests that the pattern was not axially symmetric, i.e., that the waves propagating parallel to the current had the larger wavenumber (were shorter) than those propagating perpendicularly to it. The reasons for the different behaviour in condition 4 are not clear, and warrant further investigation.

The condition 1 had the mean surface velocity U_0 which was smaller than the minimum of the phase velocity in still water, $c_{min} \approx 0.23\,\mathrm{m\,s^{-1}}$. Therefore the stationary waves could not form on this flow. In FIG. 5.18c-d the normalised frequency-wavenumber spectra for the condition 1 are shown as the function of the non-dimensional wavenumber kU_0^2/g and the non-dimensional frequency $\omega U_0/g$. The streamwise frequency-wavenumber spectrum is shown in FIG. 5.18a, c. This spectrum shows a ridge that follows closely the dispersion relation of equation (3.26) with $\theta = 0$. The root mean squared difference from this relation is $\varepsilon_k = 2.5\,\mathrm{rad\,m^{-1}}$. The behaviour is similar to what was observed in the other flow conditions, but the ridge in the spectrum for condition 1 extends to the lower frequency $\omega U_0/g = 0$, and the maximum of the spectra is near $k_x U_0^2/g = 0$. On the other hand, the ridge which had been attributed to the waves with the constant wavenumber $k = k_0$ propagating radially is absent in the spectrum obtained for condition 1, which confirms that the observed radial pattern was related to the stationary condition. There is a new ridge which was not noticed in the spectra for the other conditions, and which follows approximately the non-dispersive linear relation of equation (3.21). In FIG. 5.18c this ridge extends from the origin of the spectrum to the point with $k_x U_0^2/g = 0.3$ and $\omega U_0/g = 0.3$, after which it becomes less clear because of the limited resolution of the measurements. The transverse spectrum in FIG. 5.18d shows a clear ridge with $k_y U_0^2/g = 0$ where $0 \leq \omega U_0/g \leq 0.2$, but it also becomes less clear at the higher frequency. The non-dispersive ridge in FIG. 5.18a has the amplitude 2 to 3 times

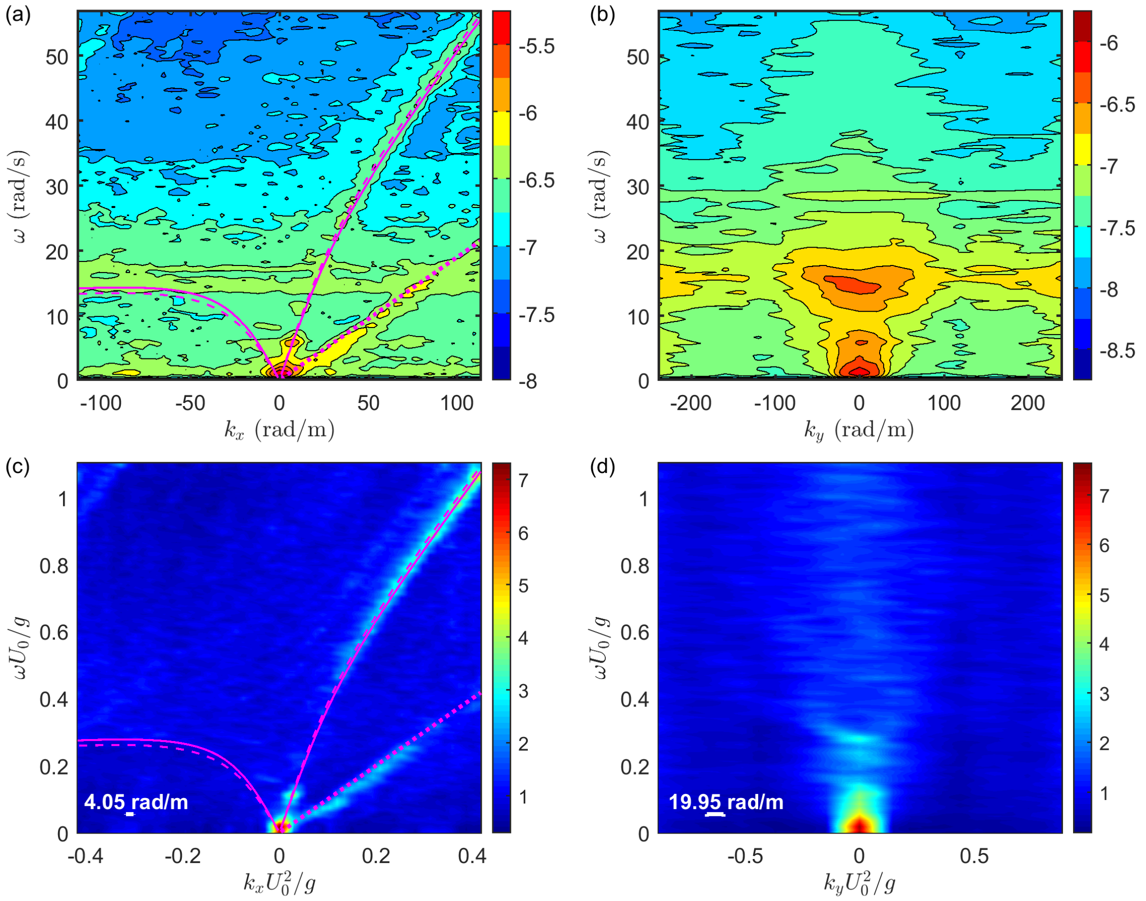

Figure 5.18: (a) Contour plot of the dimensional frequency-wavenumber spectrum for condition 1, $\log_{10}(\sigma^2 S_x(k_x,\omega))$, (b) Transverse spectrum $\log_{10}(\sigma^2 S_y(k_y,\omega))$. (c) The normalised frequency-wavenumber spectrum, $\bar{S}_x(k_xU_0^2/g,\omega U_0/g)$, (d) normalised transverse frequency wavenumber-spectrum $\bar{S}_y(k_xU_0^2/g,\omega U_0/g)$. (dashed) Irrotational dispersion relation, equation (3.20). (solid) Dispersion relation with the 1/3 velocity profile, $\theta=0$, equation (3.26). (dotted) Non-dispersive relation, equation (3.21).

larger than the dispersive ridge at each value of the wavenumber. The root mean squared difference from the relation $\omega U_0/g = k_xU_0^2/g$ is $\varepsilon_k = 5.4\,\mathrm{rad\,m^{-1}}$, evaluated in the range $0 < \omega U_0/g < 0.3$. The frequency spectra of the flow condition 1 which were shown in FIG. 5.7 had a peak at the frequency $\omega U_0/g \approx 0.3$ ($\omega \approx 15\,\mathrm{rad\,s^{-1}}$). At the same frequency the streamwise spectrum of FIG. 5.18a shows a horizontal ridge spanning the whole wavenumber range, while the transverse spectrum of FIG. 5.18b has a peak at $k_y \approx 0$.

5.3.3 Evidence of wave group dynamics

The results of the previous subsection have shown the presence of radial patterns of waves in all conditions with the mean surface velocity larger than the minimum phase velocity of gravity-capillary waves. These patterns bear a direct resemblance

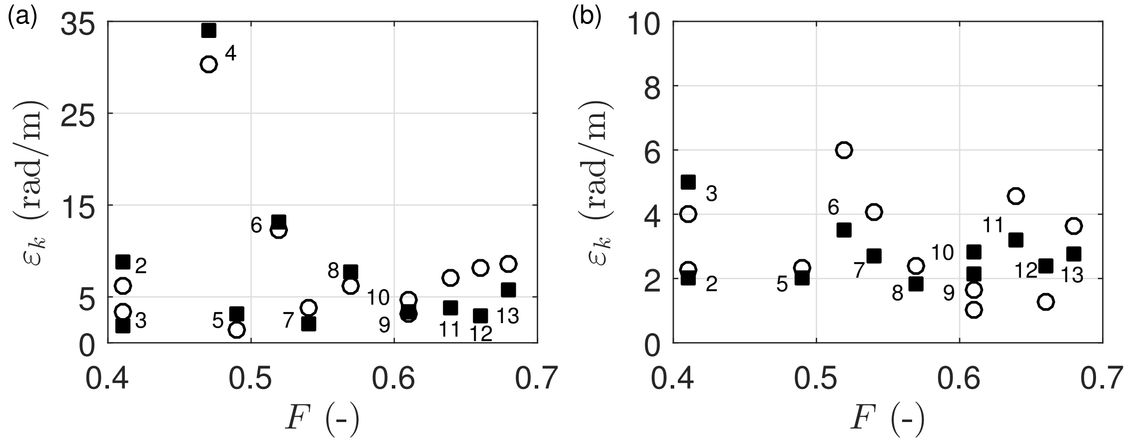

Figure 5.19: Root mean square averaged difference, ε_k, between the ridges of the measured streamwise spectra, $S_x(k_x, \omega)$, and the proposed dispersion relations, evaluated along the k_x axis in the interval (a) $\hat{\omega} < 2$, (b) $\hat{\omega} > 2$. (squares) Dispersion relation with the 1/3 velocity profile, equations (3.26) and (3.45). (circles) Irrotational dispersion relations, equations (3.20) and (3.48). The numbers indicate the flow conditions. The spectral resolution was $\Delta k_x = 4.05\,\mathrm{rad\,m^{-1}}$.

with the model of gravity waves shed radially from a localised vortex dimple, as suggested by Savelsberg and van de Water [2009]. It will be shown in subsection 5.3.4 that the Fourier representation of the radial patterns measured in subsection 5.3.2 generates structures which are also similar to the oscillons suggested by Nichols et al. [2016]. These structure advect as groups with the velocity equal to the mean surface velocity, and without change of form except for a vertical oscillation. This is in apparent contrast with the theory of gravity-capillary waves, which states that wave groups travel with their characteristic group velocity. The first objective of this subsection was to measure the group velocity of the radial patterns of waves and to compare it with the group velocity of gravity-capillary waves. This will further inform the discussion in subsection 5.3.4. The second objective of this subsection was to characterise the spatial correlation of the envelope of the surface elevation at different frequencies and in the different spatial dimensions. This characterisation is important for the application of the wavelet spectral method, which is discussed in section 5.4.

The dynamics of wave groups were investigated in terms of the envelope Z of the band-pass filtered surface elevation, following the procedure described in subsection 5.1.5. Two characteristic frequencies were investigated here, in order to show the behaviour of the different types of waves observed in subsection 5.3.2. The high-frequency dispersive waves propagating downstream with the wavenumber $k_x > k_0$ were investigated by setting the parameters of the Gaussian filter to $\omega_G = 2.5k_0U_0$ and $\sigma_{\omega,G} = k_0U_0/2$. The lower frequency radial waves were investigated by setting $\omega_G = k_0U_0$, and $\sigma_{\omega,G} = k_0U_0/2$. In condition 1, the alternative settings $\omega_G =$

$0.8g/U_0$, $\sigma_{\omega,G} = k_0U_0/5$ and $\omega_G = 0.3g/U_0$, $\sigma_{\omega,G} = k_0U_0/10$, were used for the high and for the low frequency, respectively. The frequency-wavenumber spectra and the space-time correlation functions of the envelope were indicated by the symbols $S_{x,Z}(\hat{k}_x, \hat{\omega})$, $S_{y,Z}(\hat{k}_y, \hat{\omega})$, and $W_{x,Z}(r_x, \tau)$, $W_{y,Z}(r_y, \tau)$.

It should be noted that because the filtering was not applied in the wavenumber domain, eventual multiple branches of the frequency-wavenumber spectrum could not be isolated with the analysis described here. This means that the interpretation of the results may be difficult in the lower range of frequencies, especially in conditions 1 and 13. In fact, in the first condition both dispersive and non-dispersive waves were observed in FIG. 5.18c at low frequency $\omega U_0/g \leq 0.2$. In condition 13 both radial waves and waves propagating slowly upstream were observed in FIG. 5.15c at the frequency $\hat{\omega} \leq 1$.

FIG. 5.20b, d, shows the streamwise frequency-wavenumber spectra of the envelope $S_{x,Z}(k_xU_0^2/g, \omega U_0/g)$ at the frequencies $0.8g/U_0$ and $0.3g/U_0$, respectively, for the condition 1. The corresponding lateral spectra $S_{y,Z}(k_yU_0^2/g, \omega U_0/g)$ are shown in FIG. 5.21b, d. Both spectra are compared with the frequency-wavenumber spectra of the band-pass filtered surface elevation, $S_x(k_xU_0^2/g, \omega U_0/g)$, and $S_y(k_yU_0^2/g, \omega U_0/g)$, which are shown in FIG. 5.20a, c, and FIG. 5.21a, c. The white dashed lines in FIG. 5.20 represent the group velocity of the waves with the frequency ω_G, which was determined from equations (3.15) based on the irrotational dispersion relation of equation (3.20). The frequency-wavenumber spectrum of the envelope of the high-frequency waves in FIG. 5.20b follows the group velocity in the region $0 \leq k_xU_0^2/g \leq 0.1$ and $0 \leq \omega U_0/g \leq 0.4$. This demonstrates that the wave groups with the frequency $0.8g/U_0$ propagated downstream at the velocity equal to the group velocity of gravity-capillary waves, and faster than the mean surface velocity. In FIG. 5.20c the frequency wavenumber spectrum of the filtered elevation $S_x(k_xU_0^2/g, \omega U_0/g)$ at low frequency has a wide horizontal ridge at the frequency of approximately $\omega U_0/g = 0.3$, with slightly larger amplitude at the wavenumbers $k_xU_0^2/g = 0.3$ and $k_xU_0^2/g = -0.3$. The point with $k_xU_0^2/g = -0.3$ and $\omega U_0/g = 0.3$ corresponds to the waves that propagated upstream with the group velocity equal to zero. The frequency-wavenumber spectrum of the envelope with the lower frequency $0.3g/U_0$ (FIG. 5.20d) shows a horizontal ridge near the frequency $\omega U_0/g = 0$, and with larger amplitude near the wavenumbers $k_xU_0^2/g = -0.3$, $k_xU_0^2/g = 0$, and $k_xU_0^2/g = 0.3$. The horizontal ridge of FIG. 5.20d at $\omega U_0/g = 0$ represents a group of waves with the group velocity equal to zero, and with a broad spatial spectrum. The transverse frequency-wavenumber spectra of the envelope of condition 1 in FIG. 5.21b, d, show that the envelope had a relatively broader transverse spatial spec-

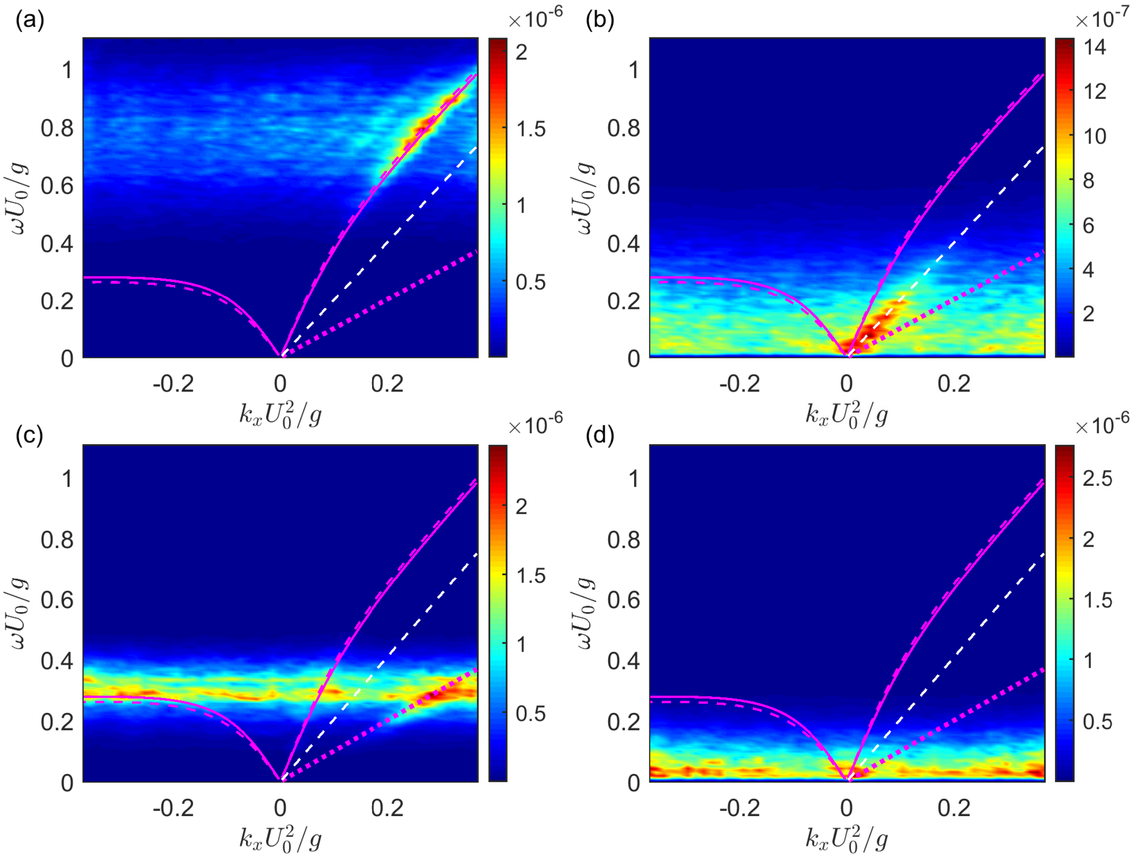

Figure 5.20: (a) The contour plot of the streamwise frequency-wavenumber spectrum of the filtered elevation for condition 1, $S_x(k_x U_0^2/g, \omega U_0/g)$, at the frequency $\omega_G = 0.8g/U_0$, (b) The streamwise frequency-wavenumber spectrum of the envelope, $S_{x,Z}(\hat{k}_x, \hat{\omega})$, for the same frequency. (c) $S_x(k_x U_0^2/g, \omega U_0/g)$, at the frequency $\omega_G = 0.3g/U_0$, (b) $S_{x,Z}(\hat{k}_x, \hat{\omega})$, for the same frequency. (magenta dashed) Irrotational dispersion relation, equation (3.20). (magenta solid) Dispersion relation with the 1/3 velocity profile, $\theta = 0$, equation (3.26). (magenta dotted) Non-dispersive relation, equation (3.21). (white dashed) Group velocity of the waves with frequency ω_G.

trum than the elevation ζ, and that it travelled principally along the direction x with $k_y \approx 0$.

The similar frequency-wavenumber spectra for condition 7 are shown in FIG. 5.22 and 5.23. The behaviour in this condition was representative of the one observed in all remaining conditions, except condition 1. In condition 7 the streamwise frequency-wavenumber spectrum of ζ did not show multiple branches of the dispersion relation, therefore the interpretation of the results was more straightforward. The lower frequency $k_0 U_0$ corresponds to the waves which travelled perpendicularly to the direction of the flow based on the model of radial waves with the wavenumber modulus k_0. The additional dashed white lines in FIG. 5.23c, d, show the expected group velocity of these waves along the y-direction, i.e., neglecting the advection by

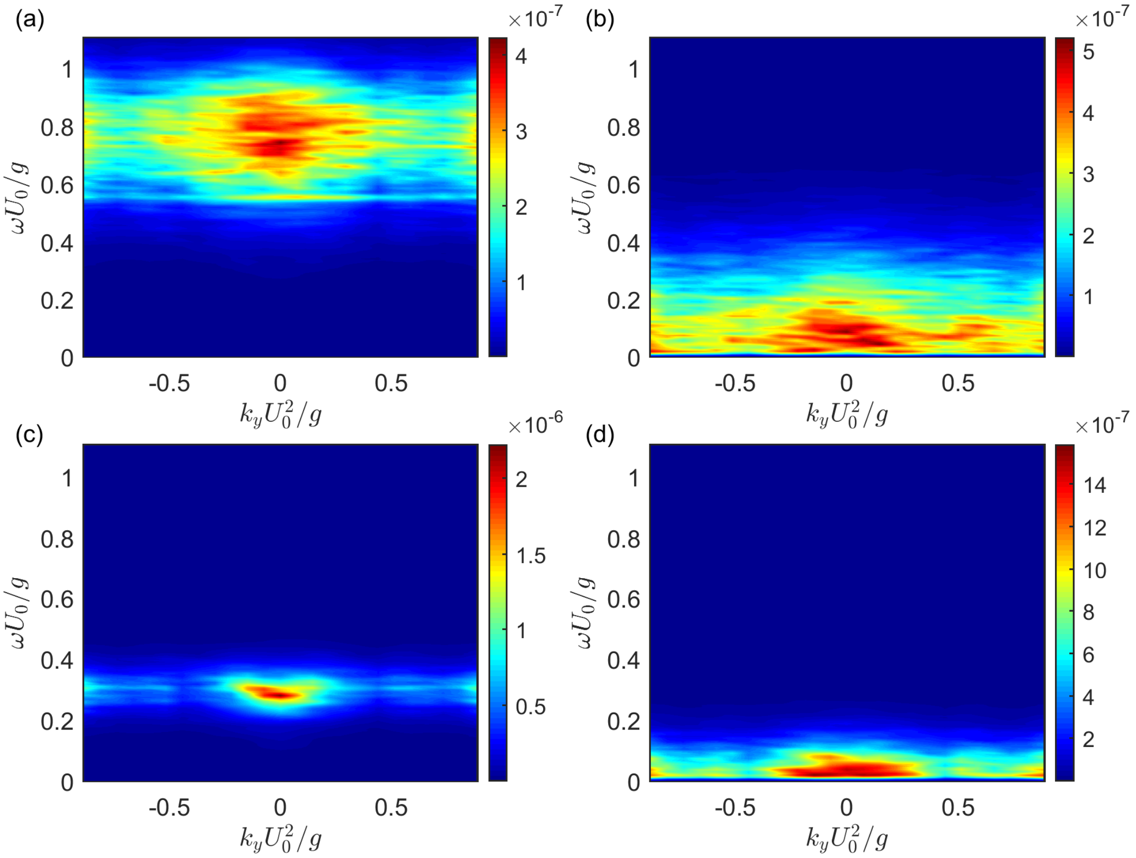

Figure 5.21: (a) The contour plot of the transverse frequency-wavenumber spectrum of the filtered elevation for condition 1, $S_y(k_yU_0^2/g, \omega U_0/g)$, at the frequency $\omega_G = 0.8g/U_0$, (b) The transverse frequency-wavenumber spectrum of the envelope, $S_{y,Z}(\hat{k}_y, \hat{\omega})$, for the same frequency. (c) $S_y(k_yU_0^2/g, \omega U_0/g)$, at the frequency $\omega_G = 0.3g/U_0$, (b) $S_{y,Z}(\hat{k}_y, \hat{\omega})$, for the same frequency.

the mean surface velocity. The advection was considered instead in the streamwise spectra of FIG. 5.23c, d and 5.23a, b.

At the higher frequency of $2.5k_0U_0$, the streamwise frequency-wavenumber spectrum of the envelope $S_{x,Z}(\hat{k}_x, \hat{\omega})$ (shown in FIG. 5.22b) follows the group velocity of the gravity-capillary waves propagating downstream according to equations (3.15) and (3.20). This is larger than the mean surface velocity U_0. The transverse spectrum $S_{y,Z}(\hat{k}_y, \hat{\omega})$ in FIG. 5.23b shows that the wave group had a broad transverse spatial spectrum with the width comparable to k_0, and that it moved mainly along the x-direction.

The streamwise spectrum at the lower frequency k_0U_0, $S_{x,Z}(\hat{k}_x, \hat{\omega})$, is shown in FIG. 5.22d. This spectrum shows that the envelope Z (the wave group) travelled in the x-direction at the velocity equal to the mean surface velocity U_0. The transverse spectrum $S_{y,Z}(\hat{k}_y, \hat{\omega})$ in FIG. 5.23d shows that the velocity of the envelope did not have components along the y-direction. This is in contrast with the theory of gravity-

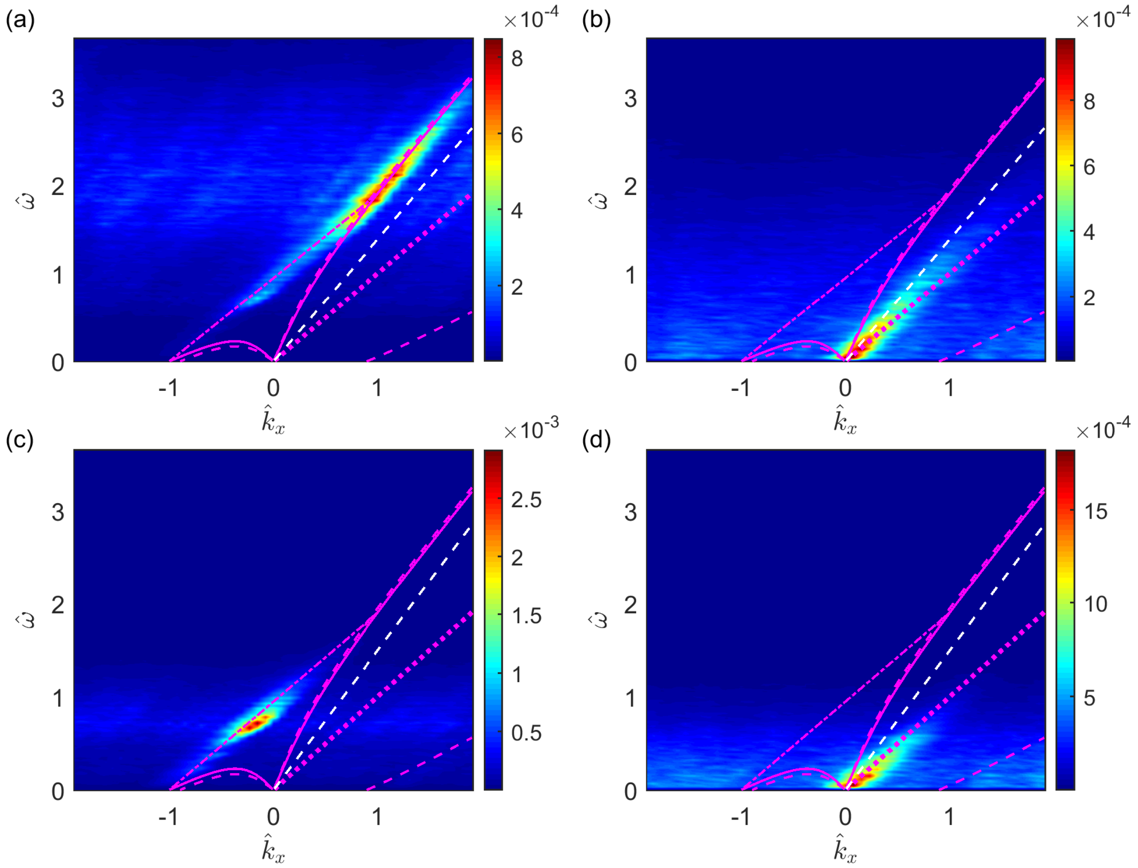

Figure 5.22: (a) The contour plot of the streamwise frequency-wavenumber spectrum of the filtered elevation for condition 7, $S_x(\hat{k}_x, \hat{\omega})$, at the frequency $\omega_G = 2.5k_0U_0$, (b) The streamwise frequency-wavenumber spectrum of the envelope, $S_{x,Z}(\hat{k}_x, \hat{\omega})$, for the same frequency. (c) $S_x(\hat{k}_x, \hat{\omega})$, at the frequency $\omega_G = k_0U_0$, (b) $S_{x,Z}(\hat{k}_x, \hat{\omega})$, for the same frequency. (magenta dashed) Irrotational dispersion relation, equation (3.20). (magenta solid) Dispersion relation with the 1/3 velocity profile, $\theta = 0$, equation (3.26). (magenta dotted) Non-dispersive relation, equation (3.21). (magenta dashed-dotted) Dispersion relation with the 1/3 velocity profile, with constant $k = k_0$, equation (3.45). (white dashed) Group velocity of the waves with frequency ω_G.

capillary waves, which predicts that the group velocity is perpendicular to the wave crests, therefore parallel to the y-direction for these waves. FIG. 5.23d also shows that the transverse spatial spectrum of the envelope is relatively narrow, and has three distinct peaks. $S_{y,Z}(\hat{k}_y, \hat{\omega})$ has a narrow peak with $\hat{k}_y = 0$ and two smaller peaks with the wavenumbers $\hat{k}_y \approx \pm 2$.

The correlation functions relative to the higher frequency $2.5k_0U_0$ are shown in FIG. 5.24. Unlike in FIG. 5.14 where the correlation functions of the surface elevation ζ were grouped based on the parameter k_0H, the different conditions represented in FIG. 5.24 were grouped based on the mean flow depth H, since this seemed to be a more relevant parameter for the behaviour of the envelope. The first difference with respect to FIG. 5.14 is the asymmetry of the correlation along the two directions

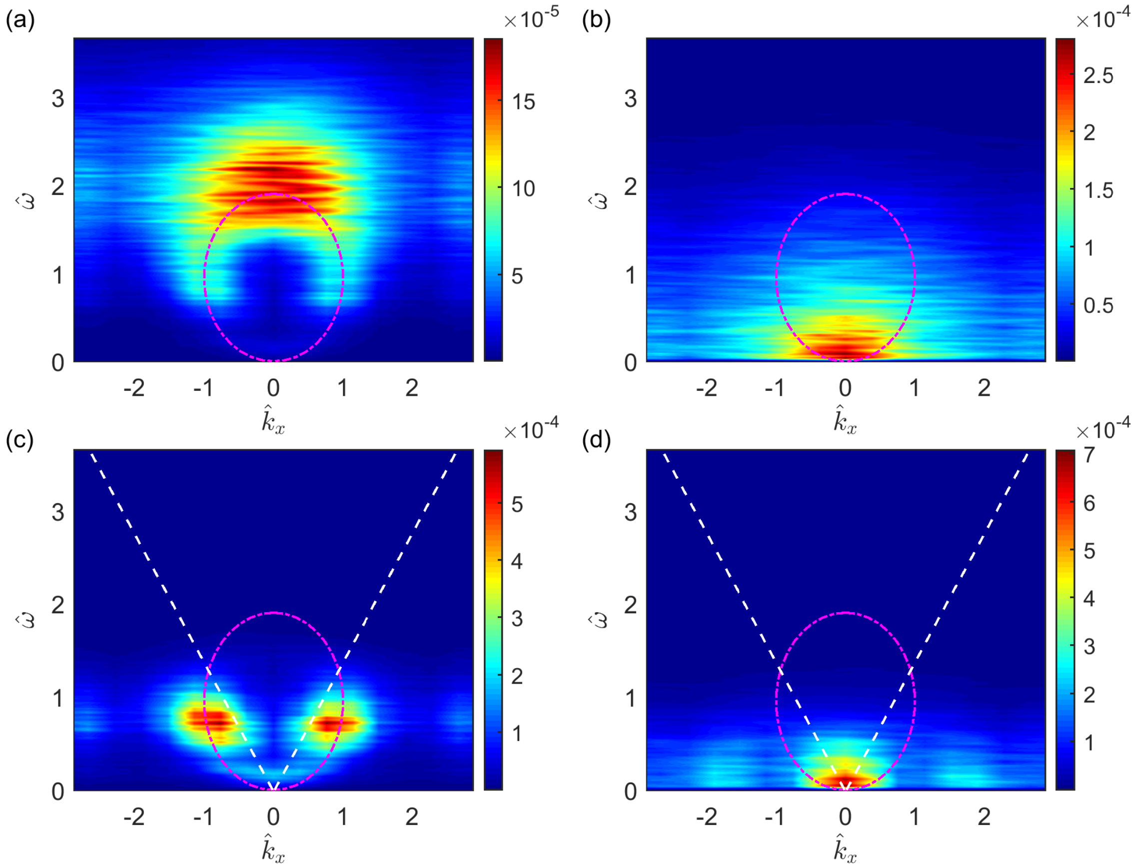

Figure 5.23: (a) The contour plot of the transverse frequency-wavenumber spectrum of the filtered elevation for condition 7, $S_y(\hat{k}_y, \hat{\omega})$, at the frequency $\omega_G = 2.5k_0U_0$, (b) The transverse frequency-wavenumber spectrum of the envelope, $S_{y,Z}(\hat{k}_y, \hat{\omega})$, for the same frequency. (c) $S_y(\hat{k}_y, \hat{\omega})$, at the frequency $\omega_G = k_0U_0$, (b) $S_{y,Z}(\hat{k}_y, \hat{\omega})$, for the same frequency. (magenta dashed-dotted) Dispersion relation with the 1/3 velocity profile, with constant $k = k_0$, equation (3.45). (white dashed) Group velocity of the waves with frequency ω_G.

x and y. The correlation $W_{x,Z}(r_x, \tau)$ in FIG. 5.24b, c, d, becomes approximately zero at $r_x/(2\pi/k_0) = 0.5$, which corresponds to half the wavelength of the stationary waves. In contrast, the transverse correlation decays more rapidly and is approximately zero already near $r_y/(2\pi/k_0) = 0.25$. Among each group of flow conditions, the rate of decay of the correlation with respect to $2\pi/k_0$ is faster when k_0H/π is smaller, more clearly so for the conditions with the depth $40.5\,\text{mm} \leq H \leq 43.4\,\text{mm}$ in FIG. 5.24b. k_0H/π decreased with the increase of the condition number, i.e., it was largest in condition 13 and smallest in condition 2. The functions $W_{x,Z}(r_x, \tau)$ and $W_{y,Z}(r_y, \tau)$ decay smoothly without fluctuations, which indicates that the envelopes of the wave groups had no periodicity in space. The correlation functions in condition 1 (shown in FIG. 5.24a) behaves similarly to those of the other flow conditions, but with different non-dimensionalised spatial scales.

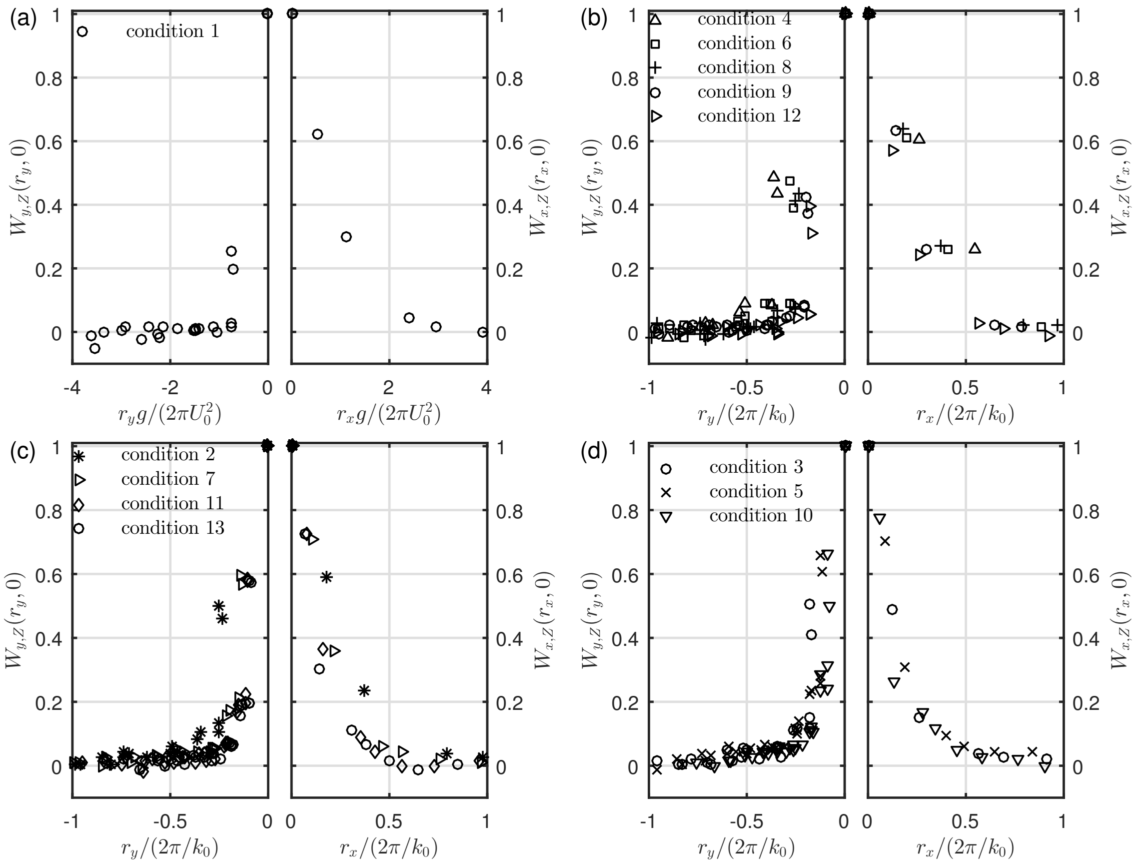

Figure 5.24: The normalised spatial correlation of the envelope Z at zero time lag, with normalised spatial separation, $rk_0/2\pi$, at the higher frequency $2.5k_0U_0$. The negative x-axis shows the lateral correlation, $W_{y,Z}(r_{n,y},0)$, while the positive x-axis shows the streamwise correlation, $W_{x,Z}(r_{n,x},0)$. (a) Condition 1, (b) conditions 4, 6, 8, 9, and 12 ($40.5\,\mathrm{mm} \leq H \leq 43.4\,\mathrm{mm}$), (c) conditions 2, 7, 11, and 13 ($72.4\,\mathrm{mm} \leq H \leq 73.2\,\mathrm{mm}$), (d) conditions 3, 5, and 10 ($99.0\,\mathrm{mm} \leq H \leq 101.3\,\mathrm{mm}$). Note the different scaling in (a), where the frequency was $0.8g/U_0$.

The behaviour of the correlation functions $W_{x,Z}(r_x,\tau)$ and $W_{y,Z}(r_y,\tau)$ at the lower frequency k_0U_0 was different, as it can be seen in FIG. 5.25. The asymmetry of the correlation in the x and y directions is still observed at the lower frequency and for all conditions, although in FIG. 5.25b, c, d, the streamwise correlation decays more slowly at the larger depth $99.0\,\mathrm{mm} \leq H \leq 101.3\,\mathrm{mm}$ (5.25d) than at the depth $40.5\,\mathrm{mm} \leq H \leq 43.4\,\mathrm{mm}$ (5.25b). In the former case the correlation is approximately zero at the larger relative separation $r_x/(2\pi/k_0) = 1$. The correlation function along the transverse direction y at the lower frequency k_0U_0 behaves similarly to that at higher frequency in the conditions with $40.5\,\mathrm{mm} \leq H \leq 43.4\,\mathrm{mm}$ (FIG. 5.25a, b). In the conditions with larger depths (FIG. 5.25c, d), $W_{y,Z}(r_y,\tau)$ decays rapidly to zero at $r_y/(2\pi/k_0) = 0.25$, then it has a peak with the amplitude as large as 0.3 at $r_y/(2\pi/k_0) = 0.5$.

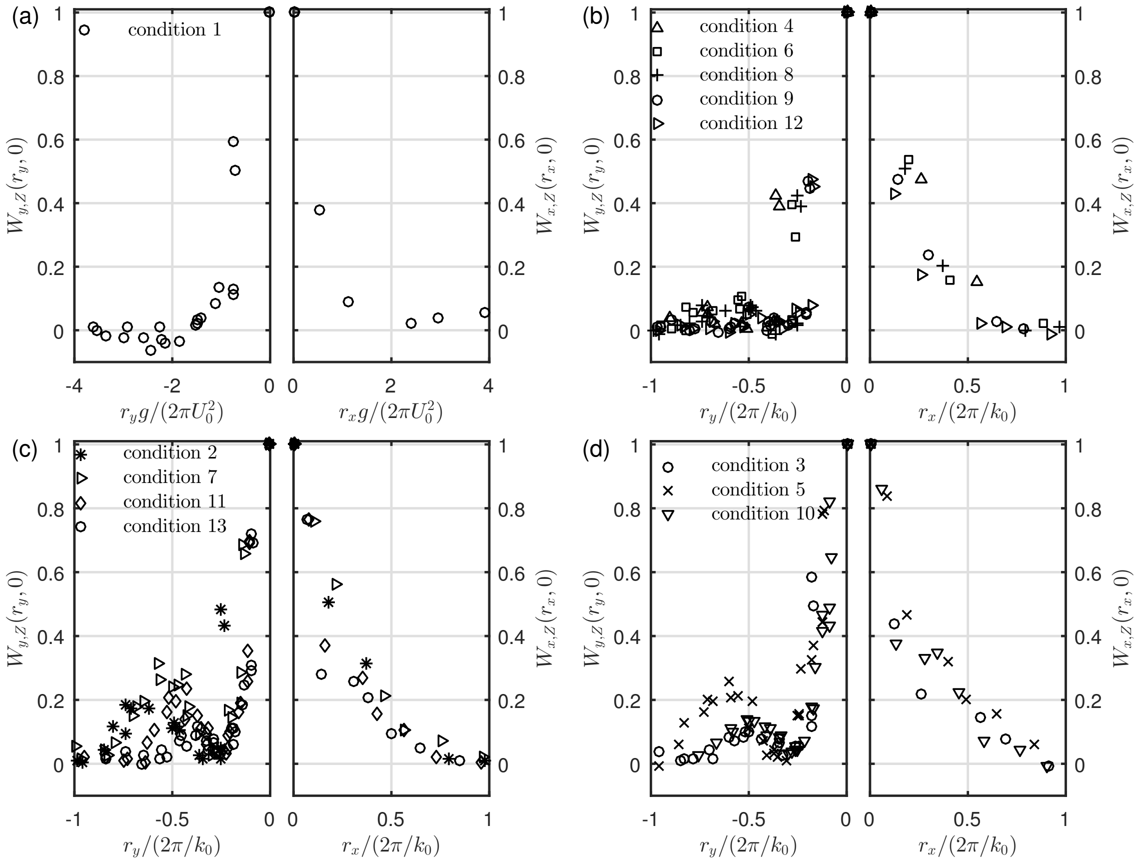

Figure 5.25: The normalised spatial correlation of the envelope Z at zero time lag, with normalised spatial separation, $rk_0/2\pi$, at the lower frequency k_0U_0. The negative x-axis shows the lateral correlation, $W_{y,Z}(r_{n,y},0)$, while the positive x-axis shows the streamwise correlation, $W_{x,Z}(r_{n,x},0)$. (a) Condition 1, (b) conditions 4, 6, 8, 9, and 12 ($40.5\,\text{mm} \leq H \leq 43.4\,\text{mm}$), (c) conditions 2, 7, 11, and 13 ($72.4\,\text{mm} \leq H \leq 73.2\,\text{mm}$), (d) conditions 3, 5, and 10 ($99.0\,\text{mm} \leq H \leq 101.3\,\text{mm}$). Note the different scaling in (a), where the frequency was $0.3g/U_0$.

5.3.4 Discussion

The results in this section have shown the spatial correlation function and the dispersion relation of the free surface patterns in turbulent shallow flows with a rough bottom boundary. It is believed that these functions were never measured before experimentally in a flow where the surface patterns occur naturally. The measurements of the zero-lag correlation function of the free surface elevation (FIG. 5.14) have shown a fluctuation with the period of approximately $2\pi/k_0$, which is the typical scale of the stationary waves. In the flow condition 1 the stationary waves could not form, and the correlation function did not fluctuate. Savelsberg and van de Water [2009] and Horoshenkov et al. [2013] associated the decay rate and the period of the correlation function of the free surface elevation with the characteristic scales of turbulence, although Horoshenkov et al. [2013] looked at the maxima in the time correlation function at each spatial separation, rather than at the zero-lag correlation at $\tau = 0$. Savelsberg and van de Water [2009] and Horoshenkov et al. [2013] found a correspondence between the scales of the correlation and the characteristic integral scales of turbulence. Savelsberg and van de Water [2009] also observed that the correlation function becomes anisotropic when the turbulence in the flow is also anisotropic. The measurements presented here have shown that when the mean surface velocity was larger than the minimum phase velocity of gravity-capillary waves, the stationary waves rather than the turbulent scales determined the dominant scales of the free surface. The Froude number also seemed to affect the spatial characteristics of the free surface. In fact, both the period of the correlation function relative to $2\pi/k_0$ and the spatial rate of decay tended to decrease when $k_0 H/\pi$ also decreased. These observations demonstrate the link between the dynamics of the free surface and the hydraulic conditions, mainly through the parameters k_0, H, and U_0. This was one of the objectives of the analysis presented in this section.

The measurements of the frequency wavenumber spectra of the surface elevation were compared with the dispersion relations presented in section 3.1.2, which correspond to a model of gravity-capillary waves propagating in a flow with a 1/3 power function velocity profile (equations (3.26) and (3.45)), and in an irrotational flow (equations (3.20) and (3.48)), respectively. The difference between the two dispersion relations and the measured spectra was quantified by the Gaussian fitting of the ridges of the streamwise spectra, $S_x(k_x, \omega)$. The root mean squared wavenumber difference, ε_k, was shown in FIG. 5.19 for all conditions except condition 1. In most flow conditions the two theories gave very similar results, close to the resolution of the spectra. In the conditions with larger Froude number, the relation based on the 1/3 velocity profile was more accurate in the region $\hat{\omega} < 2$, where most of the amplitude of the spectrum was concentrated.

FIG. 5.19 shows that the model was less accurate in the conditions 2, 4, 6, and 8. Of these, conditions 4, 6 and 8 had the lower mean depth of approximately 40 mm, and the smaller Froude number $F < 0.6$. Condition 4 showed a very different pattern from all other conditions, which is not fully understood. The theory of Cheng [2007] does not predict an observable change of the velocity profile in the condition 4, 6, and 8, but the data reported by Nichols [2015] did not include any condition with similar depth and with $F < 0.6$, so that a direct check was not possible. It is expected that when the submergence H/d becomes very small, the free surface may follow the shape of the boundary and the linearised equations would not be valid. The statistical analysis in section 5.2 showed that the surface in the conditions 2 and 4 was essentially linear, while significant non-linearities were observed in conditions 6 and 8. It is suggested that the proposed relations become less accurate when the flow is more shallow and the Froude number is relatively low, as a consequence of the change of the velocity profile and of the reduced validity of the linearisation of the surface equations. The results showed that the velocity profile influences the dispersion relation as expected, although the variation of the shape of the velocity profile was too small to be detected in most of the conditions described here. The resolution of the measurements would need to be increased if one aims to determine the shape of the velocity profile from the measurement of the free surface dynamics.

In all conditions with $U_0 > c_{min}$ (see FIG. 5.15, FIG. 5.16, and FIG. 5.17) the maxima of the frequency-wavenumber spectra was found near $k_x = \pm k_0$, which showed that the stationary waves represent the dominant pattern on the free surface. The observed patterns of waves which propagate radially in all directions resemble the model of concentric gravity waves being shed by vertical vortices suggested by Savelsberg and van de Water [2009], although in the measurements presented here the scale of the pattern was governed by the wavelength of the stationary waves rather than by the scale of the attached vortices. An exception was represented by condition 4, where the radial waves were shorter than the stationary waves, and the pattern was non-isotropic. Further investigations would be needed in order to clarify the reasons for this different behaviour.

Condition 1 showed a markedly different behaviour with respect to all the other conditions with $U_0 > c_{min}$, as it was evident from the frequency-wavenumber spectra shown in FIG. 5.18. These spectra still showed a ridge that represents gravity waves propagating downstream, but the ridge extended to very low frequencies. This is of notice, since it signifies the existence of long waves with the wavelength comparable to the length of the array of probes, whereas in the other conditions the longest waves had the wavelength of $2\pi/k_0$. The spectra shown in FIG. 5.18a, c, revealed one additional set of waves which followed the non-dispersive relation of equation (3.21). This non-dispersive ridge can represent random patterns on the surface with a broad spatial spectrum, which are advected by the flow at the constant velocity U_0. These patterns were dominating over the dispersive freely propagating gravity waves at each value of the wavenumber in condition 1. Teixeira and Belcher [2006] postulated that the direct interaction with turbulence is able to produce patterns of forced waves on the free surface, even when the conditions for the resonant interaction are not met. These waves are expected to follow the dispersion relation of the turbulence inside the flow, which, as a first approximation, corresponds to the equation (3.21) which can be observed in FIG. 5.18a, c.

In terms of the frequency-wavenumber spectrum of the low-frequency envelope in condition 1 (FIG. 5.20d), one would expect the non-dispersive waves that correspond to the peak at $k_x U_0^2/g = 0.3$ and $\omega U_0/g = 0.3$ of FIG. 5.20c to have the envelope spectrum that closely follows the same non-dispersive relation $\omega = k_x U_0$. This expected behaviour is not confirmed by the spectrum of FIG. 5.20d, which may be due to the fact that multiple branches of the frequency-wavenumber spectrum cannot be isolated without applying a spatial-temporal filter. The frequency spectrum of condition 1 in FIG. 5.7a showed a peak at the frequency $\omega U_0/g$, which corresponds to the dimensional frequency of 2.5 Hz. This is also approximately the solution of $\partial\omega/\partial k = 0$ based on the equations (3.15) and (3.20), where $\theta = \pi$. Kitaigordskii et al. [1975] showed that the frequency spectrum $S(\omega)$ and the wavenumber angular spectrum $S(k, \theta)$ are related by equation (3.14). The integral of equation (3.14) can become very large if the group velocity is small, which is possible for waves propagating against the flow. The peak of the frequency spectrum in FIG. 5.7a near the frequency where $\partial\omega/\partial k = 0$ can be justified by the existence of waves propagating upstream in the flow condition 1. These waves could also cause the broad ridge of FIG. 5.20d near the frequency $\omega = 0$, which impeded the observation of the group velocity of the non-dispersive waves in the same figure.

The presence of the dispersive ridge in the spectrum of FIG. 5.18a, c showed that the gravity waves propagating downstream (those which in the other flow conditions were identified by $k_x > k_0$) were not related to the stationary waves, which could not form in condition 1. These waves could be transient waves generated by the interaction with the fixed rough boundary, or freely propagating gravity-capillary waves that originated from the turbulence forced waves after the forcing had ended. This may happen because of the loss of coherence of the turbulent structures as they interact with the sheared flow near the surface [Teixeira and Belcher, 2006], or because the spatial scale of these shorter waves was within the dissipative range of turbulence [Borue et al., 1995].

In the conditions where U_0 was larger than c_{min}, the measurements showed that the interaction with the rough bed was the dominant mechanism that produced the fluctuations of the free surface. Non-linear phenomena such as multiple-waves interactions, or instabilities related to the critical layer, were not observed in the range of scales which have been investigated, although they may manifest more clearly at the smaller wavelengths. Bound waves would have been identified from the frequency-wavenumber spectra [e.g. Herbert et al., 2010], therefore they are excluded. The predominance of critical-layer instabilities might have caused the growth of the waves propagating upstream. These waves have been observed, but they did not appear to dominate the patterns on the free surface. The large value of the kurtosis coefficient relative to the skewness observed in section 5.2 suggests the existence of interactions among waves, according to Janssen [2009]. These types of interactions may be responsible for the radial pattern of waves with the constant modulus of the wavenumber equal to k_0, in accordance with the model of Shrira

[1993]. This model cannot be applied formally to shallow turbulent flows, and it is only valid in the limit of a narrow angular spectrum of the waves. Further investigations are required in order to establish the mechanism that can produce such a pattern.

The observed radial pattern of waves with the wavenumber k_0 relates directly to the model of oscillons suggested by Nichols et al. [2016]. This model predicts patterns that fluctuate at a frequency which is governed by the standard deviation of the surface elevation, as they advect at the mean surface velocity. The measurement of the frequency-wavenumber spectrum of the envelope at the lower frequency in FIG. 5.22 suggests that groups of waves propagate at the velocity close to the mean surface velocity. This is in apparent contrast with a model of gravity-capillary waves, where the group velocity differs from the mean surface velocity, while it provides limited evidence in support of the model suggested by Nichols et al. [2016]. It is possible to represent the radial pattern measured in subsection 5.3.2 with equation (3.10), based on the linear model with random phase. The wavenumber co-ordinates are expressed in polar form k and θ, and the dispersion relation $\omega = \Omega(k, \theta)$ is introduced. The wavenumber modulus is equal to k_0 for all waves which contribute to the radial pattern, which yields

$$\zeta(x, y, t) = \int_{-\pi}^{\pi} A(k_0, \theta, \Omega(k_0, \theta)) e^{i[k_0 x \cos\theta + k_0 y \sin\theta - \Omega(k_0,\theta)t + \phi]} k_0 d\theta. \tag{5.43}$$

The dispersion relation of the radial pattern is approximated by

$$\Omega(k_0, \theta) = k_0 U_0 (1 + \cos\theta), \tag{5.44}$$

which corresponds to equation (3.46), and the spectrum is represented as $S(k_0, \theta)$ for simplicity. Substituting equation (5.44) in equation (5.43), one obtains

$$\zeta(x, y, t) = k_0 e^{-ik_0 U_0 t} \int_{-\pi}^{\pi} A(k_0, \theta) e^{ik_0[\cos\theta(x - U_0 t) + y \sin\theta]} e^{i\phi} d\theta. \tag{5.45}$$

The integral of equation (5.45) represents a set of waves propagating in all directions, and can be very complicated in general. It is interesting to look at the solution in the vicinity of a point with the co-ordinates $x = x_0 + U_0 t$ and $y = y_0$, which travels along the x-direction with the mean surface velocity. It is easy to see that such a solution corresponds to a pattern that fluctuates vertically with the frequency $k_0 U_0$, while the shape of its envelope remains unchanged.

The representation given by equation (5.45) is very similar to that of the oscillons proposed by Nichols et al. [2016], although its interpretation can be quite different.

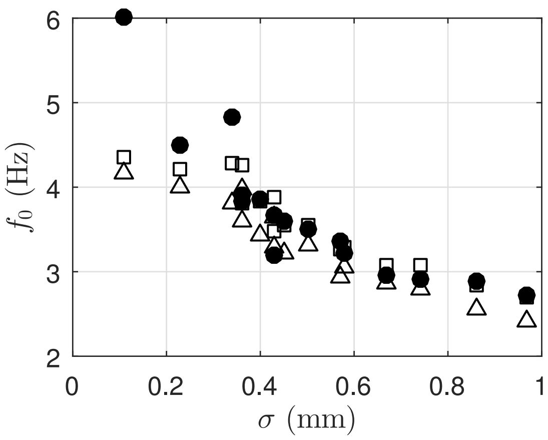

Figure 5.26: (black circles) The oscillon frequency measured by Nichols et al. [2016] compared with the characteristic frequency of the stationary waves calculated with equation (3.44) with (squares) $n = 1/2$ and (triangles) $n = 1/3$.

Nichols et al. [2016] suggested that the oscillons are the localised dynamic response to an initial disturbance of the surface, such as the impact of a turbulent structure. The form of the frequency of oscillation in equation (5.45) suggests that the patterns observed here relate to the stationary waves. During the period of one oscillation, the point with the initial streamwise location x_0 moves downstream by the distance of $2\pi/k_0$, which is the wavelength of the stationary waves. The pattern can be seen as a modulation of the stationary waves by an envelope that travels at the mean surface velocity, or equivalently as a group of stationary waves which group velocity is equal to the mean surface velocity and directed downstream. As a proof of the relevance of this interpretation for the model of oscillons, FIG. 5.26 shows the frequencies of the oscillations $k_0 U_0/2\pi$ calculated for the flow conditions reported by Nichols et al. [2016] based on equation (3.44). These are compared with the mesurements of the frequencies of the oscillons, as measured by Nichols et al. [2016]. The calculation with equation (3.44) was performed both with $n = 1/3$ and with $n = 1/2$. The values of the frequency predicted by equation (3.44) are very close to the results reported by Nichols et al. [2016]. A better fit is found with the results for $n = 1/2$. This could be an effect of the different streamwise velocity profile, since the measurements were performed with a different bottom roughness. There is a deviation from the measured frequency in the conditions with the smaller amplitude of the surface fluctuations. This could also be caused by the different velocity profile.

These results demonstrate that the dynamics of the dominant patterns on the free surface of a shallow turbulent flow can be explained by a linear model of gravity-capillary waves with random phase. In the measured conditions, no strong evidence of waves generated by the interactions with turbulent coherent structures was observed. This is in agreement with the results of the previous section. The waves follow a deterministic dispersion relation, and their scales are governed by the interaction with the rough boundary. The random superposition of the waves produces patterns which appear to travel downstream at the mean surface velocity, and which can be interpreted as a generalisation of wave group.

The shape of the groups was investigated in terms of the zero time-lag correlation functions of the envelope, $W_{x,Z}(r_x, \tau)$ and $W_{x,Z}(r_x, \tau)$. This is of interest mainly for the application of the wavelet spectral method described in the next section, since this method requires the measurements to be performed within an area smaller than the size of the wave group. The two smaller peaks with $\hat{k}_y \approx \pm 2$ of the transverse spectrum $S_{y,Z}(k_y, \omega)$ at the frequency $k_0 U_0$ for condition 7 (FIG. 5.22d) suggest the periodicity of the envelope, with the period equal to approximately half the wavelength of the stationary waves (which is also assumed to correspond to the wavelength of the carrier wave at the frequency $k_0 U_0$). This is confirmed by the measurements of the correlation function of the envelope, shown in FIG. 5.25. The peak of the correlation function corresponds to the half characteristic wavelength $2\pi/k_0$, hence to a phase difference of π. The location $r_y/(2\pi/k_0) = 0.25$ corresponds to the phase difference $\pi/2$. FIG. 5.23c showed that the surface elevation ζ at the frequency $k_0 U_0$ presents two waves with the wavelength $2\pi/k_0$ propagating in opposite directions along y. The results show that these two waves combine together to form a standing wave with the same wavelength. These standing waves determine the shape of the group along the transverse direction. In fact, the correlation is larger at the distance π/k_0, therefore between the crest and the trough of the standing waves, and it is zero at the distance $\pi/2k_0$, which corresponds to the nodal point of the system of standing waves.

The existence of transverse standing waves in channels of limited width is well known [e.g., Lamb, 1932, p.284], but these have the wavenumber which is an integer multiple of $2\pi/W_f$, where W_f is the channel width. In the measurements reported here the wavenumber of the standing waves scaled consistently with k_0, and it was generally much larger than $2\pi/W_f$ ($k_0 W_f$ varies between 14.4 in condition 10 and 60.4 in condition 4), so that the transverse waves would represent a relatively higher-order mode which is unlikely to dominate in a turbulent flow. FIG. 5.25c, d, show that the correlation of the transverse standing waves decays rapidly within a distance comparable with their wavelength. These results suggest that the observed standing-waves envelope is not related to the finite width of the channel.

5.4 Transient analysis

5.4.1 Introduction

The discussion so far was based on the assumption that the statistics of the free surface are stationary both in time and in space. The single-point statistics in section 5.2 have shown a weak nonlinearity of the free surface elevation in some flow conditions. These nonlinearities can manifest as deviations from the assumed stationarity of the free surface behaviour. The method of determining the frequency-wavenumber spectra from two orthogonal arrays of wave probes did not allow the direct observation of the three-dimensional spatial distribution of the waves, which instead had to be inferred based on the comparison with a hypothetical dispersion relation. In contrast, the analysis of the data based on the wavelet spectral method [Donelan et al., 1996] allows the relaxation of the assumption of stationarity at least in the time domain, and it allows the direct calculation of the direction of propagation of the waves in two dimensions, although it is subject to a set of strong limitations which have been discussed in section 3.1.9. The method also carries a direct relationship with the definition of wave groups, which formed the basis of the analysis described in sub-sections 5.2.3 and 5.3.3, and it allows the direct calculation of the fully three-dimensional spatial spectrum, at least in principle. The model which forms the basis of the method is that of a random combination of wave groups, each of them coherent and representable at least in a first approximation as a linear combination of two-dimensional gravity-capillary waves. The model therefore is suited for the study of the radial patterns of waves observed in the previous section. One more advantage of the wavelet spectral method compared to the measurement of the frequency-wavenumber spectra is that it only requires the measurement of the surface elevation at a limited number of locations. This makes it an attractive technique for the remote characterisation of the free surface dynamics.

The first aim of the analysis described in this section was to demonstrate that the dispersion relations which have been measured with long arrays of wave probes and based on the average frequency-wavenumber spectra still apply locally in time and in space, at least in the average sense, i.e., that the statistics of the free surface are effectively stationary. The second aim was to confirm the three-dimensional distribution of waves (the radial pattern) which had been inferred based on the frequency wavenumber spectra along the two orthogonal directions, in subsection 5.3.2. The third aim was to demonstrate that the dynamic behaviour of the free surface can be characterised based on the measurement of the free surface elevation at a limited number of points, and over a measurement area with limited size.

5.4.2 The wavelet spectral method applied to wave probes data

In the previous section the dimensions of the generalised wave groups were measured by the zero time-lag correlation of the envelope of the elevation. The knowledge of this dimension is fundamental for the correct application of the wavelet spectral method. In fact, in order for the wavelet spectral method to work effectively, each pair of probes had to be within the same wave group. Here the analysis with the wavelet spectral method was based on the measurements of the wavelet transform at probes $1_{(x)} \equiv 1_{(y)}$, $2_{(x)}$, and $3_{(y)}$. This set of probes was chosen as the best compromise between the resolution of the measurements and the requirement of both probes to be within the characteristic length of the wave groups. The distances between each pair of probes along the x- and y-directions were $r_x = 26.0\,\mathrm{mm}$ and $r_y = 35.0\,\mathrm{mm}$, respectively. Practically, it was required that the spatial correlation of the envelope be larger than zero at the distances r_x and r_y. Based on FIG. 5.24 and 5.25, the threshold on r_x was $r_x < 0.5 \times 2\pi/k_0$ at the higher frequency, and $r_x < 2\pi/k_0$ at the lower frequency. The constrain was stronger in the transverse direction, where r_y had to satisfy $r_y < 0.25 \times 2\pi/k_0$ both at the higher and at the lower frequency. At the lower frequency and with the depth $H \geq 70\,\mathrm{mm}$, the second peak of the correlation $W_{y,Z}(r_y, 0)$ at $r_y \approx 0.5 \times 2\pi/k_0$ allows the application of the method at the larger separations. The need for the correlation to be sufficiently large would suggest the reduction of the spacing between the probes. This in turn would increase the uncertainty of the analysis, since the wavenumber was calculated as the ratio between the phase difference and the separation. It is interesting to note that the shape of the envelope in the transverse direction at the frequency $k_0 U_0$ made so that the method works best in this frequency range when the separation is close to half of the wavelength of the standing waves, whereas it would not work at all if the separation equals a quarter of a wavelength. For the measurements presented here, the quarter wavelength varied between 11.9 mm in condition 4 to 50.1 mm in condition 10, and it was $0.25 \times 2\pi/k_0 = 17.5\,\mathrm{mm}$ in condition 2 and $0.25 \times 2\pi/k_0 = 34.8\,\mathrm{mm}$ in condition 5.

In order to illustrate the effect on the analysis of the separation between the probes relative to the characteristic dimensions of the groups, a different set of flow conditions were investigated here than in the previous sections. In condition 1 there were no secondary peaks of the correlation of the envelope, and the correlation decayed more slowly with respect to $r_y g/(2\pi U_0^2)$ than in the other conditions (see FIG. 5.24a, 5.25a). Both probes $1_{(y)}$ and $3_{(y)}$ were therefore expected to be within the same wave group in condition 1, which makes the wavelet spectral method applicable in this condition. The separation between probes $1_{(y)}$ and $3_{(y)}$ was within the main lobe of the correlation in condition 10, it was near half the wavelength $2\pi/k_0$ in condition 2, and it was near the quarter of the wavelength $2\pi/k_0$ in condition 5. Then, it is expected that the method would not work in condition 5, while it would work in conditions 10 and 2. The short relative distance between the probes in condition 10 is expected to reduce the resolution of the method in this condition. Therefore conditions 1, 2, 5, and 10 are representative of typical ratios between the transverse probes separation and the characteristic scales of the generalised wave group, and they represent different conditions for the validity of the method. These four conditions are analysed in this section.

Some examples of the absolute value of the wavelet transform computed from the measurement at probe $1_{(x)}$ in conditions 1, 2, 5, and 10, are shown in FIG. 5.27. In FIG. 5.27 the non-dimensional frequency scale was defined as $\hat{\omega} = \omega/k_0U_0$ for conditions 2, 5, and 10, and as $\omega U_0/g$ in condition 1. The three examples of FIG. 5.27 show that the amplitude of the wavelet transform was not constant in time at each scale, but showed a number of events with larger amplitude as well as less energetic intervals. This is consistent with the representation of the envelope of the surface elevation in FIG. 5.12. Most of the energy of the transform was near the non-dimensional frequency $\omega U_0/g = 0.5$ in condition 1 (FIG. 5.27a), and near the non-dimensional frequency $\hat{\omega} = 1$ in all the remaining conditions (see for example conditions 2, 7, and 13 in FIG. 5.27b, c, d). The behaviour at each scale appears to be independent from the other scales, which confirms the validity of a linear model of the surface elevation.

FIG. 5.28c, d shows the pdf of the wavenumbers $p_k(k_x, \omega)$ and $p_k(k_y, \omega)$ determined by the wavelet spectral method in condition 1, compared with the frequency-wavenumber spectra $S_x(k_x, \omega)$ and $S_y(k_y, \omega)$ (FIG. 5.28a, b). The resolution of the pdf $p_k(k_x, \omega)$ and $p_k(k_y, \omega)$ was clearly lower than that of the frequency-wavenumber spectra, but the ridges that represent both the non-dispersive waves and the gravity-capillary waves propagating downstream are clearly visible in FIG. 5.28c. The relationship between the scales of the wavelet and the frequency appears to be correct, since both dispersion relations approximate well the results.

The same pdf's $p_k(k_x, \omega)$ and $p_k(k_y, \omega)$ for condition 2 and for condition 5 are shown in FIG. 5.29 and 5.30, respectively. Like in the case for condition 1, the pdf of the streamwise wavenumber $p_k(k_x, \omega)$ (FIG. 5.29c and 5.30c) shows the same behaviour of the frequency-wavenumber spectrum $S_x(\hat{k}_x, \hat{\omega})$ (FIG. 5.29a and 5.30a), although its resolution is smaller. The patterns of radial waves which correspond to the ridge between $\hat{k}_x = -1$, $\hat{\omega} = 0$, and $\hat{k}_x = 1$, $\hat{\omega} = 2$ have been captured well by the wavelet spectrum, and the transition to the dispersive waves propagating upstream

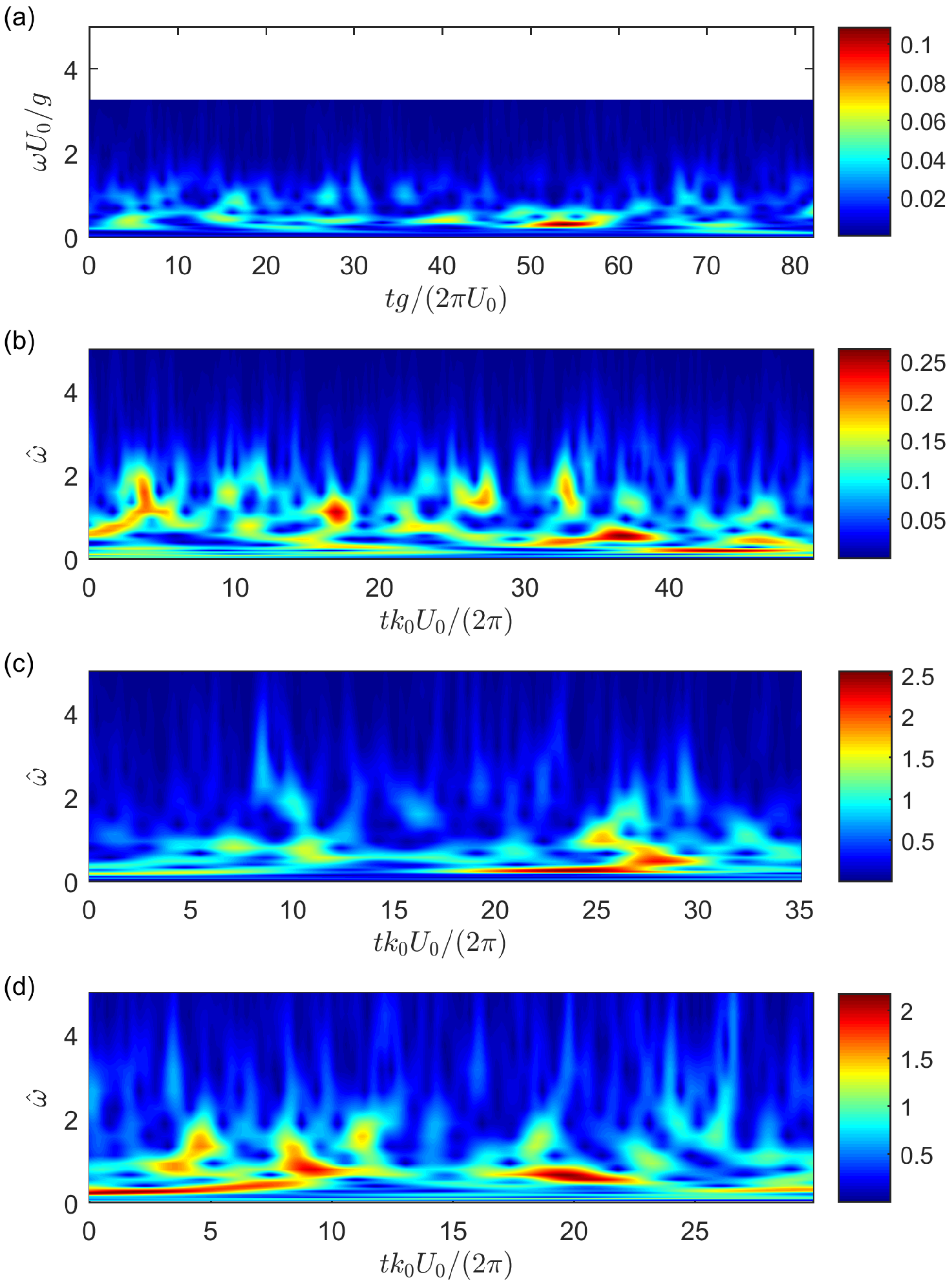

Figure 5.27: Contours of the amplitude of the wavelet transform $Z_W(t, \hat{\omega})$ of ζ measured at probe $1_{(x)}$. (a) Condition 1, (b) condition 2, (c) condition 5, and (d) condition 10.

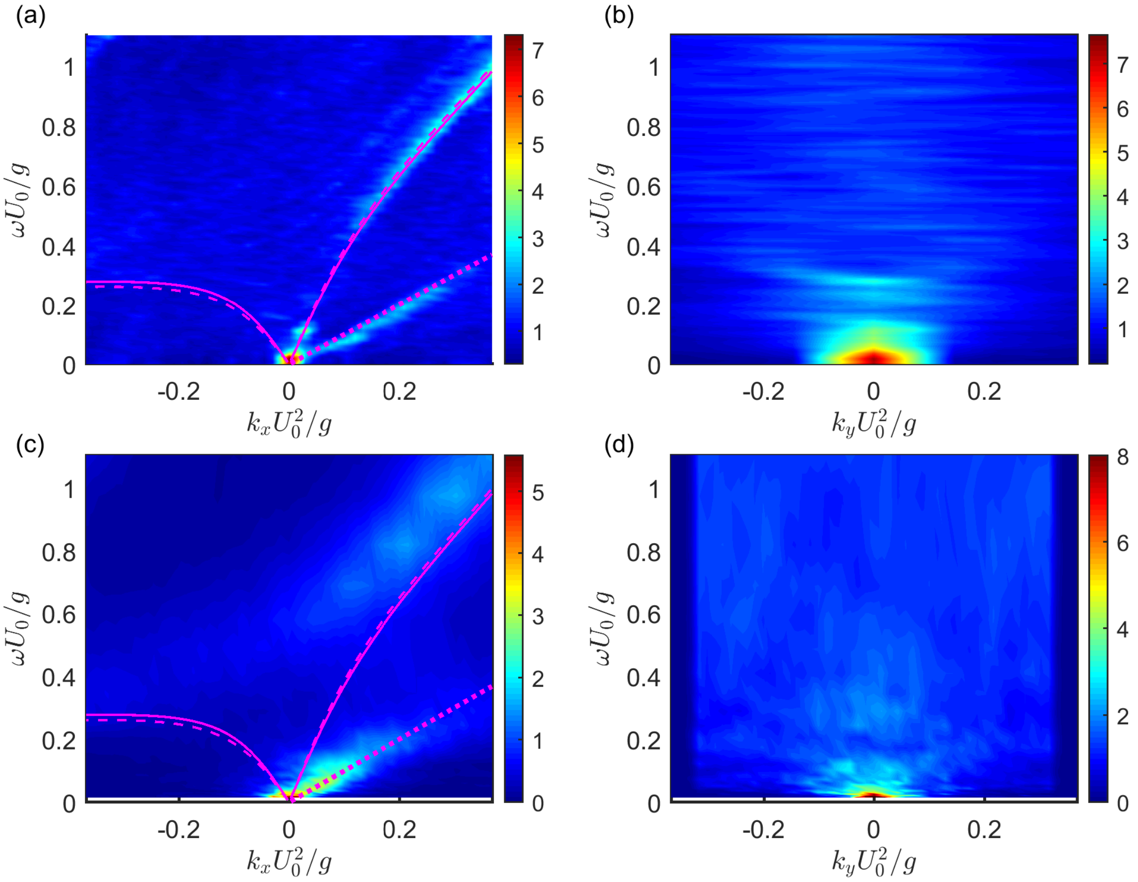

Figure 5.28: (a) The contour plot of the normalised frequency-wavenumber spectrum, $\bar{S}_x(k_xU_0^2/g, \omega U_0/g)$, for condition 1. (b) Normalised transverse frequency wavenumber-spectrum $\bar{S}_y(k_xU_0^2/g, \omega U_0/g)$. (c) The contour plot of the pdf of the streamwise wavenumber k_x, $p_k(k_xU_0^2/g, \omega U_0/g)$ determined by the wavelet spectral method. (d) The histograms of the tranverse wavenumber k_y, $p_k(k_yU_0^2/g, \omega U_0/g)$. (dashed) Irrotational dispersion relation, equation (3.20). (solid) Dispersion relation with the 1/3 velocity profile, $\theta = 0$, equation (3.26). (dotted) Non-dispersive relation, equation (3.21).

is also clearly recognisable at $\hat{k}_x = 1$ and $\hat{\omega} = 2$ in terms of the change of slope of the dispersion relation. The pdf of the transverse wavenumber $p_k(k_y, \omega)$ for condition 2 (FIG. 5.29d) shows the two symmetrical ridges which had been associated with the pattern of radial waves with the wavenumber modulus k_0. The same pattern cannot be distinguished from FIG. 5.30d for condition 5. In this condition the probes $1_{(y)}$ and $2_{(y)}$ were separated by a distance equal to half the wavelength of the standing waves, therefore their measurements had a little correlation. This demonstrates the importance of the choice of the probes separation for the accuracy of the wavelet spectral method.

The measurements of the two orthogonal wavenumbers, $k_x(t, \omega)$ and $k_y(t, \omega)$, were also used in order to estimate the direction of propagation of the waves based on the procedure described in sub-section 5.1.6. FIG. 5.31a shows an example of

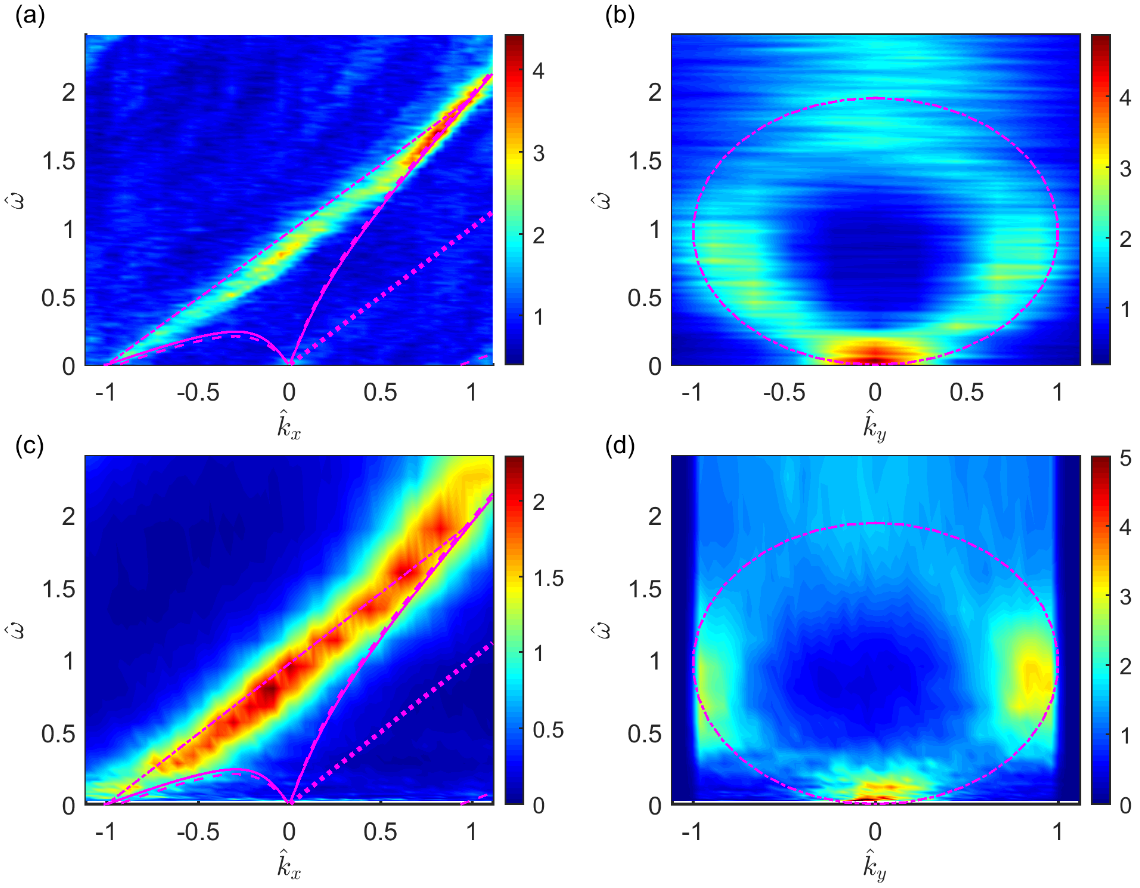

Figure 5.29: (a) The contour plot of the normalised frequency-wavenumber spectrum, $\bar{S}_x(\hat{k}_x, \hat{\omega})$, for condition 2. (b) Normalised transverse frequency wavenumber-spectrum $\bar{S}_y(\hat{k}_y, \hat{\omega})$. (c) The contour plot of the pdf of the streamwise wavenumber k_x, $p_k(\hat{k}_x, \hat{\omega})$ determined by the wavelet spectral method. (d) The histograms of the tranverse wavenumber k_y, $p_k(\hat{k}_x, \hat{\omega})$. (dashed) Irrotational dispersion relation, equation (3.20). (solid) Dispersion relation with the 1/3 velocity profile, $\theta = 0$, equation (3.26). (dotted) Non-dispersive relation, equation (3.21). (dashed-dotted) Dispersion relation with the 1/3 velocity profile, with constant $k = k_0$, equation (3.45).

the evolution in time of the angle $\theta(t, \omega)$ and of the weighted amplitude $\bar{Z}_W(t, \omega)$ measured in condition 2. The weighted amplitude $\bar{Z}_W(t, \omega)$ corresponds to the factor on the right hand side of equation (5.38), i.e.,

$$\bar{Z}_W(t, \omega) = \frac{\sqrt{Z_{W,2_{(x)}}(t, \omega) Z^2_{W,1_{(x)}}(t, \omega) Z_{W,3_{(y)}}(t, \omega)}}{\sum_\mu \sqrt{Z_{W,2_{(x)}}(t, \omega) Z^2_{W,1_{(x)}}(t, \omega) Z_{W,3_{(y)}}(t, \omega)}}. \tag{5.46}$$

The angle $\theta(t, \omega)$ in FIG. 5.31a varies smoothly in time until $t = 5.4\,\mathrm{s}$, then it changes rapidly. At the same instant $t = 5.4\,\mathrm{s}$ the normalised amplitude of the wavelet transform has a minimum. The change of both the phase and the amplitude is associated with the passage of two distinct groups of waves. It shows that

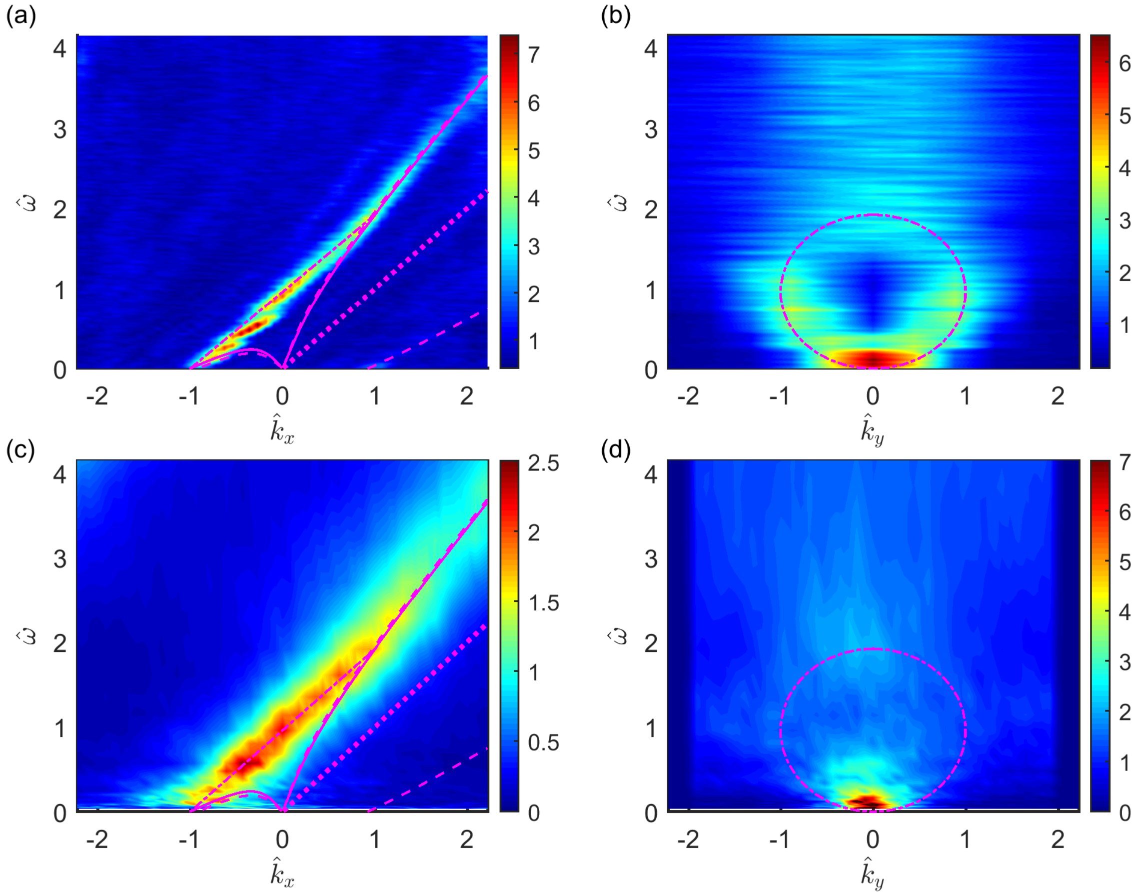

Figure 5.30: (a) The contour plot of the normalised frequency-wavenumber spectrum, $\bar{S}_x(\hat{k}_x, \hat{\omega})$, for condition 5. (b) Normalised transverse frequency wavenumber-spectrum $\bar{S}_y(\hat{k}_y, \hat{\omega})$. (c) The contour plot of the pdf of the streamwise wavenumber k_x, $p_k(\hat{k}_x, \hat{\omega})$ determined by the wavelet spectral method. (d) The histograms of the tranverse wavenumber k_y, $p_k(\hat{k}_x, \hat{\omega})$. (dashed) Irrotational dispersion relation, equation (3.20). (solid) Dispersion relation with the 1/3 velocity profile, $\theta = 0$, equation (3.26). (dotted) Non-dispersive relation, equation (3.21). (dashed-dotted) Dispersion relation with the 1/3 velocity profile, with constant $k = k_0$, equation (3.45).

each group can have a different direction of propagation of the waves that compose it. The behaviour shown in FIG. 5.31a is representative of the behaviour at all frequencies. This is demonstrated in FIG. 5.31b, which shows the average normalised correlation in time of the detrended weighted amplitude $\bar{Z}_W(t, \omega)$ with the absolute time-gradient of the angle $\theta(t, \omega)$, calculated at each frequency in condition 2. The correlation has a negative peak at $\tau = 0$, which shows that the minima of the amplitude correlate instantaneously with the gradient of $\theta(t, \omega)$, i.e., that the largest changes of the angle occur at the minima of the amplitude.

The pdf of the angle of propagation θ is shown in FIG. 5.32 for the conditions 1, 2, 5, and 10. These are compared with the relation $\Omega(k_0, \theta)$ obtained from equation (3.45). This relation represents the expected angular distribution of the radial

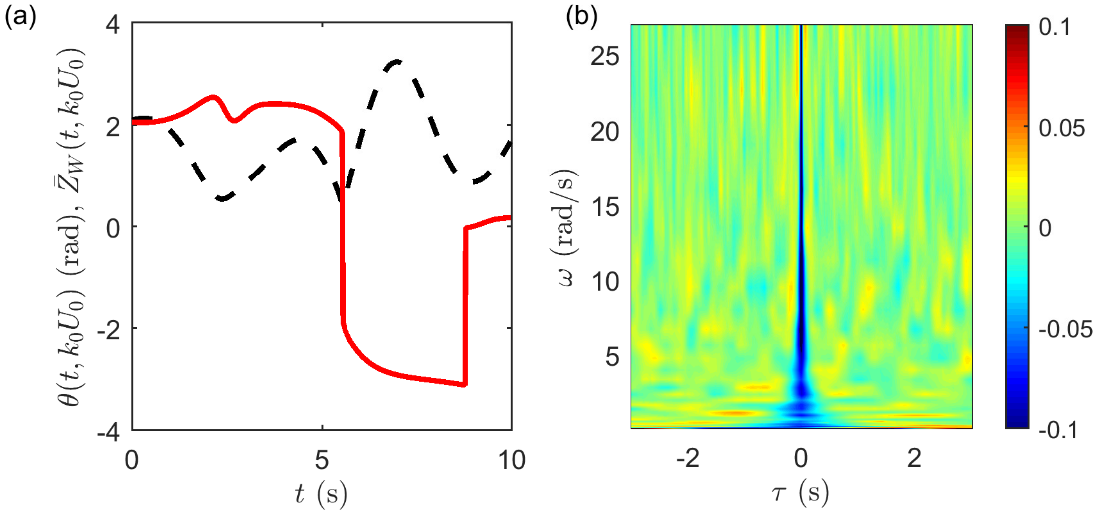

Figure 5.31: (a) An example of the evolution in time of (red) the angle $\theta(t, \omega)$ and of (black dashed) the normalised wavelet amplitude $\bar{Z}_W(t, \omega)$ at the frequency $\omega = k_0U_0$ measured in condition 2. (b) Average time-correlation of the normalised wavelet amplitude $\bar{Z}_W(t, \omega)$ with the absolute gradient of the angle $\theta(t, \omega)$ measured in the same condition.

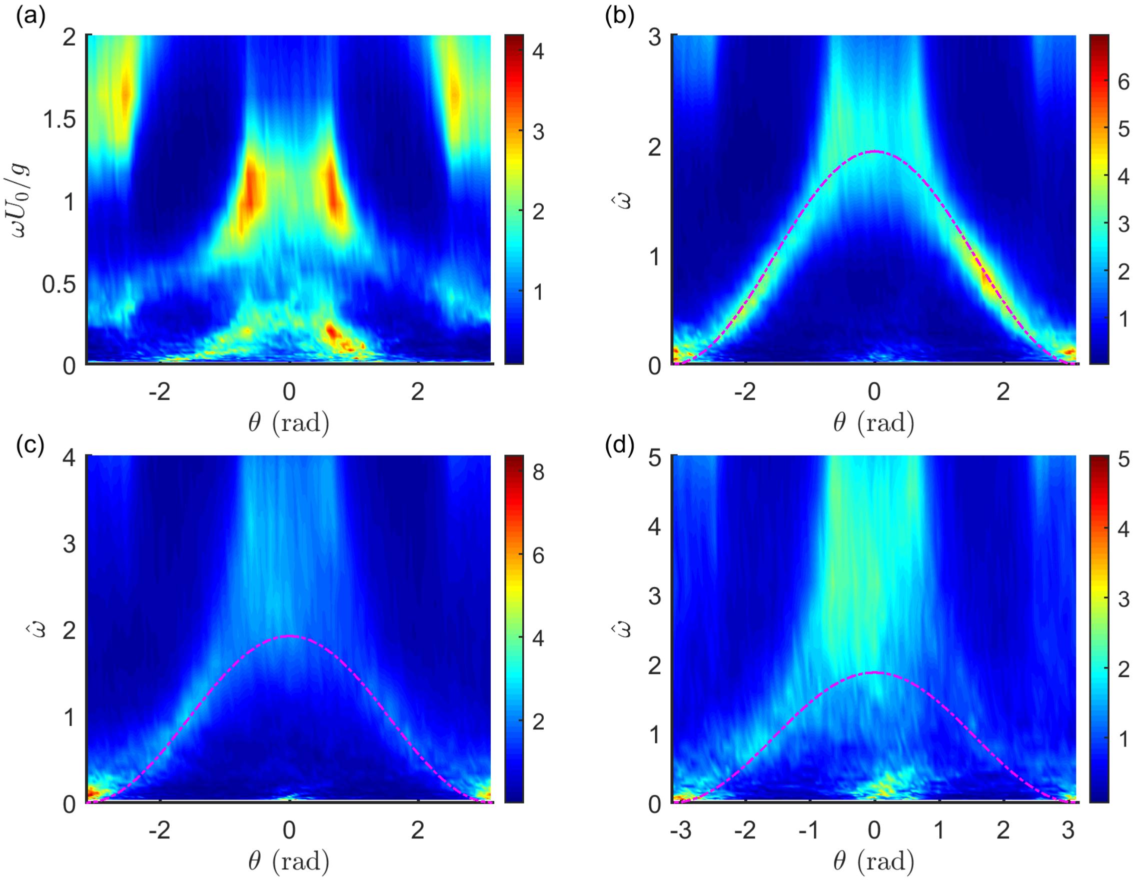

Figure 5.32: The pdf of the angle of propagation θ, $p_\theta(\theta, \omega)$ for (a) condition 1, (b) condition 2, (c) condition 5, and (d) condition 10. (dashed-dotted) Angular distribution of the radial pattern, $\omega(k_0, \theta)$, according to equation (3.45).

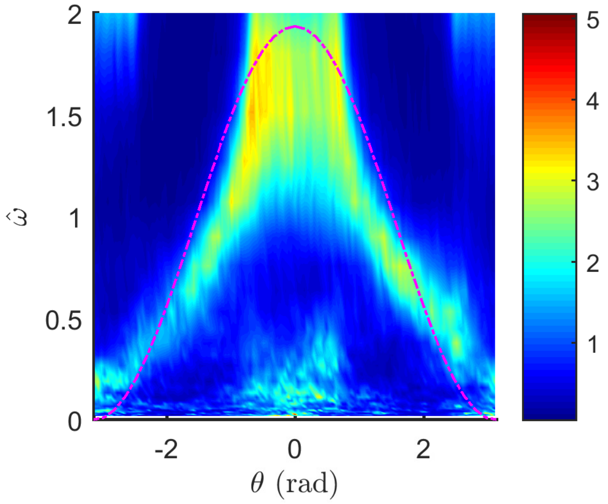

Figure 5.33: The pdf of the angle of propagation θ, $p_\theta(\theta, \omega)$ for condition 4. (dashed-dotted) Angular distribution of the radial pattern, $\omega(k_0, \theta)$, according to equation (3.45).

pattern of waves with the modulus of the wavenumber equal to k_0. FIG. 5.32 shows that the equation (3.45) represents well the measured histograms of the angle of propagation in conditions 2, 5, and 10. The best resolution is found in condition 2 (FIG. 5.32b), where the separation between the two probes $1_{(y)}$ and $3_{(y)}$ was close to half the wavelength $2\pi/k_0$, therefore to the distance between the two peaks of the standing waves envelope. FIG. 5.32d has a very low resolution especially at the lower frequency. The pdf for condition 5 shown in FIG. 5.32c shows the expected behaviour of $p_\theta(\theta, \omega)$, but this is much less clear than FIG. 5.32b. These observations can be explained based on the position of the wave probes relative to the nodes of the transverse standing wave.

The pdf $p_\theta(\theta, \omega)$ in condition 1 (see FIG. 5.32a) shows a complex pattern of waves, which are apparently three-dimensional. The waves with the frequency $\hat{\omega} < 0.5$ were believed to represent mainly non-dispersive waves propagating downstream and parallel to the mean surface velocity. The waves with the frequency $\hat{\omega} > 0.5$ were believed to represent dispersive waves propagating downstream, still parallel to the mean surface velocity. FIG. 5.32a suggests that both types of waves have a transverse component. The waves with the frequency $\hat{\omega} \approx 0.3$ appear to travel against the flow with the angle $\theta = \pi$, in accordance with the observations in the previous sections.

As a final result, FIG. 5.33 shows the pdf of the angle θ for condition 4. This condition is shown here because it was observed from the frequency-wavenumber spectra of FIG. 5.17 that the dispersion relation based on the radial pattern with the wavenumber modulus k_0 did not represent well the measured data. FIG. 5.33 confirms this observation. More specifically, it shows that the measured pattern has the larger frequency than predicted by equation equation (3.45) at the angle $\theta \approx \pm\pi$, and the lower frequency at the angles $|\theta| \leq 2$. In terms of the wavelength of the radial pattern, this appears to be approximately $0.7 \times 2\pi/k_0$, hence smaller than the expected wavelength $2\pi/k_0$.

5.4.3 Discussion

The main result of the analysis presented in this section has been to demonstrate that the dispersion relation of the waves on the free surface of a shallow turbulent flow can be determined from the measurement of the free surface elevation at three locations, based on the wavelet spectral method [Donelan et al., 1996]. The pdf obtained with the wavelet transform have less resolution than the frequency-wavenumber spectra determined from the arrays of wave probes. The resolution of the pdf of the angle of propagation depends greatly on the distance between the two probes along y relative to the dimension of the standing waves. The relative lack of clarity of FIG. 5.32c for condition 5 compared to FIG. 5.32b for condition 2 can be explained by noticing that the distance between the probes $1_{(y)}$ and $3_{(y)}$ for condition 5 was close to $0.25 \times 2\pi/k_0$, which corresponds to the node of the standing-wave envelope based on the discussion in sub-section 5.3.3. The absence of the pattern of radial waves in the histograms of the transverse spectrum for condition 5 (FIG. 5.30d) can also be explained by the same phenomenon.

In all the conditions represented in FIG. 5.32 the measured pdf show that the angle θ does not approach zero when the frequency increases above $\hat{\omega} = 2$. This is in contrast with the statements in section 5.3, where it was inferred from the frequency wavenumber spectra in the two orthogonal directions that the waves at the higher frequency were two-dimensional and propagated parallel to the mean surface velocity. This apparent contradiction can be resolved once it is noticed that the wavelet spectral method works under the assumption that all probes are within the same group, or envelope, at each wavelet scale. The apparent three-dimensionality of the shorter waves can be explained if it is assumed that the short waves that propagate downstream are also relatively short in the direction parallel to the wave crests. The consequence of this assumption would be that the groups are only detected correctly by the pair of probes $1_{(y)}$ and $3_{(y)}$ when they travel at an angle with respect to the x-direction, which explains the bias in favour of the angles $\theta \neq 0$. In condition 2, for example, the transverse correlation function of the envelope at the frequency $2.5k_0U_0$, $W_{y,Z}(r_y, 0)$, decays to zero at the separation $r_y \approx 0.3 \times 2\pi/k_0$. In this condition and at this frequency the pair of probes $1_{(y)}$ and $3_{(y)}$ is not adequate for the application of the wavelet spectral method.

In spite of the limitations of the analysis technique, the wavelet spectral method has confirmed the validity of the model of the radial pattern of waves which had been inferred in the previous section from the measurements in two orthogonal directions. The applicability of the method depends greatly on the design of the experimental apparatus. Nonetheless, the technique has large potential for application since it removes the requirement to instrument a large measurement area, which may be impractical in some situations. It also opens the possibility for the investigation of the dynamics of the free surface locally, which in turn may be helpful for the local characterisation of the flow conditions. In fact, the method allows the instantaneous calculation of the wavenumber, and of the angle of propagation. FIG. 5.31 shows that these quantities are not constant at each frequency, and that their variation occurs more rapidly near the minima of the wavelet amplitude. This suggests that the waves are coherent within one group, but independent among different groups, which is in agreement with a model of wave groups [Donelan et al., 1996]. As anticipated in the introduction to this section, this fact may be of large importance for the localisation of the phenomena that generate the free surface fluctuations.

5.5 Summary

This chapter has shown the results of an experimental investigation of the dynamic properties of the free surface elevation of a shallow turbulent flow in a flume with a homogeneously rough bed. The measurements have been analysed with a variety of techniques of increasing complexity, in order to identify the different aspects of the free surface which would allow the remote characterisation of the hydraulic properties of the flow. At all stages it was possible to identify a direct link between the statistical, spatial, and temporal characteristics of the free surface and a small set of hydraulic parameters, mainly the mean surface velocity U_0 and the characteristic wavenumber of the stationary waves, k_0. The latter can be determined from the values of U_0 and H, and from the knowledge of the streamwise average velocity profile within the flow, although the change in the streamwise velocity profile was small within the range of flow conditions studied here. The observed links apply to most of the tested conditions, and apparently relate to the fact that the interaction with the rough bed was the dominant phenomenon that caused the generation of the free surface fluctuations in these conditions.

The first section of this chapter has shown that the statistics of the free surface measured at one single point in space are generally in good agreement with a linear model based on the trigonometric expansion of the surface elevation, where all coefficients of the expansion are mutually independent and the phase of each term is uniformly distributed. Some relatively small deviations from this model have been observed, and these were represented well by a higher-order weakly nonlinear model. These small deviations can have a significant effect on the scattered acoustic field. Currently there are no simple nonlinear surface models that apply to shallow turbulent flows over a homogeneously rough bed. A linear model is used in the next chapter in order to study the scattering of the acoustic pressure field by the dynamic surface. The effect of nonlinearities will be inferred based on the deviation between the measurements and this linear model. The results of the statistical analysis also suggested that the dynamics of the free surface are the result of a combination of many independent processes, randomly distributed in time and/or in space. This suggests the marginal role of isolated coherent events such as the interaction with coherent turbulent structures in the flow, as these would have resulted in a stronger deviation from the Gaussian statistics and a larger coherence of the surface elevation itself.

The measurements with linear arrays of wave probes along two orthogonal directions allowed the estimation of the frequency-wavenumber spectra, and of the spatial correlation functions. These measurements evidenced clearly the existence of gravity-capillary waves and of non-dispersive waves with a preferred spatial directionality. The dominant role of the interaction with the rough bed was also revealed, as it caused the generation of the dominant patterns of stationary waves. Additional patterns on the free surface which could be explained by the interaction with turbulence were also observed, although the results could not be conclusive due to the lack of information regarding the dynamics of turbulence within the flow. It should be noted here that the fundamental mechanism proposed by Teixeira and Belcher [2006] does not prescribe the interaction of the free surface with individual coherent structures, but rather the resonant matching of the surface waves with turbulence with the same spectrum, similarly to Miles [1957]. In fact, the model of Teixeira and Belcher [2006] was essentially linear, and also the non-resonant forcing observed by these authors was determined from the same linear approach. These mechanisms are not in contrast with the quasi-Gaussian statistics of the surface elevation observed in this chapter.

The models of the dispersion relation presented in section 3.1 approximated well the measured frequency-wavenumber spectra in most of the tested flow conditions. Still, their interpretation is not obvious. The details of the mechanism that produced the patterns of radial waves with the wavenumber k_0 is not explained, neither is the apparent directionality of the shorter waves that propagate downstream. The waves generated by the interaction with a single disturbance on the bed have been discussed theoretically in section 3.1.5. The resulting patterns on the free surface are three dimensional and dynamic [Harband, 1976], and coherent at least away from the disturbance. When the disturbance is distributed uniformly, there are no known analytical solutions which can justify the measurements described in this chapter. It is postulated that the observed patterns may be generated by the interaction among waves propagating at different angles, as demonstrated by Shrira [1993] in conditions that do not strictly apply to the measurements reported here. Further investigations are needed in order to demonstrate the existence of these interactions.

In summary, the scenario that emerges from the experimental results described in this chapter is as follows. The main mechanism which produces the patterns on the free surface of a shallow turbulent flow with rough boundary is the interaction with the boundary. This mechanism generates gravity-capillary waves with a deterministic dispersion relation and three dimensional distribution, but which can be described approximately by the linear superposition of infinitesimal sinusoidal waves with random phase. When the mean surface velocity is larger than the minimum phase velocity of gravity capillary waves, the largest waves are stationary. The three dimensional pattern consists of waves with the wavenumber of the stationary waves which propagate in all directions. Shorter waves propagate parallel to the direction of the flow, in both directions. When the mean surface velocity is smaller than the minimum phase velocity of gravity capillary waves, there are no stationary waves and all waves are two-dimensional. There are also non-dispersive waves that propagate at the mean surface velocity. The variations of the amplitude of the surface fluctuations is explained by the random linear interaction of all types of waves. The waves that form the radial pattern originate groups that apparently fluctuate vertically as they are advected at the mean surface velocity. The waves in each group are coherent, while separate groups appear to be mutually incoherent. Their shape in the transverse direction is dominated by pairs of standing waves.

Chapter 6

Analysis of the Doppler spectra of the acoustic field scattered by the free surface

The purpose of this chapter was to investigate the relation between the hydraulic conditions and the Doppler spectrum of the acoustic field scattered by the free surface of shallow turbulent flows. In section 3.2 it was shown that the relation between the statistics of the free surface and the properties of the scattered acoustic pressure field are not trivial. The measurements described in chapter 5 identified a set of parameters and relations which characterise the topology and dynamics of the free surface in the set of conditions listed in Table 4.2. These parameters are sufficient to inform a simplified linear model of the free surface. This model is used in order to interpret the measurements of the acoustic Doppler spectra.

The methodology followed in this chapter was as follows. The Doppler spectrum of the scattered acoustic pressure field was measured in the experimental flume described in section 4.1 with the acoustic setups described in section 4.4. The tests were performed in all the experimental conditions reported in Table 4.2. The parameters of the free surface measured in chapter 5 were implemented in a linear surface model in order to generate random realisations of the dynamic roughness. For each of these realisations, the corresponding scattered acoustic field was simulated numerically with two models based on the Kirchhoff approximation. The Doppler spectra of the simulated scattered acoustic pressure field were finally compared with the experimental measurements. The comparison had two objectives. The first objective was the validation of the simplified model of the surface dynamics. The second objective was the illustration of the effects of the surface parameters on the acoustic Doppler spectra. The Doppler spectra were measured both in the backscattering (monostatic) configuration and in the forward scattering (bistatic) configuration. The first configuration corresponds to the measurement with microphone 1, while the second configuration corresponds to the measurement with microphone 2 described in subsection 4.4.2. The results are reported in subsections 6.2.1 and 6.2.2, respectively.

The experimental results in section 5.2.2 have shown that the statistics of the free surface elevation were quasi-Gaussian in all the tested flow conditions reported in Table 4.2. This justified in principle the representation of the surface in terms of a linear model with randomly distributed phase in those conditions where the observed nonlinearity was statistically not significant (conditions 1, 2, 4, 5, 7, 9, 11, and 13). In the remaining conditions, a weak but statistically significant nonlinearity of the statistics of the free surface was observed. It was suggested that these weak nonlinearity may have been caused by weak interactions among waves [Creamer et al., 1989, Janssen, 2003, 2009], as described in subsection 3.1.6. These interactions, however weak, can cause large variations of the Doppler spectrum of the scattered acoustic field (see subsection 3.2.2). Thus, a nonlinear model of the free surface dynamics would represent the scattering by the surface more accurately. None of the existing nonlinear models seem to apply to the free surface of shallow turbulent flows over a homogeneous rough bed (see the discussion in subsection 2.1.5). Therefore, a linear model was used instead. Eventual deviations between the predictions based on this model and the measurement are discussed, with reference to the analysis presented in subsection 3.2.2.

This chapter is organised as follows: Section 6.1 introduces the numerical models of the dynamic free surface and of the acoustic Doppler spectrum. Subsection 6.2.1 shows the analysis of the Doppler spectra measured in the backscattering configuration, and their comparison with the predictions by two numerical models of the same spectra. Subsection 6.2.2 presents the same type of analysis applied to the spectra measured in the forward scattering configuration. Section 6.3 summarises the main results of the chapter, and presents the final conclusions.

6.1 Numerical models of the acoustic scattering

6.1.1 Surface model

The linear model of the free surface adopted here represents a random realisation of the surface elevation ζ in terms of a double Fourier series, where the phase $\Phi_{l,m}$ of each term of the series is a random variable with uniform distribution. This type of model was introduced in subsection 3.1.1. The coefficients of the Fourier series that constitutes the linear model are proportional to amplitude spectrum at the wavenumber $\mathbf{k}_l$ and frequency ω_m, $A(\mathbf{k}, \omega)$, multiplied by a random variable $\xi_{l,m}$. The series representation is

$$\zeta(x, y, t) = \sum_l \sum_m \xi_{l,m} A\left(\mathbf{k}_l, \omega_m\right) \Re\left\{e^{i\left[\mathbf{k}_l \cdot \boldsymbol{\rho} - \omega_m t + \Phi_{l,m}\right]}\right\}, \tag{6.1}$$

where $\boldsymbol{\rho} = \sqrt{x^2 + y^2}$. Equation (6.1) is the discrete version of equation (3.1), introduced in Chapter 3. In order to obtain a relevant representation of the free surface, the measured frequency-wavenumber spectra could be introduced directly into the formulation of equation (6.1), based on equation (3.5). In practice, only the spectra in two orthogonal directions, $S(k, \omega, 0)$ and $S(k, \omega, \pi/2)$, could be measured as reported in subsection 5.3.2. The short waves with the wavelength smaller than 10 mm which will be shown to have the largest impact on the acoustic scattering could not be characterised due to the geometry of the wave probes (subsection 4.3). The noise introduced by the measurement with non-equidistant arrays of wave probes in section 5.3.2 impeded the accurate calculation of the spatial spectra $S(k, \theta)$ even in the two directions x and y. Therefore, it was decided to represent the frequency-wavenumber spectrum in terms of a simplified model of the spatial spectrum $S(k, \theta)$, which is related to the frequency-wavenumber spectrum by (see equation (3.9))

$$S(\mathbf{k}, \omega) = S(\mathbf{k}) \delta\left(\omega - \Omega(\mathbf{k})\right) = S(k, \theta) \delta\left(\omega - \Omega(k, \theta)\right). \tag{6.2}$$

The amplitude of the spectrum was modelled assuming a power-function dependence on the wavenumber k. This shape of the spectrum is widely used in a variety of applications, as discussed in subsection 2.1.6. It allows the simple computation of the average spatial statistics of the rough surface, which are used in order to predict the range of validity of the acoustic model in section 6.1.2. It can also be easily extrapolated to the shorter scales which could not be resolved by the measurements. Due to the simplified shape of the spectrum, some discrepancies between the measurements of the scattered acoustic field and the numerical models are expected. On the other hand, the adoption of a spectrum with a simple mathematical representation has the advantage of making the results presented here of more general validity.

The model of the dispersion relation $\Omega(\mathbf{k})$ in equation (6.2) was based on the measurements of the frequency wavenumber spectra of the surface elevation discussed in section 5.3.2. It represented all three types of waves that had been identified from the frequency wavenumber spectra: gravity-capillary waves propagating upstream, gravity-capillary waves propagating downstream, and non-dispersive waves moving at the velocity close to the mean surface velocity. The latter were only observed in condition 1 where the mean surface velocity was smaller than the minimum phase velocity of gravity-capillary waves, but it was suggested that they may still be present in the remaining flow conditions. Therefore they have been modelled in all flow conditions. A radial pattern of waves with the constant modulus of the wavenumber equal to k_0 was also observed in all conditions except condition 1 in section 5.3.2. In the model, the variation of the power spectrum with the angle of orientation θ was represented by a directional distribution $\Gamma(k,\theta)$, i.e.,

$$S(k,\theta) = S(k)\Gamma(k,\theta), \tag{6.3}$$

$$S(k)dk = |A(k)dk|^2 . \tag{6.4}$$

Based on equation (6.1), and with the dispersion relations measured in section 5.3, a single realisation of the surface elevation ζ was computed as

$$\begin{aligned} \zeta(x,y,t) = & \sum_n \sum_l A(k_l)\sqrt{\Gamma(k_l,\theta_n)} \\ & \Re\left\{ \xi^+_{l,n} e^{i\left[k_l \cos(\theta_n)x + k_l \sin(\theta_n)y - \Omega^+(k_l,\theta_n)t + \Phi^+_{l,n}\right]} \right. \\ & + \xi^-_{l,n} e^{i\left[k_l \cos(\theta_n)x + k_l \sin(\theta_n)y - \Omega^-(k_l,\theta_n)t + \Phi^-_{l,n}\right]} \\ & \left. + \, \xi^U_{l,n} e^{i\left[k_l \cos(\theta_n)x + k_l \sin(\theta_n)y - \Omega^U(k_l,\theta_n)t + \Phi^U_{l,n}\right]} \right\} , \end{aligned} \tag{6.5}$$

where ξ^+, ξ^-, and ξ^U are random variables with normal distribution and mean zero, and Φ^+, Φ^-, and Φ^U are random variables with uniform distribution in the interval between 0 and 2π. Equation (6.5) is a generalisation of equation (3.53), therefore $\zeta(x,y,t)$ is a random variable with Gaussian distribution. The superscripts $+$, $-$, and U represent the contributions from the dispersive downstream waves, from the dispersive upstream waves, and from the non-dispersive waves, respectively.

In chapter 5 it was shown that the dispersion relation of the free surface was represented well in the measured range of flow conditions by a model where the time averaged streamwise velocity profile follows a power-law of the depth with the exponent 1/3. This dispersion relation must be found numerically with an iterative procedure. In the same chapter it was shown that the simpler irrotational model also provides a relatively good representation of the dynamics of the free surface. The difference between the dispersion relations predicted by these two models was found to be very small, especially for the shorter Bragg waves which are more important for the backscattered acoustic field. Therefore, the three dispersion relationships in equation (6.5) were defined based on the irrotational linearised surface equations described in subsection 3.1.2. $\Omega^+(k,\theta)$ and $\Omega^-(k,\theta)$ represented the dispersive waves propagating downstream and upstream, respectively, and were defined by equation

(3.20) with the plus and minus sign, respectively. $\Omega^U(k,\theta)$ represented the non-dispersive waves that propagate with the flow mean surface velocity, and were defined by equation (3.21). Each of these three dispersion relations corresponds to one of the patterns observed in subsection 5.3.2.

The wavenumber spectrum had the simplified form

$$S(k) = \begin{cases} S_0 \left(\dfrac{k}{k_0}\right)^{-\alpha}, & \text{if } k_0 \le k \le k_1 \\ 0, & \text{otherwise} \end{cases}, \tag{6.6}$$

where the value of the normalisation factor S_0 was such that

$$\frac{1}{2\pi}\int_{-\pi/2}^{\pi/2}\int_0^{\infty} \Gamma(k,\theta)S(k)kdkd\theta = \sigma^2. \tag{6.7}$$

In the flow condition 1 where k_0 could not be defined based on equation (3.41), the characteristic wavenumber

$$k_0 = \frac{U_0^2}{2g} \tag{6.8}$$

was used instead, and the spectrum had the alternative form

$$S(k) = \begin{cases} S_0, & \text{if } k < k_0 \\ S_0 \left(\dfrac{k}{k_0}\right)^{-\alpha}, & \text{if } k_0 \le k \le k_1 \\ 0, & \text{if } k \ge k_1 \end{cases}. \tag{6.9}$$

This allowed taking into account the presence of very long waves in condition 1 and ensured that the knee of the frequency spectrum occurred at the frequency $\omega = U_0/g$ in accordance with the measurements in FIG. 5.7a, as it will be shown. The wavenumber $k_1 = 2\pi/l_1$ represented the smallest scales which were resolved by the model, in all conditions.

In order to further simplify the dependence of the spectrum on the direction of propagation, the function $\Gamma(k,\theta)$ was factorised as

$$\Gamma(k,\theta) = \Gamma_\theta(\theta)\Gamma_k(k). \tag{6.10}$$

It was decided to employ two types of standard angular distributions which are commonly applied to the study of oceanic waves [Hauser et al., 2005, p. 45], the so-called Poisson distribution

$$\Gamma_\theta(\theta) = \frac{1}{2\pi}\frac{1-b_\theta^2}{1-2b_\theta\cos(\theta)+b_\theta^2},\ 0 < b_\theta < 1, \tag{6.11}$$

and the sech^2 distribution

$$\Gamma_\theta(\theta) = \frac{1}{\tanh\left(b_\theta \pi\right)} \frac{b_\theta}{2\cosh^2\left(b_\theta \theta\right)},\ b_\theta > 0. \tag{6.12}$$

b_θ is a constant in both equations (6.11) and (6.12). The Poisson distribution is often used because of its simple Fourier representation, which makes it easy to characterise it from a limited number of measurements. The sech^2 distribution was applied by Donelan et al. [1985] because of its link to the shape of the solitary wave solution with envelope sech^2, and therefore to a model based on wave packets (see subsection 3.1.9). The geometry of the wave probes could make the sensitivity of the measurements dependent on the orientation of the waves, which made the direct measurements of the angular spectrum $\Gamma_\theta(\theta)$ of limited reliability. The sensitivity is expected to be the same for the waves that propagated parallel to the mean flow but in the two opposite directions, i.e., for the downstream waves with $\theta = 0$ and for the upstream waves with $\theta = \pi$. Therefore the amplitude of the frequency-wavenumber spectra for the two-dimensional waves propagating in these two directions were used in order to define the parameter b_θ in both equations (6.11) and (6.12), so that they fitted the experimental observations. From the frequency-wavenumber spectra for condition 1 in FIG. 5.18a one can see that the non-dispersive two-dimensional waves were approximately 2 to 3 times larger than the dispersive waves that propagated downstream in this condition. The same spectra for conditions 7 and 13 show that the spectrum of the waves with $\theta = \pi$, $k_x = -k_0$, and $\omega = 0$ was approximately one order of magnitude (10 times) larger than the spectrum of the waves with $\theta = 0$, $k_x = k_0$, and $\omega = 2k_0U_0$. Therefore the parameter b_θ for both the Poisson and the sech^2 distributions was selected in such a way that

$$\Gamma_\theta(\pi) = 10\Gamma_\theta(0), \tag{6.13}$$

i.e., $b_\theta = 0.5195$ for the Poisson distribution and $b_\theta = 0.5788$ for the sech^2 distribution. The distributions were further normalised such that

$$\Gamma_\theta(\pi/2) = 1. \tag{6.14}$$

As a result, $\Gamma_\theta(\theta)$ was represented by the equations

$$\Gamma_\theta(\theta) = \frac{1 + b_\theta^2}{1 - 2b_\theta \cos\theta + b_\theta^2}, \tag{6.15a}$$

$$\Gamma_\theta(\theta) = \frac{\cosh^2\left(b_\theta \pi/2\right)}{\cosh^2\left(b_\theta \theta\right)}, \tag{6.15b}$$

for the Poisson and for the sech^2 distribution, respectively.

In all conditions except condition 1, the wavenumber-dependent factor of the distribution, $\Gamma_k(k)$ was defined as

$$\Gamma_k(k) = \begin{cases} 0, & \text{if } k < k_0 \\ 1, & \text{if } k = k_0 \\ \delta(\theta - \theta_0), & \text{if } k > k_0, \end{cases} \tag{6.16}$$

where $\theta_0 = 0$ for the downstream waves and $\theta_0 = \pi$ for the upstream waves. This produced a radial pattern of waves with the wavenumber modulus k_0 and the amplitude governed by $\Gamma_\theta(\theta)$, and an additional pattern of waves with wavenumber modulus larger than k_0 propagating only along the x-direction, in accordance with the measurements in subsection 5.3.2. In condition 1 the radial pattern of waves was not observed in the measurements, therefore it was assumed that

$$\Gamma_k(k) = \delta(\theta - \theta_0), \tag{6.17}$$

for both types of waves.

It was always assumed that the non-dispersive waves with the frequency $\omega^U(k, \theta)$ propagate only parallel to the mean flow direction, in accordance with the measurements in subsection 5.3.2. For these waves the angular distribution was

$$\Gamma(k, \theta) = \Gamma_\theta(\pi/2)\delta(\theta), \tag{6.18}$$

where the factor $\Gamma_\theta(\pi/2)$ only ensured that the amplitude of these waves was intermediate between the upstream and the downstream propagating dispersive waves, as observed experimentally.

One additional test was performed with the distribution

$$\Gamma(k, \theta) = \Gamma_\theta(\theta), \tag{6.19}$$

which was independent of the wavenumber. This produced a pattern of waves of all wavenumbers propagating in all directions.

FIG. 6.1a shows the separate contributions to the spectrum $S(k)\Gamma(k, \theta)$ as calculated from equations (6.15a) and (6.16) for the three types of waves, as a function of the wavenumber in the streamwise direction, k_x. FIG. 6.1b shows the average across 50 realisations of the time-averaged spatial spectrum of the modelled dynamic surface, obtained for condition 7 with $\alpha = 7$, $k_1 = 2\pi/0.003\,\mathrm{rad\,m^{-1}}$, and with $\Gamma_\theta(\theta)$ given by the Poisson distribution. The spatial spectrum in FIG. 6.1b contains the contribution from the three types of waves, which combine to produce an almost

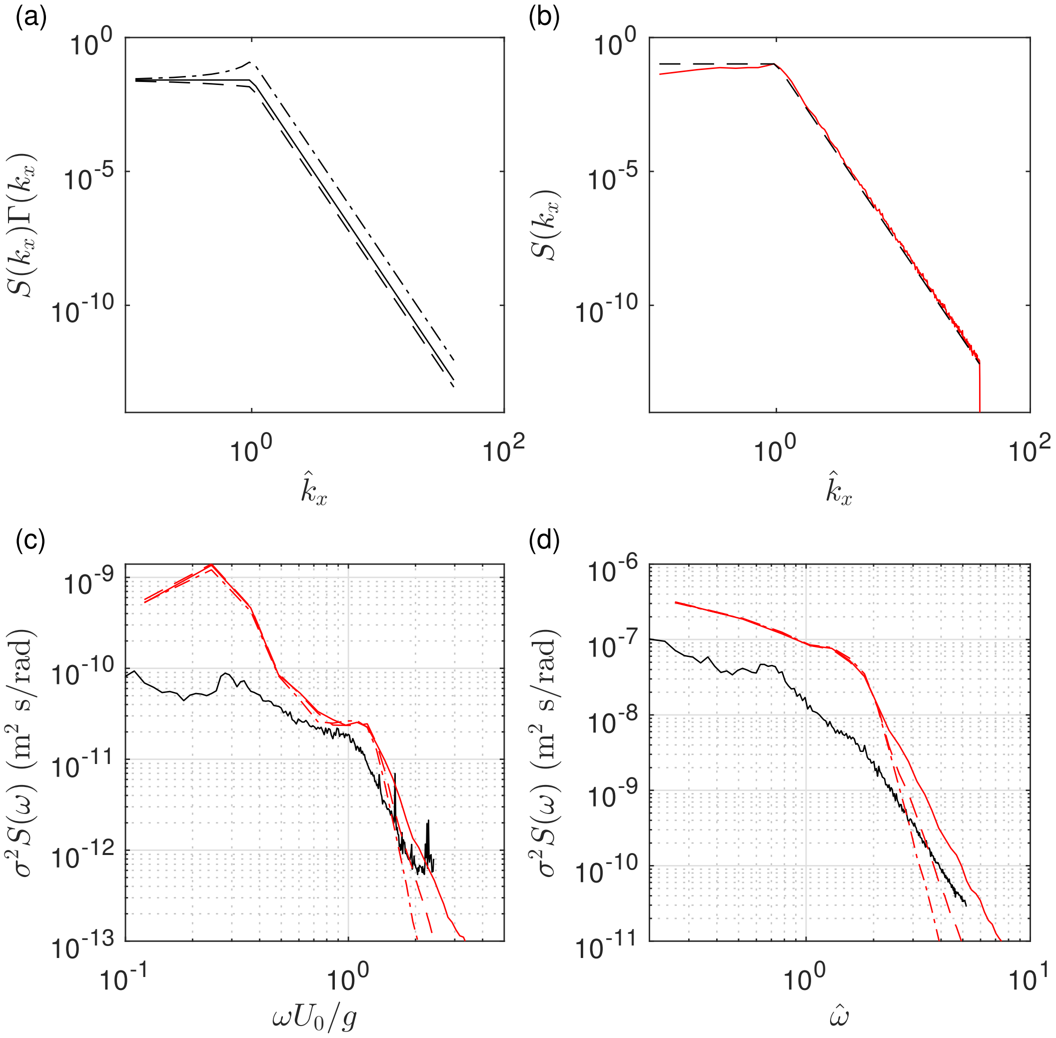

Figure 6.1: (a) The modelled spectrum $S(k_x)\Gamma(k_x)$ for (dashed-dotted) upstream dispersive waves, (solid) non-dispersive waves, and (dashed) downstream dispersive waves, as a function of the streamwise wavenumber k_x, for all conditions except condition 1. (b) (red) The average of the time-averaged modelled spatial spectrum computed from 50 independent realisations of the dynamic free surface in condition 7, with $\alpha = 7$, $k_1 = 2\pi/0.003\,\mathrm{rad\,m^{-1}}$, and with $\Gamma_\theta(\theta)$ given by the Poisson distribution, (dashed black) equation (6.20). (c-d) (red) The average of the modelled space-averaged frequency spectra computed from 50 independent realisations of the free surface in conditions (c) 1 and (d) 7, with $k_1 = 2\pi/0.003\,\mathrm{rad\,m^{-1}}$, with the Poisson distribution, and with (solid) $\alpha = 5$, (dashed) $\alpha = 7$, and (dashed-dotted) $\alpha = 9$. (black) The average frequency spectra measured with wave probes, in the same conditions.

constant plateaux at the wavenumber $k_x < k_0$. This form of the spatial spectrum at the lower wavenumber suggests an approximate definition of the two-dimensional spatial spectrum as

$$S(k_x) = \begin{cases} S_0, & \text{if } k_x < k_0 \\ S_0 \left(\dfrac{k_x}{k_0}\right)^{-\alpha}, & \text{if } k_0 \le k_x \le k_1 \\ 0, & \text{if } k_x > k_1 \end{cases} . \tag{6.20}$$

This is also shown in FIG. 6.1b. The corresponding static two-dimensional surface had the expansion

$$\zeta(x) = \Re \left\{ \sum_l \xi_l A(k_{x,l}) e^{i\left[k_{x,l}x + \Phi_l\right]} \right\} . \tag{6.21}$$

FIG. 6.1c and d show the average across 50 realisations of the space-averaged frequency spectra of the modelled surface, for condition 1 and 7, respectively, again with the Poisson distribution and with $k_1 = 2\pi/0.003\,\mathrm{rad\,m^{-1}}$. Here α was varied between 5 and 7. The spectra are compared with the measured frequency spectra, in the same conditions. In spite of the simplifications of the model, the frequency spectrum of the modelled surface retains some of the fundamental characteristics of the measured spectra. The spectra decay slowly at the frequency below $\omega U_0/g$ and $2\hat{\omega}$ in condition 1 and 7, respectively. The rate of decay in this frequency range is governed by the angular distribution in the model, and it is close to the measurements. At the higher frequency the decay rate depends on the choice of the parameter α, and the model represents well the measurements when $\alpha = 5$. The model shows the same peak of the frequency spectrum for condition 1 at the frequency $\omega U_0/g \approx 0.3$, which was related to the zero of the group velocity of the waves which propagate upstream, although the peak predicted by the model is largely overestimated. This overestimation has relatively small effect on the computation of the acoustic Doppler spectra, as it is shown in section 6.2.

6.1.2 Estimation of the Kirchhoff parameter for a surface with a power-function spectrum

All the numerical acoustic models and the reconstruction techniques described in this chapter rely on the validity of the Kirchhoff approximation. Here a simple method to estimate the conditions where the Kirchhoff approximation applies for a random linear surface with the power spectrum that follows a power-function of the wavenumber is derived. The representation of the free surface as a trigonometric series with the power-function shape of the spectrum allows the direct estimation of the Kirchhoff parameter $\kappa R_c \sin^3\psi$ from the parameters of the spectrum. Only the two-dimensional case is considered here, with $\zeta = \zeta(x)$. Based on the spectrum of equation (6.20) and the condition of equation (6.7) one can find

$$S_0 = \frac{2\pi(\alpha-1)\sigma^2}{k_0\left[\alpha - \left(\frac{k_1}{k_0}\right)^{1-\alpha}\right]}. \tag{6.22}$$

The average curvature radius for the corresponding two-dimensional surface $\zeta(x)$ can be defined as [e.g. Thorsos, 1988]

$$R_c = \left[1 + \left\langle \left(\frac{d\zeta}{dx}\right)^2 \right\rangle\right]^{3/2} \left\langle \left(\frac{d^2\zeta}{dx^2}\right)^2 \right\rangle^{-1/2}. \tag{6.23}$$

Based on the trigonometric series of equation (6.21), the surface gradient and curvature are defined as

$$\frac{d\zeta}{dx} = \Re\left\{ i \sum_l \xi_l k_{x,l} A(k_{x,l}) e^{i\left[k_{x,l}x + \Phi_l\right]} \right\} \tag{6.24}$$

and

$$\frac{d^2\zeta}{dx^2} = -\Re\left\{ \sum_l \xi_l k_{x,l}^2 A(k_{x,l}) e^{i\left[k_{x,l}x + \Phi_l\right]} \right\}, \tag{6.25}$$

respectively. This allows the definition of their squared averages as

$$\left\langle \left(\frac{d\zeta}{dx}\right)^2 \right\rangle = \frac{1}{2\pi}\int_0^{k_0} S_0 k_x^2 dk + \frac{1}{2\pi}\int_{k_0}^{k_1} S_0 k_0^{\alpha} k_x^{2-\alpha} dk, \tag{6.26a}$$

$$\left\langle \left(\frac{d^2\zeta}{dx^2}\right)^2 \right\rangle = \frac{1}{2\pi}\int_0^{k_0} S_0 k_x^4 dk + \frac{1}{2\pi}\int_{k_0}^{k_1} S_0 k_0^{\alpha} k_x^{4-\alpha} dk, \tag{6.26b}$$

where the first terms on the right hand side of equations (6.26a) and (6.26b) are called the second and fourth moments of the wavenumber spectrum, in analogy with the definition of spectral moments in equation (5.14).

Equation (6.26a) yields

$$\left\langle \left(\frac{d\zeta}{dx}\right)^2 \right\rangle = \frac{S_0 k_0^3}{6\pi(\alpha-3)}\left[\alpha - 3\left(\frac{k_1}{k_0}\right)^{3-\alpha}\right], \tag{6.27}$$

when $\alpha > 3$. Equation (6.26b) has the solution

$$\left\langle \left(\frac{d\zeta}{dx}\right)^2 \right\rangle = \begin{cases} \dfrac{S_0 k_0^5}{10\pi}\left[1 + 5\ln\left(\dfrac{k_1}{k_0}\right)\right], & \text{if } \alpha = 5 \\ \dfrac{S_0 k_0^5}{10\pi(\alpha-5)}\left[\alpha - 5\left(\dfrac{k_1}{k_0}\right)^{5-\alpha}\right], & \text{if } \alpha > 5 \end{cases}. \tag{6.28}$$

When $\alpha > 5$ the curvature radius converges to a finite value when $k_1/k_0 \to \infty$,

$$\lim_{\frac{k_1}{k_0}\to\infty} k_0 R_c = \sqrt{\frac{5}{27}}\left[\frac{3(\alpha-3)}{\sigma^2 k_0^2(\alpha-1)} + 1\right]^{3/2} \frac{(\alpha-1)(\alpha-5)^{1/2}}{(\alpha-3)^{3/2}}\sigma^2 k_0^2. \tag{6.29}$$

Conversely, if $\alpha \leq 5$ the curvature radius tends to 0 when $k_1/k_0 \to \infty$. This makes the Kirchhoff condition less likely to be satisfied due to the impact of the shorter waves.

This large impact of the very short (and small) waves on the validity of the acoustic model suggests limiting the spectrum slope to the value $\alpha > 5$, or limiting the value of the ratio k_1/k_0. In the simulations reported here, three values of the slope α were investigated, namely $\alpha = 5$, $\alpha = 7$, and $\alpha = 9$. While in the former two cases the values of σ and k_0 were such that the Kirchhoff condition was satisfied for infinitely large values of k_1/k_0, in the simulations with $\alpha = 5$ it was necessary to assume that the spectrum was band-limited with the wavenumber $k_1 \leq 2\pi/0.003\,\mathrm{rad\,m^{-1}}$. This value was larger than the wavenumber of the first order Bragg scales, but small enough to ensure that the Kirchhoff condition was satisfied based on equation (6.23) and (6.28). In practice, it will be shown that the Doppler spectra of the acoustic field converged rapidly with all values of α when k_1 was increased above $2\pi/0.005\,\mathrm{rad\,m^{-1}}$ in the tests considered here. Therefore, the spectrum was limited to $k_1 = 2\pi/0.003\,\mathrm{rad\,m^{-1}}$ even when $\alpha > 5$. As a consequence, k_1/k_0 was between 14 and 67.

FIG. 6.2a shows the predictions of the characteristic curvature radius R_c based on equations (6.23), (6.27), (6.28), and (6.29), in the range of the parameter $k_0^2\sigma^2$ which was relevant for the simulations reported here, and for $5 \leq \alpha \leq 9$. This is compared with the direct estimations of R_c from the various dynamic simulations, where the mean squared average slope and curvature were computed directly from the free surface realisations based on the model of equation (6.5). In all cases the measurements fit the predictions well. FIG. 6.2b shows the values of the parameter $2\kappa R_c \sin^3\psi_s$ which has been computed directly for each simulation, with $\psi_s = \pi/6$. In all conditions the Kirchhoff parameter was larger than 10, which justified the

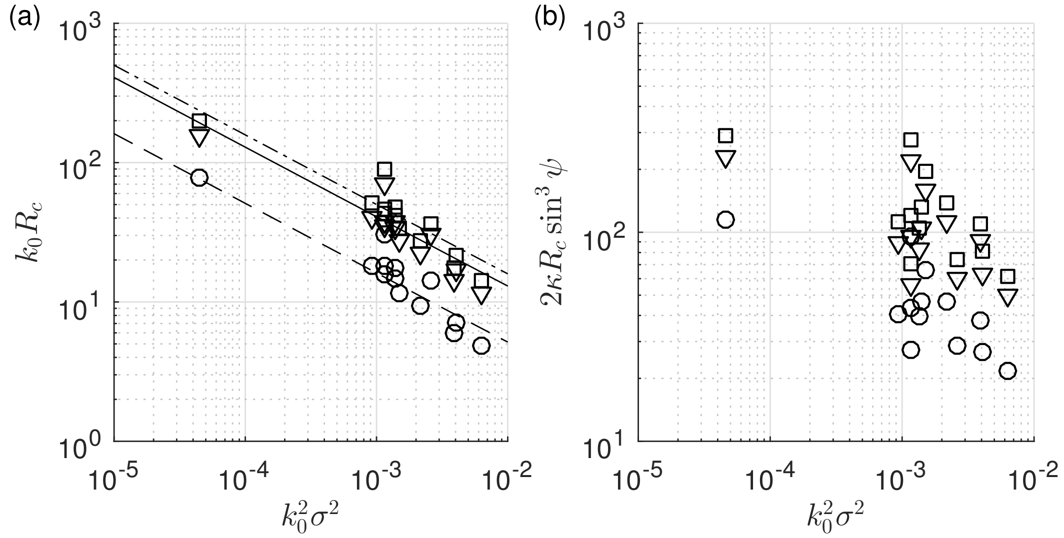

Figure 6.2: (a) The characteristic curvature radius calculated from (dashed-dotted) equation (6.29) with $\alpha = 9$, (solid) equation (6.29) with $\alpha = 7$, and (dashed) equations (6.23), (6.27), (6.28), and (6.29) with $\alpha = 5$ and $k_1/k_0 = 100$. (symbols) Direct calculations based on equation (6.23) from the random realisations of equations (6.5) and (6.6) with (squares) $\alpha = 9$, (triangles) $\alpha = 7$, and (circles) $\alpha = 5$. (b) The Kirchhoff parameter calculated from the realisations of the acoustic model.

use of the Kirchhoff approximation. The minimum of the Kirchhoff parameter was equal to 21.6 and it was found in condition 5 when $\alpha = 5$.

6.1.3 Details of the Doppler model

The parameters of the acoustic models were chosen in order to simulate the same experimental conditions described in section 4.4. The locations of the source and receivers, and their directivity patterns, were the measured ones described in subsections 4.4.2. The random realisations of the rough surface were generated with the model described by equation (6.5). The surface parameters σ and k_0 were the ones that had been measured with the arrays of conductance wave probes, and estimated from equation (3.44), respectively. All the simulations were performed with the time step $\Delta t = 1\,\mathrm{ms}$, for the duration of one second. The spatial grid had the size of 1 m in the streamwise direction and 0.5 m in the transverse direction, and it was centred about the projection of the main directivity lobe of the modelled acoustic source. The grid separation, Δx, was the smallest between $\lambda_a/10$ and $l_1/10$, where λ_a was the acoustic wavelength and $l_1 = 2\pi/k_1$ was the minimum resolved scale of the surface. FIG. 6.3 shows the convergence of the simulated acoustic potential in the forward scattering configuration, as a function of the ratio $\lambda_a/\Delta x$ for one single surface realisation based on the parameters of condition 7. Reducing the size of the spatial grid from $\lambda_a/10$ to $\lambda_a/50$ causes a relative variation of the absolute value of

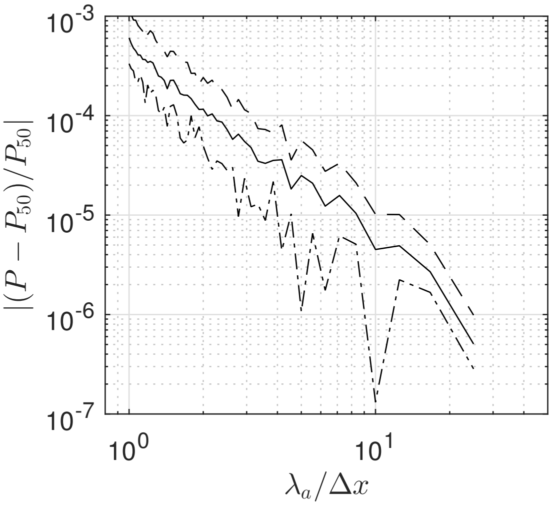

Figure 6.3: Convergence of the numerical model. (solid) absolute potential, (dashed) real part of the potential, (dashed-dotted) imaginary part of the potential calculated for the forward scattering setup based on a single realisation for flow condition 7. P_{50} is the potential when $\lambda_a/\Delta x = 50$.

the potential smaller than 10^{-5}, which is considered negligible. The equidistant set of wavenumbers k_l corresponded to the standard set of eigenvalues which are used for the discrete Fourier transform, i.e., $k_l = l\Delta k$, with $\Delta k = 2\pi/L_x$, $l = 1, 2, ..., N_k$ and L_x was the size of the spatial grid in the streamwise direction. In the two-dimensional realisations of the model θ was modelled implicitly, i.e., it was imposed

$$k = \begin{cases} k_l, & \text{when } k_l \geq k_0 \\ k_0, & \text{when } k_l < k_0 \end{cases}, \tag{6.30}$$

$$\theta = \begin{cases} 0, & \text{when } k_l \geq k_0 \\ \cos^{-1}\left(\dfrac{k_l}{k_0}\right), & \text{when } k_l < k_0 \end{cases}. \tag{6.31}$$

In the three-dimensional realisations, the wave orientation θ was varied between $-\pi/2$ and $\pi/2$ for the downstream propagating waves, and between $\pi/2$ and $3\pi/2$ for the upstream waves, with a step of $\pi/6$.

In the three-dimensional simulations the scattered acoustic field was computed by solving the integral of equation (3.105) numerically. In the two-dimensional simulations, the realisations of the free surface were computed by fixing $y = 0$ in equation (6.5), and the acoustic field was computed based on equation (3.108). The integrals of equations (3.105) and (3.108) were computed with the trapezoidal method at each time-step. These equations provide the complex modulation of the acoustic field, i.e., its value divided by the factor $\exp(i\omega_a t)$. 50 independent realisations of the acoustic field were computed.

The Doppler spectrum was determined for each realisation with the discrete Fourier transform of the complex modulation, applied with the function *fft* in Matlab 2016b. The mean Doppler spectrum was the average across all realisations. The real part of the Fourier transform at the frequency $\omega < 2\pi f_s/2$ corresponds to the spectrum of the real measured acoustic pressure field at the frequency $\omega_a + \omega$, while the real part of the Fourier transform at the frequency $\omega > 2\pi f_s$ corresponds to the real measured spectrum at the frequency $\omega_a - 2\pi f_s + \omega$. The modelled spectra were shifted and mirrored in order to compare directly with the measured spectra both above and below the frequency ω_a.

6.1.4 Validity of the linear Doppler model

The derivation of the Doppler spectrum of the scattered acoustic pressure field in the particular case of the small Rayleigh parameter and when the correlation radius is small compared to the size of the Fresnel zone allows the derivation of an approximate linear model of the Doppler spectrum. Unlike the direct computation of the Kirchhoff integral, which requires a set of random realisations of the free surface, this model only requires the knowledge of the frequency-wavenumber spectrum of the free surface. It also allows the estimation of the frequency-wavenumber spectrum based on the measurement of the acoustic Doppler spectrum. Subsection 3.2.2 showed the derivation of this linear model of the scattered Doppler spectrum, and discussed the conditions under which the model applies. These are given by a set of small non-dimensional parameters which depend on the characteristics of the free surface and on the location of the source and of the receiver. The values of each of these parameters are reported in Table 6.1, as they have been calculated for each of the flow conditions based on the geometry of the acoustic setup reported in subsection 4.4.2. Here it was assumed that the characteristic scale of the correlation function is represented by the value $2\pi/k_0$ in all conditions except condition 1. In this latter condition, the parameter $4\pi U_0^2/g$ was used instead, since this corresponded to the knee of the frequency spectrum in FIG. 5.5a.

Table 6.1: Conditions for the application of the linear Doppler model

Flow condition	$\frac{\kappa \sin^2(\psi_s)}{k_0^2 R}$	$\frac{\cos(\psi_s)}{k_0 R}$	$\frac{\sin^2(\psi_s)}{k_0^2 R^2}$	$\frac{1}{k_0^2 R^2}$	$\frac{\kappa\sigma \sin(2\psi_s)}{k_0 R}$	$\frac{\kappa\sigma \sin^3(\psi_s)}{k_0^2 R^2}$	$\frac{\kappa\sigma \sin(\psi_s)}{k_0^2 R^2}$	$[2\kappa \sin(\psi_s)\sigma]^2$
1	0.03	0.02	8.5×10^{-5}	3.4×10^{-4}	6.5×10^{-4}	1.7×10^{-6}	6.9×10^{-6}	1.6×10^{-3}
2	0.06	0.02	1.9×10^{-4}	7.8×10^{-4}	7.6×10^{-3}	3.1×10^{-5}	1.2×10^{-4}	0.10
3	0.12	0.03	3.9×10^{-4}	1.5×10^{-3}	1.3×10^{-2}	7.6×10^{-5}	3.0×10^{-4}	0.15
4	0.03	0.02	9.0×10^{-5}	3.6×10^{-4}	3.3×10^{-3}	9.1×10^{-6}	3.6×10^{-5}	0.04
5	0.24	0.05	7.7×10^{-4}	3.1×10^{-3}	6.8×10^{-2}	5.5×10^{-4}	2.2×10^{-3}	2.02
6	0.05	0.02	1.6×10^{-4}	6.3×10^{-4}	8.4×10^{-3}	3.1×10^{-5}	1.2×10^{-4}	0.15
7	0.18	0.04	5.7×10^{-4}	2.3×10^{-3}	4.0×10^{-2}	2.7×10^{-4}	1.1×10^{-3}	0.93
8	0.06	0.02	1.9×10^{-4}	7.8×10^{-4}	6.4×10^{-3}	2.6×10^{-5}	1.0×10^{-4}	0.07
9	0.09	0.03	3.0×10^{-4}	1.2×10^{-3}	1.1×10^{-2}	5.4×10^{-5}	2.2×10^{-4}	0.13
10	0.51	0.07	1.6×10^{-3}	6.4×10^{-3}	1.1×10^{-1}	1.3×10^{-3}	5.1×10^{-3}	2.59
11	0.32	0.05	1.0×10^{-3}	4.0×10^{-3}	5.1×10^{-2}	4.6×10^{-4}	1.9×10^{-3}	0.85
12	0.12	0.03	3.8×10^{-4}	1.5×10^{-3}	1.6×10^{-2}	8.8×10^{-5}	3.5×10^{-4}	0.21
13	0.41	0.06	1.3×10^{-3}	5.2×10^{-3}	5.4×10^{-2}	5.6×10^{-4}	2.3×10^{-3}	0.76

The size of the insonificated area was estimated in subsection 4.4.2 as $L_D = 239\,\mathrm{mm}$ along the x-direction, and $L_D = 56\,\mathrm{mm}$ along the y-direction. These were smaller than the distance $R = 400\,\mathrm{mm}$. All the parameters reported in Table 6.1 need to be smaller than one for the method to be asymptotically valid. There are two parameters which were close to one or even bigger than one in some of the measured conditions. These are the ratio between the correlation radius and the size of the Fresnel zone expressed by equation (3.115),

$$\frac{\kappa \sin^2(\psi_s)}{k_0^2 R}, \tag{6.32}$$

and the Rayleigh parameter,

$$\left[2\kappa \sin(\psi_s)\sigma\right]^2. \tag{6.33}$$

The first was smaller than 0.51 in all conditions, and was maximum in condition 10. The Rayleigh parameter was larger than one in conditions 5 and 10, where the linear Doppler model should not be applied. The model is expected to have limited validity in conditions 7, 11, and 13, where the Rayleigh parameter was larger than 0.75 but smaller than one. In all remaining flow conditions, the conditions for the application of the model were met, although the accuracy of the results were expected to vary based on the effective size of each parameter. In subsection 6.2.2, the results of the linear model are presented for all flow conditions, including those where the model did not strictly apply. It is shown that the linear model was able to predict the behaviour of the measured Doppler spectra in all these conditions.

6.1.5 Application of the linear model of the Doppler spectrum

The numerical solution of the linear model of the Doppler spectrum was computed as follows. A two-dimensional spatial grid was defined in the directions x and y between the values $-L_x/2$ and $L_x/2$, and $-L_y/2$ and $L_y/2$, respectively. At each location (x, y) the multiplicative factor $Q(\boldsymbol{\rho})$ (equation (3.120)) and the vector $\mathbf{q}_\perp(\boldsymbol{\rho})$ (equation (3.103)) were computed based on the position of the source and of the receiver, where $\rho = \sqrt{x^2 + y^2}$. Two equidistant sets of wavenumbers and angles of orientation of the surface waves were defined, with the wavenumber varying between 0 and k_1 and with the angle θ varying between 0 and π. For each combination of the wavenumber and angle, the corresponding frequency of the waves $\omega(k, \theta)$ was computed based on each of the three dispersion relations Ω^+, Ω^-, and Ω^U. The wavenumber spectrum $S(\mathbf{k})$ was defined by equations (6.3) and (6.6), or by (6.9) in condition 1. Each value of k and θ lead to the projections k_x and k_y according to equations (3.47a) and (3.47b). The value of $\boldsymbol{\rho}$ that corresponded to the minimum of the squared distance

$$[q_x(\boldsymbol{\rho}) - k_x(k,\theta)]^2 + [q_y(\boldsymbol{\rho}) - k_y(k,\theta)]^2 \tag{6.34}$$

was identified. This led to a unique value of $Q(\boldsymbol{\rho}(k,\theta))$ for each combination of k and θ. In this way the scattering from a region of the surface represented by the co-ordinates $\boldsymbol{\rho}$ was directly associated with the interaction with the waves that have the wavenumber k and direction θ. The Doppler spectrum at the frequency $\omega - \omega_a$ was found as the sum of all contributions

$$S(\mathbf{K}(\omega - \omega_a))Q(\boldsymbol{\rho}),\ |\omega - \omega_a - \Omega(\mathbf{k})| \leq \Delta\omega, \tag{6.35}$$

where $\mathbf{K}(\omega)$ is the inverse of the dispersion relation, i.e.,

$$\mathbf{K}(\omega) = \Omega^{-1}(\omega) \tag{6.36}$$

if

$$\Omega(\mathbf{K}(\omega)) = \omega, \tag{6.37}$$

and $\Delta\omega$ was equal to 1 Hz. The results of this analysis are described in section 6.2.

The main advantage of the linear model compared to the Monte Carlo simulations is the possibility to calculate the frequency-wavenumber spectrum of the free surface directly from the measured Doppler spectrum of the scattered acoustic field. This was noted by Barrick [1972], who suggested that this could be done by changing the frequency of the incident signal. When the measurements are performed outside of the Fraunhofer zone, the inversion of the frequency-wavenumber spectrum can be done at first order using a single frequency. If the frequency-wavenumber spectrum is known at each wavenumber $\mathbf{k}$ and frequency ω, the equation (3.123) can be rewritten in the form

$$\bar{S}_{D(N_\omega \times 1)} = \bar{\bar{S}}_{(N_\omega \times N_k)} \bar{h}_{(N_k \times 1)}, \tag{6.38}$$

where $\bar{S}_D$ is the Doppler spectrum measured at N_ω frequencies, and $\bar{\bar{S}}$ and $\bar{h}$ are defined as

$$\bar{\bar{S}} = \begin{bmatrix} S(\mathbf{k}_1,\omega_1) & S(\mathbf{k}_2,\omega_1) & \dots & S(\mathbf{k}_{N_k},\omega_1) \\ S(\mathbf{k}_1,\omega_2) & S(\mathbf{k}_2,\omega_2) & \dots & S(\mathbf{k}_{N_k},\omega_2) \\ \dots & \dots & \dots & \dots \\ S(\mathbf{k}_1,\omega_{N_\omega}) & S(\mathbf{k}_2,\omega_{N_\omega}) & \dots & S(\mathbf{k}_{N_k},\omega_{N_\omega}) \end{bmatrix}, \tag{6.39}$$

and

$$\bar{h} = \begin{bmatrix} Q(\boldsymbol{\rho}(\mathbf{k}_1)) \\ Q(\boldsymbol{\rho}(\mathbf{k}_2)) \\ \cdots \\ Q(\boldsymbol{\rho}(\mathbf{k}_{N_k})) \end{bmatrix}. \tag{6.40}$$

In most applications the frequency-wavenumber spectrum is unknown, and one needs to find $\bar{\bar{S}}$, which is difficult in general. Assuming a set of dispersion relations $\Omega^{(j)}(\mathbf{k})$, most of the values of $\bar{\bar{S}}$ could be reduced to zero by assuming that

$$S(\mathbf{k}, \omega) = \sum_j S(\mathbf{k}, \omega)\delta(\mathbf{k} - \mathbf{K}^{(j)}(\omega)), \tag{6.41}$$

where $\mathbf{K}^{(j)}(\omega)$ represents the inversion of each of the dispersion relations. In the case when there is only one dispersion relation which is univariate at each frequency, the inversion follows directly from equation (3.123), i.e.,

$$S(\mathbf{K}(\omega - \omega_a), \omega - \omega_a) = \frac{S_D(\omega - \omega_a)}{\sigma^2 q_z^2 \boldsymbol{\rho}(\mathbf{K}(\omega - \omega_a))Q(\boldsymbol{\rho})}, \tag{6.42}$$

where $\boldsymbol{\rho}(\mathbf{K}(\omega))$ can be found with the procedure described above.

The experimental results in chapter 5 showed the contemporary presence of more than one (up to three) dispersion relations. These can be represented as $\Omega^{(j)}(\mathbf{k})$, or alternatively as $\mathbf{K}^{(j)}(\omega)$, where $j = 1, 2, 3$. In this case, a solution can be found independently at each frequency if one assumes a given ratio of the frequency wavenumber spectra, e.g.,

$$\frac{S(\mathbf{K}^{(j)}(\omega), \omega)}{S(\mathbf{K}^{(j+1)}(\omega), \omega)} = C_S(\omega). \tag{6.43}$$

Without the knowledge of the full three dimensional frequency-wavenumber spectrum the definition of this ratio is arbitrary. Here it was assumed simply that

$$C_S = 1. \tag{6.44}$$

This corresponds to the assumption that the amplitude of the waves is governed by the frequency, i.e., that all three types of waves have the same amplitude at each frequency ω.

6.2 Doppler spectra of the scattered acoustic pressure field

This section reports the measurements of the Doppler spectrum of the acoustic pressure field scattered by the dynamic free surface, and its interpretation according to two models based on the Kirchhoff approximation. The Doppler spectrum is usually employed in order to measure the velocity of the patterns on the free surface. This can be easily done in some specific conditions, when the source and the receiver are both in the Fraunhofer zone, and when the source has a very narrow directivity pattern. These conditions are difficult to satisfy when the acoustic field is generated by a real source which directivity pattern is not narrow.

In the next subsections it is shown that the Doppler spectrum measured in these non ideal conditions still provides important information about the dynamic behaviour of the free surface. In fact, although the measurements are performed at one single location in space, the scattering occurs on a relatively large area of the rough surface. When the measurements are performed outside of the Fraunhofer zone it is possible to obtain information about the spatial as well as the temporal behaviour of the surface. The assumption which underlies the methods described here is that the statistics of the free surface are stationary. The linear model described in sections 3.2.2 and 6.1.5 further assumes that the statistics are Gaussian. This is not required by the Monte Carlo simulation which details have been reported in subsection 6.1.3, although this model relies on the surface realisations generated by the linear surface model described in subsection 6.1.1.

The results in this section have a direct relation with the measurements of the frequency spectra and frequency-wavenumber spectra of gravity-capillary waves which have been reported in subsections 5.2.1 and 5.3.2, respectively. This relation is made explicit by the linear Doppler model. In practice it was impossible to characterise the fully three dimensional frequency-wavenumber spectra, therefore the validation of the models was in terms of the measured frequency spectra reported in subsection 5.2.1 only.

6.2.1 Results in backscattering (mono-static configuration)

The average Doppler spectra of the backscattered acoustic field measured by the first microphone with the setup described in sub-section 4.4.2 are shown in FIG. 6.4 for all flow conditions. All spectra show some common features. There is a peak in the Doppler spectra which is centred at the frequency ω_a and has the width

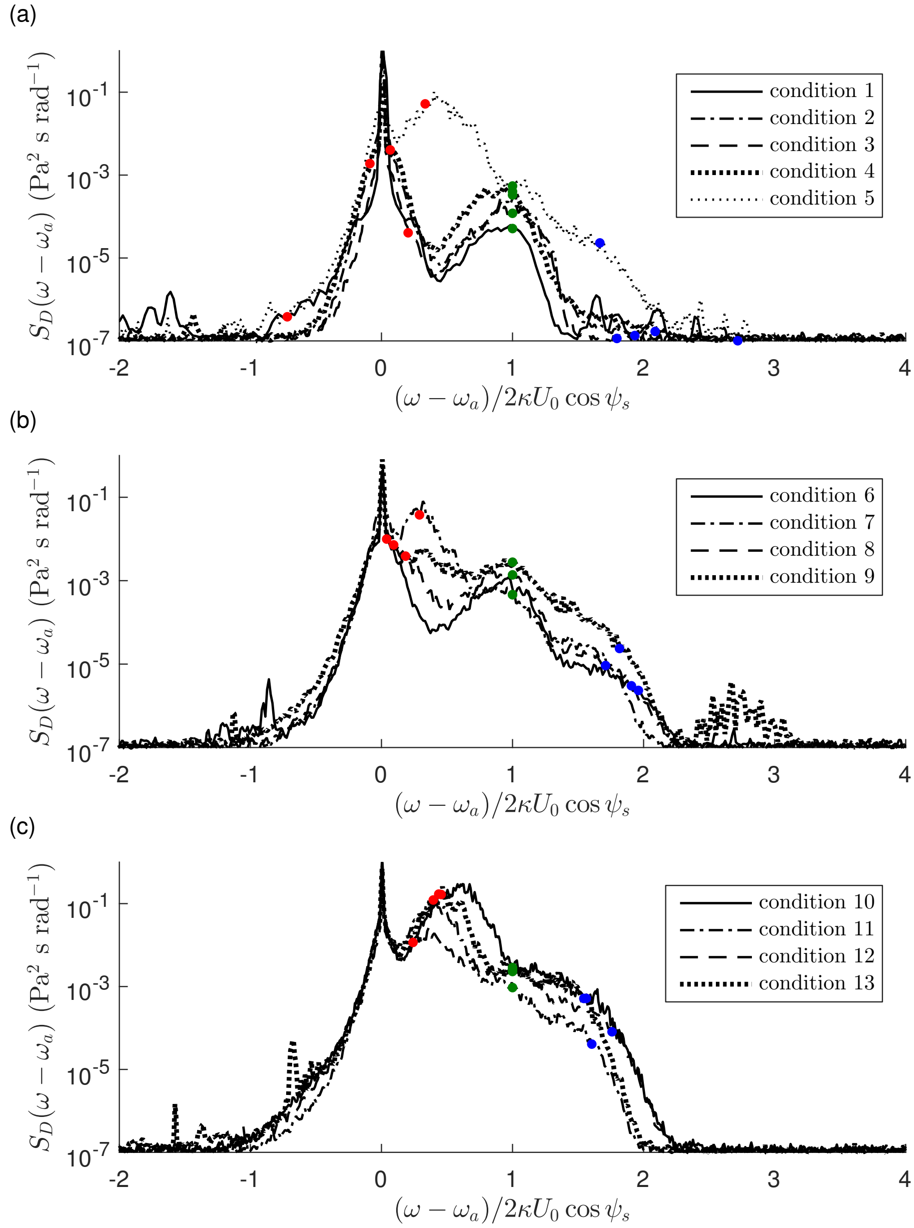

Figure 6.4: The average measured Doppler spectra of the backscattered acoustic field. The dots show the Bragg frequency of (green) non-dispersive waves, Ω_B^U, (red) upstream capillary waves, Ω_B^- and (blue) downstream capillary waves, Ω_B^+.

between 1 and 2 times $\kappa U_0 \cos\psi$. The width of the peak is larger in the conditions with the larger Froude number (FIG. 6.4c). The spectra are asymmetrical, and show one to three additional broad peaks at the positive frequency between ω_a and $\omega_a + 4\kappa U_0 \cos\psi$. The behaviour in FIG. 6.4c is reminiscent of the measurements of microwave Doppler spectra obtained in rivers by Plant et al. [2005], where a low-frequency peak largely dominated a smaller peak at higher frequency.

It was shown in section 3.2.2 that the peaks of the acoustic Doppler spectrum are associated with the Bragg resonance mechanism. The backscattering setup described in sub-section 4.4.2 had the peak of the directivity pattern at the characteristic angle of incidence $\psi_s = \pi/6$. The frequency of the acoustic signal emitted by the source was $f_a = 43\,\mathrm{kHz}$. Based on these values, the waves which are expected to give the largest contribution to Bragg scattering had the wavelength (equation (3.127))

$$k_B = 2\kappa \cos\psi_s = 1364\,\mathrm{rad\,m^{-1}}, \tag{6.45}$$

and the wavelength

$$\lambda_B = 4.6\,\mathrm{mm}. \tag{6.46}$$

These short waves are capillary waves which dynamics are dominated by surface tension effects. These waves could not be measured with the array of wave probes due to the limited spatial resolution.

It is possible to estimate the phase velocity of the Bragg waves, assuming that they follow the same three types of dispersion relations observed at the lower wavenumber, and previously indicated by Ω^+, Ω^-, and Ω^U. According to this assumption, the peaks of the Doppler spectrum are expected at the frequencies

$$\omega = \begin{cases} \omega_a + \Omega^+(k_B, 0), & \text{downstream capillary waves,} \\ \omega_a + \Omega^-(k_B, \pi), & \text{upstream capillary waves,} \\ \omega_a + \Omega^U(k_B, 0), & \text{non-dispersive capillary waves,} \end{cases} \tag{6.47}$$

These frequencies are shown for all flow conditions in FIG. 6.4, and they match the frequency of the peaks of the measured Doppler spectra. The spectra at the lower Froude number (FIG. 6.4a) show only one Bragg peak at the frequency $\Omega^U(k_B, 0)$, which corresponds to non-dispersive waves travelling at the mean surface velocity. The spectra at the intermediate Froude number (FIG. 6.4b) still show the non-dispersive peak, although there is an increasingly larger contribution from the two types of dispersive capillary waves which propagate upstream and downstream, respectively. At the larger Froude numbers (FIG. 6.4c) these contributions have grown to the extent that the intermediate peak cannot be seen any more. The peak that corresponds to the upstream propagating waves at the frequency $\Omega^-(k_B, 0)$ is always larger than the one that represents the downstream propagating waves at the higher frequency $\Omega^+(k_B, 0)$. The dependence of the Doppler spectra on the Froude number was observed consistently in all conditions except condition 5, which behaved like the larger Froude number conditions.

In order to investigate the relationship between the measured Doppler spectra and the characteristics of the free surface in the different flow conditions, two different numerical models were implemented. The first model was a Monte Carlo simulation based on the numerical solution of the Kirchhoff integral from random realisations of the dynamic free surface elevation ζ in space and in time. The surface realisations were computed from equation (6.5), based on the power-function spatial spectrum described in section 6.1.1. This model provided a set of numerical realisations of the complex modulation of the scattered acoustic field, from which the Doppler spectrum was calculated with the procedure described in sub-section 6.1.3. The second model was the linear Doppler model based on the expansion of the same Kirchhoff integral with the small Rayleigh parameter, and it allowed the direct calculation of the average Doppler spectrum from the angular spatial spectrum $S(k)\Gamma(k, \theta)$ of the free surface elevation (equation (6.6) and (6.9), and equations (6.16), (6.17), (6.18), and (6.19)). The details of this second model were described in subsection 6.1.5.

The linear model is a simplification of the model used for the Monte Carlo simulation, which was valid only in a limited range of conditions. Therefore the results of the Monte Carlo simulation will be discussed first. In the previous chapter it was shown that the choice of the smallest surface scale which is resolved by the model of the free surface impacts the validity of the Kirchhoff condition, especially when the spectrum slope α is smaller or equal than 5. A set of simulations were performed based on the surface parameters of condition 7 ($\sigma = 1.21\,\mathrm{mm}$, $k_0 = 52.4\,\mathrm{rad\,m^{-1}}$) with $\alpha = 7$ and with the maximum resolved wavenumber k_1 varying between $2\pi/0.003\,\mathrm{rad\,m^{-1}}$ and $2\pi/0.05\,\mathrm{rad\,m^{-1}}$. In this way the convergence of the simulated Doppler spectra based on k_1 was checked. In these simulations the scattered acoustic field was computed with the two-dimensional equation (3.108). The results are shown in FIG. 6.5a. The amplitude of the modelled spectra depends on a multiplicative constant which represents the amplitude of the incident acoustic potential field, and is affected by the resolution of the spatial grid and by the time step of the simulation. Here and in the following, the modelled spectra were shifted vertically by an arbitrary quantity in order to provide a better visual fitting with the measurements. It is seen in FIG. 6.5 that the peak of the spectrum at the frequency $\omega = \omega_a$ was independent on the length of the smallest surface waves. Conversely, the

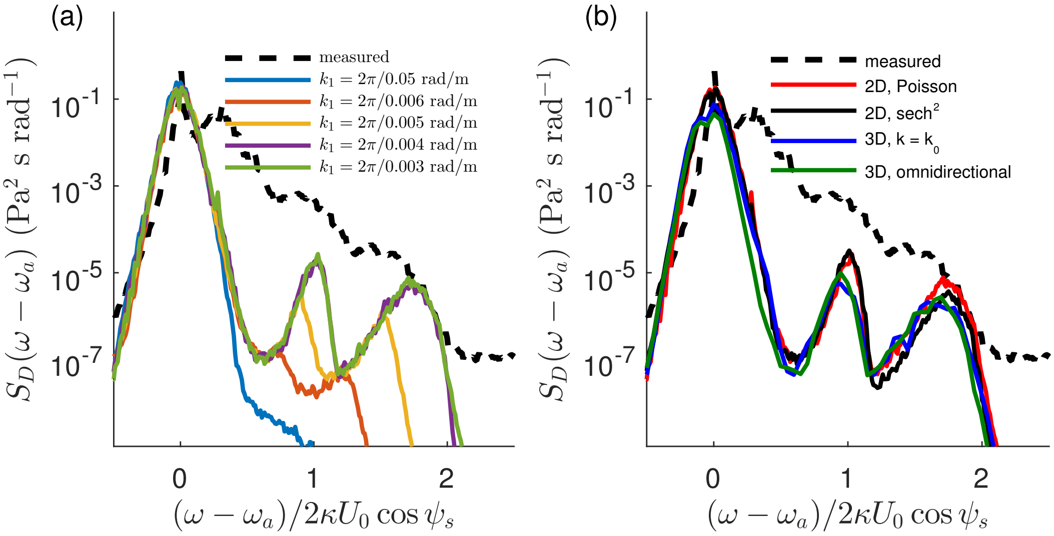

Figure 6.5: The Doppler spectrum estimated with the Monte Carlo simulation with $\sigma = 1.21\,\mathrm{mm}$, $k_0 = 52.4\,\mathrm{rad\,m^{-1}}$, and $\alpha = 7$, compared with (dashed) the measured Doppler spectrum for condition 7. (a) The effect of the maximum resolved wavenumber, k_1, evaluated with the two-dimensional model. (b) The effect of the three-dimensional surface patterns and angular distribution of the waves.

peaks at the higher frequency only began to appear when the maximum wavenumber was larger than $2\pi/0.006\,\mathrm{rad\,m^{-1}}$. The Doppler spectrum did not change when k_1 was increased from $2\pi/0.004\,\mathrm{rad\,m^{-1}}$ to $2\pi/0.003\,\mathrm{rad\,m^{-1}}$. This confirms that the peaks were caused by the scattering from the Bragg waves with the wavelength of 4.6 mm. Because of this, all the subsequent simulations were carried out with the maximum wavenumber $k_1 = 2\pi/0.003\,\mathrm{rad\,m^{-1}}$.

FIG. 6.5b shows the effect of the three dimensional patterns of the free surface on the Doppler spectrum, based on the Monte Carlo simulation. The results of two two-dimensional simulations and two three-dimensional simulations have been compared in FIG. 6.5b. The two-dimensional simulations differed in terms of their angular distribution, which was computed either from the Poisson distribution (equation (6.15a)) or from the sech^2 distribution (equation (6.15b)). The three-dimensional simulations were both based on the Poisson formula. In the simulation denoted with $k = k_0$, only the waves with the wavenumber k_0 were propagating in directions different from the streamwise one, and the directional spectrum was calculated with equations (6.16) and (6.18). In the simulation denoted with *omnidirectional*, also the shorter waves with $k > k_0$ had the same directional distribution, which was described by equation (6.19). FIG. 6.5b shows that all these choices had little effect on the modelling of the Doppler spectrum. The only noticeable difference was the slight overestimation of the amplitude of the Bragg peaks by the two-dimensional models, compared to the three-dimensional ones. The computational cost of the three-dimensional simulations was considerably larger than that of the

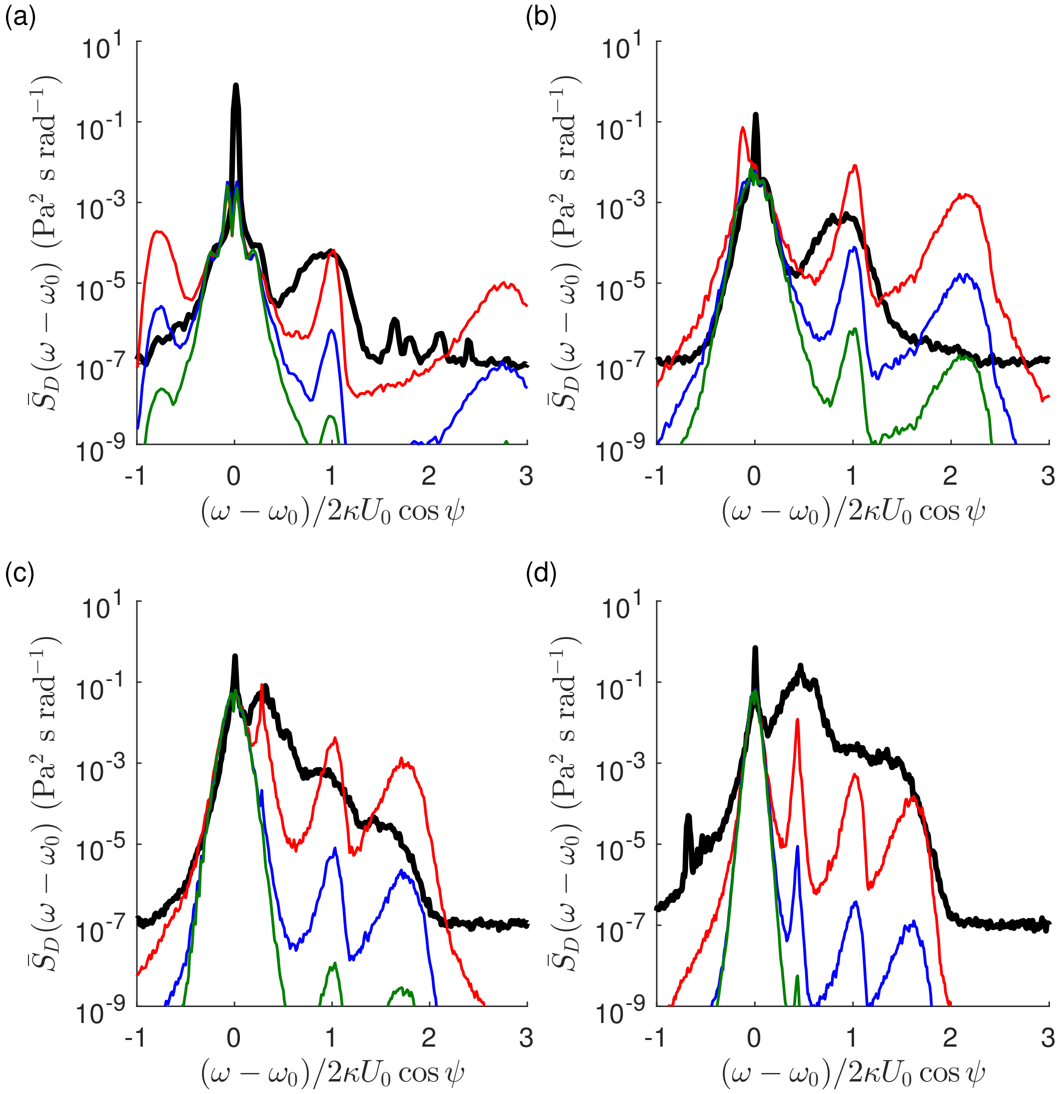

Figure 6.6: The measured Doppler spectra compared with the results of the two-dimensional Monte Carlo simulation for (a) condition 1, (b) condition 4, (c) condition 7, and (d) condition 13. (black) Measured, (red) modelled with $\alpha = 5$, (blue) modelled with $\alpha = 7$, and (green) modelled with $\alpha = 9$.

two-dimensional ones. Therefore, it was decided to use the two-dimensional model for the analysis described from here on. The Poisson distribution was preferred to the sech^2 because it decays less rapidly near $\theta = 0$, which seemed to represent better the behaviour of the measured frequency spectra (see FIG. 6.1).

FIG. 6.6 shows the results of the two-dimensional Monte Carlo simulation in terms of the Doppler spectra for the flow conditions 1, 4, 7, and 13, compared to the respective measurements. The measurements with wave probes did not allow the direct estimation of the spatial spectrum of the surface elevation, from which α can be determined. Different simulations with $\alpha = 5$, $\alpha = 7$, and $\alpha = 9$ were therefore carried out, in order to observe the effect of the spectrum slope on the Doppler spectra. The minimum value of α was limited to 5 in the simulations in order to ensure the validity of the Kirchhoff approximation. The minimum of the Kirchhoff parameter among the four conditions represented in FIG. 6.6 was calculated to be 26.6 in condition 7, based on equation (6.23) and (6.28) with $\alpha = 5$. In all cases, the model represented accurately the peak of the Doppler spectrum at the frequency near $\omega - \omega_a = 0$. The width of this peak depends mainly on the frequency spectrum of the free surface at least when the Rayleigh parameter is small, as it was shown in sub-section 3.2.2. At the frequency below $2k_0U_0$ the frequency spectrum depends on the angular distribution $\Gamma_\theta(\theta)$ only, therefore it is independent of α. There is a small peak of the Doppler spectrum of condition 1 in FIG. 6.6a, at the frequency of approximately $0.3(2\kappa U_0 \cos\psi_s)$. This peak corresponds to the peak of the surface frequency spectrum at the frequency $\omega U_0/g = 0.3$ in the same condition. It was correctly represented by the model. At the larger frequency, the Doppler spectra predicted with the different choices of α separate from each other. The best fit for condition 1 was with the model with $\alpha = 5$. The best fit was with $\alpha = 7$ in condition 4, then α appears to decrease with the increase of the Froude number. Looking at the negative-frequency tail of the Doppler spectra, the slope was approximately 5 in condition 7, and possibly smaller than 5 in condition 13. The model predicts the occurrence of the three Bragg peaks in all conditions, in contrast with the experimental measurements in conditions 1 and 4 where only the non-dispersive peak with the frequency $\Omega^U(k_B, 0)$ is observed. The Bragg peaks are also considerably wider in the measured spectra than in the simulations. This could be explained by nonlinear interactions between the surface waves or between both the surface waves and the acoustic waves, as discussed in subsection 3.2.2. These observations are discussed with more detail in subsection 6.2.3.

FIG. 6.7 shows the measured Doppler spectra in the same flow conditions, compared with the predictions by the linear Doppler model based on the small Rayleigh parameter. The results by this model are similar to the ones provided by the Monte Carlo model. The behaviour of the Doppler spectra at low frequency was represented well. In comparison with the Monte Carlo simulation, the Doppler spectra predicted by the linear model decay more rapidly with the frequency, and underestimate the amplitude of the Bragg peaks. The best fit with the measurements was found with $\alpha \approx 7$ in conditions 1 and 4, while both in conditions 7 and 13 α had to be smaller than 5. The same considerations about the presence of the three Bragg peaks and their smaller width compared to the measurements still apply to the results shown in FIG. 6.9. The validity of the simplified model was limited, especially in conditions 7 and 13 where the Rayleigh parameter was equal to 0.93 and 0.76, respectively. In spite of these limitations, the model provided a correct qualitative representation of the behaviour of the Doppler spectra, with a much simpler and fast computation.

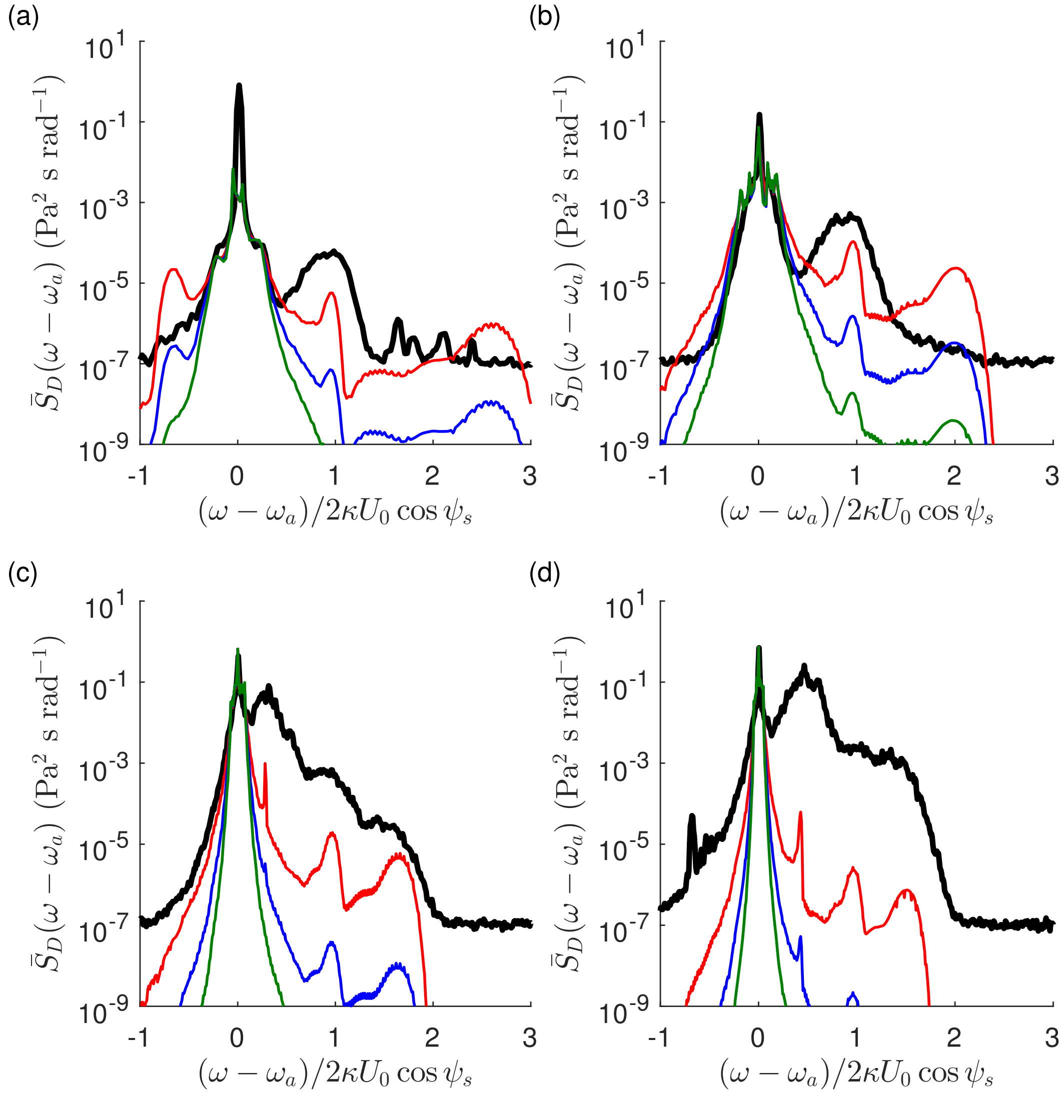

Figure 6.7: The measured Doppler spectra compared with the prediction by the linear model based on the expansion of the Kirchhoff integral for (a) condition 1, (b) condition 4, (c) condition 7, and (d) condition 13. (black) Measured, (red) modelled with $\alpha = 5$, (blue) modelled with $\alpha = 7$, and (green) modelled with $\alpha = 9$.

6.2.2 Results in forward scattering (bi-static configuration)

It is common to consider the Doppler spectra of the scattered signal in the backscattering (bi-static) configuration only. This approach ensures that the spectral resolution is maximum, and that the Bragg peaks are clearly distinguishable when the directivity pattern is narrow and the source and receiver are in the Fraunhofer zone. In the case which was studied here, the directivity pattern was relatively broad, and the source and receiver were outside of the Fraunhofer zone. A considerable portion of the emitted acoustic pressure field was reflected right below the source and the receiver. This caused the large peak of the measured Doppler spectra near the frequency ω_a in FIG. 6.4. Due to the choice of the acoustic frequency and of the angle of incidence ψ_s, the Bragg scales correspond to short capillary waves which spectrum could not be measured with the arrays of wave probes. The small distance between the source and the microphone in the backscattering configuration made so that the Fresnel zone was small and localised right below the source, near the direction of specular reflection. This hindered the validity of the linear Doppler model at the low Doppler frequency.

When the source and/or the receiver are outside of the Fraunhofer zone and the directivity pattern is not infinitely narrow, also the forward scattered signal experiences a Doppler shift. If the main directivity lobe of the source is directed towards the direction of specular reflection, the Bragg peak relates to the infinitely long waves with the wavenumber $q_x = 0$, and consequently with the frequency $\omega - \omega_a = 0$. This allows focusing the attention on the larger scales of the free surface, which behaviour is more easily characterised experimentally. The size of the Fresnel zone scales with $1/\sqrt{\sin(\psi)}$ (equation (3.115)), therefore it is larger away from the source. This makes the approximations of the linear model more accurate, hence it provides a faster method to predict the Doppler spectrum and potentially to invert it in order to determine the spectrum of the rough surface.

The measurements of the Doppler spectrum of the scattered acoustic signal recorded by the second microphone, which position was reported in equation (4.7c), are shown in FIG. 6.8 for all the tested flow conditions. These spectra have one single peak at the frequency ω_a. The spectra are asymmetric, with longer tails towards the positive frequency. This corresponds to the positive value of q_x, therefore to the scattering from the region behind the point of specular reflection, nearer to the microphone. The length of the tail increases when the Froude number increases from FIG. 6.8a to FIG. 6.8d, which suggests the decrease of the slope of the spectrum. Condition 1 again exhibits a sharper knee of the Doppler spectrum at the frequency $0.3(2\kappa U_0 \cos\psi_s)$, which relates to the peak of the frequency spectrum of the free surface elevation at the frequency $\omega U_0/g = 0.3$. The behaviour of the Doppler spectra is similar in each range of Froude numbers. The spectra in each of FIG. 6.8b, c, and d, decay with the same slope, again with the exception of condition 5 which behaves like the conditions with the larger Froude numbers.

The measured Doppler spectra have been simulated with the same two numerical models described in the previous section. The results of the two-dimensional Monte Carlo simulation are shown in FIG. 6.9 for the conditions 1, 4, 7, and 13. With respect to the measurements in backscattering, the spectra are less dependent on the shorter waves. As a result, the predictions by the model represent well the measured spectra over a wider range of frequencies. In conditions 1 and 4, the tails of the Doppler spectra follow the behaviour expected with $\alpha = 7$. In conditions

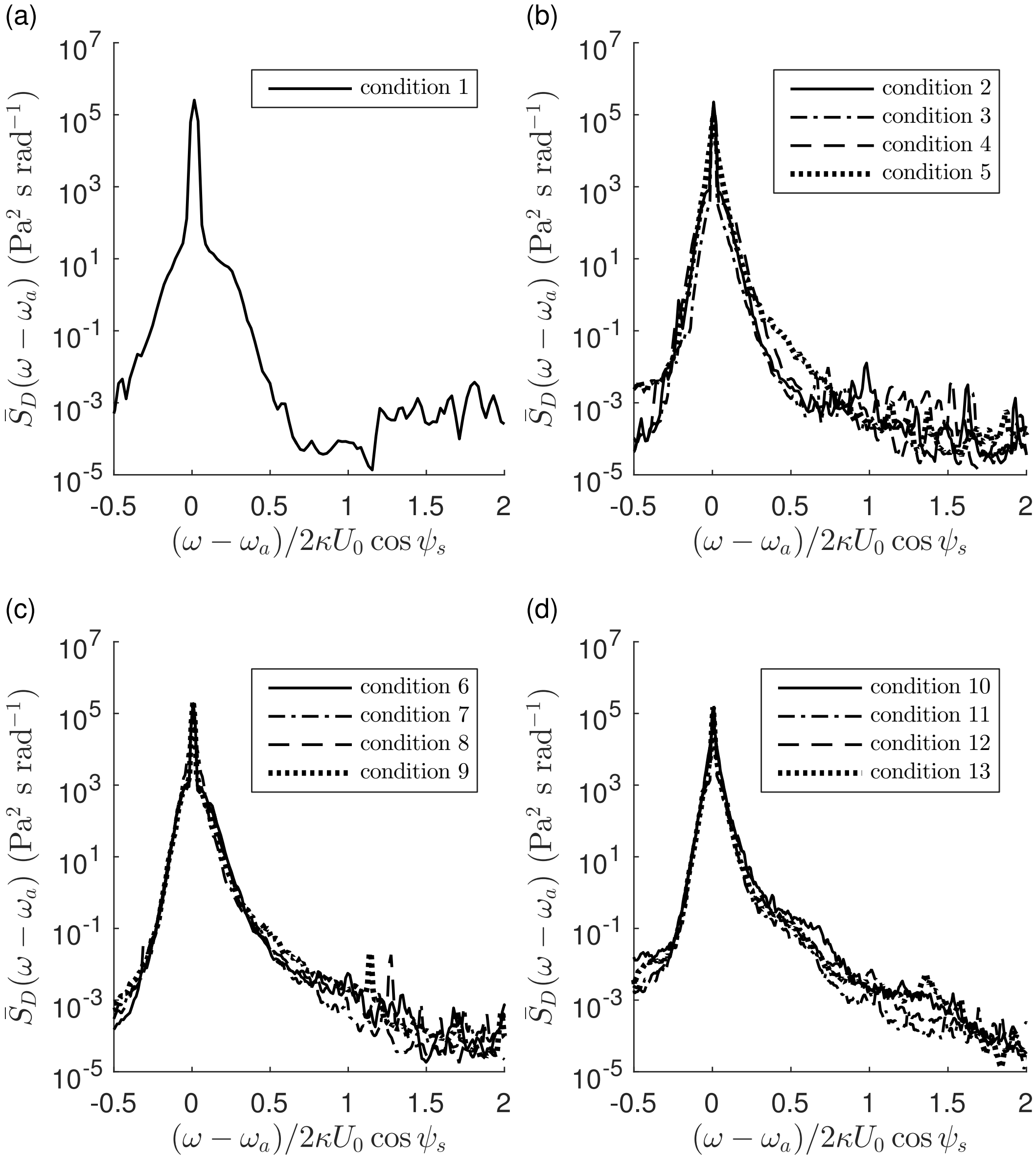

Figure 6.8: The average Doppler spectra of the forward scattered acoustic field.

7 and 13, the measured spectra depart from the modelled ones at the relatively low frequency of $0.3(2\kappa U_0\cos\psi_s)$ and $0.1(2\kappa U_0\cos\psi_s)$, respectively. At the higher frequency the decay is slower than the one predicted by the model with $\alpha = 5$, which suggests that short waves have a larger amplitude than predicted by the power-law spectrum. The departure is more evident in the condition 13 with the larger Froude number, where the gradient of the Doppler spectrum decreases sharply relative to the modelled power-law near the frequency $0.3(2\kappa U_0\cos\psi_s)$, before it increases again at the frequency $0.6(2\kappa U_0\cos\psi_s)$. This confirms that the model based on the power-function decay of the surface spectrum with the constant slope α had limited validity at the shorter scales, especially in condition 13.

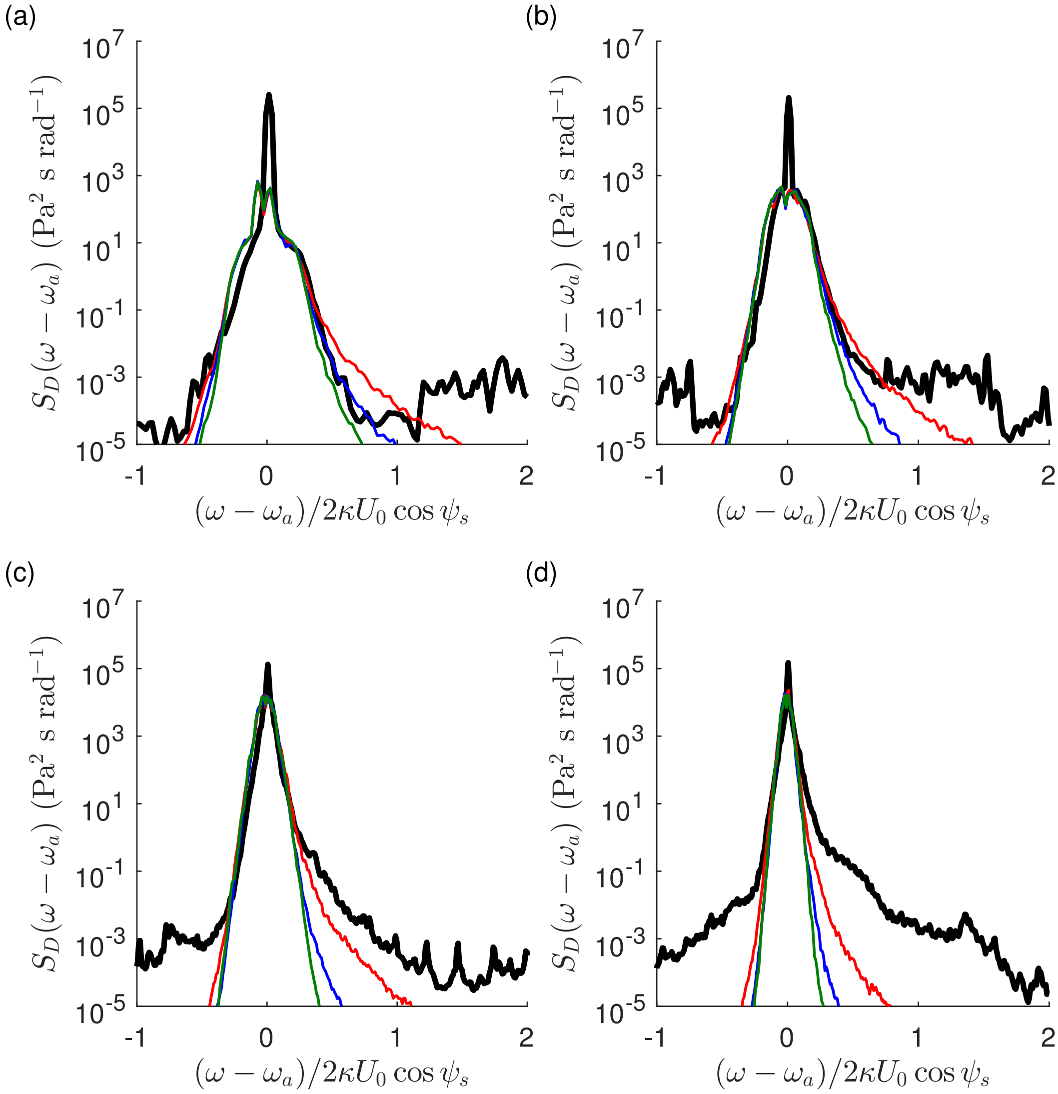

Figure 6.9: The measured Doppler spectra of the forward scattered signal compared with the results of the two-dimensional Monte Carlo simulation for (a) condition 1, (b) condition 4, (c) condition 7, and (d) condition 13. (black) Measured, (red) modelled with $\alpha = 5$, (blue) modelled with $\alpha = 7$, and (green) modelled with $\alpha = 9$.

FIG. 6.10 shows the analogous results for the linear model based on the expansion of the Kirchhoff integral. For the reasons explained above, this model was expected to give more reliable results in forward scattering than in backscattering. This is confirmed by the results of FIG. 6.10. The results of the linear model confirm the apparent decrease of the slope of the spectrum from $\alpha = 9$ to $\alpha < 5$ when the Froude number increases across the four conditions represented in FIG. 6.10. The linear model approximates the measurements apparently better than the Monte Carlo simulation. This is only apparent, since the linear model is an approximation of the more general Kirchhoff approach which was implemented in the Monte Carlo model. Especially in condition 13, where the Rayleigh parameter was equal to 0.76, the Doppler spectrum predicted by the linear Doppler model had limited validity.

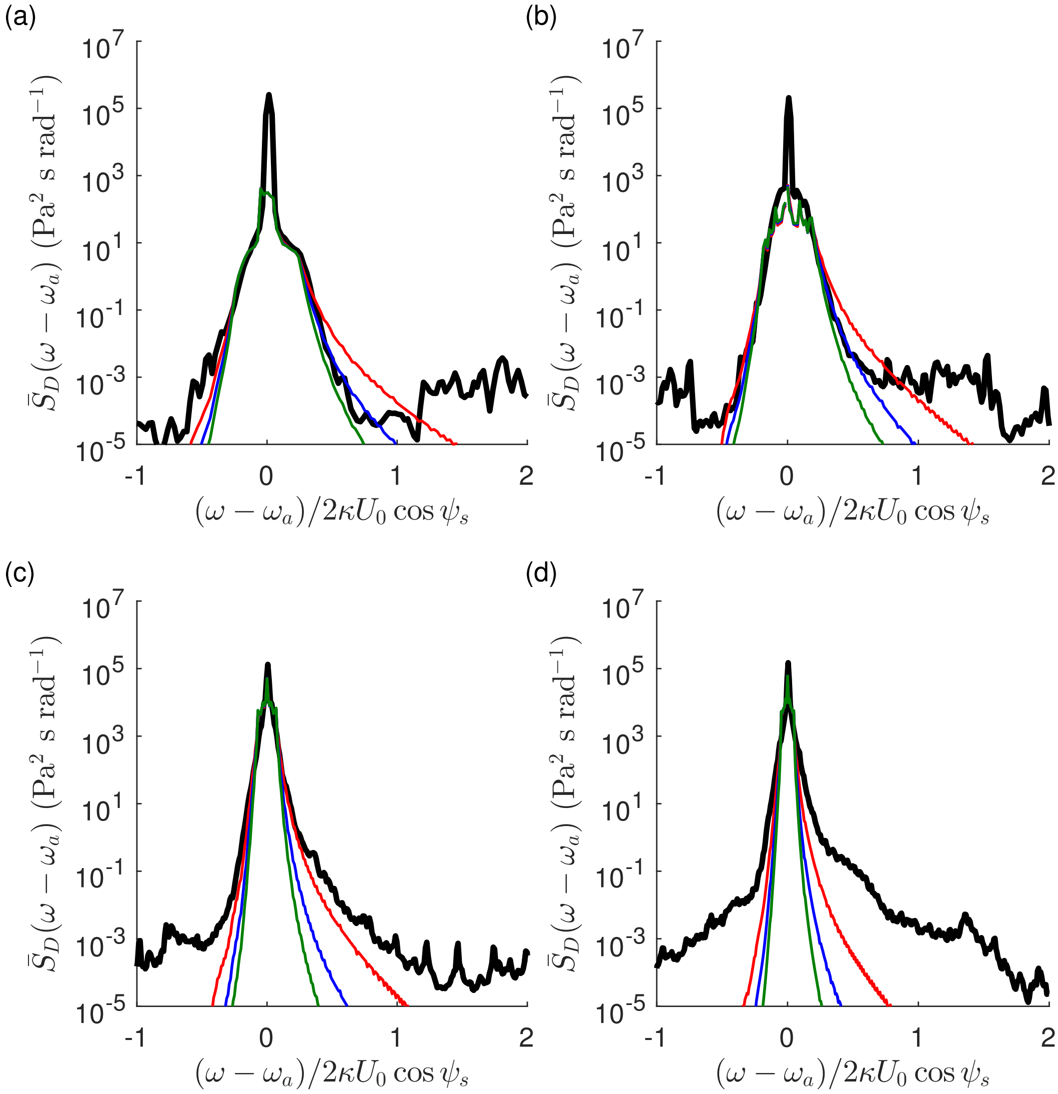

Figure 6.10: The measured Doppler spectra of the forward scattered acoustic signal compared with the prediction by the linear Doppler model for (a) condition 1, (b) condition 4, (c) condition 7, and (d) condition 13. (black) Measured, (red) modelled with $\alpha = 5$, (blue) modelled with $\alpha = 7$, and (green) modelled with $\alpha = 9$.

In light of the good performance of the forward scattering model applied to the Doppler spectra of the forward scattered field, it was decided to attempt the direct inversion of the surface spectrum based on the method derived in sub-section 3.2.2. For the inversion, only the half of the measured Doppler spectra with the positive frequency was used. For simplicity, it was assumed that the spectra of each of the three types of waves at each frequency was the same, i.e., that the ratio of their amplitudes was

$$C_S \equiv 1. \tag{6.48}$$

The three dimensionality of the surface patterns were also neglected by imposing

$$\Gamma(k,\theta) = \delta(\theta), \tag{6.49}$$

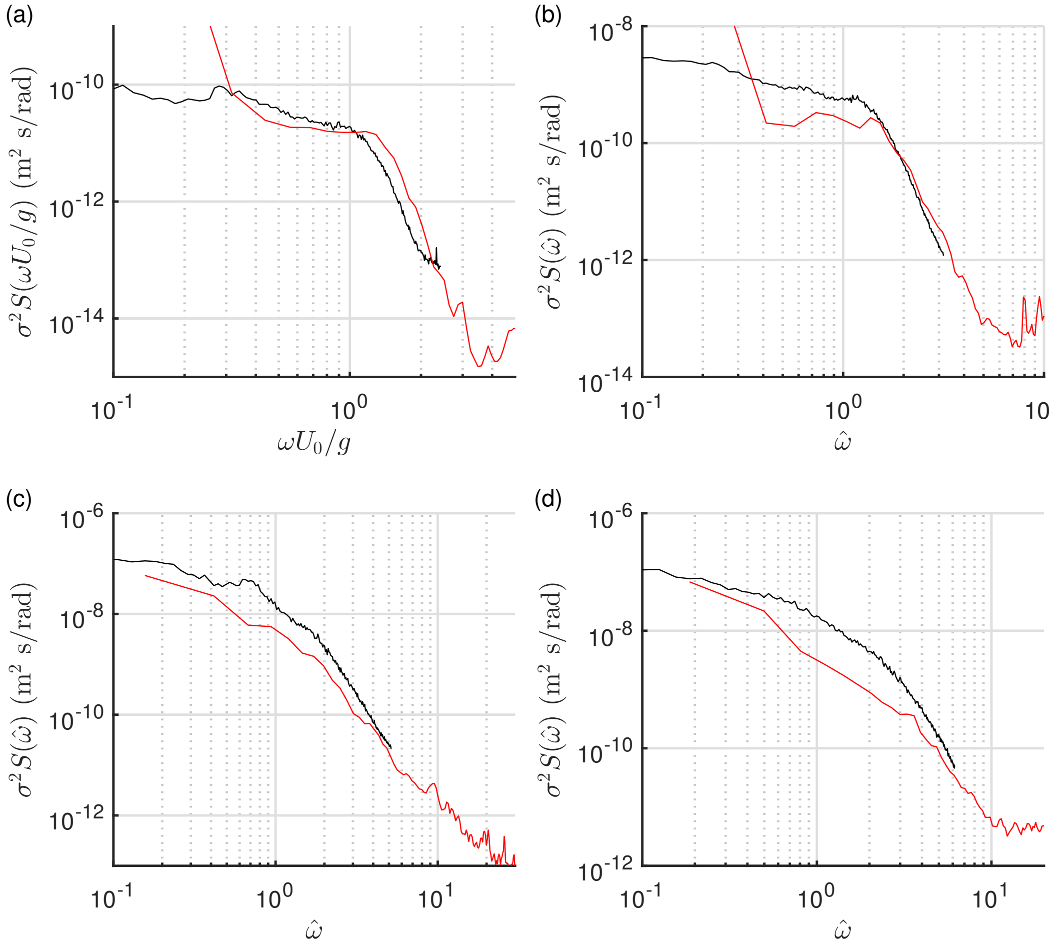

Figure 6.11: The frequency spectra of the free surface elevation (red) calculated from the Doppler spectrum of the forward scattered signal, and (black) measured with the wave probes, for (a) condition 1, (b) condition 4, (c) condition 7, and (d) condition 13.

and the inversion was based on the two-dimensional version of the Kirchhoff integral equation, i.e., on equation (3.125).

The results of the inversion applied to the forward scattered Doppler spectra are shown in FIG. 6.11 for conditions 1, 4, 7, and 13, in terms of the reconstructed frequency spectra of the surface elevation. These are compared with the same spectra measured by the wave probes. The reconstructed spectra follow the same behaviour of the measured frequency spectra. The increase of the slope of the spectra at the frequency larger than $\hat{\omega} = 1$ is captured well across the various conditions, although this increase is predicted at a slightly larger frequency than measured in condition 1. In condition 13 the reconstructed spectrum is largely underestimated in the frequency range from $\hat{\omega} = 0.5$ to $\hat{\omega} = 4$. The Rayleigh parameter was relatively large in this condition, therefore the inversion had limited validity.

The possibility of measuring the spectrum of the free surface remotely from the Doppler spectrum of the scattered acoustic field is of interest, because the first spec-

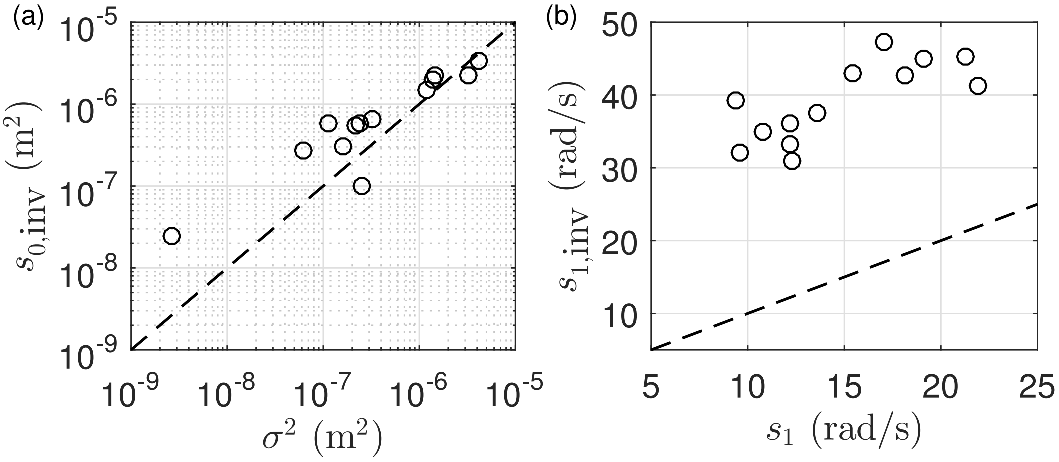

Figure 6.12: (a) The variance of the free surface elevation, $s_{0,inv}$, and (b) the first spectral moment, $s_{1,inv}$, calculated from the frequency spectrum reconstructed from the measured Doppler spectra of the forward scattered acoustic pressure field. The dashed lines represent the same quantity calculated from the measurements with wave probes.

tral moments had been related to the hydraulic quantities of the flow in section 5.2.1. Although the validity of the method was formally restricted to a narrow range of flow conditions, the inversion was applied to all the measurements of the forward scattered acoustic field. From each reconstruction, the first and second spectral moments (the standard deviation of the free surface elevation, and its average frequency) were computed. The results are shown in FIG. 6.12, compared with the same moments which had been estimated from the wave probes measurements. The calculated variance of the free surface elevation which is shown in FIG. 6.12a followed the same pattern of the measurements with the wave probes, in most flow conditions. The value of the first spectral moment was overestimated by a factor of approximately 3 in all conditions, which was due to the different spectral resolution of the measurements with wave probes compared with the acoustic reconstruction, and to the peak of the frequency spectra at the frequency near zero. In spite of this shift, the pattern of the first spectral moment was also represented well by the inversion.

6.2.3 Discussion

The results in this section have shown the information that can be extracted from the measurement of the Doppler spectrum of the scattered acoustic pressure field. These spectra can be used in order to determine the velocity of the patterns on the free surface. The Doppler spectra measured in the backscattering configuration showed the presence of Bragg peaks, which frequency is related directly to the phase velocity of the Bragg waves. The prediction of these frequencies based on a model of the dispersion relations of three characteristic types of waves (upstream capillary-gravity waves, downstream capillary-gravity waves, and non-dispersive waves) fitted the measured Doppler spectra well. This would allow the remote characterisation of the mean surface velocity, if the other variables which control the dispersion relation (the mean depth, and the vertical variation of the streamwise average flow velocity) are known.

In practice, only the non-dispersive peak with the frequency $2\kappa U_0 \cos\psi_s$ was visible in the measured spectra for the conditions 1 and 4 in FIG. 6.6a, and b, respectively. In contrast, the numerical models predicted the occurrence of three peaks of the Doppler spectrum in all conditions. This suggests that the two types of dispersive waves with the Bragg wavenumber k_B were not physically present in these conditions, in contrast with the proposed model. The relative amplitude of each of the three separate Bragg peaks in conditions 7 and 13 (FIG. 6.6c, d) differed between the model and the measurements, especially in condition 7. Here the dispersive waves with the Bragg wavenumber k_B propagating upstream (the peak with the lower frequency) were considerably larger than the other two types of waves with the same wavenumber. In the model it was assumed that at each wavenumber all three types of waves co-existed, and that their amplitude ratios were independent of the wavenumber and equal to $\Gamma_\theta(\pi)/\Gamma_\theta(\pi/2)$ between the upstream and the non-dispersive waves, and $\Gamma_\theta(\pi/2)/\Gamma_\theta(0)$ between the non-dispersive and the downstream waves, respectively. The results in FIG. 6.6 suggest that this assumption does not apply in general to the small Bragg scales, where the dispersive waves only appeared when the Froude number was larger than 0.5, and the upstream waves had a larger amplitude than it was predicted by the model. A more accurate representation of the free surface spectrum requires the measurement of the angular spatial spectrum at the wavenumber comparable with k_B, which was impossible with the available instrumentation.

The Bragg peaks were found considerably wider in the measured spectra than in the simulations. The results in FIG. 6.5b showed that the broadening of the Bragg peaks was not due to the three-dimensionality of the free surface patterns. The broadening of the Bragg peaks can be explained by the multiple scattering of the acoustic signal, or by the modulation of the short waves by the longer waves [e.g. Keller and Wright, 1975, Hara and Plant, 1994], as reported in sub-section 2.1.5. In the case of scattering in the Fraunhofer zone, these effects are modelled with a set of corrective factors to the spectrum of the free surface. In the case reported here this approach was not viable. In subsection 3.2.2 rough estimates of the widening of the Bragg peaks due to the tilt modulation and to the velocity modulation induced by longer waves on the short Bragg waves have been derived. These are represented by equations (3.132) and (3.134). The frequency broadening due to the tilt modulation is calculated based on equation (3.132) to be between 7.3 rad s^{-1} in condition 1 and 61.7 rad s^{-1} in condition 5. These correspond to a relative variation between 2.8 % of the frequency $2\kappa U_0 \cos\psi_s$ in condition 1 and 9.1 % of the same frequency in condition 5. The velocity modulation calculated from equation (3.134) (assuming $c(k_0) = U_0$) varies between 3.6 rad s^{-1} in condition 1 and 54.3 rad s^{-1} in condition 5, corresponding to the relative variations between 1.4 % and 8.1 %, respectively. It is noted that the width of the measured spectra was comparable with the frequency shift $2\kappa U_0 \cos\psi_s$. The tilt and velocity modulations estimated with equations (3.132) and (3.134) do not seem to be large enough to justify the observed widening of the Doppler spectra near the Bragg peaks, but they are significant even if the characteristic surface slope $k_0\sigma$ was small. This is caused by the high frequency of the acoustic signal, and by the large phase velocity and group velocity of the waves associated with Bragg scattering. Additional broadening of the spectra near the Bragg peaks may have derived from nonlinear interactions among the waves on the surface, and among the surface waves and the multiply scattered acoustic signal. These phenomena are represented by the hydodynamic and electromagnetic (acoustic) modulation transfer functions derived for example by Keller and Wright [1975] and Hara and Plant [1994]. These derivations do not apply strictly to the case considered here, therefore they have not been implemented.

The second-order spectrum [e.g. Lipa and Barrick, 1986] has been also associated with the broadening of the Doppler Bragg peaks and the increase of the amplitude of the spectrum of short waves [Janssen, 2009]. Even though the Monte Carlo model did not require the expansion of the spectrum of the free surface, the calculations were based on a linear surface model that does not allow interactions among surface waves. The existence of weak nonlinear interactions among waves on the surface was suggested by the measurement of the statistics of the surface elevation in section 5.2. Those measurements showed only evidence of weak nonlinearities in a limited range of flow conditions, but the measurements were limited to waves much longer than the capillary waves that are most important for Bragg scattering. It is possible that stronger nonlinearities were interesting the shorter capillary waves in all conditions. In order to investigate these phenomena, more complex models of the free surface behaviour and of the acoustic scattering would be required, such as the ones implemented by Johnson et al. [2001]. Unfortunately, there is currently no known model that is able to describe the nonlinear dynamics of the free surface in a shallow turbulent flow adequately.

In light of these limitations which are not related to the acoustic model, the simplified linear Doppler model presented in subsection 3.2.2 was able to capture the behaviour of the backscattered Doppler spectra well. The computations based on this type of model were much faster, and the model allows theoretically the calculation of the fully three-dimensional frequency-wavenumber spectrum. Unfortunately, the linear model had only limited validity in the cases investigated here, and the direct inversion of the frequency-wavenumber spectrum required a fully three-dimensional reliable model of the surface spectrum in shallow flows, which still has not been derived. For these reasons, the direct estimation of the mean surface velocity from the Doppler spectra measured in backscattering was not attempted here.

In general, the comparison between the measurements and the two Doppler models has shown that the representation of the free surface by a spatial spectrum with the constant power-function decay represents well the behaviour of the longer gravity waves, but had limited validity at the shorter scales. The slope of the spectrum appeared to increase towards the higher wavenumber, especially when the Froude number increases. The increase of the slope of the frequency spectra was already observed in section 5.2.1, and it has been confirmed here by the measurements of the scattered acoustic field. This phenomenon cannot be explained with the actual knowledge of the free surface behaviour in shallow turbulent flows. The sudden appearance of the dispersive Bragg waves when the Froude number approached 0.5 cannot be explained either, especially because the measured frequency-wavenumber spectra showed patterns of longer dispersive waves in all conditions even when the Froude number was smaller than 0.5, while the non-dispersive waves which appear consistently in all Doppler spectra were only observed in condition 1.

There are few phenomena that can cause the increase of the amplitude of the spectrum of short waves, and specifically of the dispersive waves propagating against the flow, when the Froude number increases. These phenomena are the resonant interaction with turbulence at the critical layer [Teixeira and Belcher, 2006], the shear instability discussed in subsection 2.1.3, and the resonant interaction between multiple waves (including the three dimensional instabilities) discussed in subsection 2.1.5. The short upstream waves possess a critical layer, therefore they can grow due to the first two mechanisms. Assuming the validity of the 1/3 velocity profile, the distance of the critical layer of the Bragg waves from the bed datum relative to the diameter of the spheres was

$$\frac{z_c}{d_S} = \frac{H}{d_S}\left[1 - \frac{\Omega^-(k_B, \pi)}{k_B U_0}\right]^3, \tag{6.50}$$

which varied between 0.02 in condition 4 and 1.0 in condition 10. The critical layer was above the crests of the spheres bed only in conditions 5, 10, 11, and 13, whereas the upstream Bragg scales were also observed in conditions 7 and 12. This ruled out the resonant interaction with turbulence and the shear instabilities as the mechanisms which caused the growth of short waves. In contrast, the interaction between resonant combinations of waves cannot be excluded, as well as more complex mechanisms such as the energy cascades typical of wave turbulence. These mechanisms are still not fully understood, especially in the case of gravity and capillary waves propagating in a turbulent flow with a rough boundary.

In the subsection 6.2.2 it was shown that the Doppler spectra can be measured also in the forward scattering configuration. In this configuration the spectra are less dependent on the lesser known capillary waves, and can be modelled more accurately. The conditions for the validity of the linear model are more likely to be met, which justified the inversion of the frequency spectra based on this model. Future studies may identify a way to invert the whole frequency-wavenumber spectrum directly, possibly by introducing contemporary measurements at different frequencies, or with different angles of incidence. This would allow the complete characterisation of the free surface spatial and temporal behaviour remotely. Here the inversion was based on the assumption that the amplitude of the different types of waves is governed only by the frequency of these waves and not by their wavenumber. Although this assumption was simplistic, the inversion of the surface frequency spectra compared well with the direct measurements with the conductance wave probes. The patterns of the first and second spectral moment was also determined correctly. This may allow the estimation of the hydraulic quantities of the flow, since it was found in section 5.2 that the spectral moments scaled consistently with the parameter k_0U_0.

6.3 Summary

The aim of this chapter was to demonstrate the possibility to measure the spatial and temporal statistics of the free surface of turbulent shallow flows remotely, from the measurement of the scattered acoustic pressure field. A simplified model of the free surface behaviour was suggested, and implemented numerically. The model represents the surface elevation as a linear superposition of independent trigonometric functions with a random distribution of the phase, and with the amplitude governed by a spatial spectrum following the power-function law $S(k) \propto k^{-\alpha}$. The dynamics of the surface were governed by the dispersion relations observed experimentally based on the measurements with wave probes. The angular distribution of the waves was modelled according to two simple angular distributions. The slope of the spectrum α could not be measured directly with the arrays of wave probes, therefore various tests with different values of α were performed.

The first objective of the analysis was the validation of the surface model. This was achieved mainly by comparing the measurements of the Doppler spectra of the scattered acoustic field with the predictions by two numerical models, both based on the Kirchhoff approximation. It was shown that the angular distribution of the waves and the consequent three-dimensionality of the surface patterns affect the Doppler spectra only marginally. The comparison with the Monte Carlo simulation, which is believed to be more accurate due to the characteristics of the measurements setup, showed that the surface model predicts well the behaviour of the Doppler spectra at the frequency nearer to the frequency of the source transducer. Based on the results of the numerical model, this range of frequencies corresponds to the longer waves which dominate the spectrum of the free surface. The comparison between the measurements and the numerical simulations suggests that the amplitude of the shorter waves was larger than predicted by the model with the power-function decay. The measured Bragg peaks were also wider than predicted by the numerical models. It was suggested that interactions among waves may have caused the change of the slope of the spatial spectrum as well as the broadening of the Doppler spectra. The short waves could not be measured directly with the arrays of wave probes, and there are no known simple nonlinear model that can describe the interaction between gravity and gravity-capillary waves in a shallow turbulent flow, therefore further studies are required in order to confirm this hypothesis.

The second objective was to illustrate the effects of the single parameters of the surface on the acoustic Doppler spectra. The relation between the frequency-wavenumber spectra of the surface elevation and the Doppler spectra of the scattered signal were investigated in section 6.2. This relation was made explicit by the linear Doppler model presented in subsection 3.2.2, where it was shown that the same mechanism which enhances the acoustic scattering from Bragg scale waves also creates a direct link between the Doppler spectra and the frequency spectra of the surface. This link was used in subsection 6.2.2 in order to reconstruct the frequency spectra based on the measurements of the Doppler spectra. The relative width of the Doppler spectra at low frequency was found increasing with the increase of the Froude number. This was associated with the decrease of the slope of the spectrum of the surface, which had already been suggested in chapter 5 based on the measurements of the frequency spectra of the elevation. This suggestion was confirmed here independently based on an alternative remote measurement technique. It was also observed that the relative amplitude of the short upstream waves increased apparently with the increase of the Froude number. This observation cannot be explained with the actual knowledge of the physics of the free surface of shallow turbulent flows.

The measurement of the Doppler spectra of the scattered acoustic field with the backscattering configuration has been proposed as a way to estimate the mean surface velocity of the flow [e.g. Plant et al., 2005, Costa et al., 2006, Fukami et al., 2008]. This can be found from the peak of the Doppler spectra at the frequency $\omega_a + 2\kappa U_0 \cos\psi_s$ if the Bragg scale waves are not dispersive and propagate at the mean surface velocity. When the Froude number increases additional peaks related to the Bragg scale waves propagating upstream and downstream appear. These peaks grow progressively in amplitude with the increase of the Froude number, until they ultimately shade the first peak. When this happens the mean surface velocity can still be inferred based on the known dispersion relation of the Bragg scale waves. The method allows the measurement of the mean surface velocity remotely, but its accurate application requires a better understanding of the mechanism which causes the growth of the dispersive short Bragg scale waves.

In chapter 5 it was shown that the frequency spectrum of the surface elevation scales directly with the product $k_0 U_0$ in the flow conditions with the mean surface velocity larger than the minimum of the phase velocity of gravity-capillary waves. This spectrum can be estimated from the measurement of the Doppler spectrum of the scattered acoustic pressure field. The estimation is more accurate when obtained with a forward scattering configuration, because of the smaller impact of the lesser known capillary waves. The link between the two spectra is not straightforward if the measurements are not performed in the Fraunhofer zone. In order to be able to estimate the frequency spectrum, one should perform a large number of simulations that cover a wide range of the fundamental free surface parameters. In some conditions when the Rayleigh parameter is small and the horizontal scales on the surface are also small, the spectrum can be calculated directly based on a linear model. The method relies on a model of the surface spectrum shape and of the dispersion relation. In the experiments reported here the frequency spectrum was successfully reconstructed, but not with the level of accuracy required for the direct estimation of the product $k_0 U_0$.

Chapter 7

Thesis conclusions

7.1 Main results

The aim of this thesis was to provide an answer to three research questions. These are reported here, together with a summary of the related results presented in the chapters 5 and 6.

- Is it possible to interpret the patterns at the free surface of a shallow turbulent flows based on the theory of gravity-capillary waves?

The measurements of the free surface elevation in a range of shallow turbulent flows over a homogeneously rough bed were obtained with arrays of conductance wave probes, and are described in chapter 5. In subsections 5.2.2 and 5.2.3 it was shown that the statistics of the water surface fluctuations and of their amplitude measured at a single location are compatible with a linear or weakly nonlinear model of gravity-capillary waves with random phase. The measurements of the frequency-wavenumber spectra of the water surface elevation in subsection 5.3.2 have shown that the patterns on the free surface followed the dispersion relation of gravity-capillary waves propagating in a flow where the average streamwise velocity profile is described by a power-law of the depth. The analysis of the dynamics of wave groups in subsection 5.3.3 has shown that radial patterns of random gravity-capillary waves can combine and form structures that apparently move at the velocity equal to the mean surface velocity while oscillating vertically at a characteristic frequency. These structures had previously been observed and associated with the manifestation of turbulent coherent structures that rise towards the surface [Nichols et al., 2016]. The shape of these structures was characterised in subsection 5.3.3 and confirmed by the wavelet spectral method in section 5.4. In the transverse direction it is represented by pairs of standing gravity-capillary waves. The dimensions of these structures are governed by the wavelength of the stationary waves produced by the interaction with the rough bed. These results confirm that the patterns at the free surface of shallow sub-critical turbulent flows can be described based on the theory of gravity-capillary waves, which answers the first question.

Alternative patterns that could correspond to scars or dimples originated by the interaction with coherent turbulent structures were not identified in most conditions, and their importance was suggested to be marginal in the range of conditions which have been investigated. The only exception was represented by condition 1, where the mean surface velocity was smaller than the minimum phase velocity of gravity-capillary waves. In this condition the stationary waves could not form, and the surface was dominated by non-dispersive patterns propagating at the mean surface velocity. Although the results presented here cannot be conclusive, it was postulated that the non-dispersive patterns were waves which were forced by the non-resonant interaction with turbulence, according to the mechanism proposed by Teixeira and Belcher [2006]. This mechanism is explained by a spectral model and does not require the turbulent structures to be coherent across different scales.

- Is there a relation that links the patterns of gravity-capillary waves and their statistics to the hydraulic properties of the flow, namely the mean surface velocity, the average streamwise velocity profile, and the homogeneous depth?

The dispersion relation of the patterns on the surface were approximated well by a model where the depth-wise variation of the time averaged streamwise flow velocity follows a power-function of the depth. This has been demonstrated in subsection 5.3.2. In all conditions where the mean surface velocity was larger than the minimum phase velocity of gravity-capillary waves, the patterns were dominated by the stationary waves with the wavenumber vector parallel to the direction of the flow. The wavenumber of these waves can be predicted based on the values of the mean surface velocity, of the uniform time averaged flow depth, and of the exponent of the average streamwise velocity profile. The radial patterns of waves which were also observed in the same flow conditions in subsection 5.3.2 had the same wavenumber of the stationary waves, with the exception of condition 4. The different behaviour in this condition requires further investigation.

The characteristic wavenumber and frequency of the stationary waves represent the characteristic spatial and temporal scales of the free surface, and have been found affecting directly all its statistics . The frequency spectra of the elevation (subsection 5.2.1) scale with the frequency of the stationary waves. Empirical relations were suggested that relate this frequency with both the first spectral moment and the standard deviation of the elevation. The correlation function of the elevation at zero time-lag scales with the wavenumber of the stationary waves. The Froude number of the flow also seems to affect the patterns on the free surface. The increase of the Froude number caused the decrease of the slope of the frequency spectra of the elevation, and the relatively more rapid decay of the zero time-lag correlation. This was in agreement with the observations of Smolentsev and Miraghaie [2005], and shows that the water surface becomes more rough when the Froude number increases.

- Is it possible to relate the characteristics of these patterns with the Doppler spectra of the scattered acoustic field, in order to improve the accuracy of remote measurement techniques applied to shallow turbulent flows?

The measurements of the acoustic Doppler spectra in the backscattering configuration (subsection 6.2.1) have shown three sets of peaks of these spectra, which have been associated with scattering from Bragg resonant waves. The frequency of two of these peaks was close to the prediction by the dispersion relation of capillary waves propagating upstream and downstream. A third peak has been observed, which corresponds to waves propagating at the mean surface velocity of the flow. This third peaks was measured in all conditions, while the two peaks of dispersive capillary waves only appeared when the Froude number was larger than 0.5. The Bragg peaks were broader than what is predicted by a linear model of the free surface, which suggests the existence of interactions among waves and modulations of the short Bragg waves by longer gravity waves. Currently, the sensors that measure the flow velocity based on the Doppler spectra of the backscattered electromagnetic or acoustic waves are believed to neglect the effects of gravity-capillary waves. The results in this thesis have shown that this approach is only valid in a limited range of flow conditions, when the Froude number is small. In other conditions, the Bragg peaks due to dispersive gravity-capillary waves can become dominant, and affect the estimation of the mean surface velocity. The frequency of these peaks could be used in order to estimate the mean surface velocity and the mean flow depth. In order to be reliable, this estimation requires the knowledge of the phenomena that cause the growth of the dispersive waves and the broadening of the Bragg peaks. These phenomena are not understood yet.

An alternative approach consists in measuring the Doppler spectra of the scattered signal in the forward scattering configuration. These spectra have a direct relationship with the frequency-wavenumber spectra of the surface elevation, which becomes explicit under a set of conditions (subsection 6.1.4). The Doppler spectra of the forward scattered signal are governed by the behaviour of the longer waves on the free surface, which has been characterised in chapter 5. The results in subsection 6.2.2 have shown that the frequency of these spectra scales well with the mean surface velocity. The comparison with the two numerical models have confirmed the decrease of the slope of the wavenumber spectrum with the increase of the Froude number, although the simplified power-function model of the surface spectrum was found having limited validity at the higher wavenumbers. The inversion of the Doppler spectra according to a simplified model of the frequency-wavenumber spectrum of the free surface has been able to confirm the change of slope of the frequency spectra at the characteristic frequency of the stationary waves. These observations could provide a more reliable characterisation of the hydraulic quantities, although a more refined model of the surface dynamics and of the acoustic scattering would be needed in order to ensure the required accuracy.

7.2 Future work and challenges

The results presented in this thesis are believed to be representative of shallow turbulent flows over homogeneously rough bed, where the mean flow depth is of the same order of magnitude of the wavelength of the dominant waves, and where the Froude number is smaller than one. It is postulated that shallower flows may exhibit a stronger nonlinearity of the free surface, flows with a higher Froude number may show a stronger effect of turbulence relative to that of the rough bed, and much slower and deeper flows may exhibit a larger importance of coherent turbulent structures, with the consequent generation of scars and dimples on the surface. A smooth flat bed is still expected to promote the generation of stationary waves, although these may be smaller in amplitude. These different conditions require further investigations in order to evaluate the behaviour of the free surface and therefore the applicability of remote monitoring techniques in a wider range of flow conditions. In chapter 5 it was shown that in the condition where the mean surface velocity was smaller than the minimum phase velocity of gravity-capillary waves, the surface is dominated by non-dispersive waves. The statistics of the turbulent flow were not measured in this condition. These measurements would be useful in order to verify the hypothesis that the non-dispersive waves are generated by the interaction with turbulence. It was also observed that the standard theory of the interaction between the waves on the surface and the static rough bed predicts the increase of the amplitude of the stationary waves when the mean surface velocity is close to the minimum phase velocity of gravity-capillary waves. Additional measurements at or near this condition would help clarifying the generation of stationary waves. The characterisation of the free surface patterns in chapter 5 has also shown a different behaviour in condition 4 than in all other conditions. This behaviour has not been explained, and it should be investigated further.

The accuracy of the numerical models of the acoustic Doppler spectra has been affected by the lack of knowledge about the behaviour of the shorter waves on the free surface. Short waves could not be measured with the arrays of conductance wave probes due to their limited resolution. Alternative methods based on optics (Fourier transform profilometry [Cobelli et al., 2009, Maurel et al., 2009]) or on the scattering of acoustic waves (stationary phase method [Nichols et al., 2013], or acoustic holography [Krynkin et al., 2016]) could provide a better spatial resolution, and allow the fully three-dimensional spatial and temporal characterisation of the free surface. These methods provide a direct measure of the surface elevation. Therefore, they could also be used in order to estimate the hydraulic conditions of the flow based on the statistics of the free surface measured at one single location following the analysis described in section 5.2. This latter approach would provide a very efficient alternative way of monitoring the flow conditions remotely, which has never been considered in the application.

The statistical analysis in subsection 5.2 has shown that the increase of the surface slope and of the amplitude of the surface fluctuations relative to the mean flow depth is associated with a larger deviation from the linear Gaussian statistics. It was suggested that this deviation could be caused by nonlinear interactions among waves. Nonlinear interactions may also explain the generation of the radial patterns of waves with the wavenumber modulus of the stationary waves observed in subsection 5.3.2. Currently there is no known simple model that is able to describe the nonlinear dynamics of the free surface of shallow turbulent flows over homogeneously rough beds. Such a model would be of large importance for the development of accurate remote monitoring techniques that apply to these flows. It could explain the growth of the capillary Bragg scale waves when the Froude number is larger than 0.5, as well as the modulation of these waves by the longer gravity waves. Both phenomena have large impact on the measurement of the acoustic Doppler spectra, as it was shown in chapter 6.

The wavelet spectral analysis in section 5.4 has shown that the dynamics of the free surface can be modelled in terms of a linear composition of mutually independent wave groups. These observations may help clarifying the mechanisms that govern the generation and the evolution of the patterns on the free surface of shallow turbulent flows over a homogeneously rough bed. The wavelet spectral method allows the characterisation of the dispersion relation of the free surface from the measurement at a limited number of locations. The dispersion relation provides useful information about the hydraulic quantities of the flow, such as the mean surface velocity, the mean flow depth, and the average streamwise velocity profile. Ideally, this information could be extracted by inverting the measured dispersion relation. In general the dependence between these quantities is not linear and the inversion of the hydraulic parameters could present some numerical challenges, which need to be addressed. The application of the wavelet spectral method combined with non-contact measurement techniques that allow the reconstruction of the surface elevation in an area of limited size (e.g., the Fourier transform profilometry, the stationary phase method, or the acoustic holographic method) can provide an optimal approach to monitoring of the flow conditions remotely. This would overcome the current limitations of the techniques based on Doppler scattering, which were found being due to the still partial knowledge of the free surface behaviour in shallow turbulent flows.

Bibliography

BK, Brüel & Kjær Microphone Data Disk, Type 4939 No. 2674616.

BS EN ISO 5167-1. *Measurement of fluid flow by means of pressure differential devices - part 1: Orifice plates, nozzles and venturi tubes inserted in circular cross-section conduits running full.* London: British Standards Institute, 1997.

A. J. Abdullah. Wave motion at the surface of a current which has an exponential distribution of vorticity. *Annals of the New York Academy of Sciences*, 51(3): 425–441, 1949.

B. Andreotti, P. Claudin, O. Devauchelle, O. Durán, and A. Fourrière. Bedforms in a turbulent stream: ripples, chevrons and antidunes. *Journal of Fluid Mechanics*, 690:94–128, 2012.

Q. Aubourg and N. Mordant. Nonlocal resonances in weak turbulence of gravity-capillary waves. *Physical Review Letters*, 114(14):144501, 2015.

A. Awada, M. Y. Ayari, A. Khenchaf, and A. Coatanhay. Bistatic scattering from an anisotropic sea surface: numerical comparison between the first-order SSA and the TSM models. *Waves in Random and Complex Media*, 16(3):383–394, 2006.

P. Babu and P. Stoica. Spectral analysis of nonuniformly sampled data–a review. *Digital Signal Processing*, 20(2):359–378, 2010.

M. L. Banner. Equilibrium spectra of wind waves. *Journal of Physical Oceanography*, 20(7):966–984, 1990.

D. E. Barrick. Rough surface scattering based on the specular point theory. *IEEE Transactions on Antennas and Propagation*, 16(4):449–454, 1968.

D. E. Barrick. First-order theory and analysis of MF/HF/VHF scatter from the sea. *IEEE Transactions on Antennas and Propagation*, 20(1):2–10, 1972.

F. G. Bass and I. M. Fuks. *Wave scattering from statistically rough surfaces*, volume 93. Oxford Pergamon Press International Series on Natural Philosophy, 1979.

G. K. Batchelor. *An introduction to fluid dynamics.* Cambridge university press, 2000.

P. D. Bates, M. S. Horritt, C. N. Smith, and D. Mason. Integrating remote sensing observations of flood hydrology and hydraulic modelling. *Hydrological Processes*, 11(14):1777–1795, 1997.

S. E. Belcher and J. C. Vassilicos. Breaking waves and the equilibrium range of wind-wave spectra. *Journal of Fluid Mechanics*, 342:377–401, 1997.

F. Biesel. Etude théorique de la houle en eau courante. *La Houille Blanche*, pages 279–285, 1950.

E. M. Bitner. Non-linear effects of the statistical model of shallow-water wind waves. *Applied Ocean Research*, 2(2):63–73, 1980.

E. J. Bock and T. Hara. Optical measurements of capillary-gravity wave spectra using a scanning laser slope gauge. *Journal of Atmospheric and Oceanic Technology*, 12(2):395–403, 1995.

V. Borue, S. A. Orszag, and I. Staroselsky. Interaction of surface waves with turbulence: direct numerical simulations of turbulent open-channel flow. *Journal of Fluid Mechanics*, 286:1, 1995.

M. Brocchini and D. H. Peregrine. The dynamics of strong turbulence at free surfaces. Part 1: Description. *Journal of Fluid Mechanics*, 449:225–254, 2001.

J. C. Burns. Long waves in running water. In *Mathematical Proceedings of the Cambridge Philosophical Society*, volume 49, pages 695–706. Cambridge University Press, 1953.

E. A. Caponi, H. C. Yuen, F. A. Milinazzo, and P. G. Saffman. Water-wave instability induced by a drift layer. *Journal of Fluid Mechanics*, 222:207–213, 1991.

H. Chanson. Boundary shear stress measurements in undular flows: Application to standing wave bed forms. *Water Resources Research*, 36(10):3063–3076, 2000.

N.-S. Cheng. Power-law index for velocity profiles in open channel flows. *Advances in Water Resources*, 30(8):1775, 2007.

D. E. Chimenti. Review of air-coupled ultrasonic materials characterization. *Ultrasonics*, 54(7):1804–1816, 2014.

C. R. Chou, J. Z. Yim, and W. P. Huang. Determining the hydrographic parameters of the surface of water from the image sequences of a CCD camera. *Experiments in Fluids*, 36(4):515–527, 2004.

P. J. Cobelli, A. Maurel, V. Pagneux, and P. Petitjeans. Global measurement of water waves by Fourier transform profilometry. *Experiments in Fluids*, 46(6): 1037, 2009.

P. J. Cobelli, A. Przadka, P. Petitjeans, G. Lagubeau, V. Pagneux, and A. Maurel. Different regimes for water wave turbulence. *Physical Review Letters*, 107(21): 214503, 2011.

T. F. Coleman and Y. Li. An interior trust region approach for nonlinear minimization subject to bounds. *SIAM Journal on Optimization*, 6(2):418–445, 1996.

J. E. Costa, R. T. Cheng, F. P. Haeni, N. Melcher, K. R. Spicer, E. Hayes, W. Plant, K. Hayes, C. Teague, and D. Barrick. Use of radars to monitor stream discharge by noncontact methods. *Water Resources Research*, 42(7), 2006.

D. B. Creamer, F. Henyey, R. Schult, and J. Wright. Improved linear representation of ocean surface waves. *Journal of Fluid Mechanics*, 205:135–161, 1989.

D. D. Crombie. Doppler spectrum of sea echo at 13.56 Mc./s. *Nature*, 175:681–682, 1955.

D. Dabiri. On the interaction of a vertical shear layer with a free surface. *Journal of Fluid Mechanics*, 480:217, 2003.

D. Dabiri and M. Gharib. Simultaneous free-surface deformation and near-surface velocity measurements. *Experiments in Fluids*, 30(4):381, 2001.

R. A. Dalrymple. A numerical model for periodic finite amplitude waves on a rotational fluid. *Journal of Computational Physics*, 24(1):29–42, 1977.

H. Dankert, J. Horstmann, S. Lehner, and W. Rosenthal. Detection of wave groups in SAR images and radar image sequences. *IEEE Transactions on Geoscience and Remote Sensing*, 41(6):1437–1446, 2003.

F. Dias and C. Kharif. Nonlinear gravity and capillary-gravity waves. *Annual Review of Fluid Mechanics*, 31(1):301–346, 1999.

M. A. Donelan, J. Hamilton, and W. H. Hui. Directional spectra of wind-generated waves. *Philosophical Transactions of the Royal Society of London A: Mathematical, Physical and Engineering Sciences*, 315(1534):509–562, 1985.

M. A. Donelan, W. M. Drennan, and A. K. Magnusson. Nonstationary analysis of the directional properties of propagating waves. *Journal of Physical Oceanography*, 26(9):1901–1914, 1996.

T. Elfouhaily, B. Chapron, K. Katsaros, and D. Vandemark. A unified directional spectrum for long and short wind-driven waves. *Journal of Geophysical Research: Oceans*, 102(C7):15781–15796, 1997.

E. Falcon, C. Laroche, and S. Fauve. Observation of gravity-capillary wave turbulence. *Physical Review Letters*, 98(9):094503, 2007.

A. Fenster, D. B. Downey, and H. N. Cardinal. Three-dimensional ultrasound imaging. *Physics in Medicine and Biology*, 46(5):R67, 2001.

J. D. Fenton. Some results for surface gravity waves on shear flows. *IMA Journal of Applied Mathematics*, 12(1):1–20, 1973.

F. N. Fritsch and R. E. Carlson. Monotone piecewise cubic interpolation. *SIAM Journal on Numerical Analysis*, 17(2):238–246, 1980.

I. Fujita, H. Watanabe, and R. Tsubaki. Development of a non-intrusive and efficient flow monitoring technique: The space-time image velocimetry (STIV). *International Journal of River Basin Management*, 5(2):105–114, 2007.

I. Fujita, Y. Furutani, and T. Okanishi. Advection features of water surface profile in turbulent open-channel flow with hemisphere roughness elements. *Visualization of Mechanical Processes*, 1(4), 2011.

K. Fukami, T. Yamaguchi, H. Imamura, and Y. Tashiro. Current status of river discharge observation using non-contact current meter for operational use in Japan. In *World Environmental and Water Resources Congress*, pages 1–10, 2008.

G. Gallego, A. Yezzi, F. Fedele, and A. Benetazzo. A variational stereo method for the three-dimensional reconstruction of ocean waves. *IEEE Transactions on Geoscience and Remote Sensing*, 49(11):4445–4457, 2011.

K. Gröchenig. A discrete theory of irregular sampling. *Linear Algebra and its Applications*, 193:129–150, 1993.

C.-A. Guerin, G. Soriano, and B. Chapron. The weighted curvature approximation in scattering from sea surfaces. *Waves in Random and Complex Media*, 20(3): 364–384, 2010.

X. Guo and L. Shen. Interaction of a deformable free surface with statistically steady homogeneous turbulence. *Journal of Fluid Mechanics*, 658:33–62, 2010.

T. Hara and W. J. Plant. Hydrodynamic modulation of short wind-wave spectra by long waves and its measurement using microwave backscatter. *Journal of Geophysical Research: Oceans*, 99(C5):9767–9784, 1994.

J. Harband. Three dimensional flow over a submerged object. *Journal of Engineering Mathematics*, 10(1):1–21, 1976.

K. Hasselmann, T. P. Barnett, E. Bouws, H. Carlson, D. E. Cartwright, K. Enke, J. A. Ewing, H. Gienapp, D. E. Hasselmann, P. Kruseman, et al. Measurements of wind-wave growth and swell decay during the joint north sea wave project (jonswap). Technical report, Deutches Hydrographisches Institut, 1973.

D. Hauser, K. Kahma, H. E. Krogstad, et al. *Measuring and analysing the directional spectra of ocean waves*. Luxembourg: Publications Office of the European Union, 2005.

E. Herbert, N. Mordant, and E. Falcon. Observation of the nonlinear dispersion relation and spatial statistics of wave turbulence on the surface of a fluid. *Physical Review Letters*, 105(14):144502, 2010.

B. R. Hodges and R. L. Street. On simulation of turbulent nonlinear free-surface flows. *Journal of Computational Physics*, 151(2):425–457, 1999.

G. J. Holden and L. R. Wyatt. Extraction of sea state in shallow water using HF radar. In *IEE Proceedings F-Radar and Signal Processing*, volume 139, pages 175–181. IET, 1992.

K. V. Horoshenkov, A. Nichols, S. J. Tait, and G. A. Maximov. The pattern of surface waves in a shallow free surface flow. *Journal of Geophysical Research-Earth*, 118(3):1864, 2013.

B. A. Hughes, H. L. Grant, and R. W. Chappell. A fast response surface-wave slope meter and measured wind-wave moments. *Deep Sea Research*, 24(12):1211–1223, 1977.

W. H. Hui and J. Hamilton. Exact solutions of a three-dimensional nonlinear Schrödinger equation applied to gravity waves. *Journal of Fluid Mechanics*, 93 (01):117–133, 1979.

K. Ivanova and S. L. Broschat. The method of the local parabolic approximation for rough surface scattering. *The Journal of the Acoustical Society of America*, 94(4):2326–2333, 1993.

B. Jähne, S. Waas, and J. Klinke. Critical theoretical review of optical techniques for short-ocean-wave measurements. In *San Diego'92*, pages 204–215. International Society for Optics and Photonics, 1992.

B. Jähne, M. Schmidt, and R. Rocholz. Combined optical slope/height measurements of short wind waves: principle and calibration. *Measurement Science and Technology*, 16(10):1937, 2005.

P. A. E. M. Janssen. Nonlinear four-wave interactions and freak waves. *Journal of Physical Oceanography*, 33(4):863–884, 2003.

P. A. E. M. Janssen. On some consequences of the canonical transformation in the hamiltonian theory of water waves. *Journal of Fluid Mechanics*, 637:1–44, 2009.

J.-T. Jeong and H. K. Moffatt. Free-surface cusps associated with flow at low reynolds number. *Journal of Fluid Mechanics*, 241(1):1–22, 1992.

J. T. Johnson, J. V. Toporkov, and G. S. Brown. A numerical study of backscattering from time-evolving sea surfaces: Comparison of hydrodynamic models. *IEEE Transactions on Geoscience and Remote Sensing*, 39(11):2411–2420, 2001.

W. C. Keller and J. W. Wright. Microwave scattering and the straining of wind-generated waves. *Radio Science*, 10(2):139–147, 1975.

W. C. Keller, W. J. Plant, R. A. Petitt, and E. A. Terray. Microwave backscatter from the sea: Modulation of received power and Doppler bandwidth by long waves. *Journal of Geophysical Research: Oceans*, 99(C5):9751–9766, 1994.

J. F. Kennedy. The formation of sediment ripples, dunes, and antidunes. *Annual Review of Fluid Mechanics*, 1(1):147–168, 1969.

C. J. Keylock. Constrained surrogate time series with preservation of the mean and variance structure. *Physical Review E*, 73(3):036707, 2006.

C. J. Keylock. A wavelet-based method for surrogate data generation. *Physica D: Nonlinear Phenomena*, 225(2):219–228, 2007.

C. J. Keylock. Characterizing the structure of nonlinear systems using gradual wavelet reconstruction. *Nonlinear Processes in Geophysics*, 17(6):615–632, 2010.

H. R. Khakpour, T. Igusa, and L. Shen. Coherent vortical structures responsible for strong flux of scalar at free surface. *International Journal of Heat and Mass Transfer*, 55(19):5157–5170, 2012.

J. T. Kirby. A general wave equation for waves over rippled beds. *Journal of Fluid Mechanics*, 162:171–186, 1986.

S. A. Kitaigordskii, V. P. Krasitskii, and M. M. Zaslavskii. On Phillips' theory of equilibrium range in the spectra of wind-generated gravity waves. *Journal of Physical Oceanography*, 5(3):410, 1975.

A. Krynkin, K. V. Horoshenkov, A. Nichols, and S. J. Tait. A non-invasive acoustical method to measure the mean roughness height of the free surface of a turbulent shallow water flow. *Review of Scientific Instruments*, 85(11):114902, 2014.

A. Krynkin, K. V. Horoshenkov, and T. Van Renterghem. An airborne acoustic method to reconstruct a dynamically rough flow surface. *The Journal of the Acoustical Society of America*, 140(3):2064–2073, 2016.

S. Kumar, R. Gupta, and S. Banerjee. An experimental investigation of the characteristics of free-surface turbulence in channel flow. *Physics of Fluids (1994-present)*, 10(2):437–456, 1998.

E. A. Kuznetsov. Turbulence spectra generated by singularities. *Journal of Experimental and Theoretical Physics Letters*, 80(2):83–89, 2004.

D. Lakehal, M. Fulgosi, G. Yadigaroglu, and S. Banerjee. Direct numerical simulation of turbulent heat transfer across a mobile, sheared gas-liquid interface. *Journal of Heat Transfer*, 125(6):1129–1139, 2003.

H. Lamb. *Hydrodynamics*. Cambridge university press, sixth edition, 1932.

P. A. Lange, B. Jähne, J. Tschiersch, and I. Ilmberger. Comparison between an amplitude-measuring wire and a slope-measuring laser water wave gauge. *Review of Scientific Instruments*, 53(5):651–655, 1982.

C. N. S. Law, B. C. Khoo, and T. C. Chew. Turbulence structure in the immediate vicinity of the shear-free air–water interface induced by a deeply submerged jet. *Experiments in Fluids*, 27(4):321–331, 1999.

Q. Leclère. Acoustic imaging using under-determined inverse approaches: Frequency limitations and optimal regularization. *Journal of Sound and Vibration*, 321(3): 605–619, 2009.

S.-J. Lee, G. T. Yates, and T. Y. Wu. Experiments and analyses of upstream-advancing solitary waves generated by moving disturbances. *Journal of Fluid Mechanics*, 199:569–593, 1989.

J. Lighthill. *Waves in fluids*. Cambridge University Press, 2001.

B. J. Lipa and D. E. Barrick. Extraction of sea state from HF radar sea echo: Mathematical theory and modeling. *Radio Science*, 21(1):81–100, 1986.

M. S. Longuet-Higgins. The statistical analysis of a random, moving surface. *Philosophical Transactions of the Royal Society of London A: Mathematical, Physical and Engineering Sciences*, 249(966):321–387, 1957.

M. S. Longuet-Higgins. The effect of non-linearities on statistical distributions in the theory of sea waves. *Journal of Fluid Mechanics*, 17(03):459–480, 1963.

M. S. Longuet-Higgins. Statistical properties of wave groups in a random sea state. *Philosophical Transactions of the Royal Society of London A: Mathematical, Physical and Engineering Sciences*, 312(1521):219–250, 1984.

M. S. Longuet-Higgins. Surface manifestations of turbulent flow. *Journal of Fluid Mechanics*, 308:15–29, 1996.

W. A. Marcus and M. A. Fonstad. Optical remote mapping of rivers at sub-meter resolutions and watershed extents. *Earth Surface Processes and Landforms*, 33 (1):4–24, 2008.

W. A. Marcus and M. A. Fonstad. Remote sensing of rivers: the emergence of a subdiscipline in the river sciences. *Earth Surface Processes and Landforms*, 35 (15):1867–1872, 2010.

A. Maurel, P. J. Cobelli, V. Pagneux, and P. Petitjeans. Experimental and theoretical inspection of the phase-to-height relation in Fourier transform profilometry. *Applied Optics*, 48(2):380, 2009.

S. Maymon and A. V. Oppenheim. Sinc interpolation of nonuniform samples. *IEEE Transactions on Signal Processing*, 59(10):4745–4758, 2011.

J. D. Maynard, E. G. Williams, and Y. Lee. Nearfield acoustic holography: I. Theory of generalized holography and the development of NAH. *The Journal of the Acoustical Society of America*, 78(4):1395–1413, 1985.

J. A. McGregor, E. M. Poulter, and M. J. Smith. Ocean surface currents obtained from microwave sea-echo Doppler spectra. *Journal of Geophysical Research: Oceans*, 102(C11):25227–25236, 1997.

J. W. McLean. Instabilities of finite-amplitude water waves. *Journal of Fluid Mechanics*, 114:315–330, 1982.

J. W. McLean, Y. C. Ma, D. U. Martin, P. G. Saffman, and H. C. Yuen. Three-dimensional instability of finite-amplitude water waves. *Physical Review Letters*, 46(13):817, 1981.

J. W. Miles. On the generation of surface waves by shear flows. *Journal of Fluid Mechanics*, 3(02):185–204, 1957.

F. Moisy, M. Rabaud, and K. Salsac. A synthetic Schlieren method for the measurement of the topography of a liquid interface. *Experiments in Fluids*, 46(6): 1021, 2009.

E. Mollo-Christensen and A. Ramamonjiarisoa. Modeling the presence of wave groups in a random wave field. *Journal of Geophysical Research: Oceans*, 83(C8): 4117–4122, 1978.

L. C. Morland, P. G. Saffman, and H. C. Yuen. Waves generated by shear layer instabilities. In *Proceedings of the Royal Society of London A: Mathematical, Physical and Engineering Sciences*, volume 433, pages 441–450. The Royal Society, 1991.

P. M. Morse and K. U. Ingard. *Theoretical acoustics.* Princeton university press, 1968.

R. Nagaosa. Direct numerical simulation of vortex structures and turbulent scalar transfer across a free surface in a fully developed turbulence. *Physics of Fluids (1994-present)*, 11(6):1581–1595, 1999.

R. Nagaosa and R. A. Handler. Statistical analysis of coherent vortices near a free surface in a fully developed turbulence. *Physics of Fluids (1994-present)*, 15(2): 375–394, 2003.

R. Nagaosa and R. A. Handler. Characteristic time scales for predicting the scalar flux at a free surface in turbulent open-channel flows. *AIChE Journal*, 58(12): 3867–3877, 2012.

H. Nakagawa, I. Nezu, and H. Ueda. Turbulence of open channel flow over smooth and rough beds. *Proceedings of the Japan Society of Civil Engineers*, 1975(241): 155, 1975.

S. Nazarenko and S. Lukaschuk. Wave turbulence on water surface. *Annual Review of Condensed Matter Physics*, 7:61–88, 2016.

I. Nezu and H. Nakagawa. *Turbulence in open-channel flow. IAHR Monograph.* Balkema Publication, Rotterdam, 1993.

A. Nichols. PhD thesis, University of Bradford, Bradford, 2015. `http://hdl.handle.net/10454/7345`.

A. Nichols, S. Tait, K. Horoshenkov, and S. Shepherd. A non-invasive airborne wave monitor. *Flow Measurement and Instrumentation*, 34:118–126, 2013.

A. Nichols, S. J. Tait, K. V. Horoshenkov, and S. J. Shepherd. A model of the free surface dynamics of shallow turbulent flows. *Journal of Hydraulic Research*, pages 1–11, 2016.

J. Nikuradse. *Laws of flow in rough pipes.* National Advisory Committee for Aeronautics Washington, 1950.

F. Nouguier, C.-A. Guérin, and B. Chapron. choppy wave model for nonlinear gravity waves. *Journal of Geophysical Research: Oceans*, 114(C9), 2009.

F. Nouguier, C.-A. Guérin, and G. Soriano. Analytical techniques for the Doppler signature of sea surfaces in the microwave regime I: Linear surfaces. *IEEE Transactions on Geoscience and Remote Sensing*, 49(12):4856–4864, 2011a.

F. Nouguier, C.-A. Guérin, and G. Soriano. Analytical techniques for the Doppler signature of sea surfaces in the microwave regime II: Nonlinear surfaces. *IEEE Transactions on Geoscience and Remote Sensing*, 49(12):4920–4927, 2011b.

A. R. Osborne. *Nonlinear Ocean Waves & the Inverse Scattering Transform*, volume 97. Academic Press, 2010.

A. R. Osborne, A. D. Kirwan, A. Provenzale, and L. Bergamasco. A search for chaotic behavior in large and mesoscale motions in the pacific ocean. *Physica D: Nonlinear Phenomena*, 23(1):75–83, 1986.

Y. Pan and S. Banerjee. A numerical study of free-surface turbulence in channel flow. *Physics of Fluids (1994-present)*, 7(7):1649–1664, 1995.

S. Patil and V. P. Singh. Effect of vertically logarithmic steady currents on shallow surface waves. *Physical Oceanography*, 18(3):133–153, 2008.

D. B. Percival and A. T. Walden. *Wavelet methods for time series analysis.* Cambridge University Press, 2000.

O. M. Phillips. On the generation of waves by turbulent wind. *Journal of Fluid Mechanics*, 2(5):417–445, 1957.

O. M. Phillips. The equilibrium range in the spectrum of wind-generated waves. *Journal of Fluid Mechanics*, 4(04):426–434, 1958.

O. M. Phillips. On the dynamics of unsteady gravity waves of finite amplitude Part 1. The elementary interactions. *Journal of Fluid Mechanics*, 9(02):193–217, 1960.

W. J. Pierson and L. Moskowitz. A proposed spectral form for fully developed wind seas based on the similarity theory of S. A. Kitaigorodskii. *Journal of Geophysical Research*, 69(24):5181–5190, 1964.

W. J. Plant, W. C. Keller, and K. Hayes. Measurement of river surface currents with coherent microwave systems. *IEEE Transactions on Geoscience and Remote Sensing*, 43(6):1242–1257, 2005.

O. Posdziech and R. Grundmann. A systematic approach to the numerical calculation of fundamental quantities of the two-dimensional flow over a circular cylinder. *Journal of Fluids and Structures*, 23(3):479–499, 2007.

M. Rashidi, G. Hetsroni, and S. Banerjee. Wave–turbulence interaction in free-surface channel flows. *Physics of Fluids A: Fluid Dynamics (1989-1993)*, 4(12): 2727–2738, 1992.

J. W. S. Rayleigh. The form of standing waves on the surface of running water. *Proceedings of the London Mathematical Society*, 1(1):69–78, 1883.

K. Rehfeld, N. Marwan, J. Heitzig, and J. Kurths. Comparison of correlation analysis techniques for irregularly sampled time series. *Nonlinear Processes in Geophysics*, 18(3):389–404, 2011.

C. L. Rino, T. L. Crystal, A. K. Koide, H. D. Ngo, and H. Guthart. Numerical simulation of backscatter from linear and nonlinear ocean surface realizations. *Radio Science*, 26(1):51–71, 1991.

T. J. Robertson, D. A. Hutchins, D. R. Billson, J. H. Rakels, and D. W. Schindel. Surface metrology using reflected ultrasonic signals in air. *Ultrasonics*, 39(7): 479–486, 2002.

J. F. Rodríguez and M. H. García. Laboratory measurements of 3-D flow patterns and turbulence in straight open channel with rough bed. *Journal of Hydraulic Research*, 46(4):454–465, 2008.

T. Sarpkaya. Vorticity, free surface, and surfactants. *Annual Review of Fluid Mechanics*, 28(1):83–128, 1996.

R. Savelsberg and W. van de Water. Experiments on free-surface turbulence. *J. Fluid Mech.*, 619:95, 2009.

P. Sayers, E. Penning-Rowsell, M. Horritt, and A. McKenzie. Climate change risk assessment 2017: Projections of future flood risk in the uk, 2015. URL `https://doi.org/10.13140/RG.2.1.1176.8563`.

H. Schlichting and K. Gersten. *Boundary-layer theory, McGraw-Hill series in mechanical engineering, vol. xxii, 7th ed.* McGraw-Hill, New York, 1979.

A. Schumacher. Stereophotogrammetrische wellenaufnahmen mit schneller bildfolge. *Deutsche Hydrografische Zeitschrift*, 3(1-2):78–82, 1950.

C. E. Shannon. Communication in the presence of noise. *Proceedings of the IRE*, 37(1):10–21, 1949.

L. Shen, X. Zhang, D. K. P. Yue, and G. S. Triantafyllou. The surface layer for free-surface turbulent flows. *Journal of Fluid Mechanics*, 386:167–212, 1999.

W. Shen and B. Wen. Experimental research of UHF radio backscattered from fresh and seawater surface. *Progress In Electromagnetics Research M*, 11:99–109, 2010.

V. I. Shrira. Surface waves on shear currents: solution of the boundary-value problem. *Journal of Fluid Mechanics*, 252:565–584, 1993.

V. I. Shrira, S. I. Badulin, and C. Kharif. A model of water wave horse-shoepatterns. *Journal of Fluid Mechanics*, 318:375–405, 1996.

S. Smolentsev and R. Miraghaie. Study of a free surface in open-channel water flows in the regime from weak to strong turbulence. *International Journal of Multiphase Flow*, 31(8):921, 2005.

G. Soriano, M. Joelson, and M. Saillard. Doppler spectra from a two-dimensional ocean surface at L-band. *IEEE Transactions on Geoscience and Remote Sensing*, 44(9):2430–2437, 2006.

R. H. Stewart and J. W. Joy. HF radio measurements of surface currents. In *Deep Sea Research and Oceanographic Abstracts*, volume 21, pages 1039–1049. Elsevier, 1974.

P. Stoica and N. Sandgren. Spectral analysis of irregularly-sampled data: Paralleling the regularly-sampled data approaches. *Digital Signal Processing*, 16(6):712–734, 2006.

G. G. Stokes. On the theory of oscillatory waves. *Transactions of the Cambridge Philosophical Society*, 8:441–473, 1847.

M. Takeda, H. Ina, and S. Kobayashi. Fourier-transform method of fringe-pattern analysis for computer-based topography and interferometry. *Journal of the Optical Society of America*, 72(1):156, 1982.

A. Tamburrino and J. S. Gulliver. Free-surface visualization of streamwise vortices in a channel flow. *Water Resources Research*, 43(11), 2007.

M. A. C. Teixeira and S. E. Belcher. On the initiation of surface waves by turbulent shear flow. *Dynamics of Atmospheres and Oceans*, 41(1):1, 2006.

J. Theiler, S. Eubank, A. Longtin, B. Galdrikian, and J. D. Farmer. Testing for nonlinearity in time series: the method of surrogate data. *Physica D: Nonlinear Phenomena*, 58(1-4):77–94, 1992.

R. Thomas, C. Kharif, and M. Manna. A nonlinear Schrödinger equation for water waves on finite depth with constant vorticity. *Physics of Fluids (1994-present)*, 24(12):127102, 2012.

E. I. Thorsos. The validity of the Kirchhoff approximation for rough surface scattering using a Gaussian roughness spectrum. *The Journal of the Acoustical Society of America*, 83(1):78–92, 1988.

J. V. Toporkov and G. S. Brown. Numerical simulations of scattering from time-varying, randomly rough surfaces. *IEEE Transactions on Geoscience and Remote Sensing*, 38(4):1616–1625, 2000.

J. Touboul, J. Charland, V. Rey, and K. Belibassakis. Extended mild-slope equation for surface waves interacting with a vertically sheared current. *Coastal Engineering*, 116:77–88, 2016.

P. H. Trinh and S. J. Chapman. New gravity-capillary waves at low speeds. part 1: Linear geometries. *Journal of Fluid Mechanics*, 724:367–391, 2013a.

P. H. Trinh and S. J. Chapman. New gravity–capillary waves at low speeds. part 2: Nonlinear geometries. *Journal of Fluid Mechanics*, 724:392–424, 2013b.

W.-T. Tsai. A numerical study of the evolution and structure of a turbulent shear layer under a free surface. *Journal of Fluid Mechanics*, 354:239, 1998.

R. Tsubaki and I. Fujita. Stereoscopic measurement of a fluctuating free surface with discontinuities. *Measurement Science and Technology*, 16(10):1894, 2005.

D. E. Turney and S. Banerjee. Air-water gas transfer and near-surface motions. *Journal of Fluid Mechanics*, 733:588, 2013.

G. R. Valenzuela. Scattering of electromagnetic waves from a tilted slightly rough surface. *Radio Science*, 3(11):1057–1066, 1968.

W. A. Veronesi and J. D. Maynard. Digital holographic reconstruction of sources with arbitrarily shaped surfaces. *The Journal of the Acoustical Society of America*, 85(2):588–598, 1989.

F. Vivanco, F. Melo, C. Coste, and F. Lund. Surface wave scattering by a vertical vortex and the symmetry of the Aharonov-Bohm wave function. *Physical Review Letters*, 83(10):1966, 1999.

S. P. Walstead and G. B. Deane. Reconstructing surface wave profiles from reflected acoustic pulses. *The Journal of the Acoustical Society of America*, 133(5):2597–2611, 2013.

S. P. Walstead and G. B. Deane. Determination of ocean surface wave shape from forward scattered sound. *The Journal of the Acoustical Society of America*, 140 (2):787–797, 2016.

C. J. Wang, B. Y. Wen, Z. G. Ma, W. D. Yan, and X. J. Huang. Measurement of river surface currents with UHF FMCW radar systems. *Journal of Electromagnetic Waves and Applications*, 21(3):375–386, 2007.

Y. Wang, C. Mingotaud, and L. K. Patterson. Noncontact monitoring of liquid surface levels with a precision of 10 micrometers: A simple ultrasound device. *Review of Scientific Instruments*, 62(6):1640–1641, 1991.

B. L. Weber and D. E. Barrick. On the nonlinear theory for gravity waves on the ocean's surface. Part I: Derivations. *Journal of Physical Oceanography*, 7(1):3–10, 1977.

M. Welber, J. Le Coz, J. B. Laronne, G. Zolezzi, D. Zamler, G. Dramais, A. Hauet, and M. Salvaro. Field assessment of noncontact stream gauging using portable surface velocity radars (SVR). *Water Resources Research*, 2016.

B. J. West, K. A. Brueckner, R. S. Janda, D. M. Milder, and R. L. Milton. A new numerical method for surface hydrodynamics. *Journal of Geophysical Research*, 92(11):803–11, 1987.

C. E. Willert and M. Gharib. Digital particle image velocimetry. *Experiments in Fluids*, 10(4):181–193, 1991.

E. G. Williams. Regularization methods for near-field acoustical holography. *The Journal of the Acoustical Society of America*, 110(4):1976–1988, 2001.

WMTSA. Wavelet methods for time series analysis. 2006. `http://www.atmos.washington.edu/~wmtsa/`.

D. B. Wright and J. A. Herrington. Problematic standard errors and confidence intervals for skewness and kurtosis. *Behavior research methods*, 43(1):8–17, 2011.

J. W. Wright. A new model for sea clutter. *IEEE Transactions on Antennas and Propagation*, 16(2):217–223, 1968.

C.-S. Yih. Surface waves in flowing water. *Journal of Fluid Mechanics*, 51(02): 209–220, 1972.

W. R. Young and C. L. Wolfe. Generation of surface waves by shear-flow instability. *Journal of Fluid Mechanics*, 739:276–307, 2014.

V. E. Zakharov. Stability of periodic waves of finite amplitude on the surface of a deep fluid. *Journal of Applied Mechanics and Technical Physics*, 9(2):190–194, 1968.

V. E. Zakharov. Statistical theory of gravity and capillary waves on the surface of a finite-depth fluid. *European Journal of Mechanics-B/Fluids*, 18(3):327–344, 1999.

V. E. Zakharov and N. N. Filonenko. Weak turbulence of capillary waves. *Journal of Applied Mechanics and Technical Physics*, 8(5):37–40, 1967.

V. E. Zakharov and V. I. Shrira. Formation of the angular spectrum of wind waves. *Soviet physics, JETP*, 71(6):1091–1100, 1990.

C. J. Zappa, M. L. Banner, H. Schultz, A. Corrada-Emmanuel, L. B. Wolff, and J. Yalcin. Retrieval of short ocean wave slope using polarimetric imaging. *Measurement Science and Technology*, 19(5):055503, 2008.

C. Zhang, L. Shen, and D. K. P. Yue. The mechanism of vortex connection at a free surface. *Journal of Fluid Mechanics*, 384:207–241, 1999.

J. Zhang, B. W. Drinkwater, P. D. Wilcox, and A. J. Hunter. Defect detection using ultrasonic arrays: The multi-mode total focusing method. *NDT & E International*, 43(2):123–133, 2010.

X. Zhang and C. S. Cox. Measuring the two-dimensional structure of a wavy water surface optically: A surface gradient detector. *Experiments in Fluids*, 17(4):225, 1994.

Appendix A

Derivation of the dispersion relations of gravity-capillary waves

The fluid is assumed to be inviscid and incompressible. The lateral boundaries are neglected, i.e., the fluid domain is assumed to extend to infinity along the x- and the y-direction. The flow velocity field $\boldsymbol{\mathcal{U}}(x, y, z, t)$ is decomposed in the three components

$$\begin{aligned} \mathcal{U}(x, y, z, t) =& U(z) + u(x, y, z, t), && \text{(A.1a)} \\ \mathcal{V}(x, y, z, t) =& v(x, y, z, t), && \text{(A.1b)} \\ \mathcal{W}(x, y, z, t) =& w(x, y, z, t), && \text{(A.1c)} \end{aligned}$$

where $\mathbf{u} = (u, v, w)$ is the small perturbation velocity field with the zero-average of each component. The pressure field is p, and the water density is ρ_w. The density of air is neglected. The Navier-Stokes equations under these assumptions are written as

$$\begin{aligned} u_t + (U + u)u_x + v(U + u)_y + w(U + u)_z =& -\frac{p_x}{\rho_w}, && \text{(A.2a)} \\ v_t + (U + u)v_x + vv_y + wv_z =& -\frac{p_y}{\rho_w}, && \text{(A.2b)} \\ w_t + (U + u)w_x + vw_y + ww_z =& -\frac{p_z}{\rho_w}, && \text{(A.2c)} \end{aligned}$$

where the subscripts indicate the partial derivative. The continuity equation is

$$u_x + v_y + w_z = 0. \qquad \text{(A.3)}$$

The boundary condition at the bottom boundary is

$$w = 0 \text{ where } z = -H. \tag{A.4}$$

At the free surface the kinematic boundary conditions is

$$\zeta_t + (U+u)\zeta_x + v\zeta_y = w, \text{ where } z = \zeta. \tag{A.5}$$

The pressure p at the surface is

$$p = \rho_w g\zeta - \gamma_w \left(\frac{1}{R_x} + \frac{1}{R_y}\right), \text{ where } z = \zeta, \tag{A.6}$$

where R_x and R_y are the principal radii of curvature of ζ, γ_w is the surface tension coefficient, and g is the gravity constant.

The boundary conditions and the Navier-Stokes equations are linearised by assuming

$$\frac{|\mathbf{u}|}{U_0} \ll 1, \tag{A.7a}$$

$$\frac{|\zeta|}{H} \ll 1, \tag{A.7b}$$

$$|\nabla\zeta| \ll 1, \tag{A.7c}$$

where U_0 is the value of the average streamwise velocity at $z = 0$. Equations (A.4) and (A.6) are expanded near $z = 0$. The resulting set of equations is

$$u_t + Uu_x + wU_z = -\frac{p_x}{\rho_w}, \tag{A.8a}$$

$$v_t + Uv_x = -\frac{p_y}{\rho_w}, \tag{A.8b}$$

$$w_t + Uw_x = -\frac{p_z}{\rho_w}, \tag{A.8c}$$

$$u_x + v_y + w_z = 0, \tag{A.8d}$$

$$w = 0, \qquad \text{where } z = -H, \tag{A.8e}$$

$$\zeta_t + U\zeta_x = w, \qquad \text{where } z = \zeta, \tag{A.8f}$$

$$p = \rho_w g\zeta - \gamma_w \nabla^2\zeta, \qquad \text{where } z = \zeta. \tag{A.8g}$$

These are now linear in ζ. Considering the expansion in a Fourier integral given by equation (3.10), it is possible to solve a similar set of equations for each wave with the wavenumber $\mathbf{k}$. Then the velocity perturbation $\mathbf{u}$ assumes the meaning of the perturbation velocity field induced by a single wave.

It is convenient to reformulate the problem in the system of reference (x', y', z') with x' parallel to $\mathbf{k}$ and $z' \equiv z$. Here the following apply,

$$\mathbf{U}' = (U', V', 0), \tag{A.9a}$$

$$\mathbf{u}' = (u', 0, w'), \tag{A.9b}$$

$$\zeta_{y'} = 0. \tag{A.9c}$$

The equations (A.8) become

$$u'_t + U'u'_{x'} + V'u'_{y'} + w'U'_z = -\frac{p_{x'}}{\rho_w}, \tag{A.10a}$$

$$w'V'_z = -\frac{p_{y'}}{\rho_w}, \tag{A.10b}$$

$$w'_t + U'w'_{x'} + V'w'_{y'} = -\frac{p_z}{\rho_w}, \tag{A.10c}$$

$$u'_{x'} + w'_z = 0, \tag{A.10d}$$

$$w' = 0, \qquad \text{where } z = -H, \tag{A.10e}$$

$$\zeta_t + U'\zeta_{x'} = w', \qquad \text{where } z = 0, \tag{A.10f}$$

$$p = \rho_w g\zeta - \gamma_w \zeta_{x'x'}, \qquad \text{where } z = 0. \tag{A.10g}$$

Taking twice the curl of equations (A.10a) to (A.10c) one can find an equation in the only variable w',

$$(\nabla^2 w')_t + U'(\nabla^2 w')_{x'} + V'(\nabla^2 w')_{y'} - w'_{x'}U'_{zz} - w'_{y'}V'_{zz} = 0. \tag{A.11}$$

The solution is sought for in the form

$$w'(x', z) = \Psi(z)e^{i[kx' - \omega t]}. \tag{A.12}$$

Substituting this in equation (A.11) yields

$$\Psi_{zz} - \left[k^2 + \frac{U'_{zz}}{U' - c}\right]\Psi = 0 \tag{A.13}$$

where c is the phase velocity. The surface elevation due to one single wave with the wavenumber k is

$$\zeta(x', t) = A(k, \omega)e^{i[kx' - \omega t]}. \tag{A.14}$$

Substituting in equation (A.10g) and evaluating equation (A.10a) at $z = 0$ with equation (A.10d) leads to

$$\Psi_z(U' - c) - \Psi U'_z = ik^2\left(g + \frac{\gamma_w}{\rho_w}k^2\right)A(k, \omega). \tag{A.15}$$

Combining with equation (A.10f) the boundary conditions are written as

$$\Psi = 0, \qquad \text{where } z = -H, \tag{A.16a}$$

$$(U' - c)^2\Psi_z - \left[U'_z(U' - c) + \left(g + \frac{\gamma_w}{\rho_w}k^2\right)\right]\Psi = 0, \qquad \text{where } z = 0. \tag{A.16b}$$

The solution for an irrotational flow where the average streamwise velocity is constant throughout the depth is found by substituting

$$U'_z = 0, \tag{A.17a}$$

$$U' \equiv U_0 \cos(\theta), \tag{A.17b}$$

in equations (A.13) and (A.16), where θ is the angle between the streamwise velocity of the flow and the wavenumber of the wave. The result is

$$\Psi_{zz} - k^2\Psi = 0, \tag{A.18}$$

which is satisfied by an equation of the form

$$\Psi = C_1 e^{-kz} + C_2 e^{kz}. \tag{A.19}$$

Based on the boundary conditions of equations (A.16), the phase velocity of the gravity-capillary waves in an irrotational flow is found as

$$c(k, \theta) = U_0 \cos(\theta) \pm \sqrt{\left(g + \frac{\gamma_w}{\rho_w}k^2\right)\tanh(kH)}. \tag{A.20}$$

This corresponds to equation (3.19).

The dispersion relation with the average streamwise velocity profile represented by equation (3.17) can be calculated numerically following the procedure described by Fenton [1973]. The average streamwise velocity is represented by equation (3.17) The non-dimensional variables

$$\check{z} = z/H, \tag{A.21a}$$

$$\check{\Psi}(\check{z}) = \Psi/[H\Psi_z], \tag{A.21b}$$

$$\check{k}^2(\check{z}) = k^2H^2 + H^2U'_{zz}/(U' - c). \tag{A.21c}$$

are substituted into equations (A.13) and (A.16). Assuming that the flow velocity is approximated by equation (3.17), the solution for $\check{\Psi}(\check{z})$ is found by integrating the Riccati equation

$$\frac{d\check{\Psi}(\check{z})}{d\check{z}} = 1 - \check{k}^2(\check{z})\check{\Psi}^2(\check{z}), \tag{A.22a}$$

$$\check{\Psi}(\check{z}) = 0, \qquad \text{when } \check{z} = -1, \tag{A.22b}$$

from $\check{z} = -1$ to $\check{z} = 0$. $\check{k}^2$ is found from equation (3.17) as

$$\check{k}^2 = k^2H^2 + \frac{\check{U}n(n-1)}{(1+\check{z})^2[\check{U} - (1+\check{z})^{-n}]}. \tag{A.23}$$

Introducing

$$\check{U} = U_0 \cos(\theta)/c, \tag{A.24}$$

the result is the phase velocity of gravity-capillary waves propagating in a flow with the power-function vertical profile of the streamwise velocity,

$$c^2 = \frac{\left(g + \frac{\gamma_w}{\rho_w}k^2\right)\check{\Psi}(0)}{(\check{U}-1)[(\check{U}-1) - n\check{U}\check{\Psi}(0)]}. \tag{A.25}$$

This is the same as equation (3.24). The singularity of the integration appears from equation (A.23).

Appendix B

Derivation of the Kirchhoff approximation

The acoustic velocity potential P is defined by [e.g. Morse and Ingard, 1968, p.248][Bass and Fuks, 1979, p.7]

$$p_a = \rho_a \frac{\partial P}{\partial t}, \tag{B.1a}$$

$$\mathbf{u}_a = -\nabla P, \tag{B.1b}$$

where p_a is the acoustic pressure, ρ_a is the density of air which is assumed homogeneous, and $\mathbf{u}_a$ is the velocity of the acoustic field in air otherwise at rest. All quantities are understood to be multiplied by a factor $\exp(i\omega_a t)$. The Helmholtz equation is written as

$$\left(\nabla^2 + \kappa^2\right) P = -4\pi Q_S(\mathbf{R}), \tag{B.2}$$

where κ is the acoustic wavenumber, and $Q_S(\mathbf{R})$ is the source density at the location $\mathbf{R}$. Equation (B.2) can be written in integral form using Green's formula, as in

$$P(\mathbf{R}) = \int_{\mathcal{V}} Q_S(\mathbf{R}')\mathcal{G}(\mathbf{R},\mathbf{R}')d\mathbf{R}' + \frac{1}{4\pi}\int_{\Sigma}\left[\mathcal{G}(\mathbf{R},\tilde{\boldsymbol{\rho}})\frac{\partial P(\tilde{\boldsymbol{\rho}})}{\partial \mathbf{n}} - P(\tilde{\boldsymbol{\rho}})\frac{\partial \mathcal{G}(\mathbf{R},\tilde{\boldsymbol{\rho}})}{\partial \mathbf{n}}\right] d\tilde{\boldsymbol{\rho}}, \tag{B.3}$$

where $\mathcal{V}$ is the volume that contains the sound sources, Σ is a closed surface that encloses the whole acoustic field, $\mathbf{n}$ is the unit vector normal to the surface and directed outside, and $\mathcal{G}$ is a Green's function. $\mathbf{R}'$ is the vector co-ordinate within the volume $\mathcal{V}$, and $\tilde{\boldsymbol{\rho}}$ is the co-ordinate parallel to the surface Σ.

The first term on the right hand side of equation (B.3) can be calculated for a point source with density

$$Q_S(\mathbf{R}') = \delta(\mathbf{R}' - \mathbf{S}), \tag{B.4}$$

where $\mathbf{S}$ is the vector location of the source, assumed in free field. From this equation,

$$P_i(\mathbf{R}) = \int_{\mathcal{V}} Q_S(\mathbf{R}')\mathcal{G}(\mathbf{R},\mathbf{R}')d\mathbf{R}' = \mathcal{G}(\mathbf{R},\mathbf{S}), \tag{B.5}$$

which is called the incident field.

The Green function $\mathcal{G}(\mathbf{R},\mathbf{R}')$ must satisfy equation (B.2) with the right hand side replaced by $-\delta(\mathbf{R}-\mathbf{R}')$. A solution can be expressed as [Morse and Ingard, 1968, p.319]

$$\mathcal{G}(\mathbf{R},\mathbf{R}') = G(\mathbf{R},\mathbf{R}') + \tilde{G}(\mathbf{R}) = \frac{e^{i\kappa|\mathbf{R}-\mathbf{R}'|}}{4\pi|\mathbf{R}-\mathbf{R}'|} + \tilde{G}(\mathbf{R}), \tag{B.6}$$

where $\tilde{G}(\mathbf{R})$ is a general solution of the homogeneous Helmholtz equation, including the trivial solution $\tilde{G} = 0$. The two-dimensional case is represented in the coordinates x and z. Here $\mathcal{V}$ represents a surface, while Σ is a line. In the two-dimensional case a possible shape for the Green function is given by [Morse and Ingard, 1968, p.366]

$$G(\mathbf{R},\mathbf{R}') = \frac{i}{4}H_0^{(1)}(\kappa|\mathbf{R}-\mathbf{R}'|), \tag{B.7}$$

where $H_0^{(1)}$ is the Hankel function of the first kind of order 0. In the far field from $\mathbf{R}'$ defined as the region where

$$\kappa|\mathbf{R}-\mathbf{R}'| \to \infty, \tag{B.8}$$

equation (B.7) is approximated by

$$G(\mathbf{R},\mathbf{R}') \approx \frac{i}{4}\sqrt{\frac{2}{\pi\kappa}}\frac{e^{i\kappa|\mathbf{R}-\mathbf{R}'|-i\frac{\pi}{4}}}{\sqrt{|\mathbf{R}-\mathbf{R}'|}}. \tag{B.9}$$

Let consider the case of a point source at the location $\mathbf{S} = (x_s, y_s, z_s)$, emitting acoustic waves which are reflected by a rigid flat plane represented by $z = 0$. The boundary condition at the plane is

$$\frac{\partial P}{\partial z} = 0, \text{ when } z = 0. \tag{B.10}$$

A solution of equation (B.3) with condition (B.10) is found with the Green function [Morse and Ingard, 1968, p.368]

$$\mathcal{G}(\mathbf{R},\mathbf{S}) = G(\mathbf{R},\mathbf{S}) + G(\mathbf{R},\mathbf{S}^-), \tag{B.11}$$

where $\mathbf{S}^{-} = (x_s, y_s, -z_s)$. This function also satisfies the condition

$$\frac{\partial \mathcal{G}}{\partial z} = 0, \text{ where } z = 0, \tag{B.12}$$

so that all terms of the integral of equation (B.3) are equal to zero, and

$$P(\mathbf{R}) = G(\mathbf{R}, \mathbf{S}) + G(\mathbf{R}, \mathbf{S}^{-}). \tag{B.13}$$

Therefore the potential on the flat surface is

$$P(\boldsymbol{\rho}) = 2G(\boldsymbol{\rho}, \mathbf{S}), \tag{B.14}$$

where $\boldsymbol{\rho}$ is the polar co-ordinate on the flat surface, $\rho^2 = x^2 + y^2$.

Consider a circular piston with radius r_s with the centre of its surface at the origin and with the axis parallel to the z-axis. The piston is set in a plane rigid baffle of infinite size. The boundary conditions are

$$\frac{\partial P}{\partial z} = 0, \text{ where } \rho > r_s, \tag{B.15a}$$

$$\frac{\partial P}{\partial z} = u_0 e^{-i\omega t}, \text{ where } \rho \leq r_s. \tag{B.15b}$$

The same Green function of equation (B.11) is used here, which ensures that $\partial \mathcal{G}/\partial z = 0$ at the boundary. The potential can be calculated from

$$P(R, \theta_s, \varsigma_R) = \frac{1}{4\pi} \int_0^{2\pi} \int_0^{r_s} u_0 e^{-i\omega t} \mathcal{G}(R, \theta_s, \varsigma_R, \rho, \varsigma) \rho d\rho d\varsigma, \tag{B.16}$$

where ς is the angular polar co-ordinate in the plane $x - y$ which has the value ς_R at the location $\mathbf{R}$, and θ_s is the angle with respect to the axis of the piston. Expressing $\mathcal{G}$ like in equation (B.6) with $\tilde{G} = 0$, and assuming in the far field from the piston

$$\frac{R}{\rho} \gg 1, \tag{B.17}$$

then (B.16) becomes

$$P(R, \theta_s, \varsigma_R) \approx \frac{u_0}{8\pi^2} \frac{e^{i\kappa R}}{R} \int_0^{2\pi} \int_0^{r_s} e^{-i\kappa\rho \sin(\theta_s) \cos(\varsigma_R - \varsigma)} \rho d\rho d\varsigma, \tag{B.18}$$

which has the solution [Morse and Ingard, 1968, p.381]

$$P(R, \theta_s) = \frac{u_0 r_s^2}{4\pi} \frac{e^{i\kappa R}}{R} \frac{J_1(\kappa r_s \sin\theta_s)}{\kappa r_s \sin\theta_s} = u_0 r_s^2 G(\mathbf{0}, \mathbf{R}) \frac{J_1(\kappa r_s \sin\theta_s)}{\kappa r_s \sin\theta_s}, \tag{B.19}$$

where J_1 is the Bessel function of the first kind. From equations (B.19) and (B.5) one can write

$$P_i(R, \theta_s) = P_s D_s(\theta_s) G(\mathbf{R}, \mathbf{S}), \tag{B.20}$$

where

$$D_s(\theta_s) = 2\frac{J_1(\kappa r_s \sin\theta_s)}{\kappa r_s \sin\theta_s}, \tag{B.21}$$

and P_s is an effective amplitude of the source. From now on the analysis is based on the non-dimensional normalised potential, so that the incident field is defined as

$$P_i(R, \theta_s) = D_s(\theta_s)\frac{e^{i\kappa|\mathbf{R}-\mathbf{S}|}}{|\mathbf{R}-\mathbf{S}|} \tag{B.22}$$

in the three-dimensional case, and

$$P_i(R, \theta_s) = D_s(\theta_s)\frac{e^{i\kappa|\mathbf{R}-\mathbf{S}|}}{\sqrt{|\mathbf{R}-\mathbf{S}|}} \tag{B.23}$$

in the two-dimensional case, respectively. Equations (B.21), (B.22), and (B.22) are the same as equations (3.88), (3.85), and (3.85), respectively.

The integral equation (B.3) must be solved numerically in general, since the potential appears both inside and outside of the integral. The Kirchhoff approximation allows the simplification of this equation, assuming that at all locations on a rough surface Σ the acoustic field can be represented by the reflection of the incident field P_i from the plane tangent to the surface locally [Bass and Fuks, 1979, p.220]. This is expressed by equation (B.14), which is modified in order to take into account the general shape of the reflecting surface, as

$$P(\tilde{\boldsymbol{\rho}}) = 2G(\tilde{\boldsymbol{\rho}}, \mathbf{S}), \text{ where } \tilde{\boldsymbol{\rho}} \in \Sigma. \tag{B.24}$$

From the same representation, it follows that

$$\frac{\partial P(\tilde{\boldsymbol{\rho}})}{\partial n} = 0, \text{ where } \tilde{\boldsymbol{\rho}} \in \Sigma. \tag{B.25}$$

In practice, one needs to take into account the directivity of the source based on equations (B.22) and (B.23). This can be done by defining

$$P(\tilde{\boldsymbol{\rho}}) = 2P_i(\tilde{\boldsymbol{\rho}}), \tag{B.26}$$

where P_i is given by equations (B.22) and (B.23). In this case the boundary condition is satisfied only approximately and only if the directivity pattern varies slowly in the direction $\mathbf{n}$ normal to the surface, i.e., if

$$\frac{\partial D_s}{\partial \mathbf{n}} = \nabla D_s \cdot \mathbf{n} \ll 1, \tag{B.27}$$

Eqzuation (B.3) with $\mathcal{G} = G$ and with the directivity pattern of the receiver gives the potential at the point $\mathbf{M}$ as

$$P(\mathbf{M}) = D_m(\mathbf{S})P_i(\mathbf{M}) - \frac{1}{4\pi}\int_{\Sigma+\Sigma'+\Sigma_R} D_m(\tilde{\boldsymbol{\rho}}) \left[G(\mathbf{M},\tilde{\boldsymbol{\rho}})\frac{\partial P(\tilde{\boldsymbol{\rho}})}{\partial \mathbf{n}} - P(\tilde{\boldsymbol{\rho}})\frac{\partial G(\mathbf{M},\tilde{\boldsymbol{\rho}})}{\partial \mathbf{n}}\right] d\tilde{\boldsymbol{\rho}}, \tag{B.28}$$

In equation (B.28) the boundary surface is decomposed into three parts. Σ represents the rough surface with finite extension in the directions x and y, which has the average corresponding to $z = 0$. Σ_R is a hemisphere with the radius much larger than the size of Σ. Σ' is a flat surface with $z = 0$ that connects Σ with Σ_R. The change of sign of the integral with respect to equation (B.3) derives from the orientation of $\mathbf{n}$ inside the volume. If all sources are within $\Sigma + \Sigma' + \Sigma_R$, then [i.e. Bass and Fuks, 1979, p.225]

$$\frac{1}{4\pi}\int_{\Sigma+\Sigma'+\Sigma_R} D_m(\tilde{\boldsymbol{\rho}}) \left[G(\mathbf{M},\tilde{\boldsymbol{\rho}})\frac{\partial P_i(\tilde{\boldsymbol{\rho}})}{\partial \mathbf{n}} - P_i(\tilde{\boldsymbol{\rho}})\frac{\partial G(\mathbf{M},\tilde{\boldsymbol{\rho}})}{\partial \mathbf{n}}\right] d\tilde{\boldsymbol{\rho}} = 0. \tag{B.29}$$

On the surface Σ_R, the radiation condition requires that no waves are generated at infinity, so that

$$P(\tilde{\boldsymbol{\rho}}) \approx P_i(\tilde{\boldsymbol{\rho}}) \to 0, \text{ when } \tilde{\boldsymbol{\rho}} \to \infty. \tag{B.30}$$

The Kirchhoff approximation imposes

$$P(\tilde{\boldsymbol{\rho}}) = P_i(\tilde{\boldsymbol{\rho}}), \text{ when } \tilde{\boldsymbol{\rho}} \in \Sigma' \tag{B.31}$$

on the surface Σ', and (B.26) on the surface Σ.

Thus, summing equation (B.29) and equation (B.28), considering equations (B.25), (B.26), (B.30), and (B.31), yields

$$P(\mathbf{M}) = D_m(\mathbf{S})P_i(\mathbf{M}) - \frac{1}{4\pi}\int_{\Sigma} D_m(\tilde{\boldsymbol{\rho}}) \left[G(\mathbf{M},\tilde{\boldsymbol{\rho}})\frac{\partial P_i(\tilde{\boldsymbol{\rho}})}{\partial \mathbf{n}} + P_i(\tilde{\boldsymbol{\rho}})\frac{\partial G(\mathbf{M},\tilde{\boldsymbol{\rho}})}{\partial \mathbf{n}}\right] d\tilde{\boldsymbol{\rho}}. \tag{B.32}$$

Substituting equation (B.20) for P_i yields

$$P(\mathbf{M}) = 4\pi D_m(\mathbf{S})D_s(\mathbf{M})G(\mathbf{M},\mathbf{S}) - \int_{\Sigma} D_m(\tilde{\boldsymbol{\rho}})D_s(\tilde{\boldsymbol{\rho}})\frac{\partial}{\partial \mathbf{n}}\left[G(\mathbf{M},\tilde{\boldsymbol{\rho}})G(\tilde{\boldsymbol{\rho}},\mathbf{S})\right] d\tilde{\boldsymbol{\rho}}, \tag{B.33}$$

where $\tilde{\boldsymbol{\rho}}$ is now defined on the surface Σ only, i.e.,

$$\tilde{\boldsymbol{\rho}} = (x, y, \zeta(x, y)). \tag{B.34}$$

and the function $z = \zeta(x, y)$ corresponds to the equation of the rough surface Σ. The unit vector normal to the surface is

$$\mathbf{n} = \frac{\mathbf{i}_z - \nabla\zeta}{\sqrt{1 + |\nabla\zeta|^2}}, \tag{B.35}$$

where $\mathbf{i}_z$ is the unit vector in the vertical direction z such that the average of ζ over z is 0.

The integration is carried out with respect to the co-ordinate $\boldsymbol{\rho} = (x, y)$ defined on the flat surface Σ_0 that corresponds to the plane $x - y$, i.e., with a change of variable

$$d\tilde{\boldsymbol{\rho}} = d\boldsymbol{\rho}/n_z = d\boldsymbol{\rho}\sqrt{1 + |\nabla\zeta|^2}. \tag{B.36}$$

n_z in equation (B.36) is the projection of the normal to the surface $\mathbf{n}$ in the z-direction. Equation (B.33) is written as

$$\begin{gathered} P(\mathbf{M}) = 4\pi D_m(\mathbf{S}) D_s(\mathbf{M}) G(\mathbf{M}, \mathbf{S}) \\ + \int_{\Sigma_0} D_m(\tilde{\boldsymbol{\rho}}) D_s(\tilde{\boldsymbol{\rho}}) \frac{\partial}{\partial \mathbf{n}} \left[G(\mathbf{M}, \tilde{\boldsymbol{\rho}}) G(\tilde{\boldsymbol{\rho}}, \mathbf{S}) \right] \sqrt{1 + |\nabla\zeta|^2} d\boldsymbol{\rho}. \end{gathered} \tag{B.37}$$

Scattering from a three-dimensional surface

Considering the Green function given by equation (B.6) with $\tilde{G} = 0$, one finds

$$G(\mathbf{M}, \tilde{\boldsymbol{\rho}}) G(\tilde{\boldsymbol{\rho}}, \mathbf{S}) = \frac{1}{16\pi^2} \frac{e^{i\kappa\left(\tilde{R}_s + \tilde{R}_m\right)}}{\tilde{R}_s \tilde{R}_m}, \tag{B.38}$$

where

$$\tilde{\mathbf{R}}_s = \tilde{\boldsymbol{\rho}} - \mathbf{S}, \tag{B.39a}$$

$$\tilde{\mathbf{R}}_m = \mathbf{M} - \tilde{\boldsymbol{\rho}}, \tag{B.39b}$$

The derivative with respect to $\mathbf{n}$ of equation (B.38) is equal to

$$\frac{\partial}{\partial \mathbf{n}} \left\{ \frac{e^{i\kappa\left(\tilde{R}_s + \tilde{R}_m\right)}}{\tilde{R}_s \tilde{R}_m} \right\} = \frac{i\kappa e^{i\kappa(\tilde{R}_s + \tilde{R}_m)}}{\tilde{R}_s \tilde{R}_m} \left\{ \left[1 - \frac{1}{i\kappa \tilde{R}_s} \right] \nabla \tilde{R}_s + \left[1 - \frac{1}{i\kappa \tilde{R}_m} \right] \nabla \tilde{R}_m \right\} \cdot \mathbf{n}, \tag{B.40}$$

which is approximated by

$$\frac{\partial}{\partial \mathbf{n}}\left\{\frac{e^{i\kappa\left(\tilde{R}_s+\tilde{R}_m\right)}}{\tilde{R}_s\tilde{R}_m}\right\} \approx \frac{i\kappa e^{i\kappa(\tilde{R}_s+\tilde{R}_m)}}{\tilde{R}_s\tilde{R}_m}\nabla\left(\tilde{R}_s+\tilde{R}_m\right)\cdot\mathbf{n}, \tag{B.41}$$

when $\kappa\tilde{R}_{s,m} \gg 1$. With the definitions of equations (3.92), (3.93), and (3.94), substituting equations (B.6) and (B.41) into equation (B.37) yields

$$P(\mathbf{M}) = D_m(\mathbf{S})D_s(\mathbf{M})\frac{e^{i\kappa|\mathbf{M}-\mathbf{S}|}}{|\mathbf{M}-\mathbf{S}|} + \frac{1}{i4\pi}\int_{\Sigma_0} D_m(\tilde{\boldsymbol{\rho}})D_s(\tilde{\boldsymbol{\rho}})\frac{e^{i\kappa\left(\tilde{R}_s+\tilde{R}_m\right)}}{\tilde{R}_s\tilde{R}_m}(\tilde{q}_z - \tilde{\mathbf{q}}_\perp\cdot\nabla\zeta)d\boldsymbol{\rho}, \tag{B.42}$$

which corresponds to equation (3.95).

Scattering from a two-dimensional surface

In the two-dimensional case the Green function is represented by equation (B.9), with the assumption $\kappa R_{s,m} \gg 1$ In this case

$$G(\mathbf{M},\tilde{\boldsymbol{\rho}})G(\tilde{\boldsymbol{\rho}},\mathbf{S}) = \frac{i}{8\pi\kappa}\frac{e^{i\kappa\left(\tilde{R}_s+\tilde{R}_m\right)}}{\sqrt{\tilde{R}_s\tilde{R}_m}}, \tag{B.43}$$

and

$$\frac{\partial}{\partial\mathbf{n}}\left[G(\mathbf{M},\tilde{\boldsymbol{\rho}})G(\tilde{\boldsymbol{\rho}},\mathbf{S})\right] = -\frac{e^{i\kappa(\tilde{R}_s+\tilde{R}_m)}}{8\pi\sqrt{\tilde{R}_s\tilde{R}_m}}\left\{\left[1+\frac{i}{2\kappa\tilde{R}_s}\right]\nabla\tilde{R}_s + \left[1+\frac{i}{2\kappa\tilde{R}_m}\right]\nabla\tilde{R}_m\right\}\cdot\mathbf{n}, \tag{B.44}$$

which is approximated by

$$\frac{\partial}{\partial\mathbf{n}}\left[G(\mathbf{M},\tilde{\boldsymbol{\rho}})G(\tilde{\boldsymbol{\rho}},\mathbf{S})\right] \approx \frac{e^{i\kappa(\tilde{R}_s+\tilde{R}_m)}}{8\pi\kappa\sqrt{\tilde{R}_s\tilde{R}_m}}\tilde{\mathbf{q}}\cdot\mathbf{n}, \tag{B.45}$$

when $\kappa\tilde{R}_{s,m} \gg 1$. Substituting in equation (B.37) and normalising yields equation (3.107),

$$\begin{aligned} P(\mathbf{M}) = D_m(\mathbf{S})D_s(\mathbf{M})\frac{e^{i\kappa|\mathbf{M}-\mathbf{S}|}}{\sqrt{|\mathbf{M}-\mathbf{S}|}}+ \\ -\frac{1}{8\pi\sqrt{2\kappa\pi}}\int_{\Sigma_0} D_m(\tilde{\boldsymbol{\rho}})D_s(\tilde{\boldsymbol{\rho}})\frac{e^{i\kappa\left(\tilde{R}_s+\tilde{R}_m\right)}}{\sqrt{\tilde{R}_s\tilde{R}_m}}(\tilde{q}_z - \tilde{q}_x\zeta_x)dx. \end{aligned} \tag{B.46}$$

Appendix C

Linearisation of the Kirchhoff equation with small Rayleigh parameter

The potential of the acoustic field scattered by a three-dimensional surface is given by equation (3.106) for the case where the gradient of the surface elevation is small. Substituting into equation (3.110) yields

$$S_D(\mathbf{M},\omega) = -\frac{1}{32\pi^3}\int_{-\infty}^{\infty}\iint_{\Sigma}\frac{D_m(\boldsymbol{\rho})D_s(\boldsymbol{\rho})}{R_m(\boldsymbol{\rho})R_s(\boldsymbol{\rho})}\frac{D_m(\boldsymbol{\rho}+\boldsymbol{\rho}')D_s(\boldsymbol{\rho}+\boldsymbol{\rho}')}{R_m(\boldsymbol{\rho}+\boldsymbol{\rho}')R_s(\boldsymbol{\rho}+\boldsymbol{\rho}')}q_z(\boldsymbol{\rho})q_z(\boldsymbol{\rho}+\boldsymbol{\rho}')$$

$$e^{i\kappa[R_s(\boldsymbol{\rho})+R_m(\boldsymbol{\rho})-R_s(\boldsymbol{\rho}+\boldsymbol{\rho}')-R_m(\boldsymbol{\rho}+\boldsymbol{\rho}')]} < e^{-iq_z[\zeta(\boldsymbol{\rho},t)-\zeta(\boldsymbol{\rho}+\boldsymbol{\rho}',t+\tau)]} > e^{i\omega\tau}d\boldsymbol{\rho}d\boldsymbol{\rho}'d\tau. \tag{C.1}$$

The ensemble average in equation (C.1) is called the two-dimensional characteristic function and, if ζ is Gaussian distributed, it is equal to [Bass and Fuks, 1979, p.361]

$$< e^{-iq_z[\zeta(\boldsymbol{\rho},t)-\zeta(\boldsymbol{\rho}+\boldsymbol{\rho}',t+\tau)]} >= e^{-q_z^2\sigma^2[1-W(\boldsymbol{\rho}',\tau)]}, \tag{C.2}$$

where $W(\boldsymbol{\rho}',\tau)$ is the space-time correlation of the surface elevation. It is assumed that the correlation decays rapidly in space, so that the size of the area which is important for the integration is represented by the scales l_x and l_y in the x- and in the y-direction, respectively. The scale of roughness is represented by the standard deviation of the surface elevation function, σ. The transducer and the receiver are assumed to be at the same height above the surface, and aligned along the streamwise direction. If conditions (3.112) and (3.113) are satisfied, and if the horizontal dimension of the scattering surface is large compared to $l_{x,y}$, then the spatial integrals in equation (C.1) can be extended to the interval from $-\infty$ to ∞.

With the above assumptions, R_s, R_m, and $\mathbf{q}$ can be expanded in a Taylor series near $\boldsymbol{\rho}$, with the result

$$R_s(\boldsymbol{\rho}+\boldsymbol{\rho}') = \left[1 + \frac{\rho}{R_s(\boldsymbol{\rho})}\frac{\rho'}{R_s(\boldsymbol{\rho})} + \mathcal{O}\left(\frac{\rho'^2}{R_s^2(\boldsymbol{\rho})}\right)\right] R_s(\boldsymbol{\rho}), \tag{C.3a}$$

$$R_m(\boldsymbol{\rho}+\boldsymbol{\rho}') = \left[1 - \frac{|\mathbf{M}-\mathbf{S}-\boldsymbol{\rho}|}{R_m(\boldsymbol{\rho})}\frac{\rho'}{R_m(\boldsymbol{\rho})} + \mathcal{O}\left(\frac{\rho'^2}{R_m^2(\boldsymbol{\rho})}\right)\right] R_m(\boldsymbol{\rho}). \tag{C.3b}$$

Assuming the validity of equations (3.114), it follows

$$\kappa\left[R_s(\boldsymbol{\rho}) + R_m(\boldsymbol{\rho}) - R_s(\boldsymbol{\rho}+\boldsymbol{\rho}') - R_m(\boldsymbol{\rho}+\boldsymbol{\rho}')\right] \approx -\mathbf{q}_\perp(\boldsymbol{\rho})\cdot\boldsymbol{\rho}', \tag{C.4}$$

where $\mathbf{q}_\perp = (q_x, q_y)$. If equations (3.116) and (3.117) are also satisfied, then also the terms of order $\rho'/R_{s,m}$ can be neglected in the pre-exponential term of equation (C.1). Also, $q_z(\boldsymbol{\rho}+\boldsymbol{\rho}')$ is approximated by

$$q_z(\boldsymbol{\rho}+\boldsymbol{\rho}') \approx q_z(\boldsymbol{\rho}) \tag{C.5}$$

in the argument of equation (C.2). It is assumed finally that the directivity of the transducer and of the receiver vary slowly in space in a region with size $l_{x,y}$.

With the above approximations and definitions, equation (C.1) is written as

$$S_D(\mathbf{M},\omega) = \\ -\frac{1}{32\pi^3}\int_{-\infty}^{\infty} \frac{D_m^2(\boldsymbol{\rho})D_s^2(\boldsymbol{\rho})}{R_m^2(\boldsymbol{\rho})R_s^2(\boldsymbol{\rho})} q_z^2(\boldsymbol{\rho}) \left\{\iint_{-\infty}^{\infty} e^{-q_z^2(\boldsymbol{\rho})\sigma^2[1-W(\boldsymbol{\rho}',\tau)]} e^{i[\omega\tau - \mathbf{q}_\perp(\boldsymbol{\rho})\cdot\boldsymbol{\rho}']} d\boldsymbol{\rho}' d\tau\right\} d\boldsymbol{\rho}. \tag{C.6}$$

Inverting the Fourier transform of equation (3.2), one obtains

$$W(\boldsymbol{\rho}',\tau) = \sum_j S(\mathbf{k}_j,\omega_j) e^{i[\mathbf{k}_j\cdot\boldsymbol{\rho}' - \omega_j\tau]}, \tag{C.7}$$

where $S(\mathbf{k}_j,\omega_j)$ is the frequency-wavenumber spectrum of the surface elevation. Assuming the smallness of the Rayleigh parameter, equation (3.112), and expanding the first exponential of equation (C.6) to first order of $q_z^2\sigma^2$, it is found

$$S_D(\mathbf{M},\omega) = \\ -\frac{1}{32\pi^3}\int_{-\infty}^{\infty} \frac{D_m^2(\boldsymbol{\rho})D_s^2(\boldsymbol{\rho})}{R_m^2(\boldsymbol{\rho})R_s^2(\boldsymbol{\rho})} q_z^2(\boldsymbol{\rho}) \left[1 - q_z^2(\boldsymbol{\rho})\sigma^2\right] \left\{\iint_{-\infty}^{\infty} e^{i[\omega\tau - \mathbf{q}_\perp(\boldsymbol{\rho})\cdot\boldsymbol{\rho}']} d\boldsymbol{\rho}' d\tau\right\} d\boldsymbol{\rho} + \\ -\frac{\sigma^2}{32\pi^3}\int_{-\infty}^{\infty} \frac{D_m^2(\boldsymbol{\rho})D_s^2(\boldsymbol{\rho})}{R_m^2(\boldsymbol{\rho})R_s^2(\boldsymbol{\rho})} q_z^4(\boldsymbol{\rho}) \left\{\iint_{-\infty}^{\infty} \sum_j S(\mathbf{k}_j,\omega_j) e^{i[\mathbf{k}_j\cdot\boldsymbol{\rho}' - \omega_j\tau]} e^{i[\omega\tau - \mathbf{q}_\perp(\boldsymbol{\rho})\cdot\boldsymbol{\rho}']} d\boldsymbol{\rho}' d\tau\right\} d\boldsymbol{\rho}. \tag{C.8}$$

Assuming the stationarity of the spectrum, the sum in the second term on the right hand side of equation (C.8) can be taken outside of the integrals. The integrals within the curly brackets represent delta functions, as

$$
\begin{aligned}
&S_D(\mathbf{M},\omega) = \\
&-\frac{1}{32\pi^3}\int_{-\infty}^{\infty}\frac{D_m^2(\boldsymbol{\rho})D_s^2(\boldsymbol{\rho})}{R_m^2(\boldsymbol{\rho})R_s^2(\boldsymbol{\rho})}q_z^2(\boldsymbol{\rho})\left[1-q_z^2(\boldsymbol{\rho})\sigma^2\right]\delta(\omega)\delta(\mathbf{q}_\perp(\boldsymbol{\rho}))d\boldsymbol{\rho}+ \\
&-\sum_j\frac{\sigma^2}{32\pi^3}\int_{-\infty}^{\infty}\frac{D_m^2(\boldsymbol{\rho})D_s^2(\boldsymbol{\rho})}{R_m^2(\boldsymbol{\rho})R_s^2(\boldsymbol{\rho})}q_z^4(\boldsymbol{\rho})S(\mathbf{k}_j,\omega_j)\delta(\omega-\omega_j)\delta(\mathbf{q}_\perp(\boldsymbol{\rho})-\mathbf{k}_j)d\boldsymbol{\rho}.
\end{aligned}
\tag{C.9}
$$

If equation (3.118) is valid, then

$$
d\mathbf{q}_\perp = -\kappa\left[\frac{R_s+R_m}{R_sR_m}-\frac{1}{R_{s,m}}\mathcal{O}\left(\frac{\rho^2}{R_{s,m}^2}\right)\right]d\boldsymbol{\rho}\approx-\kappa\frac{R_s+R_m}{R_sR_m}d\boldsymbol{\rho}. \tag{C.10}
$$

Changing the variable of integration in equation (C.9) to $\mathbf{q}_\perp(\boldsymbol{\rho})$ results in equations (3.119) and (3.120).